Studies in bacterial phosphotriesterase evolution, dynamics, and engineering

A thesis submitted for the degree of Doctor of Philosophy of the Australian National University

Australian National University

Eleanor C. Campbell

November 2017

DECLARATION

The work presented in this thesis has been performed by the author under the supervision of Associate Professor Colin J. Jackson at the Australian National University. Some experimental work presented was carried out by the author in the laboratory of Associate Professor David W. Lupton at Monash University.

Work presented in Chapter 2 of this thesis takes the form of two thematically-linked peer-reviewed publications, the author's contributions to which are outlined in the statements preceding the articles.

The structural data in Chapter 3 was collected, processed, refined and analysed by the author, and is presented alongside mutagenesis and kinetic characterisation performed by Dr Charlotte Miton in the laboratory of Dr Nobuhiko Tokuriki. Some structural analysis was performed by Ms. Hannah Bott under the supervision of the author.

Chapter 4 of this thesis consists of a peer-reviewed publication. Experimental work presented within was carried out by the author, with contributions from colleagues as follows; Mr. Mahakaran Sandhu assisted with enantioselectivity assays under the supervision of the author, Dr Jacob Grant synthesised the substrates and performed HPLC analysis in the laboratory of Associate Professor David W. Lupton, and Ms. Yi Wang synthesised the hydrogels under the supervision of Dr David R. Nisbet.

The work presented in this thesis has not been submitted as part of any other degrees.

Eleanor C. Campbell

ACKNOWLEDGMENTS

I would like to acknowledge the Australian Government for support through the Research Training Program Scholarship, and the Australian National University and Research School of Chemistry for support through the Alan Sargeson Merit Scholarship and the Research School of Chemistry Scholarship.

I must firstly express my gratitude to my supervisor Associate Professor Colin Jackson, who took me in as a third year undergraduate and taught me how to use a Gilson pipette. I am heartened to see academics like him becoming the norm, and I know he will continue to represent the best interests of students, and encourage the world of research to become more diverse and inclusive.

My sincere thanks must go to all of our collaborators for providing their expertise and support. My thanks to Associate Professor David Lupton for hosting me in his lab a number of times; Jacob Grant for his wisdom and resilience; Dr Adam Perriman for allowing me to spend some time working with his group; Ben Carter and Dr James Armstrong for their insight; and Dr Nobuhiko Tokuriki and Dr Charlotte Miton for challenging me with an increasingly eclectic set of variants to crystallise.

I would also like to thank my non-research-based collaborators; Sanjana Alex for turning one of my projects into a high-fashion garment, Oscar Mortlock for turning another project into an excellently nerdy T-shirt design, the cast of the Fuzzy Logic Science Show for giving me a platform to gush about crystallography and astrobiology, and the wonderful organisers of National Science Week for including me in panels and projects. Special thanks to everyone involved in teaching at the Research School of Chemistry, particularly Dr Mark Ellison and the Teaching Fellows; learning how to teach has been a highlight of this experience, and the RSC has been a fantastic environment to put these skills into practice.

To the Jackson Group in all its many iterations over the years, thank you for being a bizarre mix of personalities and neuroses. The abundance of mystery gifts, the harebrained schemes to acquire a group sushi train/sandwich press/3D printer, the near-deadly hikes in the Australian wilderness, and the collective avoidance of the Success Gong have made this experience all the richer.

I have to thank a substantial list of people I don’t know personally for the hours of comfort and entertainment they have provided in the more stressful patches of these projects; the extended

McElroy clan and the good people at Polygon for endless content; Elis and John for lighting the darkness and cleansing the world of Shame; Tom, Ben and Matthew for the puns; Austin and his friends for their world-building; Scooter for being boring; and John for his Souvenir Programme. PJ and Alex are the feeling of looking up from your computer screen and noticing the colour of the sky.

To my friends inside and outside of the RSC, thank you for being around for board games, trivia, Dungeons & Dragons, food and wine. Thank you to Lee, Jason and Louis for looking after me during my first out-of-home experience. Thank you to Michael for his unwavering support, for the useful scientific discourse, and for knowing when I need solutions and when I just want sympathy.

To Mum, Dad, Maggie, Shane and Clara; I cannot thank you all enough for your support. I have been so lucky to have you all nearby while I study. No matter where my work takes me in the future, home will always be wherever you all are.

ABSTRACT

The potential value of biocatalysts across a range of fields is substantial but not fully realised. This is due to shortcomings in both the inherent properties of enzymes, and in our understanding of how to engineer and design improved versions of the molecules we find in nature. The work presented in this thesis aims to address these shortcomings *via* two distinct approaches:

First, I aim to do this by studying the molecular evolution of enzyme function, particularly in relation to protein dynamics and mutational epistasis. The intersection of these concepts is poorly understood and could be particularly relevant to the design and construction of novel biocatalysts. To investigate the role of dynamics and epistasis in the process of molecular evolution, three laboratory directed evolution experiments were investigated; the evolution of bacterial phosphotriesterase (PTE) towards the hydrolysis of a promiscuous arylester substrate 2-naphthylhexanoate (2NH), (R0 to R22); the 'reverse' evolution of this final variant towards phosphotriesterase activity (R22/Rev0 to NeoPTE/Rev12); and a constrained evolution, incorporating a non-ideal initial substitution into PTE and evolving for enhanced hydrolysis with 2NH, (S1 to S8). X-ray crystal structures of a number of these evolutionary intermediates, endpoints, and rationally designed variants together comprise a substantial dataset that can reveal structural and dynamic changes that underpin the functional changes observed throughout the various evolutions. In the initial R0 to R22 trajectory, it was determined that unproductive conformational sub-states were 'frozen out' throughout the experiment; motions valuable in the catalysis of the native phosphotriester substrate were eliminated through intramolecular hydrogen bonding and electrostatic networks. In the reverse trajectory (Rev0 to NeoPTE), the effects of an 'epistatic ratchet' were observed; the reacquisition of native activity occurred *via* a distinct genetic pathway, although reached a similar phenotype. This implies inherent epistatic restrictions in the reversal of an evolutionary trajectory. In the third trajectory, S1 to S8, the incorporation of an initial non-ideal substitution resulted in the evolutionary pathway reaching a distinct fitness peak, both genotypically and phenotypically. The constraints placed on the evolutionary trajectory through the initial substitution were substantial. The changes in dynamics throughout this trajectory were significantly different from those observed in the original R0 to R22 experiment, indicating evolution's capacity to find multiple solutions to the same problem. These observations could prove valuable in future engineering efforts; tuning of protein conformational sampling to optimize a particular function

appears to be possible, and these observations could aid in the continued application of this method of engineering.

The second methodology investigated in this thesis is that of enzyme immobilization and the engineering of functional materials. The application of enzymes in chemical synthesis, environmental bioremediation and medicine is limited by their longevity and stability towards organic solvents. In order to address these natural shortcomings of biocatalysts, proteins can be immobilized. Numerous immobilization techniques exist, and each has its own advantages and deficits. For example, immobilization through covalent attachment is robust, but may require the use of harsh conditions for immobilization, and often the solid supports cannot be recycled. Ionic immobilization is a gentler alternative, but can result in undesirable 'leaching' of protein from the solid support. Incorporation into gel matrices can have similar shortcomings. To circumvent these deficits in immobilization techniques, it is possible to engineer enzymes to better suit the medium onto which they are to be immobilized. Additionally, the combination of ionic immobilization and gel entrapment though the use of a charged hydrogel as the chosen support can address the failings of each technique in isolation. Work in this thesis details the engineering of a 'supercharged' enzyme and its immobilization in anionic hydrogels. The enzyme:hydrogel complexes showed no loss of catalytic activity after 100 days of use and were resilient to methanol and ethylacetate. They were also successfully employed in the kinetic resolution of a racemic mixture of a phosphoester substrate in continuous flow. The use of enzyme:hydrogel complexes is likely to be of value in a diverse range of applications such as enantioselective continuous-flow chemistry, detoxification of poisons, and the formation of functionalized biomaterials.

Through the combination of these two distinct strategies – fundamental research of evolution of novel function, and application-driven production of biomaterials – our understanding of biocatalysts and their applications is expanded. Developing engineering strategies that mimic nature's precise adjustment of protein dynamics, and combining the powerful catalysts that result with novel materials, will open avenues of catalysis that can be readily applied to medicine, environmentally-friendly syntheses, and large scale industrial processes. Our reliance on harsh chemical techniques is unsustainable, and biocatalysis represents an environmentally responsible future.

TABLE OF CONTENTS

ABBREVIATIONS

2NH	2-napthyl hexanoate
AE	arylesterase
***ar*PTE**	phosphotriesterase from *Agrobacterium radiobacter*
DMF	dimethylformamide
DMPA	N,N'-Dimethyl-1,3-propanediamine
DNA	deoxyribonucleic acid
dNTP	deoxyribonucleotide triphosphate
EDC	1-Ethyl-3-(3-dimethylaminopropyl)carbodiimide
FACS	fluorescence-activated cell sorting
FTIR	Fourier-transform infrared spectroscopy
GFP	Green Fluorescent Protein
GR	glucocorticoid receptor
HLN	hexyl(naphthalen-2-yloxy)phosphinic acid
MD	molecular dynamics
NMR	nuclear magnetic resonance
PACE	phage-assisted continuous evolution
PCR	polymerase chain reaction
PON1	serum paraoxonase 1
PTE	phosphotriesterase from *Pseudomonas diminuta*
RMSD	root-mean-square deviation
RNA	ribonucleic acid
StEP	Staggered extension process
TEM	transmission electron microscopy
WT	wild type

CHAPTER 1:
EVOLUTION AND ENGINEERING - BROADENING THE APPLICATION AND UNDERSTANDING OF BIOCATALYSIS

PART 1

1.1 Directed Evolution

The evolution of organisms is caused by evolution at a molecular level. Cumulative changes in genotype are selected for by the fitness of the corresponding phenotype in response to a survival pressure. By this mechanism, populations are enriched with phenotypes better adapted to their environments, propagating the valuable genotype. The results of this are biocatalysts that are, in some cases, so finely tuned to their roles that they are limited only by the rate of diffusion of substrates into and out of their active sites. To exploit the power of these catalysts in industry, synthesis, and medicine by modifying or engineering improved traits, the mechanisms of molecular evolution must be deeply understood.

Directed evolution is a technique pioneered by Frances Arnold and Willem Stemmer. The technique aims to mimic natural evolutionary processes by introducing sequence diversity into a gene of interest, and selecting mutants that show an increase in 'fitness', or enhancement of a desired trait **(Figure 1.1)**. In the early 1990s, Chen *et al.* utilised random mutagenesis and screening to develop a variant of subtilisin E that was 256 times more efficient in 60% DMF than the wildtype[1,2]. The random mutagenesis in this instance was achieved through error-prone PCR. In 1994, Stemmer demonstrated the application of *in vitro* homologous recombination (shuffling) in the evolution of cefotaxamine resistance of a p-lactamase system[3]. A pool of DNA fragments was obtained through the DNase I digestion of a gene of interest, and these fragments were allowed to recombine by primerless PCR[4]. The error rate of the DNA polymerase used ensured the incorporation of random mutations. The application of this technique saw a 32,000-fold increase in antibiotic resistance in the model system; this significant improvement relative to error-prone PCR (16-fold increase in resistance) was attributed to homologous recombination's enhanced capacity to search sequence space. These pioneering studies paved the way for widespread application of directed evolution as a technique for protein engineering and investigation of natural evolutionary processes.

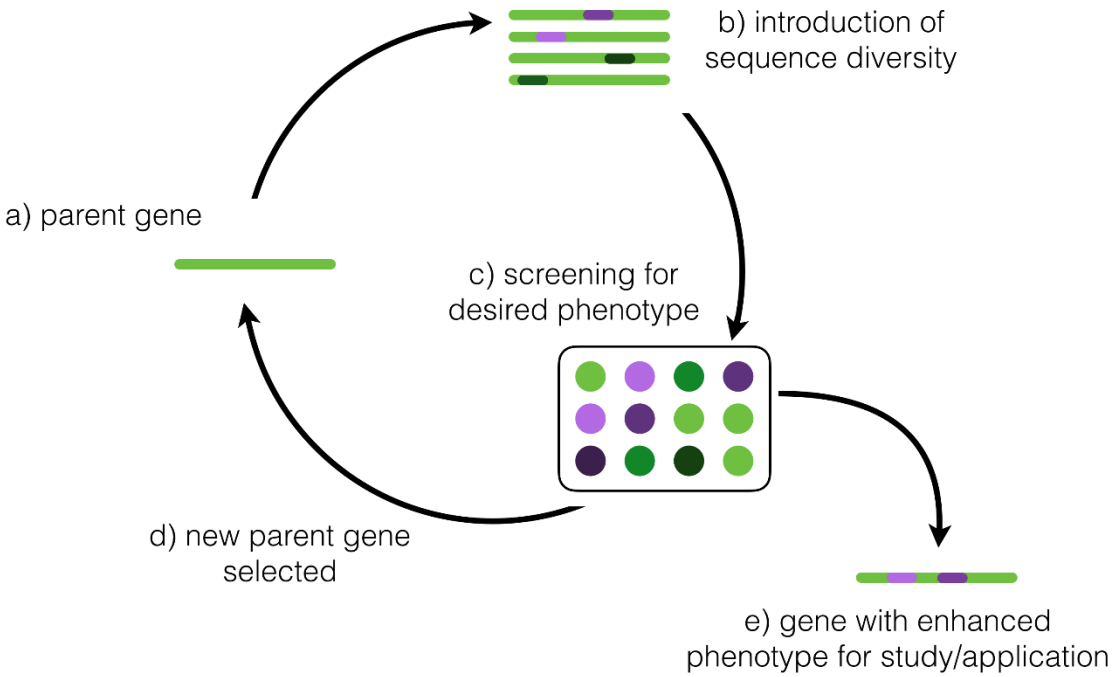

Figure 1.1 | A general workflow of laboratory directed evolution. a) A gene of interest is selected for evolution. b) A library of mutants is created through error-prone PCR, gene shuffling, staggered extension PCR, etc. c) Resulting variants are screened for the desired phenotype. d) A selected variant is isolated and used for the next round of directed evolution, or several variants are recombined to serve as a new parent gene. Stages a) to d) are repeated as required. e) The product of the directed evolution experiment, a gene encoding the enhanced phenotype, is isolated.

Methods for directed evolution have, themselves, evolved since the early 90s. The generation of mutant libraries is typically achieved through the use of error-prone PCR (random mutagenesis), site saturation mutagenesis, (focused mutagenesis) or homologous recombination (gene shuffling). *In vitro* error-prone PCR exploits the low fidelity of DNA polymerases in the presence of non-natural levels of manganese or magnesium[5,6]. When a gene is amplified by PCR under these conditions, mutation rates can be increased to 10^{-4} – 10^{-3} per base. This represents a controlled method of introducing sequence diversity, as the number of PCR cycles correlates with the number of mutations acquired. Error-prone PCR can also be achieved through the use of nucleoside analogues; PCR carried out in the presence of synthetic derivatives of dNTPs results in the incorporation of transition and transversion mutations, once again, at rates controlled by the number of PCR cycles[7]. If previous structural/functional knowledge of the system to be evolved is available, site saturation mutagenesis can be the more efficient technique. In this focused approach, individual codons can be targeted through the

application of cassette mutagenesis, generating libraries consisting of mutants varying at defined sites[8]. This technique can be used to generate combinatorial libraries, where numerous positions are scanned, revealing sites amenable to mutation and identifying regions that do not tolerate variation[9]. Homologous recombination, as discussed above, allows for mutations from different lineages to be combined, resulting in chimeric genes[4]. Alternatively, the staggered extension process (StEP) can be used to exploit partially-elongated PCR products, allowing those products to recombine through annealing[10].

After the generation of a library, the properties of mutant genes must be screened in order to identify beneficial mutations. Numerous methods for screening of libraries of mutants exist, and the efficiency of their application is dependent on the size of the library to be screened. Screening methods must incorporate a mechanism by which genotype and phenotype can be linked; once desirable phenotypes have been identified, there must be a method for retrieving the corresponding genetic information. Low-throughput screens like those employed by Chen *et al.* in the early advent of directed evolution can depend on the manual inspection of colonies on agar plates, and genetic information can be obtained by sequencing the colonies of interest[2]. Proteins with fluorescent or colorimetric properties can be similarly screened. Libraries in the order of 10^2 – 10^4 variants can be assessed this way[11]. To screen larger libraries, higher throughput methods are required. Cell surface display and phage display allow screening of candidates based on their binding to an immobilised target, and genetic information can be retrieved from the cell or bacteriophage. These methods can see libraries of 10^8 (cell surface display) to 10^{10} (phage display) screened. The use of water-oil emulsions to mimic the compartmentalisation of a cell membrane has resulted in the development of several high-throughput screening methods. *In vitro* compartmentalisation (IVC) utilising fluorescence activated cell sorting (FACS) can be used to identify fluorescent proteins or fluorescent products of enzymatic reactions, and can be applied to libraries of 10^{10}. Compartmentalisation in water-oil emulsions can also allow for screening of nucleases, DNA ligases, polymerases, and tRNA synthetases, with similar library sizes. The development of phage-assisted continuous evolution (PACE) has allowed for rapid screening of libraries consisting of up to 10^{12} mutants. By co-opting the infection cycles of bacteriophages, the expression of a desired trait can be linked to the bacteriophages' capacity to infect and hence replicate. Esvelt *et al.* demonstrated the application of PACE through the evolution of T7 RNA polymerase to recognise novel promoters, subjecting their system to 200 rounds of evolution in 8 days[12].

The generation and screening of libraries has allowed the close study of evolution on the single-molecule scale. While higher throughput techniques allow wider sequences spaces to be searched for adaptation, these methods typically neglect several aspects of natural evolution; genetic context and gene regulation[13,14], population competition and coorperativity[15], and the requirement of an organism to adapt in response to numerous selection pressures[16]. In nature, the evolution a protein does not take place in a vacuum, and adaptation on a cellular or organism level introduces new complexities. Its limitations in the broader context of evolutionary biology should be acknowledged, but directed evolution remains a powerful tool for investigating adaptation on a mechanistic level.

One appeal of directed evolution is the accessibility of intermediates along the evolutionary pathway. While the phylogeny of existing proteins can be established using methods like Maximum Likelihood reconstruction of ancestral sequences[17], directed evolution experiments provide insights that are otherwise inaccessible; having access to the entire trajectory of evolution that has occurred to reach a given end point allows for stepwise analysis of variants along a pathway, providing insights into the structural underpinnings of a functional change. Further, directed evolution does not necessarily rely on prior knowledge of the system of interest, allowing its application to proteins with unknown structures. Information gleaned from 'irrational' directed evolution experiments can inform future rational design experiments, as demonstrated by Paritala *et al.* in work that utilised directed evolution to identify previously unknown functional sites in the sulfur metabolism enzyme PAPR[18].

De novo design of proteins can benefit from the process of directed evolution. The computationally designed Kemp eliminase enzymes presented in work by Röthlisberger *et al.* initially demonstrated k_{cat}/K_M values in the range of 6 to 160 M^{-1} s^{-1} [19]. After the application of directed evolution, consisting of seven rounds of library generation and selection, Röthlisberger and co-workers obtained a variant with a 200-fold increase in catalytic efficiency. Subsequent analysis of the variants obtained along this trajectory afforded insights into the structural basis of the changes[20]. Directed evolution has been utilised to improve the efficiency of a number of de novo proteins, including retro-aldol enzymes[21] and Diels-Alderases[22], and has also found application in the design of protein-protein complexes[23].

Directed evolution experiments reveal fundamental aspects of the natural evolution process. Tokuriki *et al.* exploited the promiscuous activity of a bacterial phosphotriesterase (PTE) for arylester hydrolysis, and developed an 18 round experiment illustrating the trade-off between

the two activities, as well as the diminishing returns of later round mutations[24]. The trade-off between activities was asymmetrical, with specificity for the arylester substrate developing late in the trajectory (round 14); at the midpoint of the trajectory both activities were catalysed with high efficiency ($k_{cat}/K_M \sim 10^5$ for phosphotriester and arylester substrates) **(Figure 1.2)**. The functional promiscuity of many enzymes, thought to be a result of divergent evolution, is well-established[25], and this asymmetrical trade-off provides insights into the mechanisms of specialisation of biocatalysts; the absence of a selection pressure for phosphotriesterase activity mirrors the release from selection pressure that accompanies gene duplication events[26], allowing for promiscuous activities to be optimised.

The diminishing returns of the trajectory were attributed to the 'radiation' of mutations from the active site; later round mutations were generally distant from the active site, and only 4 of the 18 mutations accumulated were found in the first shell of the active site. The early increases in arylesterase activity were a result of mutations in or near the active site, while later round mutations stabilised earlier ones, built networks of redundancy, and compensated for the destabilising effects of the initial function-altering mutations. **(Figure 1.2)**

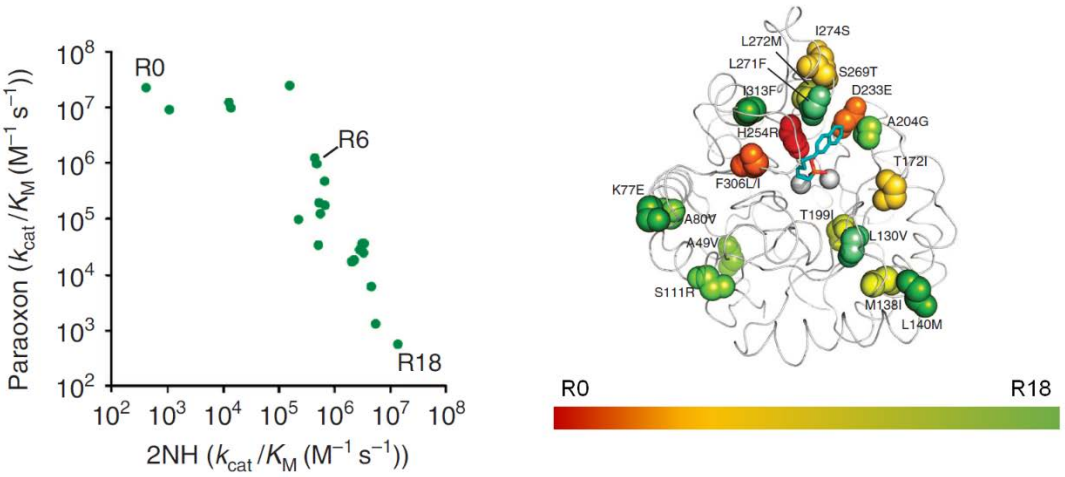

Figure 1.2 | The asymmetrical trade-off of phosphotriesterase and arylesterase activities (left), and the positions of mutations accumulated throughout the trajectory (right). While early round mutations are proximal to the active site, later round mutations radiate outwards. The active site is illustrated by bound transition state analogue HLN (teal sticks) and Zn^{2+} (white spheres). Figures adapted from Tokuriki et al.[24]

The diminishing returns of functional optimisation are well-documented, both in evolutionary biology[27–29] and in numerous other disciplines[30], and can, in some cases, be attributed to epistasis.

1.2 Epistasis

Epistatic effects are those in which the fixation of a mutation can have varying effects based on the genetic context into which it is introduced. In work by Chou *et al.*, diminishing returns in the directed evolution of engineered bacteria *Methylobacterium extorquens* AM1 for growth on methanol were attributed to epistatic effects[31]. The rational combination of beneficial adaptations in three separate alleles demonstrated 'magnitude epistasis' **(Figure 1.3)**; the higher the fitness of the genetic background, the lesser the effect of the beneficial adaptions. 'Sign epistasis' is a more extreme example of the importance of genetic contexts in the accumulation of mutations: a mutation that is advantageous in one genetic context can be deleterious in another[32] **(Figure 1.3)**. The result of this is that the order of accumulation of mutations can be as vital to evolution as the identities of those mutations. Where sequence space can be visualised as an evolutionary landscape, epistatic effects can be equated to the limitations that constrain the pathways that lead uphill to fitness peaks.

In work by Kvitek and Sherlock, two individually adaptive mutations (in different loci) in the directed evolution of *S. cerevisae* were determined to be deleterious when expressed in the same mutant[33]. This represents a 'reciprocal sign' epistatic effect **(Figure 1.3)**; one in which a deleterious 'valley' exists between two local fitness peaks, preventing the progression of one lineage towards higher fitness.

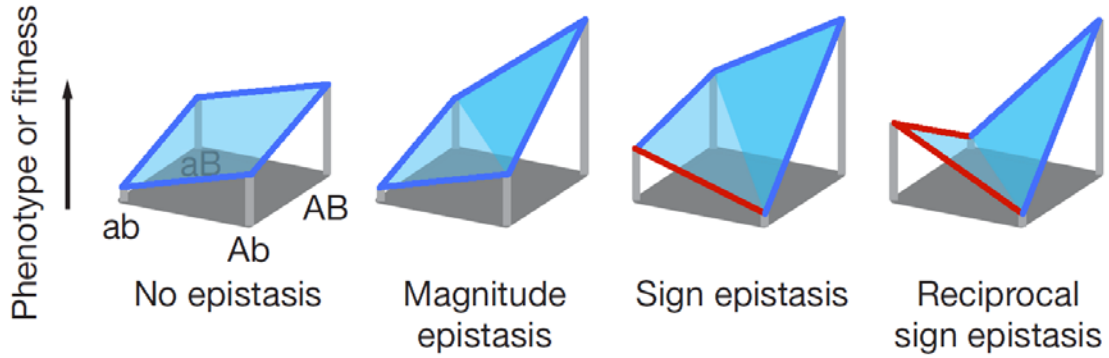

Figure 1.3 | Visual representations of a simple evolutionary trajectory from ab to AB. Blue edges represent 'allowed' pathways, along which fitness is enhanced. Red edges represent 'disallowed' pathways, or deleterious mutations. No epistasis: each mutation is equally beneficial, regardless of genetic context. Magnitude epistasis: the second mutation acquired has a greater beneficial effect in the genetic context. Sign epistasis: the acquisition of mutation A is deleterious on background ab, but beneficial against aB. Reciprocal sign epistasis: the highest fitness peak, AB, is inaccessible from ab as both pathways require acquisition of deleterious mutations. Figure adapted from Poelwijk et al.[34]

Epistatic effects can exist on genomic scales, as described above, but also in individual proteins. Work by Ortlund *et al.* reports the crystal structure of a resurrected ancestor of a vertebrate glucocorticoid receptor (GR)[35]. Ortlund *et al.* showed that evolution of the GR saw its preference for its ligand alter from aldosterone to cortisol, and that the main cause for this change in preference was an epistatic pair of mutations, Ser106Pro and Leu111Gln. One mutation introduced a potential receptor-ligand contact, while the second altered the conformation of an α-helix, positioning the first mutation such that the new receptor-ligand contact could be made. Without the conformational change caused by Ser106Pro, Gln111 would not be correctly oriented to contact cortisol. Bridgham *et al.* subsequently introduced the concept of an 'epistatic ratchet' in which key mutations in the evolution of modern GR to become specific for cortisol were shown to be irreversible; the receptor could not be mutated in the reverse order to re-acquire aldosterone specificity[36]. The basis for this was the epistatic relationship between the mutations. While the reversion of either Ser106Pro or Leu111Gln abolished cortisol binding, neither back-mutation alone provided any increase in aldosterone binding, meaning they could not be 'selected for'. Through the analysis of these mutations, Bridgham *et al.* determined that any reversion to the receptor's ancestral ligand would have to occur via an alternate pathway, as these 'ratchet' mutations form an evolutionary barrier that cannot be overcome by traditional selection and screening.

The constraints placed on evolutionary processes by epistatic effects are numerous but difficult to identify as extant proteins have already overcome epistatic barriers (or accumulated beneficial or permissive epistatic mutations) in order to exist. However, techniques for the investigation of epistasis in a broader, evolutionary context have been developed, making use of ancestral sequence reconstruction[37] (as above) and/or directed evolution[38].

In instances of directed evolution, the generation of mutant libraries plays a role in the visibility of epistatic effects. There is a relationship between the rate of mutation used to generate libraries, and the effects likely to be observed. In experiments with low rates of mutation – one mutation per mutant – single beneficial mutations will accumulate in a stepwise fashion. As they often require the concurrent acquisition of at least two mutations, rare sign epistasis events are more likely to be observed in experiments where the rate of mutation is high[38]. There are, however, instances of epistatic effects being indirectly introduced during an evolutionary trajectory; in work by Yang *et al.*, a native active site residue (Phe68) was repositioned through the introduction of two mutations (Val69Gly and Phe64Cys) during the directed evolution of bacterial lactonase (AiiA) for enhanced phosphotriesterase activity[39]. While the identity of

residue 68 did not change during the trajectory, its catalytic role did. Epistatic constraints on the trajectory were identified through alanine scanning mutagenesis; Phe68Ala was beneficial on the WT background, but deleterious against either Val69Gly or Phe64Cys, meaning that early mutation at position 68 may have trapped the system at a local maximum and prevented the accumulation of beneficial mutations at positions 64 and 69. This serves to demonstrate the high degree of complexity in an evolving system, and the challenge of mimicking nature's biocatalyst optimisation in the laboratory.

The degree to which evolution is limited within sequence space has been demonstrated elegantly by several works, including that of Weinreich *et al.*, in which they constructed and analysed the 32 possible combinations of five mutations previously identified to increase bacterial resistance to antibiotic cefotaxime[40]. The identification and mapping of neutral, beneficial and deleterious mutational effects in each combination resulted in the elimination of 102 of the possible 120 pathways that could lead to the resistant gene. This illustrates the degree to which mutational trajectories are constrained by the 'optimisation algorithm' of evolution; escaping a local maximum would require the selection of 'less fit' phenotypes, which cannot happen under typical directed evolution conditions. Nature has methods to subvert this, however: gene duplication and neutral drift. When a gene is duplicated, one copy will no longer be under strict selective pressures; organismal fitness is ensured through the maintenance of one copy, allowing the second to explore sequence spaces that may not have been possible under a selection pressure[41].

1.3 Conformational Dynamics and Evolution

The conformational dynamism of proteins is well established. Proteins undergo conformational change at a variety of time scales. On the shortest of these timescales (fs-ps), bonds vibrate and side chains rotate. On longer time scales (ns-ms), macroscale motions can take place; loops 'open' and 'close', and domains can twist relative to each other or move on hinge-like regions **(Figure 1.4)**. These larger motions are an area of continuing debate; while a large, flexible system like a protein is expected to possess conformational dynamism, how do these conformations affect the catalytic function of the enzyme? Works seek to establish the role of conformational dynamics in the catalytic step[42], and others indicate that experimental models have not yet conclusively demonstrated this link[43]. While the link, or lack thereof, between conformational dynamics and the catalytic step remains a topic of controversy, the role of protein dynamism in substrate binding is well studied[44–47], and cascades of conformational

change underpin numerous biological functions[48]. A further area of investigation is that of molecular evolution, and the degree to which conformational dynamics affects the evolution of protein function.

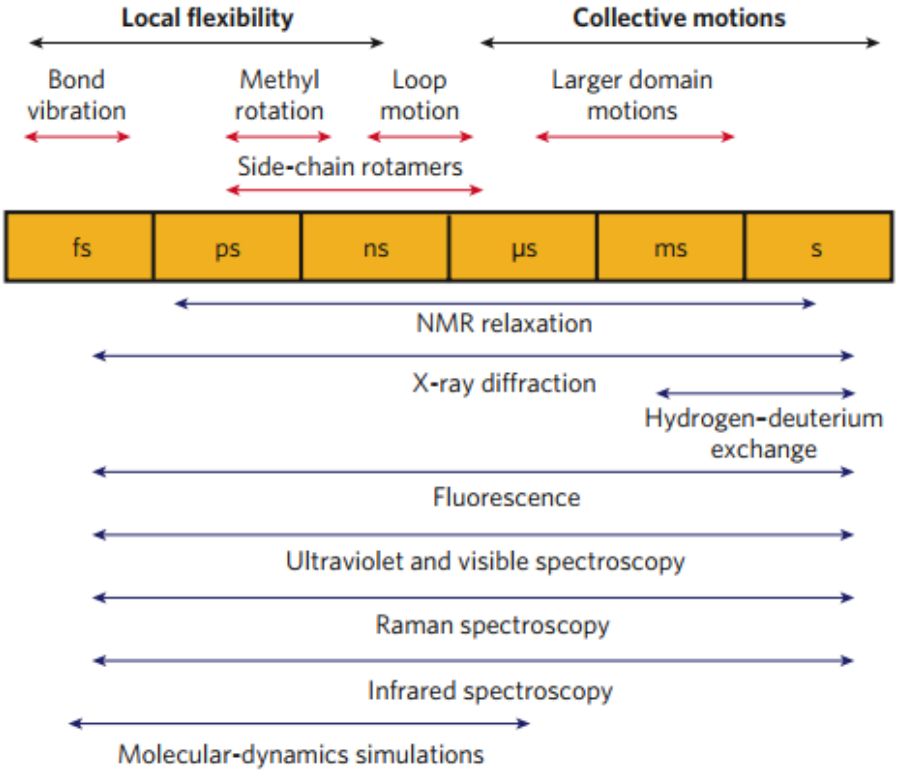

Figure 1.4 | Protein motions, the timescales on which they occur, and the tools used to quantify them. Figure from Henzler-Wildman et al.[49].

Both natural and directed evolutions point to a number of factors that affect the propensity for proteins to evolve, or their 'evolvability', and conformational dynamism plays a substantial role.

The interplay between the thermodynamic stability of a protein and its tolerance to substitutions is well documented, and a trade-off between enhanced activity upon incorporation of mutations and the stability of the protein has been consistently demonstrated[50–52]. Individual mutations are generally neutral or, on average, deleterious. A computational survey of 21 globular proteins found that mutation of surface residues was, on average, mildly destabilising ($\Delta\Delta G \sim 0.6$ kcal/mol), while mutation of core residues was more destabilising ($\Delta\Delta G \sim 1.4$ kcal/mol)[53]. The trade-off between enhanced catalytic activity and thermodynamic stability has been demonstrated in the study of mutant TEM-1 β-lactamases. Mutants with increased activity

against cephalosporin antibiotics showed decreased thermodynamic stability, and lower activity with their original penicillin substrates[54]. Conversely, substitution of *catalytic residues* has been demonstrated by Beadle and Shoichet to be thermodynamically stabilising, albeit detrimental to catalytic function[50,55]. This has been attributed to the nature of enzyme active sites, which must inhabit a higher energy state that is preorganised to accept a substrate and facilitate catalysis[56].

Further studies by Bloom *et al.* relate the structural stability of a protein to the number of mutations accumulated, and predict an exponential decline in the likelihood of structure being retained with increasing numbers of substitutions[57]. Hence, proteins that possess greater thermodynamic stability are more amenable to the accumulation of substitutions[58]. The margin of permitted destabilisation was quantified in a model system, TEM-1 β-lactamase, by Bershtein *et al.*[59]. The notion of 'threshold robustness' was introduced; under low selection pressure, the majority of mutations were tolerated, but significant magnitude epistasis was observed after a stability 'threshold' was crossed, and deleterious effects of multiple substitutions compounded. The maintenance of structural stability in the face of mutation would suggest that highly stable, rigid proteins would be the best candidates for evolution; their structural stability could mitigate the destabilising effects of function-altering mutations. This is, however, not strictly the case; robustness alone cannot explain the capacities of some enzymes to evolve more than others.

It is well-established that many, if not most, enzymes possess some degree of promiscuity; the capacity to turn over multiple substrates, or to catalyse multiple chemical reactions[60]. Of the several factors that underpin enzyme promiscuity, conformational flexibility is particularly fascinating; the capacity of a protein to interact with numerous ligands subverts both induced-fit[61] and lock-and-key[62] models of substrate recognition and binding. A newer model proposes conformational diversity as the cause of functional promiscuity; a pre-existing equilibrium of different protein sub-states, each state differently capable of interacting with a number of ligands[63]. A number of examples of different functions being linked to distinct conformations of the same protein exist. The capacity of cytochrome P450 3A4 to bind two structurally distinct drugs has been attributed to substantial conformational changes of the active site[64]. A bifunctional variant of $(\beta\alpha)_8$ barrel HisA was observed to adopt two distinct loop conformations, with one conformation productive for each activity[65]. Studies of IgE antibody (SPE7) revealed that promiscuous interactions occurred *via* specific means; each of the four

ligands crystallised in complex with SPE7 showed distinct binding modes, with subtle conformational variations accompanying each[66].

Linking this model of functional promiscuity to molecular evolution provides a new framework in which to look at the evolution of new function; flexible, dynamic proteins are more likely to possess promiscuous activities, which can be selected for and enriched through evolution **(Figure 1.5)**. The functional divergence of duplicated intrinsically disordered proteins supports this notion; the numerous metastable conformations accessible to intrinsically disordered proteins allow for interaction with an array of binding partners[67]. This framework, however, has limitations. New enzymatic function can evolve *de novo;* the ancestors of modern proteins do not always possess the modern activity, highlighted in particular by the evolution of enzymatic function from non-catalytic ancestors[68–70]. Additionally, high conformational freedom is associated with low structural stability, a factor already identified as being valuable in evolution. In fact, work by Dellus-Gur *et al.* highlights that while conformational flexibility can be important in the evolution of new function, the introduction of too much dynamism or disorder can impede evolution through negative epistasis[71]. It is important to note, also, that high conformational freedom is not a necessity for efficient catalysis; the ancestral reconstruction of ancient adenylate kinases by Nguyen *et al.* resulted in the identification of a highly thermostable, rigid ancestor that demonstrated high catalytic efficiency at low temperatures[72]. In fact, it is suggested that evolution minimises unnecessary motions, and enriches populations of conformations required for a given function[73,74].

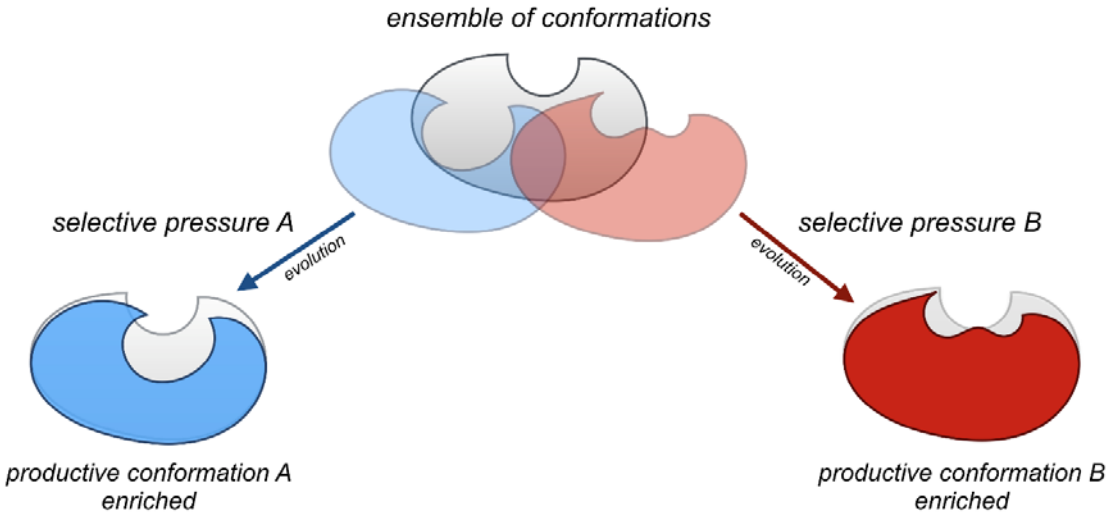

Figure 1.5 | An ensemble of conformations results in catalytic promiscuity. Selection for one of these activities results in the enrichment of the relevant conformation, and the 'freezing out' of non-productive motions. Figure adapted from Campbell *et al.*[75]

Combining and balancing robustness and innovability has resulted in a more nuanced hypothesis; evolvability requires structural 'polarity'; a stable, often rigid scaffold, and a higher energy, conformationally dynamic active site[76,77]. This view can incorporate observations from Tokuriki's analysis of core and surface mutations, (that they are, on average, detrimental to stability, although surface mutations less so[53]), and Shoichet's study of catalytic residues (that their substitution is stabilising, reflecting the necessity of a high energy, preorganised active site for catalysis[50,56]). Taken together, a pattern emerges; surface regions and loops, often involved in substrate diffusion and catalysis, are conformationally and mutationally dynamic[78]; the hydrophobic core is rigid and confers thermodynamic stability, thus is less amenable to nonconservative substitution[79–81]; and catalytic residues, which are highly conserved for a *particular function*, are energetically dynamic and therefore readily substituted in the acquisition of *new chemistry*[82].

The greater the 'disconnect' between the scaffold, loops, and active site, the more likely the development of novel conformational sub-states and hence functions. The scaffold mitigates destabilising substitutions, and can itself take on stabilising mutations without directly affecting the functional sites of the protein, and the functional sites and flexible loops can undergo mutagenesis to obtain new function without pushing the protein past its thermostability threshold.

To better understand these synergistic roles, multiple conformations of proteins must be visualised and characterised. Methods for the qualification and quantification of sub-states are varied. Solution NMR allows monitoring of motions from the ps to s range[83], and computational modelling of proteins can provide information about the energy minima that represent different sub-states, and the ways in which proteins can transition from one minimum to another[84].

X-ray crystallography, perhaps counterintuitively, can also provide detailed information about the conformational dynamism of proteins, and was utilised to great effect in the work by Dellus-Gur *et al.* discussed previously[71]. While traditionally viewed as a 'static' method of observation, X-ray crystallography can be readily applied to the study of ensembles of conformations[85]. At the most basic level is the capacity of X-ray crystallography to reveal multiple conformations of a single sidechain; two conformations of a flexible residue can be distinguished by the observation of electron density representing both conformations. In the directed evolution experiment carried out Tokuriki *et al*., two distinct conformations of Arg254, the first mutation fixed, could be visualised in the X-ray crystal structure of the first round variant[24]. Each conformation was productive for one of the activities; Arg254 acted as an activity 'switch', an observation made possible through the modelling of conformational heterogeneity present in the X-ray data.

Manual inspection of electron density typically underestimates the degree of heterogeneity present[86]; a problem exacerbated by traditional refinement techniques[87]. Modelling can be improved through the use of algorithms like qFit, which can identify and occupy instances of multiple side-chain conformations, and, more recently, multiple conformations of short glycine-rich regions and peptide flips[88,89]. The program Ringer has been demonstrated to identify alternative conformations at weak electron density levels ($< 1\ \sigma$), allowing access to conformational data that may otherwise be interpreted as noise by manual modellers[90]. Generation and refinement of an ensemble of conformations can provide information about both the experimental error of the data and the conformational dynamism[91]. Ensemble refinement utilises molecular dynamics (MD) simulations to generate a collection of physically accessible conformations, which are then used to calculate structure factors[92]. This method can be used to identify dynamic regions and improve R_{free} values[93].

While simpler than ensemble refinement, B-factors (or temperature factors) can be used as a proxy for flexibility and hence conformational variability in crystal structures **(Equation 1.1)**.

These values indicate the degree to which electron density is spread or diffused as a result of thermal motions.

$$B = 8\pi^2\langle u^2\rangle$$

Equation 1.1 | Definition of B-factor in the context of protein structures, where $\langle u^2\rangle$ indicates mean square displacement.

In highly flexible regions of a protein, high B-factors correspond to the disorder of electron density resulting from the capture of an ensemble of conformation[94]. Where resolution of multiple conformations is not initially possible, B-factor analysis can at least indicate the lack of a well-defined conformation and guide further investigation.

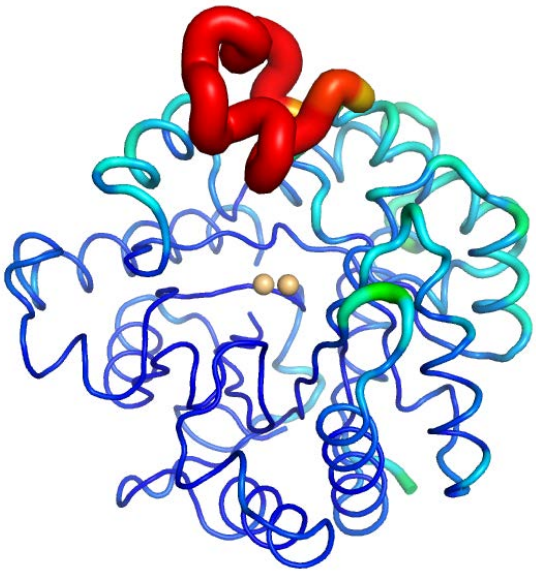

Figure 1.6 | The monomer of PTE variant R0 (4PCP)[74], represented in PyMol's 'sausage' representation and coloured according to B-factor. Highly flexible loop 7 is highlighted in red. Pale orange spheres represent Zn^{2+}.

A criticism of X-ray crystallography is that it is typically carried out at cryogenic temperatures, with streams of nitrogen at 100 K used to reduce the damaging effects of X-ray radiation on crystallised samples. These temperatures result in the capture of a structure in an energy minima that may not be representative of the structure at physiological temperatures or in solution. The practice of snap freezing crystals in streams of nitrogen gas, or indeed by immersing the crystals directly into liquid nitrogen, goes some way to mitigating these effects; a study comparing cryogenic and higher temperature structures found minimal structural differences[95]. The presence of conformational heterogeneity in X-ray data, however, is highly dependent on the temperature of collection[96]. In work by Fraser *et al.*, catalytically relevant

conformations of sidechains in cyclophilin A (CYPA) were deconvoluted through the combined application of Ringer and ambient-temperature crystallography[90,97]. Notably, the data collected at ambient temperatures agreed with sub-states identified through previous NMR analyses[98]. Further, identification of a minor rotamer through ambient-temperature crystallography allowed for the rational selection of a substitution to enrich this conformation, demonstrating the value of this sort of analysis in the biocatalyst engineering. More recently, room temperature X-ray crystallography has been applied to the investigation of redesigned ubiquitin variants[73]. A 'core' variant was designed by Zhang *et al.* for increased binding to deubiquitinase USP7, and then subjected to 'affinity maturation', in which random surface mutations were incorporated and variants screened for enhanced binding[99]. Structures of the 'core' and 'affinity matured' variants were solved through room temperature X-ray crystallography, allowing for the elucidation of conformational heterogeneity in several regions, including the hinge-like β1β2 loop. The 'core' variant possessed substantial heterogeneity in this region, while the 'affinity matured' variant did not, due to the introduction of stabilising interactions. The deliberate introduction of conformational flexibility through the rational selection of 'core' mutations was proposed to disrupt the natural dynamics of protein, allowing the variant to sample a broader ensemble of sub-states, (some of which are valuable in binding the target USP7), while the 'affinity maturation' freezes out non-functional states, resulting in a stabilised, specialised variant.

These works highlight the importance of detailed conformational analysis in protein engineering; rational mutagenesis can have far-reaching effects, shifting the equilibria between sub-states, and molecular evolution or affinity maturation can proceed through indirect alteration of conformational populations.

The intersection of conformational dynamism, epistasis, and molecular evolution is a complex but fundamentally important space. To be best equipped to design and engineer new generations of biocatalysts, the interplay of these factors must be established and understood. The directed evolution experiment carried out by Tokuriki *et al.* is unique in its scope; 18 rounds of selection, later extended to 22 rounds, has resulted in the isolation of 22 variants along the trajectory, meaning that subtle alterations to function can be identified through structural analysis of these intermediates. The role that conformational dynamics plays in the enhancement of promiscuous function can be best understood by the analysis of extant proteins, like these 22 variants.

Chapters 2 and 3 of this thesis address some of these points of intersection between directed evolution, conformational dynamics, and epistasis. The role of conformational dynamics in the PTE to AE trajectory presented in Tokuriki *et al.* is established, and reveals that the optimisation of an alternative activity proceeds through the initial incorporation of destabilising mutations, and then subsequent 'freezing out' of non-productive conformations. The epistatic ratchet is investigated in the context of enzymes, through the analysis of structural data acquired for the 'reversal' of the Tokuriki *et al.* trajectory. Finally, epistatic constraints on evolution and the 'repeatability' of evolution between two known phenotypes are investigated through the development of a new PTE to AE trajectory, containing initial constraints on sequence space that result in a new binding mode of the substrate and the loss of function of an entire loop region that was essential in the old trajectory.

PART 2

1.4 The Application of Biocatalysis

Biocatalysts possess a strange dichotomy, in that the very features that make them desirable tools in synthesis, industry, and medicine, are also often the factors that limit their application.

Most often, enzymes have evolved their high turnover numbers and specificities in physiological environments; neutral pHs, moderate temperatures, aqueous reaction media, and standard atmospheric pressure. In the case of naturally occurring extremophiles, enzyme function may be optimised for much higher or lower temperatures[100,101], substantial salt concentrations[102], or unusual pH values[103,104], but typically, the limitations of naturally occurring catalysts reflect the mild environments in which they evolved. Enzymes in solution have a limited lifespan; enzyme longevity is rarely a necessity *in vivo*. Enzymes therefore often require specialised storage, typically refrigeration or lyophilisation, the latter of which can be destabilising.

Protein engineering seeks to address these shortcomings. Rational mutagenesis or directed evolution can be used to enhance thermostability, substrate preference, or activity in organic solvents. Despite advances in these methods, several barriers to efficient application of biocatalysts remain. One of these is the practical issue of introducing an enzyme to a reaction mixture, and removing it afterwards. The appeal of an enzyme catalyst lies in its capacity to turn over numerous reactions before being depleted, but the separation of catalyst from product in large scale processes is a barrier to application of even the most precision-engineered

proteins. For an enzyme to be used to its full efficiency, it needs to be recyclable and readily removed from a reaction mixture. The immobilization of enzymes on solid supports aims to address these shortcomings.

1.5 Enzyme Immobilisation

In 1916, Nelson and Griffin observed that invertase retained its enzymatic function after having been absorbed on charcoal or aluminium hydroxide[105]. Over a century later, researchers continue to seek flexible, reliable, and applicable methods of immobilising biocatalysts. This has led to the advent of functional materials, blending the fields of biochemistry, materials chemistry, and systems engineering. Enzymes have been immobilised on beads that can be filtered out of reaction mixtures[106]; incorporated into membranes that can be washed and reused[107]; and mounted in columns over which substrates are passed[108].

In addition to the practical issues surrounding removal of catalysts from reaction mixtures, enzyme immobilisation also addresses several other shortcomings of biocatalysts. Immobilised enzymes have been demonstrated to have greater tolerance to organic solvents[109], enhanced lifespans[110], and in some cases, higher activity than enzymes in free solution[111].

Methods of immobilisation are varied **(Table 1.1)**. Covalent attachment involves the chemical crosslinking of natural sidechains or of a modified enzyme surface to a solid support. Covalent attachment can be either site-specific - for example, relying on a novel chemical functionality introduced through unnatural amino acid incorporation - or not site-specific, utilising the reactivity of amines, thiols, and carboxylic acids. Site-specific covalent immobilisation is typically regarded to be superior, as the orientation of the immobilised enzyme on the solid support can affect the activity of the resulting construct[112]. While covalent crosslinking is robust, it has several disadvantages. Covalent attachment can require multiple chemical steps in order to prepare the enzyme or medium for immobilisation, and often requires the application of harsh chemicals that can destabilise the enzyme, reducing the overall efficiency of the immobilisation process. Typically, covalent attachment is irreversible, meaning that once the immobilised enzyme is depleted, the solid media cannot be readily recycled, or will require priming before the addition of new enzyme.

Method of immobilisation	*Advantages*	*Disadvantages*	*References*
Polymer/matrix encapsulation	Access to functional nanomaterials, one system can be applied to numerous enzymes	Reduction of catalytic efficiency, mechanical stability of media can vary	113–116
Covalent crosslinking of natural amino acids	Easy to exploit amine/thiol/carboxyl reactivity, robust attachment	Requires chemical treatment of enzyme/support, often irreversible	117–119
Covalent crosslinking of unnatural amino acids	Robust attachment, site-directed immobilisation	Requires chemical treatment of enzyme/support, often irreversible	120
Physical adsorption (hydrophobic supports, physical channels/pores)	Lipophilic enzymes more likely to retain activity, high surface area of channels/pores maximises adsorption	Limited scope for soluble enzymes, enzyme leakage/leaching from media, limited recyclability of media	121,122
Affinity tags	Single-step purification, site-directed immobilisation	Interactions too weak (hexahistidine), or not readily reversible (streptavidin/biotin)	123,124
Enzyme/binding domain fusions	Moderate attachment, single step purification	Requires optimisation of fusion construct, expression system	125–127
Ionic adsorption	Rapid immobilisation and desorption in mild conditions	Enzyme leakage/leaching from media	125,127–129

Table 1.1 | Methods of enzyme immobilisation, and their advantages and disadvantages.

Affinity tags typically reserved for protein purification have found use in non-covalent site specific immobilisation. While traditional hexahistidine tags lack the affinity for long-term immobilisation of protein on Ni-NTA resin, work by Khan *et al.* has shown that a 'double' hexahistidine motif increases binding affinity by an order of magnitude, improving its application to this kind of attachment[124]. The biotin/streptavidin system has also been used to immobilise an enzyme with moderate success – biotinylated aldo/keto reductase (AKR1A1) retained activity for 1 week on streptavidin templates – and further demonstrated the importance of site-specificity to this sort of immobilisation[123].

Physical adsorption or entrapment allows for enzymes to be incorporated into polymer matrices, gels, or metal-organic frameworks. In recent work by Feng *et al.*, metal-organic frameworks containing single-molecule traps were designed for the immobilisation of three enzymes; horseradish peroxidase, cytochrome c oxidase, and microperoxidase[122]. The networks of organic linkers, metal ions, and coordinated water molecules provided sufficient physical interactions for the immobilisation of the enzymes, while having minimal negative effect on catalytic efficiency. In fact, K_M was observed to decrease in each case.

Ionic immobilisation has also been investigated as a method of attaching an enzyme to solid media. The advantages of ionic immobilization are its simplicity, speed and reversibility; adsorption onto ion exchange resin is rapid, and commercially available resins can have high enzyme loading capacities. These resins, typically used for purification of proteins, allow for quick adsorption and desorption of enzymes; gradually increasing the ionic strength of the purification buffer results in bound proteins being eluted according to their isoelectric points[130]. This rapid desorption, while beneficial for recycling of media, also represents the main disadvantage of ionic immobilization; the propensity of enzymes to leach out of charged media with prolonged use. This can be addressed by altering the surface properties of the enzyme to be immobilized.

1.6 Charge Engineering

The surface chemistry of proteins is crucial to their intermolecular interactions and stability. Numerous studies investigating the relationship between surface charge and tendency of a protein to aggregate have determined that the greater a protein's net charge is, the less likely it is that aggregation will occur. Examples of this phenomenon include intrinsically disordered proteins, which typically have primary structure consisting of numerous similarly charged residues and very few hydrophobic residues. This results in a partially or completely unfolded

native state, but high solubility[131]. The practice of storing protein solutions at a pH either substantially higher or lower that the molecule's isoelectric point, or in specific concentrations of salt, relies on the same reasoning; a protein is least soluble when its net charge is closest to zero[132]. The inverse corollary often means that screens for the crystallisation of proteins are set up at or around the isoelectric point of the protein, where solubility is lowest, encouraging the formation of crystalline solids. Thus, altering the surface charge of a protein is an effective way to adjust inter- and intra-molecular interactions.

In studies by Lawrence *et al.*, it was demonstrated that dramatically increasing the surface charge of Green Fluorescent Protein (GFP) conferred resilience against protein unfolding and aggregation[133]. Most notably, upon heating their supercharged GFP variant, GFP(+36), to 100 °C, no aggregation was observed, and 62% of initial fluorescence was recovered upon cooling **(Figure 1.7).** The lab-stabilised variant of GFP, stGFP, used as a starting point for the engineering of GFP(+36), showed a significant loss in solubility and irreversible loss of fluorescence under the same conditions. GFP(+36) also showed a remarkable resilience against chemical denaturation.

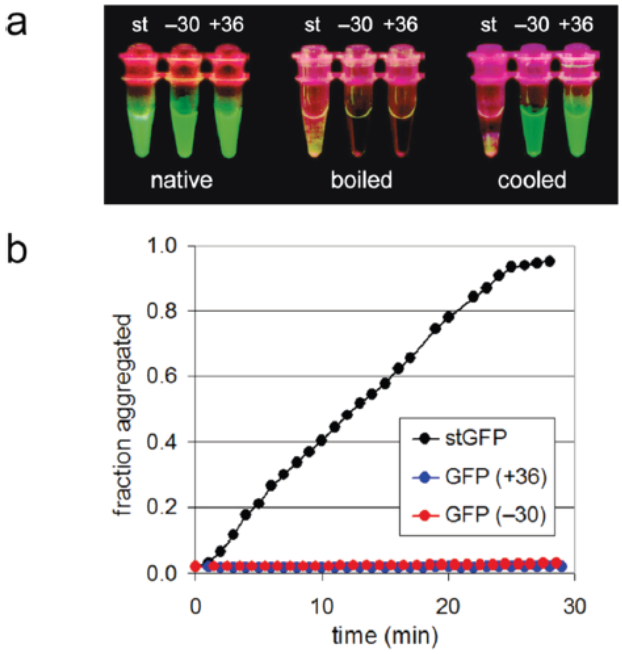

Figure 1.7 | a) Comparison of stGFP and the supercharged variants after heating to 100 °C and subsequent cooling, b) Fraction of stGFP and supercharged variants aggregated on addition of 40% TFE. Figure adapted from Lawrence *et al.*[133]

This substantial increase in resilience to aggregation and inactivation is observed in chemical modification experiments performed by Shaw *et al.*[134], albeit with a super-anionic protein. In this study, samples of α-amylase were treated with acetic anhydride resulting in the acetylation of 17 of the 28 lysine residues in the protein. This acetylation saw an increase in negative net charge of approximately 17 units compared to the unmodified α-amylase. When incubated with common industrial surfactants, the acetylated α-amylase was not inactivated.

Perriman *et al.* present further studies involving chemical modification of enzyme surfaces to yield highly charged proteins. Chemically cationized ferritin was produced through the coupling of N,N-dimethyl-1,3-propanediamine (DMPA) to negatively charged surface residues via 1-ethyl-3-(3-dimethylaminopropyl)carbodiimide (EDC). The addition of 10 DMPA molecules to each of the 24 subunits of ferritin resulted in an increased positive surface charge, which served as the basis for addition of anionic polymer surfactants[135]. When lyophilised and heated, the surfactant-enzyme complexes melted, forming novel 'liquid-phase' protein which remained stable up to 405 °C. Experiments with chemical cationization and surfactant addition to myoglobin yielded similar increases in thermostability, as well as improved refolding[136]. These works establish the alteration of enzyme surface properties as not only viable, but often advantageous.

The use of surface modification to enhance ionic immobilization of enzymes has been investigated in several studies. One example is the use of the Z_{basic2} domain by Bolivar *et al.* to mount D-Amino acid oxidase from *Trigonopsis variabilis* (TvDAO) on a derivatized mesoporous glass[125]. The cationic Z_{basic2} domain, co-opted from staphylococcal protein A by Gräslund *et al.*[137], allowed for the simultaneous purification and immobilisation of *Tv*DAO on anionic glass beads. The immobilized enzyme had enhanced resistance to bubble aeration, and was demonstrated to retain activity for approximately 12 hours of conversion in batch. In work by Montes *et al.* the surface of a penicillin G acylase (PGA) was modified genetically, with the aim of reducing the isoelectric point of the enzyme such that it could be reversibly immobilized on modified anion exchange resin[129]. The construct demonstrated enhanced stability to dioxane, which, while not a particularly polar solvent (relative polarity = 0.164[138]), goes some way to illustrating the effectiveness of hydrophilic microenvironments in protecting enzymes from the damaging effects of organic solvents.

1.7 Hydrogels in Biocatalysis

The incorporation of enzymes into hydrogels has a number of advantages; hydrogels can act as a matrix for physical adsorption[139]; the protective effect of a hydrophilic microenvironment can permit exposure of the adsorbed enzyme to organic solvents[140]; and the properties of the hydrogel can be tuned to the desired application[141]. The most commonly used purification/immobilization hydrogel is one comprising crosslinked agarose beads (Sepharose). While readily applied in research applications like affinity chromatography, there are several significant drawbacks of these polymers; agarose beads are susceptible to compression and crushing under high flow rates and pressures, and do not tolerate many organic solvents[142,143]. These factors impose serious limitations on a Sepharose-based immobilization system, particularly in industrial or synthetic contexts in which high flowrates and organic solvents can be necessary.

For application in industry, hydrogels can be contained within non-compressible porous ceramic beads. This results in a robust material, resistant to the high pressures and mechanical forces that accompany reactions performed in flow. Encapsulated hydrogels have a greater surface area for enzyme adsorption than a traditional non-porous bead, so biocatalyst loadings can be increased. For therapeutic applications, however, biocompatible hydrogels are necessary. Amino acid based hydrogels have been shown to spontaneously self-assemble and have potential for therapeutic application, as they can more closely mimic the environment of the cell[144]. The incorporation of enzymes into these self-assembling hydrogels could allow for precision delivery of enzymatic therapeutics. However, these applications require robust immobilization of the protein in the hydrogel to minimize leaching, particularly in therapeutic settings in which specific localisation of the enzyme:hydrogel construct would be vital. The combination of surface engineering, ionic immobilization, and the utilization of charged, biocompatible hydrogels, is therefore an interesting area of study.

While Montes *et al.* demonstrated the adsorption of an anionic PGA variant onto chemically-modified Sepharose, work presented in **Chapter 4** of this thesis focuses on the modification of *ar*PTE for incorporation into novel anionic biogenic hydrogels. Further, the increased surface charge of the presented *ar*PTE (pI = 10.01) puts it in the top 0.0001% of soluble proteins in the *E. coli* proteome, resulting in a single-step purification from cell lysate that could be readily scaled up without reduction in the resolution of the purification. A moderately anionic protein, like the PGA presented in Montes *et al.* (pI = 4.3) may become difficult to separate from

endogenous *E. coli* proteins - which are predominantly acidic - on large scales, increasing the cost of application to industry. The immobilized *ar*PTE variant was also subjected to rigorous testing of its application to organic synthesis, particularly its resistance to the polar solvent, methanol (relative polarity = 0.791[138]) and its capacity to perform kinetic resolutions in continuous flow systems.

High fashion garment designed and modelled by Sanjana Alex, inspired by the purification and crystallization of phosphotriesterase. Image used with permission.

CHAPTER 2:
MOLECULAR EVOLUTION, DYNAMICS, AND EPISTASIS IN A MODEL PHOSPHOTRIESTERASE SYSTEM

Declaration

The following two papers were peer-reviewed and published as regular original research articles.

In the first article presented, ‘Reverse evolution leads to genotypic incompatibility despite functional and active site convergence’, the structural determination and analysis of X-ray crystallographic data were performed by the author under the supervision of Associate Professor Colin Jackson. The author also contributed to writing the manuscript. The contributions of the other authors are as follows; Dr Miriam Kaltenbach performed the directed evolution experiments and kinetic characterisation of variants; Associate Professor Colin Jackson, Professor Florian Hollfelder, and Dr Nobuhiko Tokuriki are primary investigators.

In the second article presented, ‘The role of protein dynamics in the evolution of new function’, structural determination and analysis of X-ray crystallographic data were performed by the author under the supervision of Associate Professor Colin Jackson. The author also contributed to writing the manuscript. The contributions of other authors are as follows; Dr Miriam Kaltenbach performed the directed evolution experiments and kinetic characterisation of variants; Mr. Galen Correy performed ensemble refinement of crystallographic structures; Dr Paul Carr assisted in the collection and refinement of crystallographic data; Dr Benjamin Porebski performed molecular dynamics simulations; Ms. Emma Livingstone assisted in protein crystallisation under the supervision of the author; Dr Livnat Afriat-Jurnou assisted in protein crystallisation in collaboration with the author; Dr Ashley Buckle, Dr Martin Weik, and Professor Florian Hollfelder supervised students; Dr Nobuhiko Tokuriki and Associate Professor Colin Jackson are primary investigators.

Note that the page numbering in the follow articles has been adjusted for publication in this thesis. Online versions of these articles can be found at the DOIs listed below.

‘Reverse evolution leads to genotypic incompatibility despite functional and active site convergence’
DOI: 10.7554/eLife.06492

‘The role of protein dynamics in the evolution of new function’
DOI: 10.1038/nchembio.2175

eLIFE elifesciences.org

RESEARCH ARTICLE

Reverse evolution leads to genotypic incompatibility despite functional and active site convergence

Miriam Kaltenbach[1,2], Colin J Jackson[3], Eleanor C Campbell[3], Florian Hollfelder[2], Nobuhiko Tokuriki[1]*

[1]Michael Smith Laboratories, University of British Columbia, Vancouver, Canada; [2]Department of Biochemistry, University of Cambridge, Cambridge, United Kingdom; [3]Research School of Chemistry, Australian National University, Canberra, Australia

Abstract Understanding the extent to which enzyme evolution is reversible can shed light on the fundamental relationship between protein sequence, structure, and function. Here, we perform an experimental test of evolutionary reversibility using directed evolution from a phosphotriesterase to an arylesterase, and back, and examine the underlying molecular basis. We find that wild-type phosphotriesterase function could be restored (>10^4-fold activity increase), but via an alternative set of mutations. The enzyme active site converged towards its original state, indicating evolutionary constraints imposed by catalytic requirements. We reveal that extensive epistasis prevents reversions and necessitates fixation of new mutations, leading to a functionally identical sequence. Many amino acid exchanges between the new and original enzyme are not tolerated, implying sequence incompatibility. Therefore, the evolution was phenotypically reversible but genotypically irreversible. Our study illustrates that the enzyme's adaptive landscape is highly rugged, and different functional sequences may constitute separate fitness peaks.
DOI: 10.7554/eLife.06492.001

***For correspondence:** tokuriki@msl.ubc.ca

Competing interests: The authors declare that no competing interests exist.

Funding: See page 17

Received: 15 January 2015
Accepted: 13 August 2015
Published: 14 August 2015

Reviewing editor: Michael Laub, Massachusetts Institute of Technology, United States

Introduction

The controversy surrounding evolutionary reversibility pertains to one of the fundamental questions in evolutionary biology: the extent to which selection pressure determines evolutionary outcomes (***Teotonio and Rose, 2001***; ***Gould, 2007***; ***Collin and Miglietta, 2008***; ***Lobkovsky and Koonin, 2012***). Also, through understanding reversibility on the levels of both phenotype and genotype, one could catch a glimpse at the structure of the respective fitness (or adaptive) landscape. The extent of ruggedness of adaptive landscapes—that is, the prevalence of epistasis, and thus historical contingency—have recently received considerable attention (***Whitlock et al., 1995***; ***Poelwijk et al., 2007***; ***de Visser et al., 2011***; ***Breen et al., 2012***; ***Harms and Thornton, 2013***; ***McCandlish et al., 2013***; ***Kaltenbach and Tokuriki, 2014***). While the unlikelihood of reversing a historical pathway taken by evolution has been demonstrated (***Bridgham et al., 2009***), a large number of sequences can encode functionally identical proteins ('genotypic redundancy') and phenotypic reversion can still occur via alternative pathways (***Clarke, 1985***; ***Lenski, 1988***; ***Crill et al., 2000***; ***Teotonio and Rose, 2000***; ***Kitano et al., 2008***). Yet, the evolutionary dynamics underlying phenotypic reversion have not been addressed. Does phenotypic reversion lead back to the ancestral peak on the adaptive landscape or to a new peak (***Carneiro and Hartl, 2010***; ***Lobkovsky and Koonin, 2012***)? In other words, to what extent are the sequences of the ancestral and reverse-evolved proteins accessible via a neutral network—that is, are amino acid exchanges between the two proteins tolerated or result in loss of function? The inability to exchange amino acids between homologous proteins due to epistasis represents 'genotypic incompatibility' and can result in a non-functional enzyme, a phenomenon

eLife digest Enzymes in bacteria and other organisms are built following instructions contained within each cell's DNA. Changes in the DNA, that is to say, mutations, can alter the shape and activity of the enzymes that are produced, which can ultimately affect the ability of the organism to survive and reproduce. Mutations that are beneficial to the organism are more likely to be passed on to future generations, which can lead to populations changing over time.

The DNA sequences that an organism carries are referred to as its 'genotype' and the resulting physical characteristics of the organism are known as its 'phenotype'. Studies of evolution tend to focus on how particular species or molecules become more different over time. However, one area that remains controversial is whether it is possible for evolution to be reversed so that an organism or molecule returns to a previous form.

An enzyme called PTE is said to have phosphotriesterase activity because it catalyzes this particular type of chemical reaction. Recently, a group of researchers used a method called 'directed evolution' to demonstrate that it is possible for PTE to evolve in a way that means it loses its phosphotriesterase activity and becomes able to catalyze a different type of chemical reaction. Here, Kaltenbach et al.—including some of the researchers from the previous work—investigated whether it was possible to use the same method to reverse this evolution and restore the enzyme's original activity.

The experiments show that reverse evolution is possible as phosphotriesterase activity was restored to the PTE enzyme from the previous study. However, although the phenotype of the final enzyme matched that of the original PTE enzyme, the genotypes did not match as the DNA sequences of the genes that encode these enzymes differ. The DNA does not revert to its original sequence because the effect of individual mutations on the phenotype depends on what other mutations are present. For example, as the enzyme evolved its new activity, additional mutations accumulated that did not alter enzyme activity. During the reverse evolution experiment, some of these mutations could have started to exert influence on the phenotype so that different mutations were required to restore the phosphotriesterase activity.

In the future, Kaltenbach et al.'s findings may aid efforts to engineer artificial enzymes for use in medicine or industry.

DOI: 10.7554/eLife.06492.002

which can be compared to the 'Dobzhansky-Muller effect' of hybrid incompatibility (***Orr, 1995***; ***Kondrashov et al., 2002***).

Another important aspect to be explored is the underlying molecular mechanism of phenotypic reversibility. Restoration of function can either be brought about by the same structure and mechanism as in the ancestor, or by a distinct, alternative state. Structural convergence would indicate that functional requirements exist, which deterministically lead to one particular structural solution. On the other hand, structural divergence would imply the accessibility of various solutions that can bring about efficient catalysis. Thus, understanding the molecular basis for (ir)reversibility and (in) compatibility would provide valuable insights into protein sequence-function-structure relationships. What are the molecular requirements for a specific function? What structural changes are required to switch from one function to another? Identifying such changes, which are often based on subtle effects (e.g., on mutations occurring in remote locations, or mutations which only show a favorable effect in combination), remains a great challenge in protein science. What is the molecular basis underlying mutational epistasis, which leads to alternative evolutionary outcomes?

Directed evolution is a powerful tool to address these questions and explore adaptive landscapes because it allows the study of evolution in a highly controlled setup (***Peisajovich and Tawfik, 2007***; ***Romero and Arnold, 2009***; ***Kawecki et al., 2012***). High selection pressure can prevent fixation of neutral, functionally irrelevant mutations, resulting in an adaptive trajectory without mutational noise. All evolutionary intermediates (the 'molecular fossil record') are obtained, so the evolutionary dynamics and their molecular basis can be characterized in detail. Performing evolution in both the forward and reverse direction and comparing the changes in each direction provides a unique handle for identifying such effects. Understanding these phenomena would improve our ability to design and engineer novel proteins in the laboratory.

Here, we experimentally test the reversibility of enzyme evolution and investigate its molecular basis. We previously evolved the enzyme PTE, a phosphotriesterase, into an arylesterase (**Roodveldt and Tawfik, 2005**; **Tokuriki et al., 2012**; **Wyganowski et al., 2013**). In this work, we applied a selection pressure to restore the original phosphotriesterase activity. We characterized the entire trajectory including both the forward and reverse process in terms of phenotypic reversibility (function or enzymatic activity), genotypic irreversibility (sequence), as well as in terms of the underlying molecular basis (structure and mechanism). We find that PTE has a rugged adaptive landscape on which the accessibility of functional mutations is severely limited, and describe the mechanisms that lead to genotypic irreversibility and incompatibility.

Results

Phenotypic reversibility in the laboratory evolution of PTE

We previously reported the laboratory evolution of PTE (*wt*PTE) into a highly efficient arylesterase for 2-naphthyl hexanoate (2NH) (**Roodveldt and Tawfik, 2005**; **Tokuriki et al., 2012**; **Wyganowski et al., 2013**). In the course of the trajectory, the original phosphotriesterase activity decreased drastically (10^4-fold) although no selection pressure was applied against it. In this work, we first completed the functional transition by further decreasing the remaining phosphotriesterase activity (~10-fold) by four additional rounds of directed evolution for maintaining arylesterase but reducing phosphotriesterase activity (**Supplementary file 1**). Briefly, libraries were generated by error-prone PCR and transformed into *Escherichia coli* (BL21 (DE3)). As a pre-screen for arylesterase activity, protein expression was induced in the bacterial colonies on agar plates, and a mixture of the substrate 2NH and a product stain (Fast Red) was added as previously described (**Figure 1A**) (**Roodveldt and Tawfik, 2005**; **Tokuriki et al., 2012**; **Wyganowski et al., 2013**). Upon hydrolysis of 2NH, Fast Red forms a red complex with the naphtholate leaving group, meaning colonies that develop a red color contain active arylesterase variants. In each round, 2000–10,000 colonies were screened in this fashion, theoretically covering most single point mutations in the 330 amino acid PTE gene. Positive colonies were then re-grown and re-assayed in 96-well plates and initial rates of both 2NH and paraoxon hydrolysis were determined in clarified lysate. In our experience, activity increases >1.3-fold compared to the respective parent yielded reliably improved variants. The variant with the largest improvement in initial rate was then used as the template for the next round of error-prone PCR or several variants were subjected to DNA shuffling. To buffer the destabilizing effects of functional mutations and minimize reductions in soluble protein expression levels, we used GroEL/ES overexpression as previously described (**Supplementary file 1**) (**Tokuriki and Tawfik, 2009**; **Wyganowski et al., 2013**). In total, with 22 rounds of 'forward evolution', the accumulation of 26 mutations from *wt*PTE resulted in a highly efficient and specialized arylesterase (AE) with a ~10^5-fold increase in arylesterase rates (k_{cat}/K_M for 2NH >10^6 $M^{-1}s^{-1}$) and an overall ~10^5-fold decrease in phosphotriesterase activity (k_{cat}/K_M for paraoxon ≈10^2 $M^{-1}s^{-1}$, **Figure 1B,C**). Because selection was specific for arylester hydrolysis until round 18, the change in phosphotriesterase activity was stochastic: many mutations decreased phosphotriesterase activity (11 mutations), some were neutral (nine mutations), and others increased phosphotriesterase activity (six mutations). Starting from AE, we then performed the reverse evolution to restore phosphotriesterase activity using an experimental setup equivalent to the forward process (**Figure 1A**) with the following modifications: the pre-screen was carried out using a fluorogenic phosphotriester as a surrogate for paraoxon (**Supplementary file 1**) and then validated in 96-well format as described above. The selection criterion was now an increased initial rate of paraoxon hydrolysis. In our evolutionary model system, variant fitness is defined as the level of enzymatic activity in cell lysate. All variants were also purified and the kinetic parameters determined, which correlated well with lysate activity (**Figure 1—figure supplement 1**, **Supplementary file 2**).

The restoration of phosphotriesterase activity in the reverse evolution followed a pattern similar to that observed for arylesterase activity in the forward evolution: increasing smoothly and gradually through the stepwise accumulation of mutations (**Figure 1B,C**). Moreover, it followed a 'diminishing returns' pattern characteristic for the development of a function under selection—that is, the activity gain per mutation gradually decreased in later stages of the functional transition, where fitness reached a plateau (**Figure 1B**) (**Stebbins, 1944**; **MacLean et al., 2010**; **Chou et al., 2011**; **Khan et al., 2011**; **Tokuriki et al., 2012**). Furthermore, trade-offs between the two activities were weak in the early rounds of evolution, resulting in a generalist, bifunctional intermediate (**Aharoni et al., 2005**;

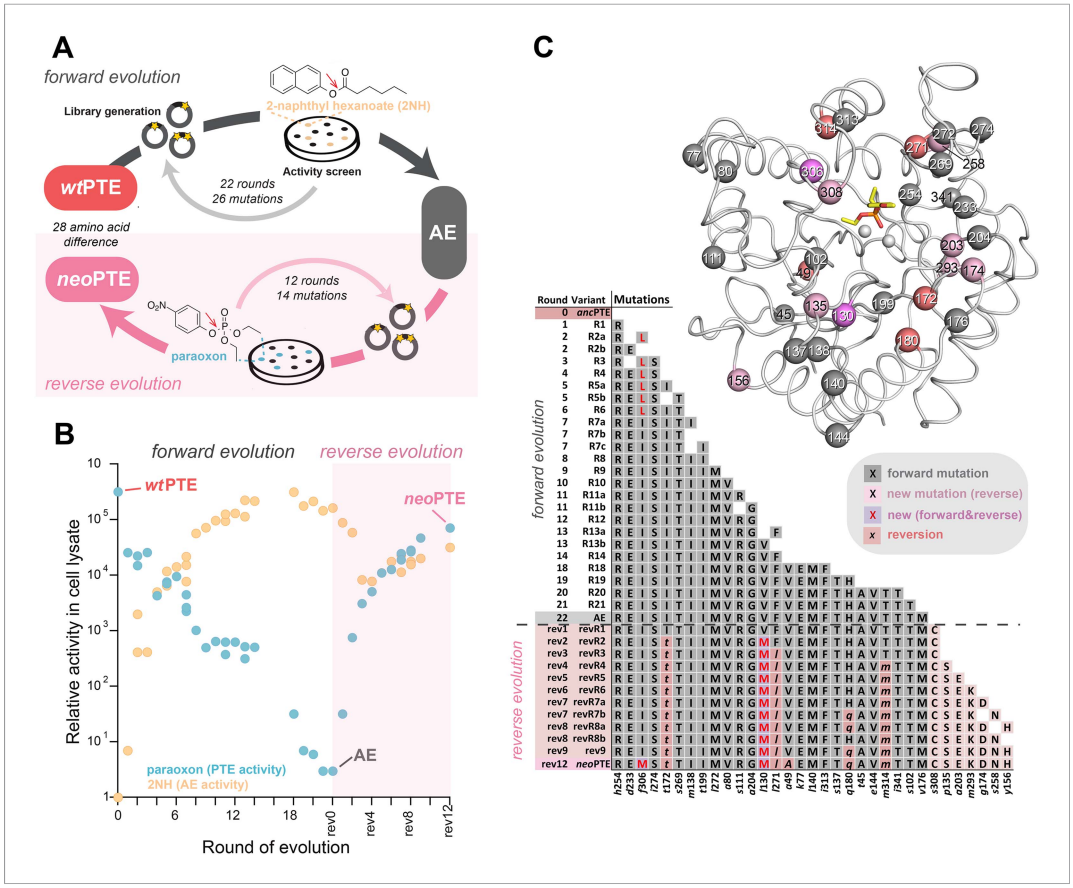

Figure 1. Activity and sequence changes of PTE over the evolution. (**A**) Overview of the experimental evolution. Libraries were generated and transformed into *Escherichia coli*. Proteins were expressed and screened for paraoxon and/or 2NH hydrolysis in bacterial lysates. Several thousand variants were screened per round, theoretically covering most single point mutations in the ~1000 bp PTE gene. Details are given in ***Supplementary file 1***. (**B**) Activity changes during the forward (screening for arylesterase hydrolysis) and reverse evolution (screening for re-increase in phosphotriesterase hydrolysis). Steady-state kinetic parameters for all variants are provided in ***Supplementary file 2A***. (**C**) Type, position, and order of occurrence of the 33 mutations obtained in the evolution. Mutations are shown relative to *wt*PTE (GenBank accession number KJ680379) with lower case italics denoting the amino acid found in *wt*PTE. Note that *wt*PTE was obtained in previous screens for improved expression levels in *E. coli* and contains six mutations relative to the naturally occurring PTE (I106L, F132L, K185R, D208G, R319S) (***Roodveldt and Tawfik, 2005***; ***Tokuriki et al., 2012***). The following mutations occurred in individual variants, but were not fixated after DNA shuffling: R7a: *a*204G, R7c: *a*102V, R19: *a*78T, *v*143A, *t*311A, revR1: *c*59Y, *s*238R, revR5: *i*176V, revR8a: *d*264E, revR8b: *i*296V. All additional variants characterized and sequenced in each round are shown in ***Supplementary file 1***.

DOI: 10.7554/eLife.06492.003

The following figure supplement is available for figure 1:

Figure supplement 1. Correlation between activities measured in cell lysate and using purified enzyme for all variants selected over the evolution (***Supplementary file 2***).

DOI: 10.7554/eLife.06492.004

Khersonsky and Tawfik, 2010). In the forward evolution, trade-offs then became stronger, leading to specialization of the arylesterase. The reverse evolution, however, retained characteristics of a generalist: the large increase in phosphotriesterase activity (>10^4-fold) was accompanied by only a small (five-fold) reduction in arylesterase activity. A possible reason for this is that the reverse evolution is still at an early phase of the functional transition after 12 rounds (vs. 22 in the forward evolution). Because we were unable to isolate any variant with further improved phosphotriesterase activity, it might be necessary to impose a negative selection pressure to specialize the enzyme. The molecular basis of substrate binding and trade-offs is described further below (see also ***Figure 2*** and

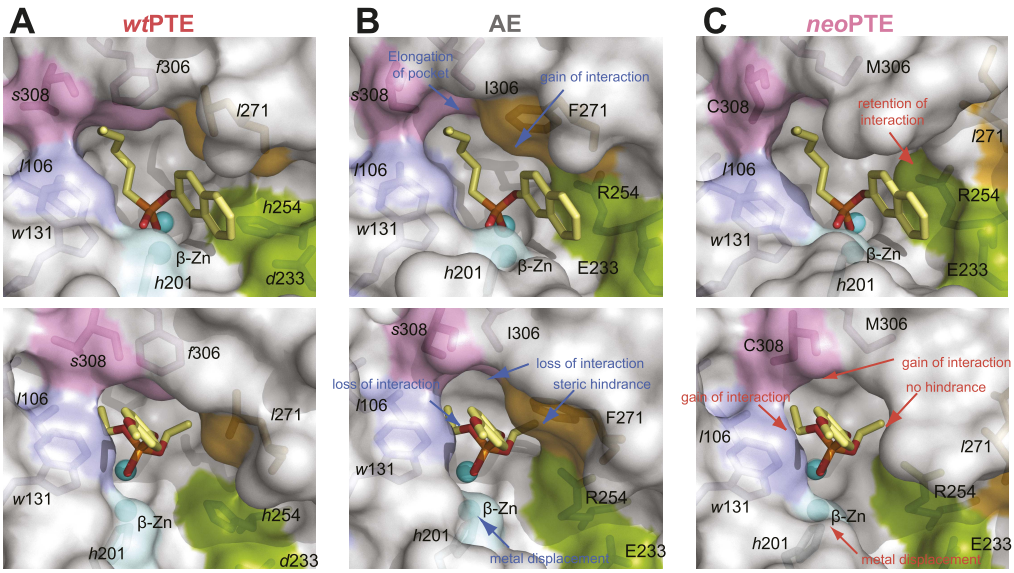

Figure 2. Reshaping of the PTE active site over the evolution. (**A**) *Wt*PTE (PDB ID: 4PCP) features an active site which is well adapted for paraoxon hydrolysis, but suboptimal for 2NH. (**B**) In the forward evolution, selection for arylesterase activity leads to several changes in the binding pocket from *wt*PTE to AE (PDB ID: 4PCN). (**C**) The reverse evolution leads to restoration of the ancestral state in *neo*PTE (PDB ID: 4PBF). The four regions of change are highlighted in different colors. Top row: the 2NH analogue (yellow) was modeled into the three structures by superposition with PTE-R18 in complex with the analogue (PDB ID: 4E3T) (***Tokuriki et al., 2012***). Bottom row: the paraoxon analogue diethyl 4-methoxyphenyl phosphate (yellow) was modeled into the structures by superposition with *Agrobacterium radiobacter* PTE in complex with the analogue (PDB ID: 2R1N) (***Hong and Raushel, 1996***). Amino acids found in *wt*PTE are shown in lower case italics.

DOI: 10.7554/eLife.06492.005

The following figure supplements are available for figure 2:

Figure supplement 1. Details of the active site changes.

DOI: 10.7554/eLife.06492.006

Figure supplement 2. Overlay of electron density maps for the active sites of (**A**) *wt*PTE (salmon) and AE (cyan) and (**B**) *wt*PTE (salmon) and *neo*PTE (magenta).

DOI: 10.7554/eLife.06492.007

Figure supplement 3. Development of B-factors over the evolution.

DOI: 10.7554/eLife.06492.008

Figure supplement 4. Linear free energy relationships of *wt*PTE, AE, and *neo*PTE.

DOI: 10.7554/eLife.06492.009

Figure 2—figure supplement 1). Overall, we obtained a new efficient, enzyme (*neo*PTE) on par with *wt*PTE (k_{cat}/K_M>10^6 $M^{-1}s^{-1}$ for paraoxon in both cases). The recovery of identical phosphotriesterase rates in *neo*PTE compared to *wt*PTE establishes that evolution of the phenotype was fully reversible.

Genotypic irreversibility and constraints underlying phenotypic reversion

To examine the genetic changes causing phenotypic reversion, the sequence of all evolutionary intermediates was determined. Only five of the 26 mutations that accumulated in the forward evolution were reverted to the original sequence ('reversions', A49*v*, I172*t*, Q180*h*, L271*f*, M314*t*, ***Figure 1C***; amino acids shown in lower case italics denote the *wt*PTE state, while amino acids not present in the wild type are shown in capital letters). Nine additional 'new mutations' accumulated, two of which occurred in positions that were mutated in the forward evolution (V130M—originally *leu*, I306M—originally *phe*), and seven were in positions that were not previously mutated (*p*135S, *y*156H, *g*174D, *a*203E, *m*293K, *s*258N, *s*308C). Overall, *neo*PTE is separated further from *wt*PTE (28 out of

333 amino acids) than AE from *wt*PTE (26 amino acids). Additional rounds of evolution failed to yield more reversions or activity increases (***Supplementary file 1***). In the forward evolution, the loss of phosphotriesterase activity was largely a side product of the property under selection, the increase in arylesterase activity. Therefore, not all mutations decreased phosphotriesterase activity (***Figure 1B***), and it is not surprising that phenotypic reversion did not require full genotypic reversion. However, a number of mutations that did contribute to decreasing phosphotriesterase in the forward process were also not reverted. Moreover, the new mutations are located in the same mutational clusters seen in the forward evolution (***Figure 1C***), indicating they may be alternative solutions to the same functional requirement and replace reversions, as detailed further below. Taken together, although the phenotype was reversible, PTE evolution was genotypically irreversible, but an alternative trajectory was readily taken.

The active site converged towards its original state in the reverse evolution

To unravel the molecular basis of the observed genotypic irreversibility, we solved crystal structures of *wt*PTE, AE, and *neo*PTE (***Supplementary file 3***). We compared the structures and modeled both a paraoxon and a 2NH analogue into each active site (by superposition with structures containing these analogues [***Hong and Raushel, 1996***; ***Tokuriki et al., 2012***]). The phosphotriester paraoxon is characterized by tetrahedral ground-state geometry and P–O cleavage proceeds via a trigonal bipyramidal transition state. The arylester 2NH is planar and C–O bond hydrolysis proceeds via a tetrahedral transition state. The structural comparison indicates that AE adapted to the planar substrate 2NH in the forward evolution, but that this came at a cost of phosphotriesterase activity, as the bulky paraoxon is no longer efficiently recognized (***Figure 2***). We identify several regions of the active site that may be responsible for the functional transition (***Figure 2*** and ***Figure 2—figure supplement 1***). First, a binding pocket for the naphthyl leaving group of 2NH was excavated through the combined action of *h*254R and *d*233E (***Figure 2A,B***, green region) (***Hong and Raushel, 1996***; ***Tokuriki et al., 2012***). Leaving group coordination was further improved through a subtle ~1.0 Å shift of *Trp*131 (***Figure 2A,B***, purple region). Moreover, the pocket was elongated through the *f*306I mutation (***Figure 2A,B***, pink region) and narrowed by *l*271F (***Figure 2A,B***, orange region), resulting in better accommodation of the long hexanoate chain of 2NH. These changes may lead to the reduction of phosphotriesterase activity through loss of interactions (either shape complementarity, hydrophobicity, or π-π stacking) in several regions and steric hindrance in others, as described in further detail below (***Figure 2—figure supplement 1***). Additionally, the distance between the two active site zinc ions decreased from 3.8 Å to 3.3 Å (***Figure 2A,B***, light blue region and ***Figure 2—figure supplement 1***). The observed structural changes are subtle, at the sub-angstrom scale, and their contributions to catalysis unquantified. However, the dispersion precision indicator (DPI; ***Cruickshank, 1999***) for each of the structures is less than one-tenth of an angstrom, meaning that the observed distance changes (including the 0.5 Å shift in the metal position) are significant (***Figure 2—figure supplement 2***).

In *neo*PTE, the part of the active site necessary for phosphotriesterase activity has converged back towards its original state. The regions of suboptimal binding were re-optimized for paraoxon and the metal distance was restored to the 3.8 Å (***Figure 2C***). Moreover, the pattern of loop flexibility that is characteristic of *wt*PTE was also restored in *neo*PTE (***Figure 2—figure supplement 3***). Furthermore, we measured linear free energy relationships for *wt*PTE, AE, and *neo*PTE for both arylester and phosphotriester hydrolysis (***Figure 2—figure supplement 4***), that is, the dependence of the catalytic parameters k_{cat}/K_M on the pKa of the leaving group. For phosphotriester hydrolysis by *wt*PTE, a break in pKa dependence around 7 is consistent with the rate-limiting step changing on either side of this break (***Hong and Raushel, 1996***; ***Tokuriki et al., 2012***). By contrast, AE shows a continuous, linear dependence over the whole pKa range, indicating that the rate-limiting step does not change. In *neo*PTE, the pattern characteristic for *wt*PTE was restored. Together with the observed structural convergence, the simplest assumption must be that the very similar active site environment enables similar residue contributions to catalysis in *wt*- and *neo*PTE on phosphotriesterase activity. However, active site convergence is not complete, as the naphthyl binding pocket remains intact (***Figure 2C***, green region, Arg254 and Glu233), which likely explains why *neo*PTE is still bifunctional.

It should be pointed out that, at this stage, we do not know the extent to which the modification of each structural element contributes to the overall >10^4-fold activity change. Also, we cannot exclude the existence of alternative substrate binding modes from our model, as well as the role protein dynamics play in the functional switch. However, in the combined forward and reverse evolution, which involved a change in catalytic activity of >10^4 $M^{-1}s^{-1}$ in each direction, only four mutations were located in the active site. Instead, most functional mutations occur in more remote positions. Therefore, it is likely that fine-tuning of the active site by these remote mutations contributes significantly to the activity changes. Taken together, the restoration of all structural elements key for phosphotriesterase activity as well as the catalytic mechanism occurred despite the alternative genotypic trajectory, suggesting that biophysical requirements exist for this particular active site shape, and that phosphotriesterase activity may otherwise be inefficient.

To further investigate whether mutational accessibility is dictated by the necessity for structural convergence to the wild-type active site, a parallel evolutionary experiment was performed. In this experiment, we attempted to restore phosphotriesterase activity by a trajectory containing only new mutations. To this end, we sequenced the improved variants after each round and removed all those containing reversions. This trajectory only resulted in a 70-fold improvement in five rounds (***Figure 3A***), after which the activity plateaued and no further improved variants could be found. This failure to reach wild-type activity levels without reversions, as well as the fact that three out of the five new mutations obtained (*p*135S, *a*203E, *s*308C, ***Figure 3B***) were identical to the successful trajectory containing reversions, emphasizes that the number of adaptive trajectories that lead to a wild-type level fitness peak from AE are highly limited. However, trajectories involving neutral mutations, or trajectories which do not pass through the best variant in each round but through less improved intermediates, may exist. It is likely that a wild-type-like paraoxon binding pocket is compulsory to achieve efficient phosphotriesterase activity, and only a small set of mutations (e.g., reversions or the combination of reversions and new mutations that we identified) can provide such a solution.

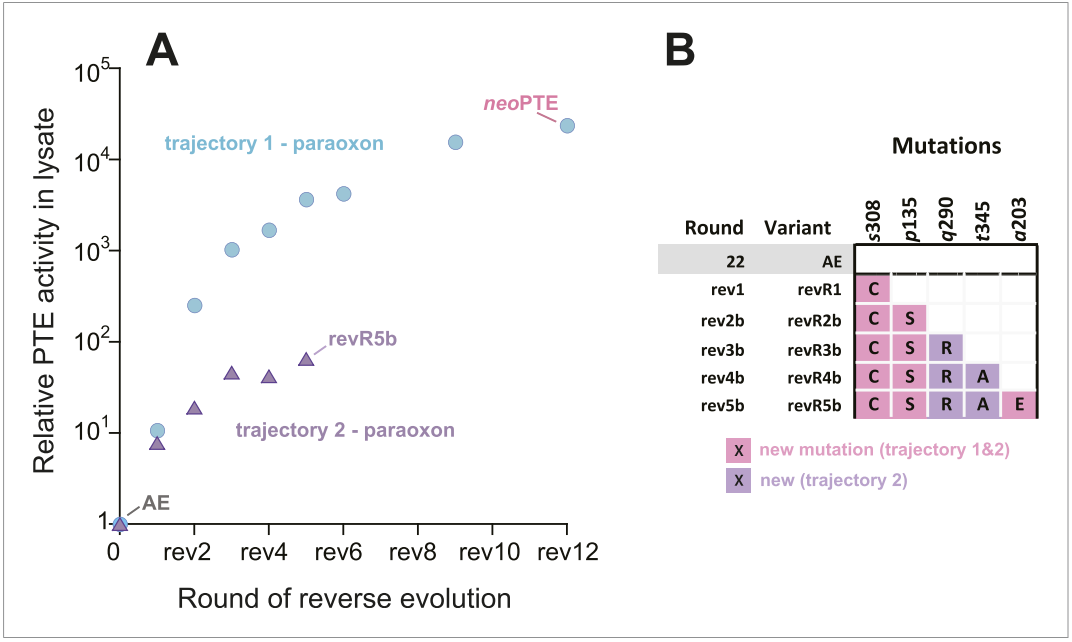

Figure 3. An alternative experimental evolution, where fixation of back-to-wild-type reversions was prohibited, failed to restore the original level of PTE activity. (**A**) Activity changes in the alternative trajectory. After five rounds, PTE activity plateaued at a 65-fold improvement (trajectory 2), 340-fold lower than the main trajectory (trajectory 1). (**B**) Mutations accumulated in the alternative trajectory. All clones containing reversions, which occurred frequently, were removed after sequencing and thereby prohibited from fixating. Three of the five new mutations also fixated in the main trajectory. The mutations *c*59Y and *s*238R occurred in variants revR1 and revR2b, but were not fixated after DNA shuffling. Amino acids found in *wt*PTE are shown in lower case italics. All additional variants characterized and sequenced in each round are shown in ***Supplementary file 1***.

DOI: 10.7554/eLife.06492.010

Emergence of sequence incompatibility between the two PTEs

Next, we set out to answer the question how the two enzymes exhibiting identical phosphotriesterase activity, *wt*- and *neo*PTE, are connected on the adaptive landscape. If they populate the same fitness plateau, amino acid exchanges between them should be neutral. On the other hand, a loss of function upon interconversion between amino acids would indicate genotypic incompatibility (***Kondrashov et al., 2002***; ***Lunzer et al., 2010***; ***Wellner et al., 2013***), meaning that the two enzymes occupy distinct positions on the landscape that are poorly connected through a neutral network. To this end, we characterized the effect of all 28 single point exchanges separating the two enzymes in each background (56 mutants in total, ***Figure 4*** and ***Supplementary file 2***). Mutations are considered non-neutral if they cause a >1.3-fold change in phosphotriesterase activity in lysate compared to the parent background because, in our screening system, this cut-off enabled us to reliably identify improved variants. Moreover, we have performed a statistical analysis of the mutational effects, which confirms that a >1.3-fold change is significant (p-values <0.05) in almost all cases (statistics are provided in ***Figure 4—source data 1*** and ***Supplementary file 2B***). According to this analysis, only eight of 28 exchanges were compatible; they were neutral in both backgrounds (***Figure 4A***). The remaining 20 positions showed incompatibility, 15 of which were partially incompatible, as the exchange was neutral in one background but deleterious in the other (***Figure 4B,C***). Five exchanges were completely incompatible; they severely decreased activity in both backgrounds (***Figure 4D***). Taken together, despite >90% sequence identity between *wt*- and *neo*PTE, the reverse trajectory led to a functional sequence that is poorly connected with the original one. It remains unknown whether the two sequences comprise completely separate peaks on the adaptive landscape or are connected through a neutral network, that is, if the neutral exchanges would permit the subsequent occurrence of initially deleterious exchanges. However, because >70% of the mutated positions cause incompatibility, only one out of the 54 exchanges confers higher fitness, and this exchange (*neo*PTE + *f*306M) would require two simultaneous base changes, it is unlikely that an evolutionary transition between the two could easily occur by adaptive or strong purifying selection.

Mutational epistasis underlies genotypic irreversibility

To understand how convergence to the original function and architecture was achieved despite genotypic irreversibility and incompatibility, we performed a comprehensive mutational analysis. All 33 mutated positions were examined in the background of the three enzymes (*wt*PTE, AE, and *neo*PTE), and in the background in which they originally occurred in the evolution (i.e., in the different rounds) to identify mutations that are epistatic—that is, change their effect depending on the genetic background (***Figure 5*** and ***Supplementary file 2***). To determine whether or not the measured changes were significant, the same stringent cut-off as described above for the comparison between *wt*- and *neo*PTE was applied (statistics are provided in ***Supplementary file 2B–G***). Furthermore, we analyzed the crystal structures to determine which mutations caused the divergence and convergence of the active site configuration.

The analysis revealed extensive epistasis during the forward and reverse evolution. In the forward evolution, the effect of mutations is significantly altered after their fixation due to epistasis caused by mutations subsequently accumulated in the trajectory. For example, some mutations initially increased (*t*172I in round 6 and *l*271F in round 14) or were neutral to (*l*130V in round 14) phosphotriesterase activity when they occurred in the trajectory, and were thus unfavorable to revert as their reversion would not change (V130*l*) or decrease (I172*t*, F271*l*) activity (***Figure 6A***). However, reversion of these mutations became possible (i.e., would lead to an increase in activity) in the background of AE (***Figure 6A***). On the contrary, *h*254R decreased phosphotriesterase activity when it occurred in round 1 and therefore its reversion (R254*h*) would initially be favorable. However, the effect of this reversion switched to unfavorable (R254*h*) when it was tested in AE (***Figure 6B***). Moreover, mutations in the forward evolution had a permissive effect on the accumulation of new mutations and, in this way, opened up a path towards the alternative trajectory taken in the reverse process; all new mutations had a neutral or negative effect on phosphotriesterase activity in the genetic background of *wt*PTE but most of them become positive in AE (***Figure 6C***); for example, AE-s308C (6.4-fold), AE-V130M (5.4-fold) and AE-*p*135S (2.9-fold). Because these mutations can compete with the most favorable reversions (>1.3–8-fold effect, ***Supplementary file 2***), they were selected in the early rounds of the reverse evolution, laying the foundation for the alternative trajectory.

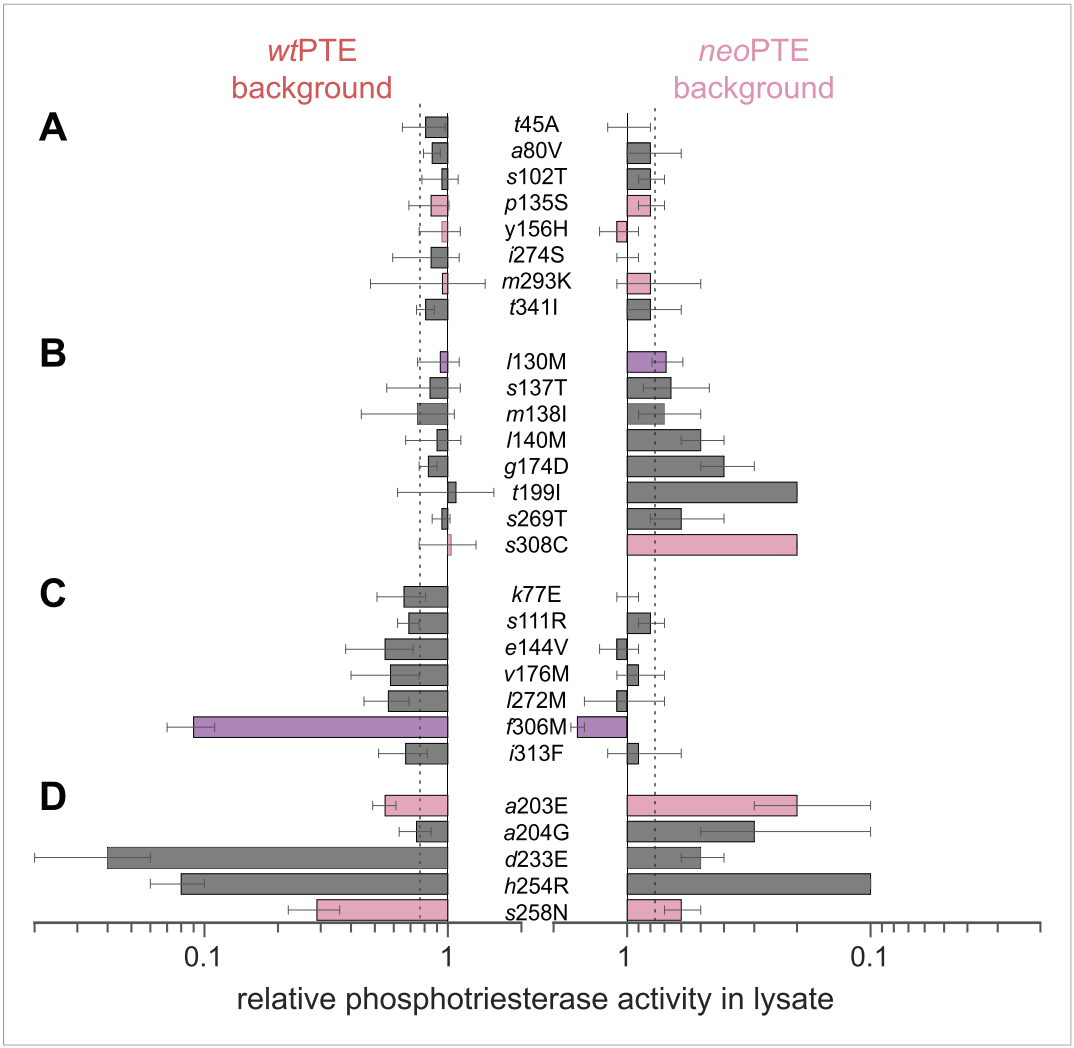

Figure 4. Genotypic incompatibility between *wt*PTE and *neo*PTE. (**A**–**D**) The effect of the 28 amino acid exchanges separating the two enzymes was tested in the background of *wt*PTE and *neo*PTE, respectively. Activities are given relative to the parent mutational background, *wt*PTE or *neo*PTE. Amino acids found in *wt*PTE are shown in lower case italics. Color code as in ***Figure 1***. (**A**) Compatible exchanges, neutral in both backgrounds. (**B**, **C**) Partially incompatible exchanges, neutral in one background but deleterious for another. (**D**) Mutually incompatible exchanges. Mutations causing a >1.3-fold change compared to the respective parent mutant (dotted line) are considered non-neutral. p-values compared to each parent (***Supplementary file 2B***) and p-values for the effect of each mutation ***Figure 4—source data 1*** in the two backgrounds were calculated. Note that the effect of *i*313F, which causes a significant decrease in *wt*PTE, is statistically not significant between *wt*PTE and *neo*PTE.

DOI: 10.7554/eLife.06492.011

The following source data is available for figure 4:

Source data 1. Comparison of the effect of mutations in *wt*- and *neo*PTE.

DOI: 10.7554/eLife.06492.012

In the reverse evolution, the active site architecture necessary for phosphotriesterase activity was restored largely through new mutations, which restricted the reversion of mutations accumulated in the forward evolution. Overall, nine of the 10 reversions that were initially favorable in the background of AE lost their favorable effect in *neo*PTE because of epistasis during the reverse evolution (***Figure 7A***). We were able to trace the molecular basis of this effect in several cases as described in the following. First, *f*306I enlarged the active site in the forward evolution, resulting in a loss of shape complementarity to paraoxon. In the reverse evolution, the nearby *s*308C offsets this effect by increasing the hydrophobicity of the pocket (***Figure 2***, ***Figure 7C***, ***Figure 2—figure supplement 1A***).

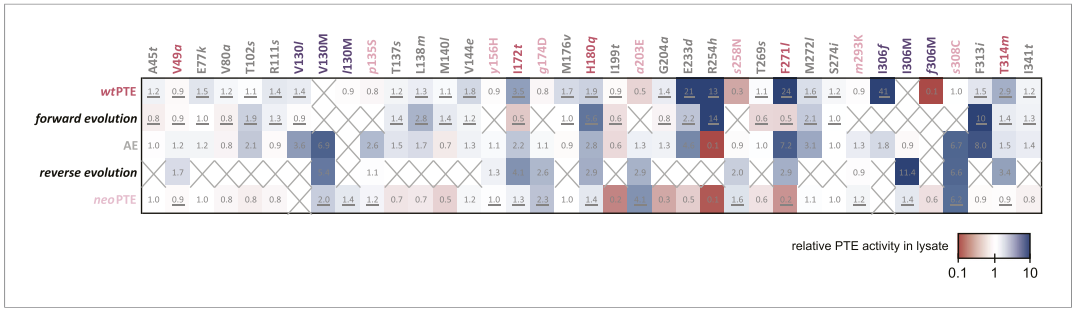

Figure 5. Changes in phosphotriesterase activity upon mutations in five different backgrounds: *wt*PTE in the forward evolution, AE in the reverse evolution, and *neo*PTE. Thirty-three positions were mutated in the entire evolution, two of which (130 and 306) were mutated to two different amino acids. Amino acids found in *wt*PTE are shown in lower case italics. Numbers indicate the fold change in activity caused by a mutation in a certain background (***Supplementary file 2B–F***). Mutations causing a >1.3-fold change compared to the respective parent mutant are considered non-neutral. p-values compared to each parent were calculated (***Supplementary file 2B,D,F***). The mutations T341*i* in AE, *l*140M and *t*199I in the forward evolution, and V49*a* and *s*258N in the reverse evolution are not significant (p-values >0.05). Therefore, out of 144 mutations, only five show a >1.3-fold effect, but are statistically not significant. Boxes that are crossed out indicate that a mutation did not occur in this background. For direct comparison, the activity changes resulting from a mutation are adjusted to the same direction—from the amino acid found in AE to the respective other amino acid (label at the top). To illustrate, the effect of R254*h* was measured as follows: AE and *neo*PTE contain Arg254, and thus the effect of R254*h* is directly calculated based on the comparison between AE and AE-R254*h* (Fold change$_{R254h}$ = Acticity$_{AE\text{-}R254h}$/Activity$_{AE}$) and between *neo*PTE and *neo*PTE-R254*h* (Fold change$_{R254h}$ = Acticity$_{neoPTE\text{-}R254h}$/Activity$_{neoPTE}$). However, because *wt*PTE and the forward evolution background already contain *His*254, the effect of introducing this amino acid has to be calculated 'in reverse' by first assuming to remove this mutation and then adding it back in, that is, based on the comparison between *wt*PTE-*h*254R and *wt*PTE (Fold change$_{R254h}$ = Acticity$_{wtPTE}$/Activity$_{wtPTE\text{-}h254R}$). All mutational effects that were calculated in this 'reverse' way are underlined. Note that *wt*PTE-*h*254R is identical to the round 1 variant and therefore the effect in the forward evolution is the same as in the *wt*PTE background. Because R254*h* did not occur in the reverse evolution, no effect could be calculated in this background and the respective box is crossed out.

DOI: 10.7554/eLife.06492.013

The redundancy of the mutations *f*306I and *s*308C was also evidenced by combinatorial mutational analysis; incorporation of *s*308C restricts subsequent reversion of I306*f* due to sign epistasis (***Figure 7B***). While this reversion would have been favorable in isolation, phosphotriesterase activity of the double mutant AE-I306*f*-*s*308C is reduced compared to AE-*s*308C. Second, the active site was narrowed in the forward evolution by *l*271F and several other mutations in loop7/8 including *l*272M and *i*313F (***Figure 7C*** and ***Figure 2—figure supplement 1B***), causing steric hindrance for paraoxon. The pocket was re-opened initially by the reversion F271*l*. Subsequently, the new mutation *s*258N destabilized and altered the conformation of loop 7 and further enlarged the pocket (***Figure 2***, ***Figure 2—figure supplement 1B***). We also observed that incorporation of *s*308C and F271*l* restricted the reversion of both *l*272M and *f*313I (M272*l* and I313*f*, ***Figure 7B***). Third, the active site was reshaped by a subtle ~1.0 Å shift of *Leu*106 and *Trp*131, which was likely triggered by a cluster of remote mutations occurring in the same loops (*s*102T, *l*130V, *m*138I, *s*137T, and *v*140M, ***Figure 7D***, and ***Figure 2—figure supplement 1C***). In the reverse evolution, these residues are shifted back to their original positions through two new remote mutations, *p*135S and V130M (***Figure 7D***). Again, the two mutations are redundant and mutually exclusive; *p*135S restricts the reversion of *m*138I (I138*m*, ***Figure 7B***). Fourth, the distance between the two active site zinc ions decreased from 3.8 to 3.3 Å in the forward evolution through displacement of the metal-chelating *His*201 and the β-metal (***Figure 7E***), which was likely triggered by the combined action of several remote mutations in loops 4 and 5 (*t*172I, *q*180H, *t*199I, and *a*204G, ***Figure 2***). In the reverse evolution, the positions of *His*201 and the β-metal, as well as the original inter-metal distance of 3.8 Å, were restored through the reversion I172*t* and formation of a new hydrogen bonding network with two additional new mutations, *a*203E and *g*174D (***Figure 7E***). These examples demonstrate that rewiring the intramolecular interaction network of the protein can result in the same physical solution in key elements in the active site. Rewiring occurs because new mutations act as 'epistatic ratchets'

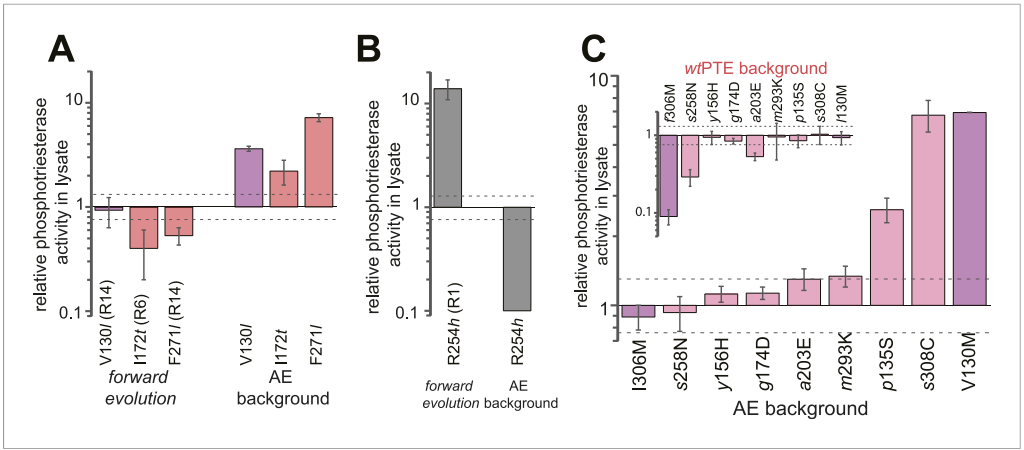

Figure 6. Epistasis between mutations in the forward evolution restricts some reversions while permitting others as well as new mutations. (**A**) Several reversions change their effect from unfavorable upon their initial occurrence in the forward evolution to favorable in AE. (**B**) Other reversions change their effect from favorable to unfavorable. Note that, in the forward evolution, mutations occurred in the opposite direction as shown (*l*130V, *t*172I, *l*271F, and *h*254R), but are given in the same direction as AE for direct comparison. Phosphotriesterase activity was too low to be determined in AE + R254h, but at least 10-fold reduced. (**C**) The effect of new mutations changes from *wt*PTE (small panel) to AE (large panel). Relative activities were calculated by comparing a variant containing a certain mutation with one lacking only this mutation. Mutations causing a >1.3-fold change compared to the respective parent mutant (dotted line) are considered non-neutral. p-values compared to each parent (***Supplementary file 2B***) and p-values for the effect of each mutation in the two respective backgrounds shown in each panel were calculated (***Figure 6—source data 1, 2***). Note that the mutation *m*293K, which causes a significant increase in AE, does not have a significantly different effect in the two backgrounds. Amino acids found in *wt*PTE are shown in lower case italics. Color code as in ***Figure 1***. All other mutational effects in the different backgrounds are given in ***Figure 5*** and ***Supplementary file 2***.

DOI: 10.7554/eLife.06492.014

The following source data are available for figure 6:

Source data 1. Comparison of the effect of mutations in the forward evolution and in AE (panels A, B).

DOI: 10.7554/eLife.06492.015

Source data 2. Comparison of the effect of mutations in *wt*PTE and AE (panel C).

DOI: 10.7554/eLife.06492.016

(***Bridgham et al., 2009***) for potential reversions, restricting their fixation and thus leading to the incompatible new enzyme *neo*PTE.

Discussion

Our work demonstrated that a >10^4-fold loss in phosphotriesterase activity, which accompanied the functional transition to a distinct chemical reaction—arylester hydrolysis—via accumulation of 26 mutations, is readily restored when the selection pressure is reverted. Phenotypic reversal has been observed in previous cases (***Clarke, 1985***; ***Lenski, 1988***; ***Crill et al., 2000***; ***Teotonio and Rose, 2000***; ***Kitano et al., 2008***), supporting the notion that the phenotype is largely subject to deterministic forces. The likelihood of evolutionary reversibility depends on the complexity of the system and the distance in sequence and function from the ancestor, and it is possible that starting from a more distantly evolved arylesterase would have failed to restore phosphotriesterase function. Moreover, we modulated protein stability throughout the entire trajectory using overexpression of GroEL/ES to avoid evolutionary dead ends caused by stability bottlenecks (***Socha and Tokuriki, 2013***; ***Wyganowski et al., 2013***). In the absence of chaperones, adaptation may have occurred through a different pathway. Another limitation of our work is that we only examined two evolutionary trajectories (the main trajectory and the trajectory without reversions). One could imagine conducting multiple parallel evolutionary experiments to shed light on the repeatability of the trajectory taken, but unfortunately our screening system is not amenable to such a throughput. Nevertheless, our experiment shows that the genotype is subject to strong constraints: an alternative mutational

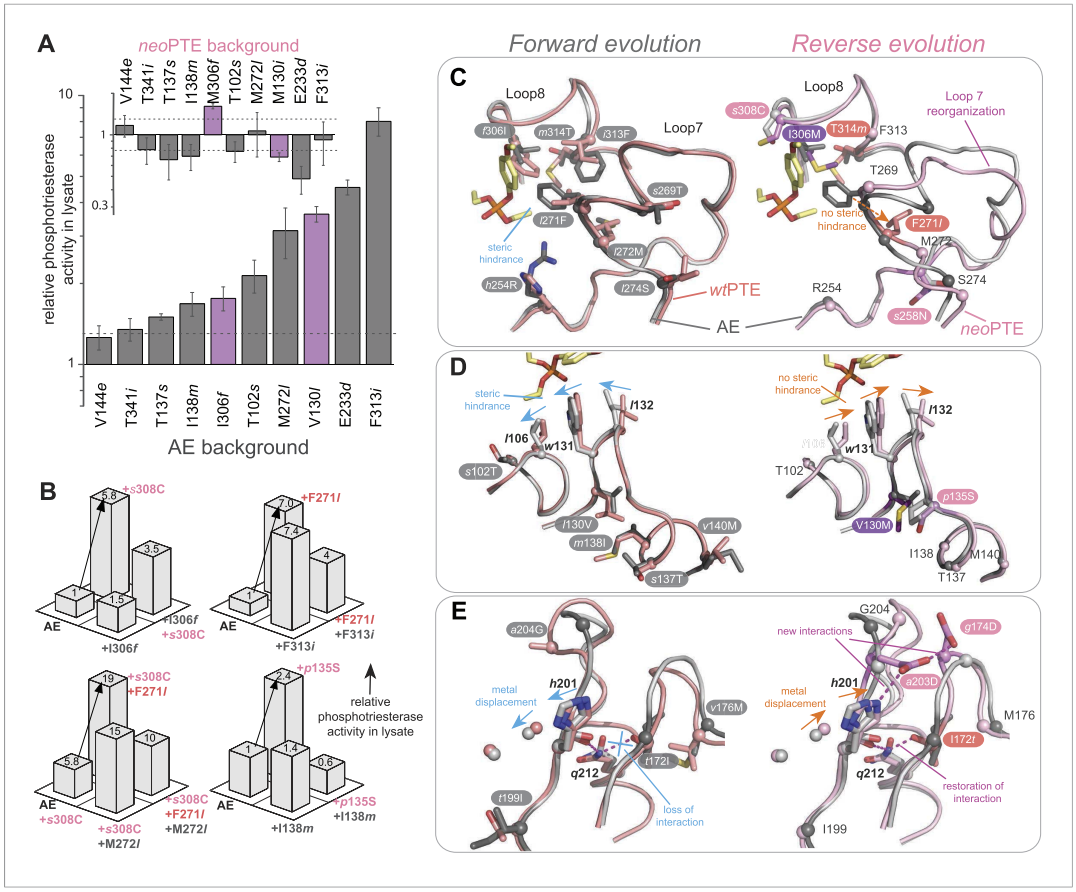

Figure 7. Convergence to the original active site configuration in the reverse evolution through rewiring of the molecular interaction network leads to genetic incompatibility. (**A**, **B**) Epistasis during the reverse evolution causes irreversibility and incompatibility. (**A**) The activity change of mutations that were favorable in the initial stage of reverse evolution, but not reverted. *neo*PTE background: small panel; AE background: large panel. Color code as in ***Figures 1, 2***. Mutations causing a >1.3-fold change compared to the respective parent mutant (dotted line) are considered non-neutral. p-values compared to each parent (***Supplementary file 2B***) and p-values for the effect of each mutation in the two respective backgrounds shown in each panel were calculated (***Figure 7—source data 1***). (**B**) Combinations of mutations that constrained the evolutionary trajectory due to sign epistasis. Phosphotriesterase activity is shown on a linear scale. p-values are given in ***Supplementary file 2G***. Note that the two mutants AE + F271*l* + *s*308C and AE + M272*l* + *s*308C have non-significant p-values compared to the 'double mutant' in this series, AE + F271*l* + M272*l* + *s*308C. However, determination of k_{cat}/K_M values confirms sign epistasis in this series (see also ***Supplementary file 2G***). (**C**–**E**) Amino acid changes in the forward (left panel) and reverse evolution (right panel). (**C**) Reorganization of loops 7 and 8. A new mutation, *s*258N, caused the reorganization (see also ***Figure 2—figure supplement 1A,B***). (**D**) Different combinations of remote mutations in loop 3 resulted in identical positioning of *Leu*106, *Trp*131, and *Leu*132 in *wt*PTE and *neo*PTE (see also ***Figure 2—figure supplement 1C***). (**E**) Rewiring the interaction network in *neo*PTE by remote mutations in loops 4 and 5 led to β-metal displacement (see also ***Figure 2—figure supplement 1D***). Amino acids found in *wt*PTE are shown in lower case italics.

DOI: 10.7554/eLife.06492.017

The following source data is available for figure 7:

Source data 1. Comparison of the effect of mutations in *wt*PTE and AE (panel A).

DOI: 10.7554/eLife.06492.018

pathway was taken which prevented retracing of the original pathway. Genotypic irreversibility was caused by several factors. First, because selection in the forward evolution was only for increased arylesterase activity (except in rounds 19–22), the effect of the mutations on phosphotriesterase activity was stochastic: most decreased phosphotriesterase activity, some did not affect it, and some increased phosphotriesterase activity. Therefore, even if one were to revert the mutations in the reverse order of their occurrence (from rounds 22 back to 1), the lack of continuous activity increases

would prevent a gradual adaptive trajectory. Second, by the end of the forward evolution, several new mutations able to increase paraoxonase activity emerged due to epistasis. The fixation of these mutations then acts as an epistatic ratchet (**Bridgham et al., 2009**) that prevents reversions. Therefore, as soon as the first new mutation accumulates, the trajectory deviates further from the original path.

Our work suggests that only certain sets of mutations are able to cause phenotypic reversal. Although genotypic redundancy was observed, the presence of at least some reversions was essential for complete restoration of catalytic activity, and several new mutations were shared between the two trajectories examined. Similarly, other experimental evolution studies that examined parallel evolutionary trajectories starting from the same sequence often resulted in accumulation of the same mutations (**Bull et al., 1997**; **Salverda et al., 2011**; **Dickinson et al., 2013**; **Khanal et al., 2014**). These observations indicate that a number of functional mutations accessible from a particular starting point are highly limited, and that the genotype is also subjected to deterministic forces to some extent. In our case, the limited accessibility to functional mutation can be explained by the requirement to adapt the wild-type active site configuration in order to obtain efficient phosphotriesterase hydrolysis. Recent work by Harms et al. showed that the accessibility of functional and permissive mutations on hormone receptors is also strongly constrained by biophysical requirements imposed on the binding pocket as well as by protein dynamics (**Harms and Thornton, 2014**). Understanding such biophysical requirements and, in the case of enzymes, imperatives of chemical reactivity, is essential to develop our knowledge of evolutionary dynamics and constraints, although the exact nature of such requirements may be unique to each protein.

In the case of PTE, the combination of multiple subtle changes is required to fulfill these biophysical requirements and completely switch the enzyme's ability to recognize two different substrates (paraoxon vs. 2NH: tetrahedral vs. planar, P–O bond vs C–O bond cleavage, trigonal bipyramidal vs. tetrahedral transition state geometry). All but four of the 33 mutations occur in locations remote from the active site and act by fine-tuning rather than directly changing the active site configuration. Some changes occur at the sub-Å level (e.g., the shift in *Trp*131, *Leu*132, and the β-metal), and possibly act by influencing the dynamics of the active site loops. It may be that only remote mutations can achieve such subtle optimization. A mutation directly in the active site would result in a larger, more disruptive change (e.g., even a single additional carbon center would fill an additional 4 Å radius) and therefore be unable to provide the necessary fine-tuning. Other directed evolution studies also observed the accumulation of remote mutations (**Morley and Kazlauskas, 2005**), suggesting that fine-tuning of the active site may be a common strategy to implement a new function.

Our work reveals that the adaptive landscape of PTE is highly rugged: even single amino acid changes can regulate activities upwards or downwards and also predetermine the potential effect of subsequent mutations. As discussed above, because multiple mutations can directly or indirectly affect the same key component for catalysis, their effects are likely to be epistatic. Therefore, the alternative trajectory is caused by epistasis between mutations: frequently, those mutations that accumulate first have a permissive or restrictive effect on subsequent mutations. Overall, >70% of mutations have highly variable effects on phosphotriesterase activity, depending on the genetic background (26 out of 33 positions, **Figure 5**), and ~40% showed sign epistasis (7 out of 33). The role of epistasis in natural evolution has recently received much attention, but its extent and prevalence are still under debate (**Whitlock et al., 1995**; **Poelwijk et al., 2007**; **de Visser et al., 2011**; **Breen et al., 2012**; **Harms and Thornton, 2013**; **McCandlish et al., 2013**; **Kaltenbach and Tokuriki, 2014**). Our findings suggest a high frequency of strong epistatic interactions during functional adaptation and therefore support the view that epistasis is paramount in shaping evolution. However, while restrictive mutations block many of the possible evolutionary trajectories, as has been previously emphasized, permissive mutations simultaneously open up new pathways, avoiding 'evolutionary dead-ends' and contributing to the diversity of enzyme homologs found in nature.

Moreover, our study demonstrates how genotypic irreversibility leads to the emergence of a functional sequence incompatible with the original one (**Kondrashov et al., 2002**; **Maheshwari and Barbash, 2011**), and implies the importance of evolutionary contingency on the genotypic level. In nature, the environment never ceases to change and a temporary relaxation in selection pressure (i.e., the level and type of nutrients or toxins) followed by re-adaptation (through both reversions and new compensatory mutations) may be common (**Akashi et al., 2012**). Higher levels of organization (such as metabolic or regulatory networks) might be subject to similar contingency; restoration of

a certain function may be achieved by alternative mutations in other parts of the protein structure, in other domains, or in a different protein altogether. If the mutations are mutually exclusive, sequence incompatibilities may arise rapidly. Therefore, in addition to proposed mechanisms such as genetic drift (**Akashi et al., 2012**), genotypic irreversibility may contribute to the prevalence of incompatibility between orthologous enzymes (**Lunzer et al., 2010**; **Kvitek and Sherlock, 2011**; **Corbett-Detig et al., 2013**; **Wellner et al., 2013**; **Schumer et al., 2014**; **Shafee et al., 2015**).

Finally, our observations have important implications for the engineering of highly efficient enzymes—for example, how fine-tuning of multiple active site regions can confer significant activity changes, and how context-dependent such changes are. As our understanding of protein sequence-structure-function relationships grows, further rational and computational approaches need to be developed to address the role of remote mutations and epistasis to enhance our ability to create tailor-made proteins.

Materials and methods

Error-prone PCR

Error-prone PCR libraries were generated using nucleotide analogues (8-oxo-2′-deoxyguanosine-5′-triphosphate [8-oxo-dGTP] and 2′-deoxy-P-nucleoside-5′-triphosphate [dPTP]) or Mutazyme (GeneMorph II Random Mutagenesis kit, Agilent, Santa Clara, CA, United States). A typical protocol using nucleotide analogues can be found in **Tokuriki and Tawfik (2009)**. A typical protocol using Mutazyme starts with a 50 µl PCR reaction containing 50 ng of pET-Strep-PTE template and 0.8 µM of outer primers (forward TTCCCCATCGGTGATGTC, reverse GTCACGCTGCGCGTAAC). Cycling conditions were: initial denaturation at 95˚C for 2 min followed by 10 cycles of denaturation (30 s, 95˚C), annealing (30 s, 63˚C) and extension (1 min, 72˚C), and a final extension step at 72˚C for 10 min. Plasmid was removed by treatment with *Dpn* I (NEB, Ipswich, MA, United States). The PCR product was purified using the QIAquick PCR purification kit (Qiagen, Netherlands), and amplified further with BIOTAQ DNA polymerase (Bioline, United Kingdom) using inner primers (forward ACGATGCGTCCGGCGTA, reverse GCTAGTTATTGCT CAGCG) and starting from 20 ng of template in a 100 µl reaction volume. Cycling conditions were: initial denaturation at 95˚C for 2 min followed by 20 cycles of denaturation (30 s, 95˚C), annealing (1 min, 58˚C) and extension (30 s, 72˚C), and a final extension step at 72˚C for 2 min. This gave an average of two amino acid substitutions per gene.

DNA shuffling

PTE genes of selected variants were amplified by PCR from pET-Strep-PTE plasmids using the outer primers and BIOTAQ DNA polymerase. Cycling conditions were: initial denaturation at 95˚C for 2 min followed by 25 cycles of denaturation (30 s, 95˚C), annealing (1 min, 63˚C) and extension (1 min, 72˚C), and a final extension step at 72˚C for 2 min. PCR products were purified using the QIAquick PCR purification kit and mixed at equal amounts. Before the preparative digest, conditions were optimized by digesting 1 µg of template DNA with a range of *DNase* I concentrations (Fermentas, Waltham, MA, United States). DNase digest buffer (10×) consists of 0.5 M Tris-HCl pH 7.5 supplemented with 0.5 mg/ml BSA. In addition, reactions contained 10 mM $MnCl_2$. Reactions were incubated for 10 min at 37˚C, stopped by addition of 1/5 vol of stop buffer (30 mM EDTA pH 8.0, 30% glycerol and ≈0.6× of a DNA loading buffer) and analyzed by agarose gel electrophoresis in TBE buffer (2% agarose gel, 45 mM Tris, 45 mM boric acid, and 1 mM EDTA pH 8.0; for all other agarose gel electrophoresis procedures, we used 1% agarose gels and TAE buffer, which is 40 mM Tris, 20 mM acetic acid, and 1 mM EDTA pH 8.0). Reactions were scaled up to 10–15 µg of DNA and the digest repeated at the appropriate DNase dilution to give fragments in the range of 50–150 bp. Fragments were purified by gel extraction and 60–80 ng used in a 20 µl assembly PCR. This PCR was performed with Herculase I (Stratagene, La Jolla, CA, United States). Cycling conditions were: initial denaturation at 96˚C for 90 s followed by 35 cycles of denaturation (30 s, 94˚C), annealing (incremental 3˚C steps from 65˚C down to 41˚C, 90 s each) and extension (2 min, 72˚C), and a final extension step at 72˚C for 10 min. Full-length assembly products were amplified using the inner primers and BIOTaq DNA polymerase under the following cycling conditions: initial denaturation at 95˚C for 2 min followed by 25 cycles of denaturation (30 s, 95˚C), annealing (1 min, 58˚C) and extension (1 min, 72˚C), and a final extension step at 72˚C for 2 min. The amount of assembly product used as template for this reaction was varied and

product formation verified by 1% agarose gel electrophoresis. Fractions containing product were pooled and purified using the QIAquick PCR purification kit.

Construction of single and double mutants

Mutants were constructed by site-directed mutagenesis as described in the QuikChange Site-Directed Mutagenesis manual (Agilent).

Cloning

PCR products and pET-Strep-ACP vector were digested with Fermentas FastDigest *Nco* I and *Hind* III (or *Kpn* I, see ***Supplementary file 1***) for 1 hr at 37˚C. The vector was treated with CIP (calf-intestinal alkaline phosphatase, NEB, Ipswich, MA, United States) for an additional hour and subsequently insert and vector were purified from 1% agarose gel using the QIAquick gel extraction kit followed by the Qiagen PCR purification kit. Ligations were performed at a vector:insert mass ratio of 1:1 using T4 DNA ligase (NEB, Ipswich, MA, United States) supplemented with 0.5 mM ATP (NEB, Ipswich, MA, United States) for 2 hr at 22˚C or 16˚C overnight. Prior to transformation, reactions were purified by ethanol/glycogen (Fermentas, Waltham, MA, United States) precipitation. Transformation into electrocompetent E. cloni 10G (Lucigen, Middleton, WI, United States) yielded at least 10^5 colonies.

Pre-screen on agar plates

Plasmids were extracted and re-transformed into *E. coli* BL21 (DE3) containing pGro7 plasmid for overexpression of the GroEL/ES chaperone system. Transformation reactions were plated on an average of 10 agar plates (140 mm diameter) containing 100 μg/ml ampicillin (or 50 μg/ml kanamycin, see ***Supplementary file 1***) and 34 μg/ml chloramphenicol such that each plate contained 200–1000 colonies, leading to a final library size of 2000–10,000 variants. Colonies were transferred onto nitrocellulose membrane (BioTrace NT Pure Nitrocellulose Transfer Membrane 0.2 μm, PALL Life Sciences, Port Washington, NY, United States), which was then placed onto a second plate additionally containing 1 mM isopropyl β-D-1-thiogalactopyranoside (IPGT) 200 μM $ZnCl_2$ (to ensure availability of Zn^{2+} ions necessary for enzymatic activity), and either 20% (wt/vol) arabinose for chaperone overexpression or 20% (wt/vol) glucose for repression of chaperone expression. After expression overnight at room temperature for plates containing arabinose or for 1 hr at 37˚C for plates containing glucose, the membrane was placed into an empty petri dish. For low activity levels of the parent gene where a maximum signal is desirable, cells were lysed prior to the activity assay by alternating three times between storage at −20˚C and 37˚C. For higher activities, the lysis step was omitted, making it easier to differentiate between different colonies. For the activity assay, 20–25 ml of 0.5% Agarose in 50 mM Tris-HCl buffer, pH 7.5 containing 200 μM 2NH (Sigma, St. Louis, MO, United States) and Fast Red (Sigma, St. Louis, MO, United States) was poured onto the membrane. Red color developed within 30 min. To screen for phosphotriesterase activity, the buffer contained varying concentrations of fluorogenic phosphotriester instead of 2NH/Fast Red as indicated in ***Supplementary file 1***. Turnover of O-fluoresceinyl-O,O-diethyl-thiophosphate (fluoresceinyl-DETP, excitation 495 nm, emission 520 nm) was detected in a Typhoon 9400 scanner (GE Healthcare, Wauwatosa, WI, United States) after an appropriate incubation time (0–3 hr). In the case of 7-O-diethylphosphoryl-3-cyano-4-methyl-7-hydroxycoumarin (Me-DEPCyC), activity was detected in an agarose gel imager (excitation 365 nm) using a SYBR Safe filter.

Screens in 96-well plates

Colonies exhibiting high enzymatic activity identified in the pre-screen were picked and re-grown in four to six 96-deep well plates overnight at 30˚C, leading to a library of 400–600 pre-selected variants. Wells contained 200 μl lysogeny broth (LB) supplemented with 100 μg/ml ampicillin and 34 μg/ml chloramphenicol. Subsequently, deep well plates containing 500 μl LB per well supplemented with ampicillin, chloramphenicol, and 20% (wt/vol) arabinose or glucose (depending on whether chaperone overexpression was to be induced or repressed) were inoculated with 25 μl of pre-culture and grown for 2–3 hr at 37˚C until the OD_{600} reached ~0.6. Expression of PTE variants was induced by adding IPTG to a final concentration of 1 mM and cultures were incubated for an additional 2 hr at 30˚C or for 1 hr at 37˚C in rounds aimed at reducing chaperone dependence. Cells

were spun down at 4˚C at maximum speed (3320×*g*) for 5–10 min and the supernatant was removed. Pellets were frozen for a minimum of 30 min at −80˚C and subsequently lysed by addition of 200 µl 50 mM Tris-HCl pH 7.5 supplemented with 0.1% (wt/vol) Triton-X100, 200 µM $ZnCl_2$, 100 µg/ml lysozyme, and ~1 µl of benzonase (25 U/µl, Novagen, Madison, WI, United States) per 100 ml. After 30 min of lysis at room temperature, cell debris was spun down at 4˚C at 3320×*g* for 20 min. Depending on the activity level of the library, clarified lysate was diluted prior to the activity assay to obtain a good signal in the initial linear phase of the reaction. Reactions were performed in transparent 96-well plates containing 200 µl per well (20 µl lysate + 180 µl of 200 µM substrate in 50 mM Tris-HCl, pH 7.5 supplemented with 0.02% Triton-X100 in the case of paraoxon and 0.1% in the case of 2NH/FR). Paraoxon hydrolysis was monitored at 405 nm; 2NH hydrolysis was monitored at 500 nm via complex formation with Fast Red. Improvements >1.3-fold relative to the previous round were considered significant. The best clones were picked and re-grown in triplicate. The observed initial rates were normalized to cell density (determined by the OD_{600}) and the average values determined. Approximately 10 improved variants were sequenced after each round. A description of each directed evolution round including selection criteria, the mutations found in each sequenced variant, and mention of the variants chosen as templates for the next library generation can be found in ***Supplementary file 1***.

Purification of Strep-tagged proteins for enzyme kinetics

pET-Strep-PTE plasmids were transformed into *E. coli* BL21 (DE3) and grown at 37˚C in TB medium containing 100 µg/ml ampicillin and 200 µM $ZnCl_2$. Expression was induced with 0.4 mM IPTG when cell density reached an OD_{600} of 0.6 units and cells grown overnight at 20˚C. Cells were harvested by centrifugation at 3320×*g* and 4˚C for 10 min, resuspended and lysed for 1 hr at room temperature using a 1:1 mixture of B-PER Protein Extraction Reagent (Thermo Scientific, Waltham, MA, United States) and 50 mM Tris-HCl buffer, pH 7.5 containing 200 µM $ZnCl_2$, 100 µg/ml lysozyme and ~1 µl of benzonase per 100 ml. Cell debris was removed by centrifugation at 30,000×*g* and 4˚C for 45 min and the clarified lysate passed through a 45 µm filter before loading onto a Strep-Tactin Superflow High capacity column (1 ml column volume). After several washes with 50 mM Tris-HCl buffer, pH 7.5 containing 200 µM $ZnCl_2$, Strep-PTE variants were eluted in the same buffer containing 2.5 mM desthiobiotin according to the manufacturer's instructions (IBA BioTAGnology, Germany). Protein was dialyzed overnight against 50 mM Tris-HCl buffer, pH 7.5 containing 100 mM NaCl and concentrated if necessary. This protocol was adapted for purification in 96-well format by using AcroPrep 96 Filter Plates (Pall Life Sciences, Port Washington, NY, United States) according to the manufacturer's instructions. Lysates were clarified using Lysate Clearance plates (3 µm GxF, 0.2 µm Supor) and transferred to filter plates (0.45 µm GHP) containing 50 µl Strep-tactin resin per well. Wells were washed 3× with 50 mM Tris-HCl pH 8.5 containing 100 mM NaCl and 200 µM $ZnCl_2$ and 3× with pH 7.5 buffer. After elution, samples were concentrated and elution buffer removed using ultrafiltration plates (Omega 10K membrane).

Kinetic characterization of variants

Paraoxon, 2NH, and Fast Red were purchased from Sigma (St. Louis, MO, United States). Substrates for linear free energy relationships were gifts from Dan Tawfik's laboratory and their synthesis is described in ***Khersonsky and Tawfik (2005)***. Absorbance wavelengths and extinction coefficients are given in ***Supplementary file 2***. For determination of initial rates in lysate, cells were grown and assayed in at least duplicate as described under the section 'Screens in 96-well plates'. The experiment was repeated and the average change relative to the respective parent variant and the standard deviation were determined (***Supplementary file 2***). A Student's *t*-test was performed to obtain p-values. Where applicable, p-values were also calculated to determine whether the effect of a certain mutation in two different backgrounds (rather than compared to the parent mutant lacking this mutation) is significant. For determination of initial rates using purified enzyme, variants were expressed and purified in 96-well format in at least duplicate and assayed as described above in 'Screens in 96-well plates'. For determination of Michaelis–Menten parameters, reactions were performed in triplicate at a range of substrate concentrations (0–2000 µM). Reactions were initiated by addition of 180 µl of substrate solution (in 50 mM Tris-HCl, pH 7.5 supplemented with 0.02–0.1% Triton X-100) to 20 µl of enzyme in 50 mM Tris-HCl, pH 7.5 supplemented with 200 µM $ZnCl_2$ and 0.02% Triton X-100. Data were fit to Michaelis–Menten kinetics in Kaleidagraph.

Purification of untagged proteins for crystallization

AE and *neo*PTE genes were cloned into pET32-trx plasmid without Strep-tag using FastDigest *Nco*I and *Hind*III as described above, transformed into *E. coli* BL21 (DE3), and grown for 72 hr at 30˚C in TB medium containing 100 μg/ml ampicillin and 500 μM $ZnCl_2$. Cells were harvested by centrifugation at 3320×*g* and 4˚C for 10 min, resuspended in 20 mM Tris-HCl pH 8 containing 100 μM $ZnCl_2$ and lysed by sonication (OMNI Sonic Ruptor 400, Thermo Scientific, Waltham, MA, United States, 3× 30 s on/60 s off, amplitude 40%). Cell debris was removed by centrifugation at 30,000×*g* and 4˚C for 45 min and lysate filtered through 45 μm filters (Millipore). The lysate was loaded onto two HiPrep Q FF columns (GE Healthcare, Wauwatosa, WI, United States) in series. PTE elutes in the flow through as well as the early wash fractions. Active fractions were pooled and passed through a 45 μm filter. The sample was concentrated over a Millipore spin column (MWCO 30,000) and purified by gel filtration (HiLoad 16/60 Superdex 200 prep grade, GE Healthcare, Wauwatosa, WI, United States). Protein was concentrated to 12 mg/ml and stored at 4˚C.

Crystallization, data collection and structure determination

Crystals of *wt*PTE, AE, and *neo*PTE were obtained by vapor diffusion from a solution containing protein (10 mg/ml) plus 20–30% wt/vol 2-methane-4-pentane diol (MPD), buffered to pH 6.5 by 0.1 M sodium cacodylate, as described previously (***Tokuriki et al., 2012***). Serial microseeding was performed to increase crystal size (***Bergfors, 2003***). Crystals grew to approximately 200 micrometers and were soaked in 40% MPD, 0.1 M sodium cacodylate as cryoprotectant for 5–10 min and then flash-cooled to 100 K in the gaseous nitrogen cryostream of a cooling device (Oxford Cryosystems, United Kingdom). Data were collected from frozen crystals on beamline MX1 of the Australian Synchrotron (AS). The data were indexed and integrated by XDS (***Kabsch, 2010***) and Aimless (***Evans and Murshudov, 2013***), with data cut-off being made at the highest resolution that retained a mean half dataset correlation coefficient ($CC^{1/2}$) of at least 0.5 in the outer shell (***Supplementary file 3***) (***Karplus and Diederichs, 2012***). Although all three crystals were crystallized in the same conditions, *neo*PTE crystallized in a different space group with different unit cell dimensions (p65, with a h, −h−k, l merohedral twin operator, vs C2221). A starting model for refinement (R18; PDB ID: 4E3T) (***Tokuriki et al., 2012***) was used to provide initial phases. Structures were refined with phenix.refine (***Afonine et al., 2012***) and validated with molprobity (***Chen et al., 2010***), as implemented in the phenix software suite (***Supplementary file 3***) (***Adams et al., 2010***).

Acknowledgements

We thank Dan S Tawfik and members of the Tokuriki laboratory for comments on the manuscript and Kirsten Wyganowski for technical support. This work was supported by the Natural Sciences and Engineering Research Council of Canada. MK was partially supported by the EU ITN ProSA. NT is a CIHR new investigator and a Michael Smith Foundation of Health Research (MSFHR) career investigator. CJJ acknowledges an ARC Discovery Early Career Researcher Award. FH is an ERC Starting Investigator.

Additional information

Funding

Funder	Grant reference	Author
Natural Sciences and Engineering Research Council of Canada (Conseil de Recherches en Sciences Naturelles et en Génie du Canada)	Discovery Grants RGPIN 418262-12	Nobuhiko Tokuriki
Australian Research Council (ARC)	FT140101059	Colin J Jackson
European Commission (EC)	MRTN-CT-2005-019475	Florian Hollfelder

Funder	Grant reference	Author
Biotechnology and Biological Sciences Research Council (BBSRC)	BB/I004327/1	Florian Hollfelder
European Research Council (ERC)	208813	Florian Hollfelder

The funders had no role in study design, data collection and interpretation, or the decision to submit the work for publication.

Author contributions

MK, NT, Conception and design, Acquisition of data, Analysis and interpretation of data, Drafting or revising the article; CJJ, Acquisition of data, Analysis and interpretation of data, Drafting or revising the article; ECC, Acquisition of data, Analysis and interpretation of data; FH, Analysis and interpretation of data, Drafting or revising the article

Additional files

Supplementary files

- Supplementary file 1. Description of the directed evolution rounds.
DOI: 10.7554/eLife.06492.019
- Supplementary file 2. Kinetic parameters of all variants.
DOI: 10.7554/eLife.06492.020
- Supplementary file 3. Crystallographic information.
DOI: 10.7554/eLife.06492.021

References

Adams PD, Afonine PV, Bunkoczi G, Chen VB, Davis IW, Echols N, Headd JJ, Hung LW, Kapral GJ, Grosse-Kunstleve RW, McCoy AJ, Moriarty NW, Oeffner R, Read RJ, Richardson DC, Richardson JS, Terwilliger TC, Zwart PH. 2010. PHENIX: a comprehensive Python-based system for macromolecular structure solution. *Acta Crystallographica Section D: Biological Crystallography* **66**:213–221. doi: 10.1107/S0907444909052925.

Afonine PV, Grosse-Kunstleve RW, Echols N, Headd JJ, Moriarty NW, Mustyakimov M, Terwilliger TC, Urzhumtsev A, Zwart PH, Adams PD. 2012. Towards automated crystallographic structure refinement with phenix.refine. *Acta Crystallographica Section D: Biological Crystallography* **68**:352–367. doi: 10.1107/S0907444912001308.

Aharoni A, Gaidukov L, Khersonsky O, Mc QG, Roodveldt C, Tawfik DS. 2005. The 'evolvability' of promiscuous protein functions. *Nature Genetics* **37**:73–76. doi: 10.1038/ng1482.

Akashi H, Osada N, Ohta T. 2012. Weak selection and protein evolution. *Genetics* **192**:15–31. doi: 10.1534/genetics.112.140178.

Bergfors T. 2003. Seeds to crystals. *Journal of Structural Biology* **142**:66–76. doi: 10.1016/S1047-8477(03)00039-X.

Breen MS, Kemena C, Vlasov PK, Notredame C, Kondrashov FA. 2012. Epistasis as the primary factor in molecular evolution. *Nature* **490**:535–538. doi: 10.1038/nature11510.

Bridgham JT, Ortlund EA, Thornton JW. 2009. An epistatic ratchet constrains the direction of glucocorticoid receptor evolution. *Nature* **461**:515–519. doi: 10.1038/nature08249.

Bull JJ, Badgett MR, Wichman HA, Huelsenbeck JP, Hillis DM, Gulati A, Ho C, Molineux IJ. 1997. Exceptional convergent evolution in a virus. *Genetics* **147**:1497–1507.

Carneiro M, Hartl DL. 2010. Colloquium papers: adaptive landscapes and protein evolution. *Proceedings of the National Academy of Sciences of USA* **107**((Suppl 1)):1747–1751. doi: 10.1073/pnas.0906192106.

Chen VB, Arendall WB III, Headd JJ, Keedy DA, Immormino RM, Kapral GJ, Murray LW, Richardson JS, Richardson DC. 2010. MolProbity: all-atom structure validation for macromolecular crystallography. *Acta Crystallographica Section D: Biological Crystallography* **66**:12–21. doi: 10.1107/S0907444909042073.

Chou HH, Chiu HC, Delaney NF, Segre D, Marx CJ. 2011. Diminishing returns epistasis among beneficial mutations decelerates adaptation. *Science* **332**:1190–1192. doi: 10.1126/science.1203799.

Clarke CA. 1985. Evolution in reverse: clean air and the peppered moth. *Biological Journal of the Linnean Society* **26**:189–199. doi: 10.1111/j.1095-8312.1985.tb01555.x.

Collin R, Miglietta MP. 2008. Reversing opinions on Dollo's Law. *Trends in Ecology & Evolution* **23**:602–609. doi: 10.1016/j.tree.2008.06.013.

Corbett-Detig RB, Zhou J, Clark AG, Hartl DL, Ayroles JF. 2013. Genetic incompatibilities are widespread within species. *Nature* **504**:135–137. doi: 10.1038/nature12678.

Crill WD, Wichman HA, Bull JJ. 2000. Evolutionary reversals during viral adaptation to alternating hosts. *Genetics* **154**:27–37.

Cruickshank DW. 1999. Remarks about protein structure precision. *Acta Crystallographica. Section D, Biological Crystallography* **55**:583–601. doi: 10.1107/S0907444998012645.
de Visser JA, Cooper TF, Elena SF. 2011. The causes of epistasis. *Proceedings of the Royal Society B: Biological Sciences* **278**:3617–3624. doi: 10.1098/rspb.2011.1537.
Dickinson BC, Leconte AM, Allen B, Esvelt KM, Liu DR. 2013. Experimental interrogation of the path dependence and stochasticity of protein evolution using phage-assisted continuous evolution. *Proceedings of the National Academy of Sciences of USA* **110**:9007–9012. doi: 10.1073/pnas.1220670110.
Evans PR, Murshudov GN. 2013. How good are my data and what is the resolution? *Acta Crystallographica Section D: Biological Crystallography* **69**:1204–1214. doi: 10.1107/S0907444913000061.
Gould SJ. 2007. *Wonderful life: burgess shale and the nature of history*. New York: W.W. Norton & Company, Inc.
Harms MJ, Thornton JW. 2013. Evolutionary biochemistry: revealing the historical and physical causes of protein properties. *Nature Reviews Genetics* **14**:559–571. doi: 10.1038/nrg3540.
Harms MJ, Thornton JW. 2014. Historical contingency and its biophysical basis in glucocorticoid receptor evolution. *Nature* **512**:203–207. doi: 10.1038/nature13410.
Hong SB, Raushel FM. 1996. Metal-substrate interactions facilitate the catalytic activity of the bacterial phosphotriesterase. *Biochemistry* **35**:10904–10912. doi: 10.1021/bi960663m.
Kabsch W. 2010. Xds. *Acta Crystallographica Section D: Biological Crystallography* **66**:125–132. doi: 10.1107/S0907444909047337.
Kaltenbach M, Tokuriki N. 2014. Dynamics and constraints of enzyme evolution. *Journal of Experimental Zoology B: Molecular and Developmental Evolution* **322**:468–487. doi: 10.1002/jez.b.22562.
Karplus PA, Diederichs K. 2012. Linking crystallographic model and data quality. *Science* **336**:1030–1033. doi: 10.1126/science.1218231.
Kawecki TJ, Lenski RE, Ebert D, Hollis B, Olivieri I, Whitlock MC. 2012. Experimental evolution. *Trends in Ecology & Evolution* **27**:547–560. doi: 10.1016/j.tree.2012.06.001.
Khan AI, Dinh DM, Schneider D, Lenski RE, Cooper TF. 2011. Negative epistasis between beneficial mutations in an evolving bacterial population. *Science* **332**:1193–1196. doi: 10.1126/science.1203801.
Khanal A, Yu McLoughlin S, Kershner JP, Copley SD. 2014. Differential effects of a mutation on the normal and promiscuous activities of orthologs: implications for natural and directed evolution. *Molecular Biology and Evolution* **32**:100–108. doi: 10.1093/molbev/msu271.
Khersonsky O, Tawfik DS. 2005. Structure-reactivity studies of serum paraoxonase PON1 suggest that its native activity is lactonase. *Biochemistry* **44**:6371–6382. doi: 10.1021/bi047440d.
Khersonsky O, Tawfik DS. 2010. Enzyme promiscuity: a mechanistic and evolutionary perspective. *Annual Review of Biochemistry* **79**:471–505. doi: 10.1146/annurev-biochem-030409-143718.
Kitano J, Bolnick DI, Beauchamp DA, Mazur MM, Mori S, Nakano T, Peichel CL. 2008. Reverse evolution of armor plates in the threespine stickleback. *Current Biology* **18**:769–774. doi: 10.1016/j.cub.2008.04.027.
Kondrashov AS, Sunyaev S, Kondrashov FA. 2002. Dobzhansky-Muller incompatibilities in protein evolution. *Proceedings of the National Academy of Sciences of USA* **99**:14878–14883. doi: 10.1073/pnas.232565499.
Kvitek DJ, Sherlock G. 2011. Reciprocal sign epistasis between frequently experimentally evolved adaptive mutations causes a rugged fitness landscape. *PLOS Genetics* **7**:e1002056. doi: 10.1371/journal.pgen.1002056.
Lenski RE. 1988. Experimental studies of pleiotropy and epistasis in *Escherichia coli*. II. Compensation for maladaptive effects associated with resistance to T4 virus. *Evolution; International Journal of Organic Evolution* **42**:433–440. doi: 10.2307/2409029.
Lobkovsky AE, Koonin EV. 2012. Replaying the tape of life: quantification of the predictability of evolution. *Frontiers in Genetics* **3**:246. doi: 10.3389/fgene.2012.00246.
Lunzer M, Golding GB, Dean AM. 2010. Pervasive cryptic epistasis in molecular evolution. *PLOS Genetics* **6**:e1001162. doi: 10.1371/journal.pgen.1001162.
MacLean RC, Perron GG, Gardner A. 2010. Diminishing returns from beneficial mutations and pervasive epistasis shape the fitness landscape for rifampicin resistance in Pseudomonas aeruginosa. *Genetics* **186**:1345–1354. doi: 10.1534/genetics.110.123083.
Maheshwari S, Barbash DA. 2011. The genetics of hybrid incompatibilities. *Annual Review of Genetics* **45**:331–355. doi: 10.1146/annurev-genet-110410-132514.
McCandlish DM, Rajon E, Shah P, Ding Y, Plotkin JB. 2013. The role of epistasis in protein evolution. *Nature* **497**:E1–E2. discussion E2–E3. doi: 10.1038/nature12219.
Morley KL, Kazlauskas RJ. 2005. Improving enzyme properties: when are closer mutations better? *Trends in Biotechnology* **23**:231–237. doi: 10.1016/j.tibtech.2005.03.005.
Orr HA. 1995. The population genetics of speciation: the evolution of hybrid incompatibilities. *Genetics* **139**:1805–1813.
Peisajovich SG, Tawfik DS. 2007. Protein engineers turned evolutionists. *Nature Methods* **4**:991–994. doi: 10.1038/nmeth1207-991.
Poelwijk FJ, Kiviet DJ, Weinreich DM, Tans SJ. 2007. Empirical fitness landscapes reveal accessible evolutionary paths. *Nature* **445**:383–386. doi: 10.1038/nature05451.
Romero PA, Arnold FH. 2009. Exploring protein fitness landscapes by directed evolution. *Nature Reviews Molecular Cell Biology* **10**:866–876. doi: 10.1038/nrm2805.
Roodveldt C, Tawfik DS. 2005. Shared promiscuous activities and evolutionary features in various members of the amidohydrolase superfamily. *Biochemistry* **44**:12728–12736. doi: 10.1021/bi051021e.

Salverda ML, Dellus E, Gorter FA, Debets AJ, van der Oost J, Hoekstra RF, Tawfik DS, de Visser JA. 2011. Initial mutations direct alternative pathways of protein evolution. *PLOS Genetics* **7**:e1001321. doi: 10.1371/journal.pgen.1001321.

Schumer M, Cui R, Powell DL, Dresner R, Rosenthal GG, Andolfatto P. 2014. High-resolution mapping reveals hundreds of genetic incompatibilities in hybridizing fish species. *eLife* **3**:e02535. doi: 10.7554/eLife.02535.

Shafee T, Gatti-Lafranconi P, Minter R, Hollfelder F. 2015. Handicap-recover evolution leads to a chemically versatile, nucleophile-permissive protease. *Chembiochem*. doi: 10.1002/cbic.201500295.

Socha RD, Tokuriki N. 2013. Modulating protein stability—directed evolution strategies for improved protein function. *The FEBS Journal* **280**:5582–5595. doi: 10.1111/febs.12354.

Stebbins J. 1944. The Law of diminishing returns. *Science* **99**:267–271. doi: 10.1126/science.99.2571.267.

Teotonio H, Rose MR. 2000. Variation in the reversibility of evolution. *Nature* **408**:463–466. doi: 10.1038/35044070.

Teotonio H, Rose MR. 2001. Perspective: reverse evolution. *Evolution; International Journal of Organic Evolution* **55**:653–660. doi: 10.1554/0014-3820(2001)055[0653:PRE]2.0.CO;2.

Tokuriki N, Jackson CJ, Afriat-Jurnou L, Wyganowski KT, Tang R, Tawfik DS. 2012. Diminishing returns and tradeoffs constrain the laboratory optimization of an enzyme. *Nature Communications* **3**:1257. doi: 10.1038/ncomms2246.

Tokuriki N, Tawfik DS. 2009. Chaperonin overexpression promotes genetic variation and enzyme evolution. *Nature* **459**:668–673. doi: 10.1038/nature08009.

Wellner A, Raitses Gurevich M, Tawfik DS. 2013. Mechanisms of protein sequence divergence and incompatibility. *PLOS Genetics* **9**:e1003665. doi: 10.1371/journal.pgen.1003665.

Whitlock MC, Phillips PC, Moore FB, Tonsor SJ. 1995. Multiple fitness peaks and epistasis. *Annual Review of Ecology, Evolution, and Systematics* **26**:601–629. doi: 10.1146/annurev.es.26.110195.003125.

Wyganowski KT, Kaltenbach M, Tokuriki N. 2013. GroEL/ES buffering and compensatory mutations promote protein evolution by stabilizing folding intermediates. *Journal of Molecular Biology* **425**:3403–3414. doi: 10.1016/j.jmb.2013.06.028.

Supplementary file 1 for Kaltenbach at al., Reverse evolution leads to genotypic incompatibility despite functional and active-site convergence

Description of the directed evolution rounds

Supplementary File 1A. Library creation and screening conditions for rounds 19-22 of the forward evolution and all rounds of the reverse evolution. Rounds 1-18 have been described in (Tokuriki et al., 2012).

Round	Mutagenesis method	Template	pET-Strep construct used		Substrate used in pre-screen	Property under selection
			Restriction sites[a]	*Resistance*[a]		
19	epPCR (mutazyme)	R18	NcoI/HindIII	Amp	200 µM 2NH/Fast Red	specificity (2-NH/paraoxon)
20	shuffling	10 R19 clones	NcoI/HindIII	Amp	200 µM 2NH/Fast Red	specificity (2-NH/Paraoxon)
21	epPCR (mutazyme)	R20	NcoI/HindIII	Amp	200 µM 2NH/Fast Red	specificity (2-NH/Paraoxon)
22	epPCR (mutazyme)	R21	NcoI/HindIII	Amp	200 µM 2NH/Fast Red	reduced chaperone dependence
rev1	epPCR (mutazyme)	AE	NcoI/HindIII	Amp	10 µM Fluoresceinyl-DETP[b]	paraoxonase
rev2	shuffling	10 rev1 & 4 R25 clones	NcoI/HindIII	Amp	10 µM Fluoresceinyl-DETP	paraoxonase
rev3	epPCR (mutazyme)	revR2	NcoI/HindIII	Amp	1 µM Fluoresceinyl-DETP	paraoxonase
rev4	shuffling	13 rev3 clones	NcoI/HindIII	Amp	20 nM Fluoresceinyl-DETP	paraoxonase
rev5	epPCR (mutazyme)	revR4	NcoI/HindIII	Amp	100 nM Fluoresceinyl-DETP	reduced chaperone dependence
rev6	shuffling	17 rev5 clones	NcoI/HindIII	Amp	100 nM Fluoresceinyl-DETP	reduced chaperone dependence
rev7	epPCR (mutazyme)	revR6	NcoI/HindIII	Amp	100 nM Fluoresceinyl-DETP	paraoxonase
rev8	epPCR (8-Oxo-dGTP+dPTP)	revR7a and revR7b	NcoI/HindIII	Amp	10 µM Me-DEPCyC[b]	paraoxonase
rev9	epPCR (8-Oxo-dGTP+dPTP)	5 rev8 clones	NcoI/HindIII	Kan	10 µM Me-DEPCyC	paraoxonase
rev10	epPCR (8-Oxo-dGTP+dPTP)	revR9	NcoI/HindIII	Amp	10 µM Me-DEPCyC	paraoxonase
rev11	epPCR (8-Oxo-dGTP+dPTP)	228 rev9 clones	NcoI/HindIII	Amp	10 µM Me-DEPCyC	Reduced chaperone
rev12	epPCR (8-Oxo-dGTP+dPTP)	135 rev10 clones	NcoI/HindIII	Amp	10 µM Me-DEPCyC	paraoxonase
rev13	epPCR (8-Oxo-dGTP+dPTP)	168 rev12 clones	NcoI/HindIII	Amp	10 µM Me-DEPCyC	paraoxonase
rev14	shuffling	*neo*PTE and revR8a	NcoI/HindIII	Amp	10 µM Me-DEPCyC	paraoxonase
rev2b	epPCR (mutazyme)	revR1	NcoI/HindIII	Amp	10 µM Fluoresceinyl-DETP	paraoxonase
rev3b	shuffling	AE and 2 rev2b clones	NcoI/HindIII	Kan	10 µM Fluoresceinyl-DETP	paraoxonase
rev4b	epPCR (8-Oxo-dGTP+dPTP)	3 rev3b clones	NcoI/HindIII	Kan	10 µM Me-DEPCyC	reduced chaperone dependence
rev5b	epPCR (8-Oxo-dGTP+dPTP)	revR4b	NcoI/HindIII	Kan	10 µM Me-DEPCyC	paraoxonase
rev6b	epPCR (mutazyme)	revR5b	NcoI/KpnI	Kan	10 µM Me-DEPCyC	paraoxonase
rev6b-2	epPCR (8-Oxo-dGTP+dPTP)	revR5b	NcoI/KpnI	Kan	10 µM Me-DEPCyC	paraoxonase

[a] To avoid cross-contamination between libraries, the second trajectory library was placed into a pET-Strep vector with kanamycin resistance from round rev3b. Additionally, the *Hind*III restriction site was replaced by a *Kpn*I site from round rev5b to prevent cross-contamination during cloning.

[b] Fluoresceinyl-DETP: O-fluoresceinyl-O,O-diethyl-thiophosphate, Me-DEPCyC: 7-O-diethylphosphoryl-3-cyano-4-methyl-7-hydroxycoumarin.

Information about Supplementary Files 1B-V. These files give an overview of all selected clones. For activity measurements, cells were grown in triplicate. Cell lysates were sufficiently diluted to determine initial rates using paraoxon and/or 2NH as substrates, normalized to cell density (determined by absorption at 600 nm) and averaged. Activities are given relative to the activity of the parent mutant (columns "2NH" and "paraoxon"). The activity of the parent mutant is shown in the first row of each table in italics. Specificity for 2NH (column "2NH/paraoxon") is given as the ratio of 2NH activity to paraoxon and is not normalized to the parent mutant. Chaperone dependence (column "+GroEL/-GroEL") is the ratio of the activity measured in the presence of GroEL/ES to the activity in the absence of GroEL/ES and is also not normalized. Note that data from different tables is not directly comparable as lysates were diluted to different extents in different rounds (ranging from no dilution to 5×10^4-fold) depending on the activity of the variants. Mutations are given relative to the parent mutant unless otherwise indicated. Enriched mutations are shown in grey boxes. For the reverse evolution, all changes in previously mutated positions are shown in bold, and back-to-ancestor mutations are additionally written in small, italic letters.

Forward evolution

Round 1-18. These rounds have been described in detail in the Supporting Information of reference (Tokuriki et al., 2013).

Round 19. The library was created by error-prone PCR from PTE-R18 using mutazyme and screened for increased specificity for 2NH.

Supplementary File 1B. Activity, selectivity (2NH/paraoxon), and mutations of round 19 variants.

Variant	paraoxon	2NH	2NH/ paraoxon	Mutations			
R18	*1.0*	*1.0*	*1.5*				
19_1	0.2	0.5	3.4	*m*314T	*r*356Q	STOP365	
19_2	0.6	1.2	2.8	[a]			
19_3	0.4	1.2	4.6	*v*183A	*i*288V	*i*341T	
19_4 "**R19**"	0.1	0.7	11.9	*a*74T	*v*143A	*q*180H	*t*311A
19_5	0.1	0.5	9.4	*l*132F	*t*177I	*p*342S	
19_6	0.04	0.3	11.6	*g*101M			
19_7	0.1	0.6	7.2	*v*183E			
19_8	0.5	1.1	3.7	*m*317L			
19_9	0.3	0.9	4.1	*t*45A	*v*183L		
19_10	0.2	0.5	3.5	*l*113M	*e*144V	*t*202A	

[a] This variant contained only synonymous mutations.

Round 20. The library was created by DNA shuffling of the 10 round 19 variants (**Supplementary File 1B**) and screened for increased specificity for 2NH.

Supplementary File 1C. Activity (relative to R19), selectivity (2NH/paraoxon), and mutations (relative to R18) of round 20 variants.

Variant	paraoxon	2NH	2NH/ paraoxon	Mutations			
R19	*1.0*	*1.0*	*1.7*				
20_1	0.2	0.6	4.7	*v*183E	*v*292H	*m*317L	*p*342S
20_2	0.2	0.6	5.8	*q*180H	*s*238C		
20_3 "**R20**"	0.2	0.7	6.2	*t*45A	*e*144V	*q*180H	
				*m*314T	*i*341T		
20_4	0.2	0.6	5.1	*t*45A	*q*180H		
20_5	0.2	0.6	5.5	*v*183E	*m*317L		
20_6	0.2	0.7	3.9	*e*144V	*v*183A	*m*317L	
20_7	0.4	0.9	5.4	*r*36Q	*v*183E		
20_8	0.2	0.7	5.6	*t*45A	*q*180H	*m*317L	
20_9	0.3	0.9	6.7	*t*45A	*v*183E		
20_10	0.3	1	5.3	*v*183L	*m*317L		
20_11	0.3	1	3.6	*m*314T			

Round 21. The library was created by error-prone PCR from PTE-R20 using mutazyme and screened for increased specificity for 2NH.

Supplementary File 1D. Activity, selectivity (2NH/paraoxon), chaperone dependence (+GroEL/-GroEL), and mutations of round 21 variants.

Variant	paraoxon	2NH	2NH/ paraoxon	+GroEL/ -GroEL	Mutations		
R20	*2.7*	*12.3*	*4.6*	*17.3*			
21_1 "**R21**"	0.5	1	8.1	6.4	*s*102T		
21_2	0.8	1	5.8	18.4	*t*361A		
21_3	0.9	1	5.3	18.4	**[b]**		
21_4	0.3	0.6	9.9	n.d.[a]	*y*156N	*a*193T	
					*s*238N	*y*292H	*I*362M
21_5	0.4	0.7	8.4	n.d.[a]	*a*126P	*g*261D	

[a] n.d.: Activity in the absence of GroEL/ES was not detected; therefore, chaperone dependence could not be determined.

[b] This variant contained only synonymous mutations.

Round 22. The library was created by error-prone PCR from PTE-R21 using mutazyme and screened for reduced chaperone dependence.

Supplementary File 1E. Activity, selectivity (2NH/paraoxon), chaperone dependence (+GroEL/-GroEL), and mutations of round 22 variants.

Variant	paraoxon	2NH	2NH/ paraoxon	+GroEL/ -GroEL	Mutations
R21	*15.7*	*41*	*0.4*	*3.1*	
22_1	1.1	1.1	0.4	3.4	**[a]**
22_2	1.1	1.2	0.4	3	**[a]**
22_3	0.6	1.1	0.2	3.9	*e*263Q
22_4	0.5	1	0.1	2.9	*r*363Q
22_5 "**AE**"	3.5	0.9	0.3	1.5	*v*176M
22_6	0.8	1.2	0.3	3.3	**[a]**
22_7	0.9	1	0.4	2.7	*r*363Q

[a] These variants contained only synonymous mutations.

Round 23-25. Three additional rounds of forward evolution were performed, but no variants with further reduced phosphotriesterase activity could be found without compromising arylesterase activity.

Reverse evolution

Round rev1. The library was created by error-prone PCR from AE using mutazyme and screened for increased phosphotriesterase activity.

Supplementary File 1F. Phosphotriesterase activity and mutations of round rev1 variants.

Variant	paraoxon	Mutations		
AE	*1.0*			
rev1_1	3.1	**M176A**	*s*308I	
rev1_2	4.6	**I172*t***		
rev1_3	4	**I172*t***	*s*222N	
rev1_4 "**revR1**"	9.9	*c*59Y	*s*238R	*s*308C
rev1_5	9.2	*f*104Y	*q*290H	
		F313*i*	**T314S**	
rev1_6	5.4	**I172*t***		
rev1_7	6.3	**V130M**		
rev1_8	1.7	*d*35G	*s*308N	
rev1_9	2.2	*h*257L		

Round rev2. The library was created by DNA shuffling of 9 round rev1 variants (**Supplementary File 1F**) and 4 round 25 variants (**Supplementary File 1G**) and screened for increased phosphotriesterase activity.

Supplementary File 1G. Activity, selectivity (2NH/paraoxon), and mutations of round 25 variants.

Variant	paraoxon	2NH	2NH/ paraoxon	Mutations				
AE	*1.0*	*1.0*	*1.3*					
25_1	2.4	0.2	0.1	*d*121G	*i*284V	*k*285N	**I172*t***	*m*293K
25_2	1.8	0.2	0.1	**I172*t***	*l*283S			
25_3	15.2	0.3	0	*s*308C				
25_4	4.5	0.4	0.1	*t*234I	**M272*l***	*k*175M	*k*339Q	

Supplementary File 1H. Phosphotriesterase activity and mutations of round rev2 variants.

Variant	paraoxon	Mutations				
AE	*1.0*					
rev2_1	151	**V130M**	**I172*t***	*s*308C		
rev2_2	151.7	**V130M**	**I172*t***	*s*308C		
rev2_3	145.7	*a*92T	**V130M**	**I172*t***	*s*308C	**T341*i***
rev2_4	136	*i*37V	**I172*t***	*s*205G	*s*308C	*d*232G
rev2_5	124.7	*k*82R	**V130M**	**I172*t***	*s*308C	
rev2_6 "**revR2**"	142	**V130M**	**I172*t***	*s*308C		
rev2_7	172.7	**V130M**	**I172*t***	*s*308C		
rev2_8	141.7	**V130M**	**I172*t***	*s*308C		
rev2_9	173.3	**V130M**	**I172*t***	*s*308C	*i*328V	
rev2_10	168.7	**V130M**	**I172*t***	*s*308C		
rev2_11	160.3	**V130M**	**I172*t***	*m*293K	*s*308C	
rev2_12	164.3	**V130M**	**I172*t***	*s*308C		
rev2_13	160.7	**V130M**	**I172*t***	*s*308C		
rev2_14	46.3	*f*104Y	**I172*t***	*s*308C		
rev2_15	49	*f*104Y	**I172*t***	*s*308C		
rev2_16	55	*f*104Y	**I172*t***	*s*308C		

Round rev3. The library was created by error-prone PCR from PTE-revR2 using mutazyme and screened for increased phosphotriesterase activity.

Supplementary File 1I. Phosphotriesterase activity and mutations of round rev3 variants.

Variant	paraoxon	Mutations		
revR2	*1.0*			
rev3_1	3.5	**[a]**		
rev3_2 "**revR3**"	6.5	**F271*l***		
rev3_3	5.3	*t*137S	*h*257P	*i*296V
rev3_4	4.7	**[a]**		
rev3_5	4.3	*t*177S	**F271*l***	
rev3_6	4.4	**[a]**		
rev3_7	4.6	*p*135S		
rev3_8	3.6	**[a]**		
rev3_9	5.1	*p*135S		
rev3_10	3.4	*i*44V		
rev3_11	1.8	**[a]**		
rev3_12	3	**[a]**		
rev3_13	1.7	*r*85G		

Round rev4. The library was created by DNA shuffling of 13 round rev3 variants (**Supplementary File 1I**) and screened for increased phosphotriesterase activity.

Supplementary File 1J. Phosphotriesterase activity (relative to revR3) and mutations (relative to revR2) of round rev4 variants.

Variant	paraoxon	Mutations				
revR3	*1.0*					
rev4_1	1.8	*i*44V	**F271*l***	*s*276P		
		T314*m*	*t*350I			
rev4_2	1.6	**M176A**	*t*202S	**F271*l***	*i*296V	
rev4_3	1.4	*p*135S	**F271*l***			
rev4_4	2.8	**V49*a***	**T137*s***	**F271*l***		
rev4_5	1.4	*i*44V	**F271*l***	I296V	*I*362M	
rev4_6	1.3	*p*135S	**F271*l***			
rev4_7	2	**V49*a***	*p*135S	*r*189Q	*i*296V	**T314*m***
rev4_8 "**revR4**"	2.7	*p*135S	**F271*l***	**T314*m***		
rev4_9	1.9	**F271*l***	**T314*m***			
rev4_10	1.3	**F271*l***				
rev4_11	3.7	*p*135S	**F271*l***	**T314*m***		
rev4_12	2.2	*p*135S	**F271*l***	**T314*m***		
rev4_13	1.8	*p*135S	*r*88L	**F271*l***	*s*276P	
rev4_14	1.3	**F271*l***				

Round rev5. The library was created by error-prone PCR from PTE-revR4 using mutazyme and screened for reduced chaperone dependence.

Supplementary File 1K. Phosphotriesterase activity, chaperone dependence (+GroEL/-GroEL), and mutations of round rev5 variants.

Variant	paraoxon	+GroEL/ -GroEL	Mutations	
revR4	*1.0*	*7.6*		
rev5_1	1.9	6.7	*g*174D	*a*347T
rev5_2	1.8	7.2	*k*175N	STOP366C
rev5_3	1.5	8.5	*t*52A	
rev5_4 "**revR5**"	1.6	4.6	*m*293K	
rev5_5	1	4.1	*a*347E	
rev5_6	0.5	2.3	*t*345S	
rev5_7	4.3	6.4	**M176*v***	*a*203E

Round rev6. The library was created by DNA shuffling of the 7 round rev5 variants shown in **Supplementary File 1K** and an additional 10 unsequenced variants and screened for reduced chaperone dependence.

Supplementary File 1L. Phosphotriesterase activity (relative to revR5), chaperone dependence (+GroEL/-GroEL), and mutations (relative to revR4) of round rev6 variants.

Variant	paraoxon	+GroEL/ -GroEL	Mutations		
revR4	*0.4*	*10.3*			
revR5	*1.0*	*9.2*	*m*293K		
rev6_1	1.0	6.6	*a*203E	*m*293K	
rev6_2	1.1	8.7	*a*203E		
rev6_3	0.8	6.9	*t*52A	*i*167V	*a*203E
rev6_4 "**revR6**"	0.7	6.9	*a*203E		
rev6_5	0.8	6.8	*a*203E	*m*293K	*t*345S
rev6_6	1.2	8.7	*k*175E	*a*203E	
rev6_8	1.2	10	*a*203E		
rev6_10	1.8	12.7	*a*203E		
rev6_11	1.1	9.7	*t*173A	*a*203E	A203E

Round rev7. The library was created by error-prone PCR from PTE-revR6 using mutazyme and screened for increased phosphotriesterase activity.

Supplementary File 1M. Phosphotriesterase activity and mutations of round rev7 variants.

Variant	paraoxon	Mutations	
revR6	*1.0*		
rev7_1 "**revR7a**"	1.5	**H180*q***	*s*258N
rev7_2	1.2	**[a]**	
rev7_3	1.4	**[a]**	
rev7_4 "**revR7b**"	2.4	*g*174D	
rev7_5	1.2	**[a]**	
rev7_6	1.3	**[a]**	
rev7_7	0.9	**M130V**	*l*237S

[a] These variants contained only synonymous mutations.

Round rev8. The library was created by error-prone PCR from PTE-revR7a and PTE-revR7b using deoxynucleotide analogues and screened for increased phosphotriesterase activity.

Supplementary File 1N. Phosphotriesterase activity (relative to revR7a) and mutations (relative to revR6) of round rev8 variants.

Variant	paraoxon	Mutations			
revR7a	*1.0*				
rev8_1	1.1	*g*174D			
rev8_2	1.1	*g*174D			
rev8_3	1.3	**I138*m***	**H180*q***	*s*256N	
		*e*344D			
rev8_4	1	*g*174D			
rev8_5	0.8	**V144A**	**H180*q***		
		*s*258N			
rev8_6 "**revR8a**"	2	*g*174D	*s*258N	*i*296V	
rev8_7	1.3	*g*174D			
rev8_8	1.4	*g*174D	*n*265S		
rev8_9 "**revR8b**"	2	*y*156H	*g*174D	**H180*q***	*d*264E

Round rev9. The library was created by error-prone PCR from 5 revR8 variants (rev8_1, 3, 5, revR8a, and revR8b) using deoxynucleotide analogues and screened for increased phosphotriesterase activity.

Supplementary File 1O. Phosphotriesterase activity (relative to revR8b) and mutations (relative to revR6) of round rev9 variants.

Variant	paraoxon	Mutations			
revR8a	*1.0*				
rev9_1	1.9	**I138*m***	*g*174D	**H180*q***	*s*258N
		*i*296V			
rev9_2 "**revR9**"	2.0	*y*156H	*g*174D	**H180*q***	*s*258N

Round rev10. The next library was made by error-prone PCR from PTE-revR9 using deoxynucleotide analogues. Because no improved variants were identified, a pool of the best 228 clones (with phosphotriesterase activities ≥ 0.5-fold relative to PTE-revR9) was taken into the next round.

Round rev11. Error-prone PCR (deoxynucleotide analogues) was performed on top of the plasmid mix from round rev10 and screened for reduced chaperone dependence. Again, no improved variants were identified, and 135 clones (with phosphotriesterase activities ≥ 0.5-fold relative to PTE-revR9) were taken into the next round.

Round rev12. Screening of a new error-prone library (deoxynucleotide analogues) using the plasmid mix from round rev11 yielded one variant with increased phosphotriesterase activity (1.3-fold relative to PTE-revR9), which contained the back-mutation V49A and a new mutation in a known position, I306M. This variant is "*neo*PTE".

Round rev13-14. To corroborate that no further improvements could be found, a rev13 library was constructed by error-prone library (deoxynucleotide analogues) using a mix of 168 plasmids including *neo*PTE from round rev12. No significantly improved variants were found. The best variants had *neo*PTE-like activity and showed enrichment of I306M and a high fraction of synonymous mutations, indicating that no functional mutations could be found. To confirm whether the mutation V49*a* was also relevant or hitchhiking, *neo*PTE was back-shuffled with revR8x (round rev14). All variants kept the I306M mutation, and all but 1 the V49*a* reversion.

Supplementary File 1P. Phosphotriesterase activity and mutations of round rev13 variants.

Variant	paraoxon	Mutations			
neoPTE	*1.0*				
rev13_1	1.1	**I306M**			
rev13_2	1	**I306M**			
rev13_3	1	*e*81G	*w*302R	**I306M**	*a*355V
rev14_4	1.2	**I306M**			
rev13_5	1.2	**[a]**			
rev13_6	1.2	**I306M**			
rev13_7	1.1	**I306M**			
rev13_8	1.1	**I306M**			
rev13_9	1	*i*284V	**I306M**		

[a] This variant contained only synonymous mutations.

Supplementary File 1Q. Phosphotriesterase activity and mutations of round rev14 variants.

Variant	paraoxon	Mutations	
neoPTE	*1.0*		
rev14_1	1.2		
rev14_2	1		
rev14_3	0.7	N258s[a]	*d*264E
rev14_4	1.5		
rev14_5	1.2		
rev14_6	1.3		
rev14_7	1.4		
rev14_8	1.7		
rev14_9	1.2	*a*49V[a]	

[a] Because mutations are given relative to *neo*PTE, the table shows that Ser258 and *Ala*49 were present in all but the indicated variants.

Reverse evolution: Alternative trajectory excluding back-to-ancestor mutations

In this trajectory, variants with improved phosphotriesterase activity were only accepted as templates for library generation for the next round if they did not contain any back-to-ancestor mutations.

Round revR1b. The first library was identical to round rev1. However, instead of shuffling selected clones, only PTE-revR1 was chosen for the next round as it exhibits the greatest increase in phosphotriesterase activity and lacks back-to-ancestor mutations.

Round revR2b. The library was created by error-prone PCR from PTE-revR1 using mutazyme and screened for increased phosphotriesterase activity.

Supplementary File 1R. Phosphotriesterase activity and mutations of round rev2b variants.

Variant	paraoxon	Mutations				
revR1	*1.0*					
rev2b_1	4.2	*p*354S	**I172*t***			
rev2b_2	2.7	**H180*q***				
rev2b_3	1.6	*i*167V	*s*224T	**I172*t***	*i*333V	
rev2b_4	1.8	**T314*m***				
rev2b_5	3.2	**V130*l***				
rev2b_6	1.3	*l*146I	*t*173S			
rev2b_7 "**revR2b**"	2.1	*p*135S				
rev2b_8	1.6	*i*37V	*d*121N	**M176I**	**M272*l***	
rev2b_9	3.7	**E233*d***				

Round revR3b. The library was created by DNA shuffling of AE, rev2B_6 and revR2b, and screened for increased phosphotriesterase activity.

Supplementary File 1S. Phosphotriesterase activity (relative to revR2b) and mutations (relative to AE) of round rev3b variants.

Variant	paraoxon	Mutations				
revR2b	*1.0*					
rev3b_1 "**revR3b**"	1.9	*p*135S	*q*290R	*s*308C		
rev3b_2	1.5	*p*135S	*t*173S	*s*238R	*s*308C	
		*p*135S	*s*308C	*p*342S		
rev3b _3	1.7	*v*101A	*p*135S	*s*308C		
rev3b _4	1.6	*c*59Y	*p*135S	*s*308C		
rev3b _5	1.5	*c*59Y	*p*135S	*g*162E	*t*173S	*s*308C
rev3b _6	1.5	*p*135S	*s*238R	*s*308C		
rev3b _7	1.6	*p*135S	*s*238R	*s*308C		
rev3b _8	2.8	**T102s**	*p*135S	*s*308C		
rev3b _9	1.7	*p*135S	*s*238R	*s*308C		

Round revR4b. The library was created by error-prone PCR from revR3b, rev3b_2, and 7 using deoxynucleotide analogues and screened for reduced chaperone dependence.

Supplementary File 1T. Phosphotriesterase activity (relative to rev4b_0), chaperone dependence (+GroEL/-GroEL), and mutations (relative to AE+P135S+S308C) of round rev4b variants.

Variant	paraoxon	+GroEL/ -GroEL	Mutations		
rev4b_0 [a]	*1.0*	*4.2*			
rev4b_1	1.0	3.4	*i*167V	**I306L**	*q*290R
rev4b_2 "**revR4b**"	0.9	3.8	*q*290R	*t*345A	
rev4b_3	1.4	13.2	*f*270L	*q*290R	

[a] Round rev4b was initially conducted in the presence of chaperones, but no improved variants were found. Because chaperone dependence was high in many clones, this round was repeated without chaperones and a clone from the first try with phosphotriesterase activity similar to revR3b and low chaperone dependence ("rev4b_0") used for comparison.

Round revR5b. The library was created by error-prone PCR from PTE-revR4b using mutazyme and screened for increased phosphotriesterase activity.

Supplementary File 1U. Phosphotriesterase activity and mutations of round rev5b variants.

Variant	paraoxon	Mutations	
revR4b	*1.0*		
rev5b_1	1.8	**M272*I***	
rev5b_2	1.4	*r*85I	*d*105H
rev5b_3 "**revR5b**"	2.7	*a*203E	
rev5b_4	2.4	**M272*I***	
rev4b_5	1.4	**I172S**	

Round rev6b. PTE-rev5b was used as template for error-prone PCR to give library rev6b. All clones with improved phosphotriesterase carried back-to-ancestor mutations (**Supplementary File 1V**). Library creation was repeated but again, the screen yielded no improved variants devoid of back-mutations (not shown). Therefore, this trajectory reached an activity plateau in round rev5b.

Supplementary File 1V. Phosphotriesterase activity, chaperone dependence (+GroEL/-GroEL), and mutations of round rev6b variants.

Variant	paraoxon	Mutations	
revR5b	*1.0*		
rev6b_1	1.5	*v*84A	**H180q**
rev6b_2	2.3	**H180q**	
rev6b_3	1.7	**T314*m***	**T341S**
rev6b_4	3.5	**I172S**	

References

Tokuriki N, Jackson CJ, Afriat-Jurnou L, Wyganowski KT, Tang R, Tawfik DS. 2012. Diminishing returns and tradeoffs constrain the laboratory optimization of an enzyme. *Nature Communications* **3**:1257.

Supplementary file 2 for Kaltenbach at al., Reverse evolution leads to genotypic incompatibility despite functional and active-site convergence

Kinetic parameters of all variants

Information about Supplementary Files 2A-G. These files give an overview of the kinetic parameters of all PTE variants. *Lysate measurements:* Cells were grown in at least duplicate and lysates sufficiently diluted (~1-10,000-fold) to determine initial rates of paraoxon and/or 2NH hydrolysis at a substrate concentration of 200 µM, normalized to cell density, corrected for the dilution factor, and averaged. This experiment was repeated twice and the combined average determined. *Purified enzyme measurements:* Variants were purified in at least duplicate in a 96-well format and sufficiently diluted (~ 0.1 nM - 10 µM) to determine initial rates of paraoxon and/or 2NH hydrolysis at a substrate concentration of 200 µM, corrected for the dilution factor, and averaged. Selected variants were purified on a larger scale to determine initial rates over a range of substrate concentrations and calculate Michaelis Menten parameters. For back-to-wild-type mutations, wild-type amino acid is shown in lower case italics.

Supplementary File 2A. Enzymatic activities of selected variants from the forward and reverse evolution in lysate and using purified enzyme.

Variant	Round	Paraoxon				2NH			
		lysate[a]	purified[b]			lysate[a]	purified[b]		
		relative to *wt*PTE	k_{cat} [s^{-1}]	K_M [μM]	k_{cat}/K_M [$M^{-1}s^{-1}$]	relative to *wt*PTE	k_{cat} [s^{-1}]	K_M [μM]	k_{cat}/K_M [$M^{-1}s^{-1}$]
***wt*PTE-1**[c]	0	1.0	$(1.3\pm0.1)\times10^{-3}$	57±5	2.3×10^{7}	1.0	0.035±0.002	83±19	420
R1	1	0.08±0.003	62±3	7±1	8.9×10^{6}	6.6±1.5	0.27±0.01	250±30	1.1×10^{3}
R2a	2	0.071±0.007	160±50	13±3	1.2×10^{7}	430±80	2.9±0.1	220±10	1.3×10^{4}
R2b	2	0.049±0.023	440±10	18±1	2.4×10^{7}	$(2.1\pm0.6)\times10^{3}$	24±3	150±30	1.6×10^{5}
R3	3	0.082±0.014	200±60	21±3	9.5×10^{6}	430±90	3.3±0.1	230±20	1.4×10^{4}
R4	4	0.014±0.004	300±10	250±20	1.2×10^{6}	$(5.6\pm3.8)\times10^{3}$	54±2	120±20	4.5×10^{5}
R5a	5	0.024±0.003	60±1	310±20	1.9×10^{5}	$(1.3\pm0.7)\times10^{4}$	65±3	120±10	5.4×10^{5}
R5b	5	0.022±0.003	63±1	67±4	9.4×10^{5}	$(7.1\pm3.8)\times10^{3}$	54±1	110±10	4.9×10^{5}
R6	6	0.03±0.004	65±2	120±20	4.6×10^{5}	$(1.5\pm0.7)\times10^{4}$	130±10	190±20	6.8×10^{5}
R7a	7	0.015±0.006	20±4	120±2	1.7×10^{5}	$(1.7\pm0.9)\times10^{4}$	110±10	160±10	6.9×10^{5}
R7b	7	$(7.1\pm0.2)\times10^{-3}$	53±3	430±60	1.2×10^{5}	$(2.3\pm1.1)\times10^{4}$	74±2	130±10	5.7×10^{5}
R7c	7	$(8.2\pm0.4)\times10^{-3}$	17±1	180±10	9.4×10^{4}	$(8.3\pm3.7)\times10^{3}$	28±1	120±10	2.3×10^{5}
R8	8	$(3.2\pm0.5)\times10^{-3}$	10±1	300±80	3.3×10^{4}	$(6.1\pm2.2)\times10^{4}$	73±2	140±10	5.2×10^{5}
R9	9	$(1.5\pm0.3)\times10^{-3}$	11±1	320±10	3.5×10^{4}	$(7.1\pm3.1)\times10^{4}$	350±10	110±10	3.2×10^{6}
R10	10	$(2.0\pm0.01)\times10^{-3}$	5.7±0.2	240±20	2.4×10^{4}	$(1.0\pm0.4)\times10^{5}$	650±20	190±10	3.4×10^{6}
R11a	11	$(1.2\pm0.3)\times10^{-3}$	4.2±0.1	250±20	1.7×10^{4}	$(1.0\pm0.5)\times10^{5}$	340±10	160±10	2.1×10^{6}
R11b	11	$(2.0\pm0.3)\times10^{-3}$	4.2±0.1	240±20	1.8×10^{4}	$(1.3\pm0.3)\times10^{5}$	250±10	110±10	2.3×10^{6}
R12	12	$(2.0\pm0.1)\times10^{-3}$	6.4±0.1	240±10	2.7×10^{4}	$(1.4\pm0.4)\times10^{5}$	400±10	140±10	2.9×10^{6}
R13a	13	$(1.6\pm0.1)\times10^{-3}$	17±0.1	480±10	3.5×10^{4}	$(2.4\pm0.7)\times10^{5}$	420±20	120±10	3.5×10^{6}
R13b	13	$(1.0\pm0.2)\times10^{-3}$	2.2±0.1	360±40	6.1×10^{3}	$(1.2\pm0.6)\times10^{5}$	470±10	100±10	4.7×10^{6}
R14	14	$(1.6\pm0.1)\times10^{-3}$	0.8±0.02	640±50	1.3×10^{3}	$(2.3\pm1.0)\times10^{5}$	490±10	88±22	5.6×10^{6}
R18-1[d]	18	$(9.9\pm1.3)\times10^{-5}$	0.73±0.1	$(1.3\pm0.2)\times10^{3}$	560	$(3.3\pm0.9)\times10^{5}$	880±30	63±9	1.4×10^{7}
R18-2[d]	18		0.69±0.03	480±50	1.4×10^{3}		500±30	89±10	5.7×10^{6}
R19	19	$(2.0\pm0.4)\times10^{-5}$	0.15±0.01	$(1.0\pm0.1)\times10^{3}$	150	$(1.9\pm0.6)\times10^{5}$	390±10	200±10	1.9×10^{6}
R20	20	$(2.0\pm0.1)\times10^{-5}$	0.11±0.02	750±250	150	$(2.3\pm0.8)\times10^{5}$	560±20	110±20	7.6×10^{5}
R21	21	$(9.1\pm0.1)\times10^{-6}$	0.07±0.02	$(1.1\pm0.1)\times10^{3}$	68	$(1.6\pm0.6)\times10^{5}$	150±10	130±10	1.1×10^{6}
AE	22	$(1.0\pm0.01)\times10^{-5}$	0.12±0.01	$(1.2\pm0.1)\times10^{3}$	100	$(1.7\pm0.6)\times10^{5}$	870±50	130±20	6.5×10^{6}
revR1	rev1	$(1.0\pm0.1)\times10^{-4}$	0.85±0.02	790±40	1.1×10^{3}	$(9.7\pm5.3)\times10^{4}$	670±10	140±10	4.7×10^{6}
revR2	rev2	$(2.4\pm0.1)\times10^{-3}$	13±1	350±10	3.7×10^{4}	$(6.1\pm1.5)\times10^{4}$	500±30	38±9	1.3×10^{7}
revR3	rev3	$(9.4\pm4.0)\times10^{-3}$	34±1	200±10	1.7×10^{5}	$(8.9\pm3.7)\times10^{3}$	99±2	150±10	6.6×10^{5}
revR4	rev4	0.016±0.003	34±1	90±4	3.7×10^{5}	$(8.3\pm3.3)\times10^{3}$	69±1	120±10	5.8×10^{5}
revR5	rev5	0.033±0.018	24±1	88±4	2.7×10^{5}	$(1.2\pm0.3)\times10^{4}$	77±2	200±20	4.0×10^{5}
revR6	rev6	0.04±0.01	28±1	74±2	3.8×10^{5}	$(1.9\pm0.6)\times10^{4}$	280±10	130±10	2.1×10^{6}
revR7a	rev7	0.075±0.024	35±1	73±2	4.7×10^{5}	$(2.4\pm0.5)\times10^{4}$	300±10	140±10	2.1×10^{6}
revR7b	rev7	0.06±0.005	340±10	91±2	3.7×10^{6}	$(1.2\pm0.5)\times10^{4}$	240±1	160±4	1.5×10^{6}
revR8a	rev8	0.089±0.001	140±10	66±2	2.0×10^{6}	$(1.9\pm0.7)\times10^{4}$	230±10	140±4	1.7×10^{6}
revR8b	rev8	0.082±0.01	48±1	140±10	3.5×10^{5}	$(1.6\pm0.4)\times10^{4}$	70±1	170±10	4.2×10^{5}
revR9	rev9	0.014±0.003	420±10	110±10	3.9×10^{6}	$(2.1\pm0.3)\times10^{4}$	200±1	170±10	1.2×10^{6}
***neo*PTE**	rev12	0.022±0.05	270±10	130±10	2.1×10^{6}	$(3.4\pm1.2)\times10^{4}$	110±10	180±20	6.1×10^{5}
***wt*PTE-2**[c]	0		360±10	65±5	5.5×10^{6}		0.026±0.001	210±20	120

[a] Note that the kinetic parameters from variant *wt*PTE to R18-1 were published in (Tokuriki et al., 2012). [b] Cells were grown in at least duplicate and lysates sufficiently diluted to determine initial rates of paraoxon and/or 2NH hydrolysis at a substrate concentration of 200 μM, normalized to cell density, corrected for the dilution factor, and averaged. The experiment was repeated twice and the combined average determined. [c] For better comparison, *wt*PTE was repuried and remeasured in parallel with the reverse evolution variants (*wt*PTE-2). [d] For better comparison, PTE-R18 was repurified and remeasured in parallel with the subsequent variants (R18-2).

Supplementary File 2B. Kinetic parameters of *wt*PTE, AE, and *neo*PTE variants (**Figure 4-7**) in lysate and using purified enzyme.

Mutation[a]	amino acid in each background			Paraoxon in *wt*PTE				Paraoxon in AE				Paraoxon in *neo*PTE			
	*wt*PTE	AE	*neo*PTE	lysate[b]	T-test[b]	purified[c]		lysate[b]	T-test[b]	purified[c]		lysate[b]	T-test[b]	purified[c]	
				relative	p-value	[1/sec]	relative	relative	p-value	[1/sec]	relative	relative	p-value	[1/sec]	relative
/	/	/	/	1.0	/	140±20	1.0	1.0		0.016±0.004	1.0	1.0		87±16	1.0
A45*t*	*t*	A	A	1.2±0.3	0.04	150±20	0.9±0.1	1.0±0.1	0.56	0.012±0.002	0.8±0.1	1.0±0.2	0.93	110±10	1.2±0.2
V49a	*v*	A	*v*	0.9±0.1	0.23	120±10	1.2±0.1	1.2±0.2	0.05	0.013±0.003	0.9±0.2	0.9±0.1	0.51	91±5	1.0±0.1
E77*k*	*k*	E	E	1.5±0.4	2.5×10^{-3}	110±10	1.3±0.1	1.2±0.1	0.10	0.012±0.001	0.8±0.1	1.0±0.1	0.90	120±30	1.4±0.3
V80*a*	*a*	V	V	1.2±0.1	0.04	130±10	1.1±0.1	0.8±0.2	0.08	$(9.8\pm5.3)\times10^{-3}$	0.6±0.3	0.8±0.2	0.21	89±19	1.0±0.2
T102*s*	*s*	T	T	1.1±0.2	0.51	100±20	1.4±0.3	2.1±0.3	3.1×10^{-5}	0.011±0.004	0.7±0.3	0.8±0.1	0.06	84±25	1.0±0.3
R111*s*	*s*	R	R	1.4±0.1	0.01	140±10	1.0±0.1	0.9±0.1	0.27	0.018±0.002	1.2±0.1	0.8±0.1	0.32	94±12	1.1±0.1
*p*135S	*p*	*p*	S	0.8±0.2	0.10	120±50	0.8±0.3	2.6±0.3	1.0×10^{-5}	0.07±0.01	4.5±0.6	1.2±0.2	0.16	68±4	1.3±0.1
T137*s*	*s*	T	T	1.2±0.5	0.21	150±20	0.9±0.1	1.5±0.04	7.4×10^{-5}	0.013±0.001	0.8±0.05	0.7±0.2	0.03	76±30	0.9±0.4
I138*m*	*m*	I	I	1.3±0.6	0.10	200±10	0.7±0.1	1.7±0.2	9.2×10^{-5}	0.018±0.002	1.2±0.1	0.7±02	0.03	53±8	0.6±0.1
M140*l*	/	M	M	1.1±0.3	0.35	120±20	1.1±0.2	0.7±0.1	0.01	$(9.9\pm2.4)\times10^{-3}$	0.6±0.2	0.5±0.1	2.8×10^{-3}	120±10	1.4±0.2
V144*e*	*e*	V	V	1.8±0.6	7.6×10^{-4}	83±2	1.7±0.1	1.3±0.1	0.01	0.024±0.017	1.5±1.1	1.2±0.2	0.17	110±10	1.3±0.2
*y*156H	*y*	*y*	H	0.9±0.2	0.48	130±20	1.0±0.1	1.1±0.1	0.16	0.01 [e]	0.7 [e]	1.0±0.2	0.70	79±4	1.1±0.1
I172*t*	*t*	I	*t*	3.5±0.7	1.3×10^{-6}	110±30	1.3±0.4	2.2±0.6	4.5×10^{-4}	0.047±0.001	3.0±0.1	1.3±0.5	0.17	77±4	1.1±0.1
*g*174D	*g*	*g*	D	0.8±0.1	0.01	81±15	0.6±0.1	1.1±0.1	0.10	0.016±0.003	1.0±0.2	2.3±0.5	6.8×10^{-4}	150±70	0.6±0.3
M176*v*	*v*	M	M	1.7±0.6	1.3×10^{-3}	140±10	1.0±0.01	0.9±0.1	0.31	0.016±0.003	1.0±0.6	1.0±0.2	0.97	90±20	1.0±0.2
H180*q*	*q*	H	*q*	1.9±0.5	1.3×10^{-4}	120±40	1.1±0.4	2.8±0.3	1.4×10^{-6}	0.026±0.0001	1.7±0.1	1.4±0.1	0.02	74±9	1.2±0.1
I199*t*	*t*	I	I	0.9±0.5	0.67	120±10	1.1±0.1	0.6±0.1	4.1×10^{-4}	0.014±0.005	0.9±0.3	0.2±0.04	1.6×10^{-6}	100±10	1.2±0.1
*a*203E	*a*	*a*	E	0.5±0.1	1.5×10^{-6}	160±70	1.1±0.5	1.3±0.1	3.6×10^{-3}	0.011±0.0001	0.7±0.01	4.1±3.2	1.5×10^{-4}	27±1	3.2±0.1
G204*a*	*a*	G	G	1.4±0.2	4.7×10^{-3}	170±10	0.9±0.1	1.3±0.2	0.02	0.011±0.0001	0.7±0.1	0.3±0.2	1.3×10^{-4}	19±2	0.2±0.02
E233*d*	*d*	E	E	21±15	6.3×10^{-9}	37±13	3.7±1.5	4.6±0.3	7.8×10^{-11}	0.029±0.005	1.9±0.3	0.5±0.1	1.3×10^{-3}	110±10	1.3±0.1
R254*h*	*h*	R	R	13±3	5.9×10^{-7}	49±6	2.8±0.1	<0.1	n.d. [d]	n.d. [d]	<0.1	0.1±0.03	6.1×10^{-7}	1.3±0.5	0.02±0.01
*s*258N	*s*	*s*	N	0.3±0.1	5.7×10^{-8}	200±50	1.4±0.3	0.9±0.2	0.46	0.01 [e]	0.7 [e]	1.6±0.3	3.4×10^{-3}	86±9	1.0±0.1
T269*s*	*s*	T	T	1.1±0.1	0.17	130±30	1.1±0.3	1.0±0.1	0.02	$(5.1\pm3.2)\times10^{-3}$	0.3±0.2	0.6±0.2	0.02	73±12	0.8±0.1
F271*l*	*f*	L	*f*	24±7	4.2×10^{-10}	15±1	9.3±0.9	7.2±0.6	7.6×10^{-9}	$(3.4\pm0.01)\times10^{-3}$	2.2±0.01	0.2±0.1	7.6×10^{-5}	32±2	2.7±0.2
M272*l*	/	M	M	1.6±0.3	9.5×10^{-5}	110±10	1.3±0.1	3.1±0.7	3.1×10^{-5}	$(6.1\pm4.7)\times10^{-3}$	0.4±0.3	1.1±0.4	0.70	85±1	1.0±0.01
S274*i*	*i*	S	S	1.2±0.4	0.24	110±20	1.2±0.2	1.0±0.1	0.84	$(5.3\pm3.6)\times10^{-3}$	0.3±0.2	1.0±0.1	1.00	130±10	1.5±0.1
*m*293K	*m*	*m*	K	0.9±0.5	0.79	170±30	1.2±0.2	1.3±0.1	4.2×10^{-3}	0.013 [e]	0.8 [e]	1.2±0.5	0.28	120±10	0.7±0.05
*s*308C	*s*	*s*	C	1.0±0.3	0.81	160±30	1.2±0.2	6.7±1.1	8.6×10^{-7}	0.059±0.001	3.8±0.1	6.2±0.7	2.8×10^{-5}	25±7	3.4±1.0
F313*i*	*i*	F	F	1.5±0.3	3.0×10^{-3}	130±20	1.0±0.1	8.0±1.0	9.3×10^{-8}	0.12 [e]	7.6 [e]	0.9±0.3	0.63	170±60	2.0±0.7
T314*m*	*m*	T	*m*	2.9±0.8	4.8×10^{-6}	94±10	1.5±0.2	1.5±0.1	3.4×10^{-4}	0.017±0.002	1.1±0.1	0.9±0.2	0.57	130±30	0.7±0.2
T341*i*	*t*	I	I	1.2±0.1	0.01	120±10	1.2±0.1	1.4±0.1	0.15	0.019±0.003	1.2±0.2	0.8±0.2	0.15	96±6	1.1±0.1
V130*l*	*l*	V	/	1.4±0.3	0.02	200±60	0.7±0.2	3.6±0.2	1.6×10^{-8}	0.026±0.004	1.7±0.3	/		/	/
V130M	/	V	M	/	/	/	/	6.9±0.01	1.2×10^{-9}	0.071±0.001	4.5±0.1	2.0±0.5	1.5×10^{-3}	42±10	2.0±0.5
*l*130M	*l*	/	M	0.9±0.2	0.48	160±40	1.1±0.3	/		/	/	1.4±0.1	0.03	57±2	1.5±0.1
I306*f*	*f*	I	/	41±8	5.3×10^{-8}	10±2	13±2	1.8±0.2	9.3×10^{-6}	$(7.2\pm3.1)\times10^{-3}$	0.5±0.2	/		/	/
I306M	/	I	M	/	/	/	/	0.9±0.1	0.21	$(6.0\pm0.9)\times10^{-3}$	0.4±0.1	1.4±0.1	0.02	76±18	1.1±0.3
*f*306M	*f*	/	M	0.1±0.02	9.4×10^{-8}	2±3	0.2±0.02	/	/	/	/	0.6±0.03	3.3×10^{-4}	260±20	0.3±0.02

[a] For comparison, the effect of each mutation is given in the same direction, e.g. A45*t* means the effect of introducing *Thr* into each background (AE-A45*t*, *neo*PTE-A45*t*). When the amino acid in question (*Thr* in this case) is already present in a certain background, the effect is calculated as its reintroduction after removal (reversion of *wt*PTE-*t*45A to *wt*PTE).

[b] Cells were grown in at least duplicate and lysates sufficiently diluted (~1-10,000-fold) to determine initial rates of paraoxon hydrolysis at a substrate concentration of 200 µM, normalized to cell density, and corrected for the dilution factor. This experiment was repeated twice and the average change relative to the respective parent variant (*wt*PTE, AE, and *neo*PTE) and the standard deviation were determined. A t-test was performed to obtain p-values. Only mutants with an average >1.3-fold difference from the respective parent mutant AND a p-value <0.05 are considered significant. Non-significant values are underlined. Note that the only >1.3 fold change with non-significant p-value is AE+T341*i* (1.4-fold, p-value 0.15).

[c] Variants were purified in at least duplicate in a 96-well format and sufficiently diluted to determine initial rates of paraoxon hydrolysis at a substrate concentration of 200 µM, corrected for the dilution factor, averaged and the standard deviation determined.

[d] Phosphotriesterase activity was too low to be determined.

[e] No standard deviation is given because only a single measurement is shown.

Supplementary File 2C. Kinetic parameters of additional variants made to determine mutational effects over the forward evolution in lysate and using purified enzyme. The mutational effects are given in **Figure 5** and **6** and were calculated by comparing each variant to its parent indicated in the name (e.g. R8+I138M to R8) and as shown in **Supplementary File 2D**. The effect of all mutations not listed could be calculated directly by comparing variants from the forward evolution as shown in **Supplementary File 2D**.

Variant	Paraoxon	
	lysate[a] relative to AE	purified[b] [1/sec]
AE	1	0.015±0.003
R8+I138*m*	850±280	5.8±1.0
R8+I199*t*	190±40	3.4±0.4
R18+V49*a*	9.1±0.1	0.073±0.001
R18+E77*k*	10±1	0.079±0.004
R18+M140*l*	14±8	0.12±0.06
R18+F313*i*	100±10	0.83±0.04
R20+A45*t*	1.5±0.2	0.022±0.013
R20+T137*s*	2.6±0.1	0.023±0.002
R20+V144*e*	2.3±0.2	0.021±0.001
R20+H180*q*	8.9±0.7	0.30±0.01
R20+T314*m*	2.6±0.1	0.029±0.001
R20+T341*i*	2.4±0.1	0.022±0.001

[a] Cells were grown in at least duplicate and lysates sufficiently diluted (~1-10,000-fold) to determine initial rates of paraoxon hydrolysis at a substrate concentration of 200 μM, normalized to cell density, and corrected for the dilution factor. This experiment was repeated twice and the average change relative to the respective parent variant AE and the standard deviation were determined. P-values are shown in **Supplementary File 2D**.

[b] Variants were purified in at least duplicate in a 96-well format and sufficiently diluted to determine initial rates of paraoxon hydrolysis at a substrate concentration of 200 μM, corrected for the dilution factor, averaged and the standard deviation determined.

Supplementary File 2D. Mutational effects over the forward evolution in lysate and using purified enzyme.

Mutation	Paraoxon		Calculation
	lysate[a] relative to parent	T-test[a] p-value	
*t*45A	1.3±0.1	0.72	R20 / R20+A45*t*
*a*49V	1.1±0.1	0.14	R18 / R18+V49*a*
*k*77E	1.0±0.1	0.58	R18 / R18+E77*k*
*a*80V	1.3±0.4	0.19	R10 / R9
*s*102T	0.51±0.07	1.7×10^{-4}	R21 / R20
*s*111R	0.80±0.15	0.03	R12 / R11b
*l*130V	1.0±0.1	0.68	R14 / R13a
*s*137T	0.74±0.07	1.1×10^{-3}	R20 / R20+T137*s*
*i*138M	0.36±0.1	2.0×10^{-3}	R8 / R8+I138*m*
*l*140M	0.74±0.05	0.41	R18 / R18+M140*l*
*e*144V	0.84±0.08	0.04	R20 / R20+V144*e*
*t*172I	2.2±0.4	4.4×10^{-3}	R6 / R5b
*v*176M	1.0±0.1	0.72	AE / R21
*q*180H	0.18±0.02	4.9×10^{-5}	R20 / R20+H180*q*
*t*199I	1.6±0.6	0.06	R8 / R8+I199*t*
*a*204G	1.2±0.2	0.10	R12 / R11a
*d*233E	0.45±0.04	0.01	R2b / R1
*h*254R	0.072±0.022	3.0×10^{-5}	R1 / *wt*PTE
*s*269T	1.8±0.3	4.4×10^{-3}	R6 / R5a
*l*271F	1.9±0.1	3.0×10^{-6}	R14 / R13b
*l*272M	0.48±0.16	6.4×10^{-3}	R9 / R8
*i*274S	1.0±0.2	0.78	R3 / R2a
*i*313F	0.10±0.01	7.8×10^{-9}	R18 / R18+F313*i*
*m*314T	0.73±0.07	1.0×10^{-3}	R20 / R20+T314*m*
*i*341T	0.80±0.08	3.3×10^{-3}	R20 / R20+T341*i*

[a] Cells were grown in at least duplicate and lysates sufficiently diluted (~1-10,000-fold) to determine initial rates of paraoxon hydrolysis at a substrate concentration of 200 μM, normalized to cell density, and corrected for the dilution factor. This experiment was repeated twice and the average change relative to the respective parent variant (shown in the column "Calculation") and the standard deviation were determined. A t-test was performed to obtain p-values. Only mutants with an average >1.3-fold difference from the respective parent mutant AND a p-value <0.05 are considered significant. Non-significant values are underlined. Note that *l*140M and *t*199I have a >1.3 fold effect but non-significant p-values.

Supplementary File 2E. Kinetic parameters of additional variants made to determine mutational effects over the reverse evolution in lysate and using purified enzyme. The mutational effects are given in **Figure 5** and **7** and were calculated by comparing each variant to its parent indicated in the name (e.g. revR3+T172I to revR3) and as shown in **Supplementary File 2F**. The effect of all mutations not listed could be calculated directly by comparing variants from the reverse evolution as shown in **Supplementary File 2F**.

Variant	Paraoxon	
	lysate[a] relative to AE	purified[b] [1/sec]
AE	1.0	0.015±0.003
AE+*s*308C	6.6±0.9	0.059±0.001
revR3	900±260	7.6±1.7
revR3+*t*172L	220±20	3.0±0.1
revR3+M130V	170±40	1.1±0.1
revR3+*p*135S	400±170	9.9±5.0
revR3+T314*m*	$(1.3\pm0.5)\times10^3$	19±5
revR4	$(1.4\pm0.5)\times10^3$	23±5
revR6+K293*m*	$(3.9\pm2.0)\times10^3$	32±13
revR9	$(1.8\pm1.1)\times10^4$	100±10
revR9+D174*g*	$(7.0\pm4.0)\times10^3$	70±14
revR9+*q*180H	$(6.3\pm2.0)\times10^3$	55±5
revR9+N258*s*	$(9.2\pm4.9)\times10^3$	69±13
revR9+H156*y*	$(1.4\pm0.4)\times10^4$	70±21
*neo*PTE+*a*49V	$(1.5\pm0.6)\times10^4$	140±20
*neo*PTE+M306I	$(1.8\pm0.1)\times10^3$	92±29
*neo*PTE	$(2.0\pm0.8)\times10^4$	110±40

[a] Cells were grown in at least duplicate and lysates sufficiently diluted (~1-10,000-fold) to determine initial rates of paraoxon hydrolysis at a substrate concentration of 200 µM, normalized to cell density, and corrected for the dilution factor. This experiment was repeated twice and the average change relative to the respective parent variant AE and the standard deviation were determined. P-values are shown in **Supplementary File 2F**.

[b] Variants were purified in at least duplicate in a 96-well format and sufficiently diluted to determine initial rates of paraoxon hydrolysis at a substrate concentration of 200 µM, corrected for the dilution factor, averaged and the standard deviation determined.

Supplementary File 2F. Mutational effects over the forward evolution in lysate and using purified enzyme.

Mutation	Paraoxon		Calculation
	lysate[a] relative to parent	T-test[a] p-value	
V49*a*	1.7±0.3	0.12	*neo*PTE+*a*49V / *neo*PTE
V130M	5.4±1.6	4.9×10^{-5}	*rev*R3 / revR3+M130V
*p*135S	1.1±0.4	0.83	*rev*R3 / revR3+*p*135S
*y*156H	1.3±0.8	0.42	revR9 / revR9+H156y
I172*t*	4.1±1.2	3.5×10^{-3}	revR3 / revR3+*t*172L
*g*174D	2.6±1.6	0.04	revR9 / revR9+D174*g*
H180*q*	2.9±1.8	0.03	revR9 / revR9+*q*180H
*a*203E	2.9±1.2	5.4×10^{-3}	revR6+K293*m* / revR4
*s*258N	2.0±1.2	0.09	revR9 / revR9+N258*s*
F271*l*	2.9±0.8	4.9×10^{-4}	revR3 / revR2
*m*293K	0.9±0.4	0.8	revR6 / revR6+K293*m*
I306M	11±5	8.2×10^{-3}	*neo*PTE / *neo*PTE+M306I
*s*308C	6.6±0.9	7.4×10^{-8}	AE+*s*308C / AE
T314*m*	3.4±1.2	2.4×10^{-4}	revR4 / revR3+*p*135S

[a] Cells were grown in at least duplicate and lysates sufficiently diluted (~1-10,000-fold) to determine initial rates of paraoxon hydrolysis at a substrate concentration of 200 µM, normalized to cell density, and corrected for the dilution factor. This experiment was repeated twice and the average change relative to the respective parent variant (shown in the column "Calculation") and the standard deviation were determined. A t-test was performed to obtain p-values. Only mutants with an average >1.3-fold difference from the respective parent mutant AND a p-value <0.05 are considered significant. Non-significant values are underlined. Note that V49*a* and *s*258N have a >1.3 fold effect but non-significant p-values.

Supplementary File 2G. Kinetic parameters of variants made for combinatorial mutational analysis (**Figure 7**) in lysate and using purified enzyme.

Variant	Paraoxon						
	lysate[a]	T-test[a]	single/ double[b]	T-test[b]	purified[e]		
	relative to AE	p-value		p-value	k_{cat} [s^{-1}]	K_M [μM]	k_{cat}/K_M [$M^{-1}s^{-1}$]
AE	1.0				0.12±0.01	(1.2±0.1)×10^3	100
AE+*p*135S	2.4±0.1	5.4×10^{-10}	4.3	1.0×10^{-10}	0.26±0.01	740±110	350
AE+I138*m*	1.4±0.2	6.4×10^{-4}	2.6	3.0×10^{-6}	0.20±0.01	(1.3±0.1)×10^3	150
AE+F271*l*	7.0±0.8	5.8×10^{-9}	1.8[c]	2.2×10^{-5}[c]	0.37±0.01	970±50	380
AE+I306*f*	1.5±0.3	6.8×10^{-4}	0.4	1.2×10^{-7}	0.21±0.01	(1.2±0.2)×10^3	170
AE+*s*308C	5.8±0.3	8.4×10^{-13}	1.7[c]	4.3×10^{-8}[c]	0.42±0.02	460±50	910
AE+F313*I*	7.4±0.7	1.2×10^{-9}	1.9	4.6×10^{-6}	1.0±0.01	(1.6±0.1)×10^3	650
AE+*p*135S+I138*m*	0.6±0.1	6.9×10^{-6}			0.052±0.002	760±80	68
AE+F271*l*+*s*308C	19±9	5.4×10^{-4}	1.8[d]	0.25	5.2±0.1	870±30	6.0×10^3
AE+M272*l*+*s*308C	15±2	1.6×10^{-8}	1.4[d]	0.06	3.0±0.1	930±50	3.2×10^3
AE+F271*l*+F313*I*	4.0±0.6	2.2×10^{-7}			0.13±0.01	620±50	200
AE+I306*f*+*s*308C	3.5±0.3	7.8×10^{-10}			0.64±0.03	(1.2±0.1)×10^3	540
AE+F271*l*+M272*l*+*s*308C	10±3	1.3×10^{-4}			1.8±0.1	(1.5±0.1)×10^3	1.2×10^3

[a] Cells were grown in at least duplicate and lysates sufficiently diluted (~1-10,000-fold) to determine initial rates of paraoxon hydrolysis at a substrate concentration of 200 μM, normalized to cell density, and corrected for the dilution factor. This experiment was repeated twice and the average change relative to the parent variant AE and the standard deviation were determined. A t-test was performed to obtain p-values. Only mutants with an average >1.3-fold difference from the respective parent mutant AND a p-value <0.05 are considered significant. Non-significant values are underlined.

[b] Fold changes between the single and double mutants of each series shown in **Figure 7B** (*e.g.*, AE+*p*135S differs by 4.3-fold from the double mutant AE+*p*135S+I138*m*, AE+I138*m* differs by 2.6-fold). A t-test was performed to obtain p-values. Note that the two mutants AE+F271*l*+*s*308C and AE+M272*l*+*s*308C have non-significant p-values compared to the "double mutant" in this series, AE+F271*l*+M272*l*+*s*308C.

[c] Values for AE+F271*l* are compared to the double mutant AE+F271*l*+F313*I*. Values for AE+*s*308C are compared to the double mutant AE+I306*f*+*s*308C.

[d] AE+F271*l*+*s*308C and AE+M272*l*+*s*308C are "single mutants" of the parent AE+*s*308C and values are compared to the "double mutant" AE+F271*l*+M272*l*+*s*308C.

[e] Variants were purified to determine initial rates of paraoxon hydrolysis over a range of substrate concentrations and calculate Michaelis Menten parameters.

Supplementary File 2H. Absorption wavelength λ, extinction coefficient ε_λ, and leaving group pKa values for substrates used for kinetic analysis. Values were taken from (Khersonsky and Tawfik, 2005).

Substrate	λ [nm]	ε_λ [M^{-1}][a]	pKa
Phosphotriesters			
Paraoxon	405	10510	7.14
2,4-dinitrophenyl diethyl phosphate	360	9160	4.08
2-fluoro 4-nitrophenyl diethyl phosphate	395	11080	5.45
3-fluoro 4-nitrophenyl diethyl phosphate	390	11676	5.94
2,6-difluorophenyl diethyl phosphate	270	950	7.3
4-cyanophenyl diethyl phosphate	275	7495	7.95
diethyl phosphate acetophenone	320	8080	8.05
3-fluorophenyl diethyl phosphate	270	656	9.28
Arylesters			
2-naphthyl hexanoate (2NH)	320	800	[b]
4-nitrophenyl acetate	405	10510	7.14
4-acetoxy benzaldehyde	330	12620	7.66
4-cyanophenyl acetate	275	7495	7.95
4-acetoxy acetophenone	320	8080	8.05
3-nitrophenyl acetate	340	840	8.39
3-cyanophenyl acetate	295	1610	8.61
4-chlorophenyl acetate	280	838	9.38
Phenyl acetate	270	700	10
3,4-dimethyl phenyl acetate	276	850	10.36

[a] Extinction coefficients are given for a pathlength of 0.58 cm, which results from a 200 µL reaction volume in a 96-well plate.
[b] 2NH was not used for linear free energy relationship analysis.

References

Khersonsky O, Tawfik DS. 2005. Structure-reactivity studies of serum paraoxonase PON1 suggest that its native activity is lactonase. *Biochemistry* **44**:6371-6382.

Tokuriki N, Jackson CJ, Afriat-Jurnou L, Wyganowski KT, Tang R, Tawfik DS. 2012. Diminishing returns and tradeoffs constrain the laboratory optimization of an enzyme. *Nature Communications* **3**:1257.

Supplementary file 3 for Kaltenbach at al., Reverse evolution leads to genotypic incompatibility despite functional and active-site convergence

Crystallographic information

Supplementary File 3A. Data collection and refinement statistics for structures reported in this work.

	***wt*PTE**	**AE**	***neo*PTE**
Wavelength (Å)	0.9537	0.9537	0.9537
Resolution range (Å)[a]	43.16-1.63 (1.68-1.63)	39.44-1.54 (1.60-1.54)	48.33-1.9 (1.94-1.9)
Space group	P 21 21 2	P 21 21 2	P 65
Unit cell			
a, b, c (Å)	86.14, 86.33, 88.72	85.9, 86.27, 88.68	123.7, 123.7, 112.13
a, b, g (°)	90, 90, 90	90, 90, 90	90, 90, 120
Total reflections	598370 (60391)	707292 (70797)	841841 (46861)
Unique reflections	83078 (8191)	97912 (9642)	76542 (4520)
Multiplicity	7.2 (7.4)	7.2 (7.3)	11.0 (10.4)
Completeness (%)	99.98 (99.99)	99.97 (100.00)	100 (100)
Mean <*I*/s(*I*)>	13.19 (2.35)	11.44 (1.52)	14.6 (2.4)
Wilson B-factor	17.33	15.17	14.4
$R_{merge(I)}$[b]	0.101 (0.7993)	0.1111 (1.237)	0.163 (1.322)
$CC_{1/2}$[c]	0.998 (0.83)	0.998 (0.694)	0.996 (0.684)
R_{work}/R_{free}[d]	0.1789/0.2190	0.1703 (0.2051)	0.1405 (0.1728)
No. of non-hydrogen atoms	5791	5964	5591
macromolecules	5394	5389	5216
ligands	14	44	30
water	383	531	345
Protein residues	659	655	660
R.m.s deviations			
Bond lengths (Å)	0.009	0.015	0.006
Bond angles (°)	1.18	1.55	0.97
PDB ID	**4PCP**	**4PCN**	**4PBF**

[a] Values in parenthesis are for the highest-resolution shell.

[b[$R_{merge(I)} = (\Sigma_{hkl} \Sigma_j |I_{hkl,j} - \langle I_{hkl} \rangle|)/(\Sigma_{hkl} \Sigma_j I_{hkl,j})$ where $\langle I_{hkl} \rangle$ is the average intensity of *j* symmetry-related observations of reflections with Miller indices *hkl*.

[c] $CC_{1/2}$ = percentage of correlation between intensities from random half-datasets.

[d] $R_{work} = \Sigma_{hkl} |F_{(obs)} - F_{(calc)}| / \Sigma_{hkl} |F_{(obs)}|$; 5% of the data that were excluded from the refinement were used to calculate R_{free}.

nature chemical biology

ARTICLE

PUBLISHED ONLINE: 12 SEPTEMBER 2016 | DOI: 10.1038/NCHEMBIO.2175

The role of protein dynamics in the evolution of new enzyme function

Eleanor Campbell[1,7], Miriam Kaltenbach[2,3,7], Galen J Correy[1], Paul D Carr[1], Benjamin T Porebski[4,5], Emma K Livingstone[1], Livnat Afriat-Jurnou[1], Ashley M Buckle[4,5], Martin Weik[6], Florian Hollfelder[3], Nobuhiko Tokuriki[2]* & Colin J Jackson[1]*

Enzymes must be ordered to allow the stabilization of transition states by their active sites, yet dynamic enough to adopt alternative conformations suited to other steps in their catalytic cycles. The biophysical principles that determine how specific protein dynamics evolve and how remote mutations affect catalytic activity are poorly understood. Here we examine a 'molecular fossil record' that was recently obtained during the laboratory evolution of a phosphotriesterase from *Pseudomonas diminuta* to an arylesterase. Analysis of the structures and dynamics of nine protein variants along this trajectory, and three rationally designed variants, reveals cycles of structural destabilization and repair, evolutionary pressure to 'freeze out' unproductive motions and sampling of distinct conformations with specific catalytic properties in bi-functional intermediates. This work establishes that changes to the conformational landscapes of proteins are an essential aspect of molecular evolution and that change in function can be achieved through enrichment of preexisting conformational sub-states.

The remarkable catalytic power of enzymes is thought to derive from the preorganization of enzyme active sites, which allows them to stabilize the transition states (TSs) of chemical reactions and lower the activation energy, thereby increasing the rate[1–4]. Although it is recognized that active site residues need to be precisely positioned for efficient TS stabilization[5], recent studies have described a link between active site dynamics and catalysis of the chemical step[6,7]. Separate from the discussion of protein dynamics and the chemical step, several studies have observed enzymes undergoing conformational change throughout their catalytic cycle[8–11], adopting various configurations that are suited to different roles, such as substrate binding, catalysis and product release. Despite substantial work, several questions still remain relating to the role of protein dynamics in enzyme function, and it remains a controversial topic[12–14].

Although the majority of the studies that have investigated structural protein dynamics examined extant and specialized enzymes[15,16], some studies highlight a potential role for structural dynamics in the molecular evolution of enzymes[8,11,17], demonstrating that the equilibrium between sub-states can be modified by mutagenesis[11,18]. It is also suggested that conformational plasticity and changes in the conformational landscapes of proteins contribute to catalytic promiscuity and the diminishing returns observed during protein specialization[19–21]. Despite substantial evidence from these studies that suggests that protein dynamics are under evolutionary selection, little is understood of the molecular basis for the evolution of protein dynamics or how they could affect activity. Indeed, recent work shows that excessive structural mobility can actually impede enzyme evolution, providing some balance to the generally positive view of protein dynamics in activity and evolution[22].

An evolutionary process can only be understood if we can examine the intermediate states that together comprise the trajectory. Laboratory (directed) evolution is invaluable to the study of molecular evolution because it permits the isolation of every intermediate along a trajectory and the use of high selective pressure to minimize the level of noise, or neutral variation, in the sequence. Bacterial phosphotriesterases (PTEs) catalyze the hydrolysis of organophosphates at rates limited by product release, which involves opening of an active site loop (loop 7)[11,23]. We have previously reported the laboratory evolution from wild-type PTE (round 0; R0) to an efficient and specialized arylesterase (AE; R22), in which a 10^9-fold switch in the ratio of catalytic specificities (measured by comparison of k_{cat}/K_M) was achieved over 22 generations (**Supplementary Results**, **Supplementary Table 1** and **Supplementary Fig. 1**)[21,24]. More recently, we carried out the same experiment in reverse[24], i.e., we evolved AE back into an efficient PTE (neoPTE) over 12 generations (Rev12). These experiments provide us with a 'molecular fossil record' that we can use to determine the biophysical changes that are causally related to the change in function. Previous structural analysis, comparing the start (PTE: R0), end (AE: R22) and restored (neoPTE: Rev12) points, shows that the overall structures are nearly identical in terms of enzyme ground state (^{Enz}GS) structure. The relative activities of R0 and R18 have been investigated computationally through analysis of the altered active sites, showing that differences between the active sites of the two enzymes largely account for the changes in activation energy[25]. However, the process by which these new active sites were established, and the biophysical basis for their gradual optimization, cannot be understood without analysis of the structures and dynamics of the intermediate states.

In this work, we analyzed nine crystal structures that are representative of several intermediate points and end points along the trajectory, as well as three rationally designed variants. Altogether, this data set reveals the destabilizing effects that many mutations can have and how these can be repaired in subsequent generations, evolutionary pressure to 'freeze out' or minimize unproductive motions, and specific conformational sampling of unique

[1]Research School of Chemistry, Australian National University, Canberra, Australia. [2]Michael Smith Laboratories, University of British Columbia, Vancouver, British Columbia, Canada. [3]Department of Biochemistry, University of Cambridge, Cambridge, UK. [4]Biomedicine Discovery Institute, Monash University, Clayton, Victoria, Australia. [5]Department of Biochemistry and Molecular Biology, Monash University, Clayton, Victoria, Australia. [6]Institut de Biologie Structurale, University Grenoble Alpes, Commissariat à l'Energie Atomique and Centre National de la Recherche Scientifique, Grenoble, France. [7]These authors contributed equally to this work. *e-mail: colin.jackson@anu.edu.au or tokuriki@msl.ubc.ca

conformations that can catalyze either phosphotriester or arylester hydrolysis in bifunctional intermediates.

RESULTS

Structure determination and comparison

In addition to the three previously described structures (R0, R22 and Rev12)[24], we selected for structural analysis a series of intermediate variants along the forward (PTE activity with paraoxon to AE activity with 2-naphthyl hexanoate (2NH)) and reverse evolutionary trajectories (**Supplementary Fig. 1**, and **Supplementary Tables 1** and **2**). The end points R0 and R22 are relatively specialized catalytic mirror images (k_{cat}/K_M for primary activity > 10^4-fold higher than that for secondary activity), R6 and Rev6 represent true bi-functional intermediates in that they have approximately equal, and substantial, second-order rate constants ($k_{cat}/K_M \approx 10^6$ M^{-1} s^{-1}) for both substrates, whereas R1, R2, R8, R18 and Rev12 are variants with relatively uniform activity increases in between. We solved crystal structures of all of these variants, which diffracted to similar resolution (1.5–1.9 Å) in the same crystallization conditions, and all but Rev12 crystallized in the same space group. This was an important aspect of the analysis, allowing direct comparison between the structures without confounding due to crystal-packing artifacts.

As noted previously, despite 10^4-fold and 10^5-fold changes in k_{cat}/K_M for the phosphotriester and arylester between R0 and R22, respectively, these structures are almost identical to each other (R0 versus R22; ~90% sequence identity; the maximum r.m.s. displacement over Cα atoms was only 0.4 Å) (**Fig. 1a**). This is highlighted through analysis of a Cα distance matrix between the R0 and R22 variants (**Fig. 1b**): in terms of backbone changes, the only substantial difference is a relatively minor shift in the conformation of loops 4 and 5 and a very slight difference in the conformation of loop 7. The shift in loop 5 contributes to additional enzyme–substrate interactions (**Fig. 1c**,**d**). Other substitutions that contributed to the specificity change reshaped the substrate-binding pocket and introduced charged groups to the active site (**Fig. 1c**,**d**). Briefly, Phe306Ile slightly widened the binding pocket for the aryl side chain of 2NH, Leu271Phe reduced available space for an ethyl side chain of paraoxon and His254Arg introduced a cation-π interaction with the naphthol leaving group of 2NH. These substitutions were, individually, only responsible for no more than an ~3-fold improvement in the k_{cat}/K_M, or a cumulative ~12-fold increase, i.e., ~1% of the final 10^4-fold increase. Recent structural and computational analysis of the catalytic mechanism of PTE and AE has revealed that small changes in the Zn^{2+}-Zn^{2+} metal-ion distance also occur, although the catalytic effect is unclear[25]. Thus, the structural basis for the scale of the change in function must involve more than direct changes to the substrate-binding site. The mean distance of the mutations from the active site increased throughout the trajectory, with the first substitutions close to or within the active site, and the bulk of subsequent substitutions located at or near the surface of the protein (**Fig. 1e**,**f**). In fact, specialization for the new activity occurred without the addition of any active site substitutions in the latter part of the trajectory (R6-R22) (**Supplementary Table 1**).

Changes to the internal protein interaction network

To investigate the interplay between structural and functional changes, we analyzed how the substitutions affected the internal protein interaction network. Comparison between the intramolecular interaction networks (hydrogen bonds, salt bridges and hydrophobic interactions) using RINalyzer[26] revealed that, unlike the average atomic positions of the atoms, the intramolecular interaction network of the protein underwent dramatic alterations throughout the evolutionary trajectory (**Fig. 2**). Three areas of the protein are of particular interest with respect to the change in function: loops 5 and 7, which overhang the active site from opposite sides, and Arg254, which forms cation-π interactions with the substrate. Loops 4 and 5

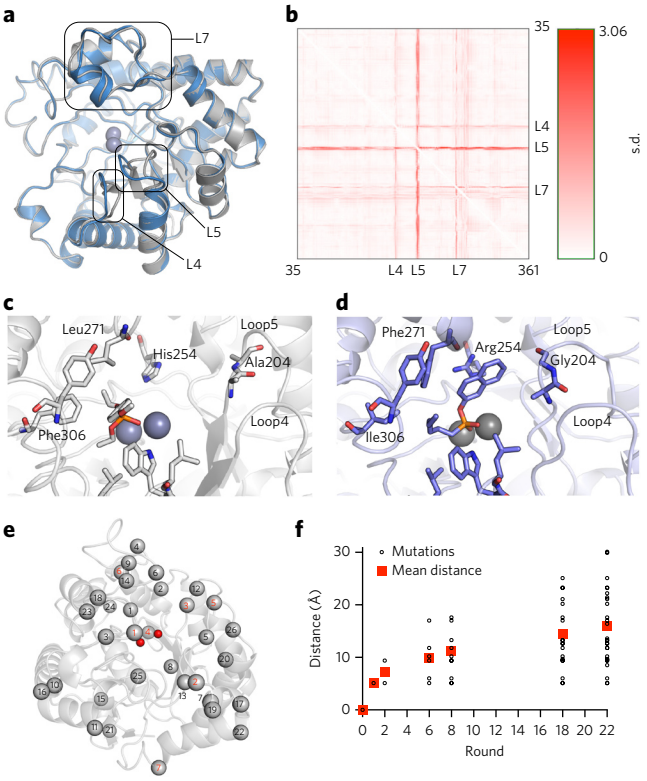

Figure 1 | Locations and effects of substitutions that accumulated across the evolutionary trajectory. (**a**) R0 is shown as a gray cartoon, and R22 as a blue cartoon. Loops 4, 5 and 7 are shown to overhang the active site from each side. The only substantial conformational changes between R0 and R22 were in loops 4, 5 and 7. (**b**) A C-α distance matrix between the R0 and R22 variants highlights the absence of conformational differences outside of loops 4, 5 and 7. s.d., standard deviation of distances among equivalenced residue pairs. (**c**) The structure of R0 with phosphotriester docked (superimposed from 2R1N) shows the absence of any interaction with loop 5. (**d**) The structure of R22 with docked arylester TS analog shows the close contacts between new loop 5 configuration and the substrate. (**e**) The substitutions are scattered throughout the protein, but the first substitutions, in both the forward and reverse trajectory, are located closest to the active site, whereas the latter substitutions are frequently located on the surface. (**f**) The mean distance of the substitutions from the active site increases quickly at the start, but begins to plateau by R22.

are the only loops that underwent substantial Cα backbone alteration throughout the evolutionary trajectory. Loop 7 has previously been shown to undergo functionally important conformational fluctuations between open (poised for substrate and product diffusion) and closed (catalytic) conformations[11], and Arg254 is the first mutation accumulated in the evolution toward AE activity and hydrogen bonds to a backbone carbonyl of loop 7. The residues in loop 7 are largely unconnected to the $(\alpha/\beta)_8$ barrel in R0 (**Fig. 2a**), but they become highly interconnected, for example, via hydrogen bonding with Arg254, en route to R22 (**Fig. 2b**). In R0, the residues in loop 5 are highly connected to each other (**Fig. 2c**), whereas this interaction network almost completely disappears by R22, with few intra-loop interactions remaining (**Fig. 2d**). Thus, while the average positions of the backbone and side chain atoms in the protein changed little over the evolutionary trajectory, the intramolecular interaction network has undergone substantial reorganization.

Structural dynamics are altered through evolution

We investigated the hypothesis that altered conformational dynamics are under evolutionary selection by solving structures of

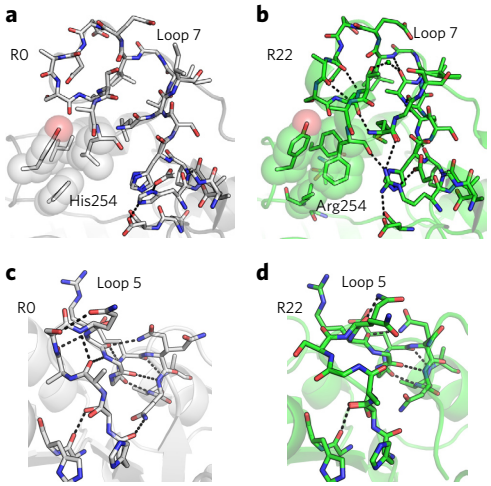

Figure 2 | Intermolecular interaction networks in R0 and R22. (**a**) In R0, loop 7 has very few intra-loop bonds and little interaction (electrostatic or hydrophobic) with the $(\alpha/\beta)_8$-barrel body of the protein. (**b**) By R22, a number of new electrostatic interactions form (dashed lines) as well as increased hydrophobic interactions (transparent spheres). This includes new hydrogen bonds with the $(\alpha/\beta)_8$-barrel via Arg254. (**c**) In R0, loop 5 is highly interconnected to the $(\alpha/\beta)_8$-barrel and within itself. (**d**) By R22 the majority of these bonds are lost.

five intermediates between R0 and R22 (R1, R2, R6, R8 and R18), and focusing on the three functionally relevant areas: Arg254, loop 7 and loop 5. The mobility of loops 4, 5, and 7 changed substantially across the evolutionary trajectory in a manner that was consistent with the observed changes to the intermolecular interaction network; namely, loop 7 became more stable upon gaining additional intramolecular interactions, whereas the loss of interactions destabilized loop 5 (**Fig. 3a**,**b** and **Supplementary Fig. 2**). Moreover, the level of disorder in each region changed gradually over the course of the evolutionary trajectory, i.e., there was a consistent directional change in terms of the stability of these loops and it was not a random fluctuation. An analysis of the pathways of communication between loops 5 and 7, which can be used to assess the strength of the allosteric interaction between them[27,28], showed substantial change between R0 and R22 (**Supplementary Fig. 3**). In R0 there is an optimal path extending from Ala204 in loop 5 to Ala270 in loop 7, via Thr279 and Leu283 in the rear of the protein, with suboptimal paths extending through His254 and Asp232, consistent with a widely distributed network involving substantial motion of loop 7. In R22, the optimal path has shortened, with the original path, and the suboptimal path through His254, being lost (potentially owing to the His254Arg substitution), and the previously suboptimal path through Asp232 becoming dominant and involving the two substitutions to loop 7 (Leu272Met and Leu271Phe), consistent with the observed reduction in the mobility of loop 7.

The active site mutation His254Arg was the first mutation (R1) to fixate in the evolution. Arg254 can adopt either bent (Cβ-Cγ-Cδ-Nε dihedral angle ~40–70°) or extended (Cβ-Cγ-Cδ-Nε dihedral angle ~170°) rotamers (**Fig. 3c**). Both rotamers are compatible with the PTE activity, and His254Arg is a naturally occurring polymorphism[29]. In contrast, only the bent conformation is catalytically productive for the AE activity, forming cation-π interactions with the naphthol leaving group of the arylester. The extended conformation is nonproductive and is involved in a steric clash with the arylester binding mode[21]. Both bent and extended conformations of Arg254 were apparent in R1 and R2 structures, either through inspection of electron density maps or through automated fitting of multiple conformations with QFit[30,31]. The bent conformation of Arg254 is enriched and stabilized through evolution: the refined occupancy increased from 61% (R1) to 100% by R6. The bent conformation was further stabilized through the later rounds: when we refined the structure with only the bent conformation, the B-factor progressively decreased from R1 to R22 (**Fig. 3d** and **Supplementary Fig. 4**). This illustrates that new mutations can arise in structural contexts that initially prevent side chains from adopting an optimal geometry. The substituted amino acids are likely to be loosely positioned at first, dynamically sampling a number of nonproductive conformations, and their full catalytic effect will only be manifested once nonproductive conformations are 'frozen out'. In this case, the

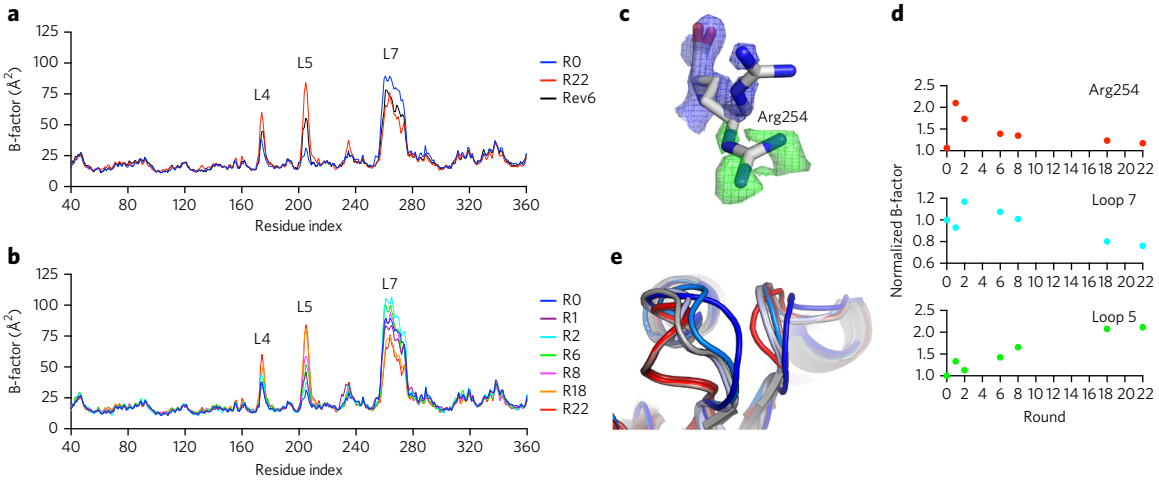

Figure 3 | Changes in protein disorder and conformation across an evolutionary trajectory. (**a**) A plot of the averaged (A and B chains) main chain B-factor of R0, R22 and Rev6, showing level of disorder of loops 5 (200–210) and 7 (257–275). The disorder in loops 5 and 7 of Rev6 began to return to the ancestral state (R0). (**b**) The disorder in loops 4 and 5 increased gradually from R0 to R22, whereas the disorder in loop 7 decreased gradually along the trajectory. (**c**) Arg254 sampled both open and closed conformations in R1. $2mF_{obs} - DF_{calc}$ maps are contoured at 1.5σ and shown in blue; $mF_{obs} - DF_{calc}$ difference density contoured at 3σ is shown in green. (**d**) The changes in disorder of the various loops occurred at different rates along the trajectory for different regions. Arg254 (red) peaked in R1 and was stable by R6. Loop 7 (cyan) peaked at R2 and continued to decrease to R18. Loop 5 (green) underwent its most substantial increase between R9 and R18. (**e**) The conformation of loops 5 (left) and 4 (right) did not substantially change between R1 (red), R2 (orange) and R6 (salmon), but shifted by R9 (gray) and R18 (light blue) before adopting the final conformation in R22 (dark blue).

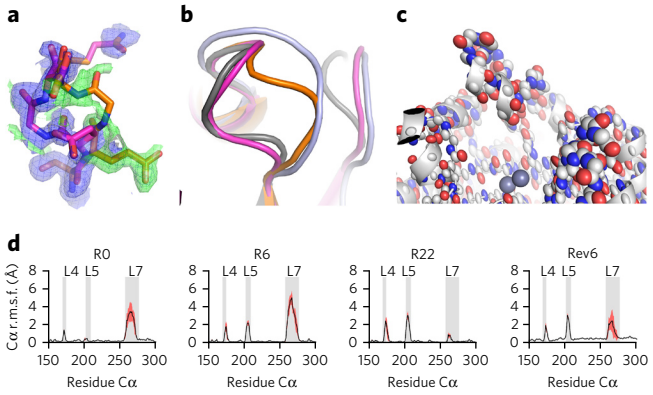

Figure 4 | Conformational sampling of PTE-like and AE-like states by evolutionary intermediates R6 and Rev6. (**a**) Loop 5 can be modeled in two conformations: a dominant PTE-like conformation that is modeled into $2mF_{obs} - DF_{calc}$ electron density (blue), contoured at 1.5σ, and a second AE-like conformation that is modeled into $mF_{obs} - DF_{calc}$ difference density (green), contoured at 2.5σ. (**b**) Overlay of the two Rev6 conformations of loop 5 (magenta and orange) onto structures of R0 (gray) and R22 (sky blue). (**c**) Anisotropic refinement of Rev6, showing the directional atomic displacements of the atoms in loop 7, consistent with fluctuation between states, rather than random disorder. (**d**) Flexibility of loop 4, loop 5 and loop 7 of R0, R6, R22 and Rev6 revealed by ensemble refinement. The single line represents the mean Cα r.m.s. fluctuation across the five replicate refinements with the uncertainty (s.d.) shaded in red.

shift in the conformational equilibrium of Arg254 occurs as a result of the Asp233Glu substitution and a series of changes that stabilize loop 7, which is discussed in detail below. The major changes in the B-factor at position 254 occurred before round 6, when the refined occupancy of Arg254 reached its maximum.

The rate-limiting fluctuation of loop 7 between open (diffusive) and closed (catalytic) conformations in PTE is a specific movement that is essential to the PTE activity[11,23] but not the AE activity. As with the extended conformation of Arg254, we measured the stability of the modeled closed conformation by the change in B-factor throughout the trajectory (**Fig. 3d** and **Supplementary Fig. 4**), i.e., if the loop is in a well-ordered, high occupancy, closed conformation it will have a lower B-factor than if it is highly disordered. Loop 7 became more ordered in R1, because a hydrogen bond formed between Leu271 of loop 7 and the bent conformer of Arg254 in the body of the protein[11]. However, Arg254 then formed a salt bridge with Glu233 in R2, which competes with the hydrogen bond to Leu271 formed in R1, reducing the Arg254–loop 7 interaction and increasing the disorder of loop 7. A series of mutations (encoding substitutions Leu271Phe, Leu272Met, Phe306Ile and Ile313Phe) then accumulated over the course of the trajectory, progressively stabilizing the closed conformation of loop 7 by increasing the hydrophobic contacts between loop 7 and the $(\alpha/\beta)_8$ barrel of the protein (**Fig. 2b**). Thus, the nonproductive open conformation and loop dynamics were reduced through evolution.

The change in B-factor of loop 5, which was also the only region to undergo substantial conformational rearrangement (**Fig. 3d**,**e** and **Supplementary Fig. 4**), was particularly pronounced. The dominant conformation of loop 5 did not change over the first three rounds (R0 to R2), yet there was a slight shift in the adjacent loop 4 (**Fig. 3e**). This scenario provides sufficient conformational freedom for loop 5 to have undergone a small shift over rounds 6–18, before it adopted its final structure in R22. In terms of dynamics, the B-factor underwent little change over R0 to R6, with the most substantial increases in B-factor occurring over the second half of the evolution (between rounds 8 and 18). When examined in conjunction with the change in activity, we observed that the change in loop 5 appeared to correspond to the specialization of the enzyme for AE from round 7 onward (increase of AE:PTE ratio, largely through loss of PTE activity), rather than the initial increases in AE activity over the first six generations that yielded the bifunctional intermediate R6 (**Supplementary Table 1**).

The biophysical basis of catalytic promiscuity

It is unclear how proteins, whose genes undergo discreet changes, often (although not always) evolve new function in a fluid and gradual manner, yielding characteristically smooth transitions such as those observed here (**Supplementary Fig. 1**). A gradual shift in the conformational landscape was apparent when we examined the bifunctional R6 and Rev6 intermediate variants (**Supplementary Fig. 1** and **Supplementary Table 1**). These enzymes were truly bifunctional ($k_{cat}/K_M = 10^5$–10^6 M^{-1} s^{-1} for both PTE and AE activities), and were more active with either substrate than many natural proteins are for their native substrate. The high-resolution diffraction data we obtained for these intermediate structures allowed detailed analysis of the conformational mobility of certain regions. First, we observed electron density in Rev6 that was consistent with loop 5 sampling both R0-like and R22-like conformations (**Fig. 4a**,**b**). Likewise, anisotropic refinement of the atomic displacement parameters illustrated that, although loop 7 in Rev6 displayed substantial disorder (**Fig. 4c**), the disorder was directional and consistent with the population of molecules in the crystal sampling a range of states between the open and closed conformations of this loop[11]. This was supported by crystallographic ensemble refinement (Online Methods, **Supplementary Figs. 2** and **5**, and **Supplementary Table 3**)[32]. These results revealed that R6 and Rev6 are true dynamic intermediates of R0 and R22: whereas the mobility of loops 4, 5 and 7 was opposite at the start and end points of the evolutionary trajectories, R6 and Rev6 exhibited high flexibility in both loop 7 and loops 4 and 5, and could sample both R0-like and R22-like conformations, suggesting the presence of R0-like and R22-like ^{Enz}GS conformational sub-states in these enzymes, which can rapidly interconvert (**Fig. 4d** and **Supplementary Fig. 6**).

Table 1 | Kinetic parameters for all rationally designed variants with the arylester 2-napthyl hexanoate

	k_{cat} (s^{-1})	K_M (μM)	k_{cat}/K_M (s^{-1} M^{-1})	Substitutions					
R0	0.035 ± 0.002	83 ± 19	4.2×10^2						
E1a	0.068 ± 0.006	393 ± 61	1.7×10^2		D233E				
E1b	0.53 ± 0.06	256 ± 45	2.1×10^3			L271F	L272M	F306I	I313F
R1	0.27 ± 0.1	250 ± 30	1.1×10^3	H254R					
E2a	1.1 ± 0.5	374 ± 151	3.0×10^3		D233E	L271F	L272M	F306I	I313F
E2b	43 ± 3	124 ± 19	3.4×10^5	H254R		L271F	L272M	F306I	I313F
R2	24 ± 3	150 ± 30	1.6×10^5	H254R	D233E				
E3	55 ± 4	56 ± 10	9.8×10^5	H254R	D233E	L271F	L272M	F306I	I313F

Assays were performed in 100 mM Tris-HCl, pH 7.5, 100 μM $ZnCl_2$ and 0.02% Triton X-100 at 20 °C.

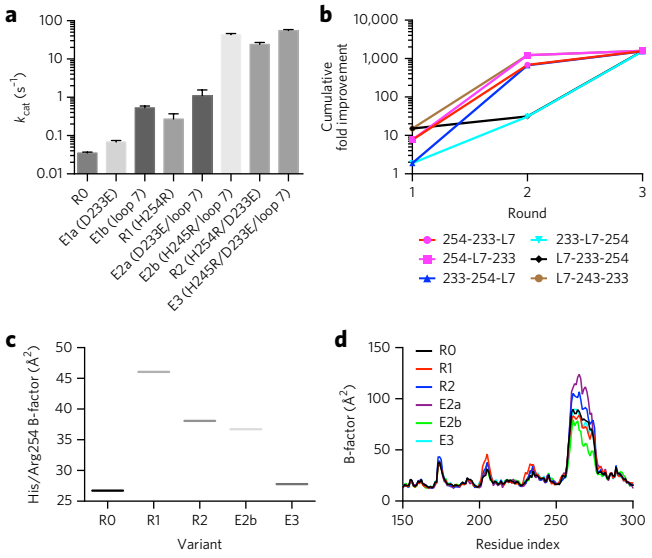

Figure 5 | Epistatic interactions between mutations that accumulate in R22. (**a**) The k_{cat} values, with 2-naphthyl hexanoate, of the E2b, R2 and E3 variants, in which Arg254 is combined with either Asp233Glu, the loop 7 substitutions (Leu271Phe, Leu272Met, Phe306Ile and Ile313Phe), or both, are substantially higher than in variants in which His254Arg is not combined with these substitutions. (**b**) Pathways to higher activity that proceed through intermediates with Asp233Glu and L7 (but not Arg254) gained little activity in round 2. (**c**) The B-factor of the residue at position 254 (His, Arg refined as the bent rotamer) increased in R1, and can be stabilized similarly through addition of Asp233Glu, loop 7, or both. (**d**) The B-factor of loop 7 was substantially lower in variants with Arg254 (R1, E2b and E3).

Remote mutations control conformational sampling

Although the efficiency of R22 was due to the ability of the active site to catalyze the reaction, it was the gradual evolutionary optimization of the configuration of the active site (via remote mutations; **Fig. 1e**) that allowed it to reach its potential. This evolutionary process resulted in the accumulation of a number of mutations around Arg254, specifically Glu233 and a cluster of interacting hydrophobic mutations in and adjacent to loop 7 (L7; Phe271-Met272-Ile306-Phe313) (**Fig. 2b**). We made site-directed mutants to examine the impact of these mutations on catalytic activity and loop dynamics (**Table 1** and **Fig. 5a**,**b**). When we introduced His254Arg (R1), Asp233Glu (E1a) or the L7 substitutions (E1b) into R0, they resulted in 8-fold, 2-fold and 15-fold improvements in the turnover rate (k_{cat}), respectively. The Asp233Glu and L7 mutations combined additively (E2a), resulting in a 30-fold (i.e., 2 × 15) improvement. In contrast, when we combined His254Arg with either Asp233Glu or L7, we observed 90-fold and 160-fold increases in k_{cat}, respectively, revealing strong epistatic relationships[33]. When we combined Asp233Glu with His254Arg/L7, or L7 with His254Arg/Asp233Glu, we observed improvements of only <2-fold, suggesting that these second-shell substitutions have the same role: the conformational optimization of the bent conformation of Arg254 (**Fig. 5c**). Crystal structures of these variants showed that the B-factor of His at position 254 increased when Arg was introduced (R1) and was comparably stabilized by either Asp233Glu, or the L7 substitutions. The increased stability of the bent conformation correlated with increased turnover of the arylester substrate (**Fig. 5a**). Asp233Glu substitutions resulted in a stabilizing salt bridge to the bent conformation[21], whereas stabilization of Arg254 by the L7 substitutions was due to stabilization of loop 7 via increased van der Waals interactions between loop 7 and the rest of the enzyme (**Fig. 5d**), leading to a more stable hydrogen bond between the bent conformation of Arg254 and the carbonyl oxygen of the residue at position 271 of loop 7 in its closed conformation (**Fig. 2b**). This Arg254-loop 7 interaction is highlighted in the variance of the flexibility of loop 7 over this series of variants (**Fig. 5d**): a decrease in the observed B-factors of loop 7 after the introduction of Arg254 and the L7 substitutions was in contrast to the effects of the Asp233Glu substitution, which resulted in an increase in the disorder of this loop, because it distorted the alignment of the hydrogen bond between Arg254 at the carbonyl oxygen of position 271, weakening it and reducing the stabilizing effect it has on loop 7 (**Supplementary Fig. 7**). Taken together, these results are consistent with a model in which most of the mutations that accumulate in evolutionary trajectories are remote from the active site and have little direct catalytic impact, but serve to optimize the conformational landscape of a few catalytically important regions of the protein, particularly Arg254 and loop 7 in this example.

DISCUSSION

New substitutions, such as Arg254, often appear to be conformationally unstable and can adopt nonproductive rotamers that limit their potential catalytic benefit. It is only through minimization of unproductive flexibility or dynamics that their full potential is realized. Likewise, mobility that might be valuable to an ancestral activity (for example, loop 7 with PTE activity) is reduced through evolution if it is not beneficial to the new activity. It is also notable that the changes to the dynamics of different regions do not occur simultaneously. There appears to be a defined order in which these changes must occur, i.e., Arg254 is optimized first, followed by loop 7. Once Arg254 is stabilized and loop 7 has begun to stabilize, the level of disorder around loop 5 begins to increase (**Fig. 3d** and **Supplementary Fig. 4**). Such a series of sequential adjustments makes biophysical sense given the detrimental effect that simultaneous destabilization of all three regions would have on catalytic activity and structural integrity of the enzyme, i.e., mutants appear to survive the mutational destabilization in one site at a time, whereas simultaneous acquisition of mutations in three loci would exceed the stability threshold. This explanation is consistent with recent work showing that excessive dynamics can lead to negative epistasis and limit the evolution of a TEM-1 β-lactamase[22].

R6 and Rev6 appear to be both bifunctional and multiconformational as they can interconvert between dominant ^{Enz}GSs; a R0-like ^{Enz}GS with loop 5 close to the active site, and R22-like ^{Enz}GS with loop 5 away from the active site (**Fig. 4b**). The R0 conformation is adept at catalyzing PTE hydrolysis, whereas the R22 conformation is adept at catalyzing arylester hydrolysis[19,25]; i.e., the disorder or dynamics observed in these intermediates is a reflection of interconversion between two distinct, catalytically relevant, ^{Enz}GSs that are suited to different reactions. In contrast, in R0 and R22, loop 5 and loop 7, respectively, are substantially more conformationally homogeneous (**Fig. 4d** and **Supplementary Fig. 6**). These results suggest that the dynamic nature of these proteins is responsible for the gradual evolutionary transition and catalytic promiscuity: from one gene sequence, multiple enzyme configurations that are optimized for distinct substrates can be attained.

Changes to the active site provide the catalytic potential that is optimized through the changes in the conformational distribution. Thus, these intermediates are not efficient because of their dynamics *per se*; rather, their structural dynamics allow interconversion between two distinct and stable active site configurations. Specialization in evolution is then characterized by a drive to minimize, or 'freeze out' unnecessary dynamics and catalytic promiscuity.

These results show that protein structural dynamics are nuanced: one mutation can result in far reaching dynamic effects. It also emphasizes that, in this example, structural dynamics themselves are not intrinsically beneficial to activity in a general or nonspecific fashion (assuming there is sufficient energy in the system for

conformational change to occur). This trajectory is marked by strong selection against mobility in the key areas of Arg254 and loop 7. In this example, where the highly optimized wild-type enzyme has considerable mobility, any changes during evolution are highly directional and required in a functional role (for example, loop 7 opening or closing for diffusion or catalysis). Our observations establish that changes in the conformational landscape of a protein are essential to evolutionary functional change, and strongly suggest that enzyme design and engineering will require the development of means to tune the conformational landscapes as well as to design efficient TS stabilization in the active site. However, these changes were attainable by single point mutations to achieve what is, in many ways, a simple redistribution of hydrogen bonds and salt bridges throughout an otherwise almost identical structure. This suggests that substantial changes in function might be achieved through dynamic enrichment of pre-existing (but low fractional occupancy) catalytic states, rather than direct mutational active site remodeling. Instead, positioning of active site features can be achieved through optimizing the conformation of the active site residues. Indeed, it has previously been shown that the introduction of flexibility is an important feature of emerging primordial enzymes[34], and it has also been observed that if computational enzyme design does not initially yield an efficient enzyme, the designed protein can be optimized by remote mutations[35–38]. The observation that most substitutions in directed evolution experiments are remote from the active site[39] and (in this instance) highly epistatic, stabilizing a preorganized active site configuration, suggests that laboratory evolution can heuristically uncover features that mechanistic work would not necessarily find, and pave the ground for extrapolation from ^{Enz}GS structures to mechanisms of TS stabilization.

Received 21 January 2016; accepted 17 June 2016;
published online 12 September 2016

METHODS

Methods and any associated references are available in the online version of the paper.

Accession codes. Protein Data Bank: coordinates for the structures described in this work have been deposited under the accession codes 4PCP (R0), 4XAF (R1), 4XD5 (R2), 4XAG (R6), 4XAY (R8), 4XAZ (R18), 4PBE (Rev6), 4PBF (Rev12), 4PCN (R22), 4XD6 (E2a), 4XD4 (E2b) and 4XD3 (E3).

References

1. Kirby, A.J. & Hollfelder, F. *From Enzyme Models to Model Enzymes* (Royal Society of Chemistry, 2009).
2. Kraut, D.A., Carroll, K.S. & Herschlag, D. Challenges in enzyme mechanism and energetics. *Annu. Rev. Biochem.* **72**, 517–571 (2003).
3. Ma, B. & Nussinov, R. Enzyme dynamics point to stepwise conformational selection in catalysis. *Curr. Opin. Chem. Biol.* **14**, 652–659 (2010).
4. Warshel, A. Computer simulations of enzyme catalysis: methods, progress, and insights. *Annu. Rev. Biophys. Biomol. Struct.* **32**, 425–443 (2003).
5. Elias, M., Wieczorek, G., Rosenne, S. & Tawfik, D.S. The universality of enzymatic rate-temperature dependency. *Trends Biochem. Sci.* **39**, 1–7 (2014).
6. Bhabha, G. *et al.* A dynamic knockout reveals that conformational fluctuations influence the chemical step of enzyme catalysis. *Science* **332**, 234–238 (2011).
7. Silva, R.G., Murkin, A.S. & Schramm, V.L. Femtosecond dynamics coupled to chemical barrier crossing in a Born-Oppenheimer enzyme. *Proc. Natl. Acad. Sci. USA* **108**, 18661–18665 (2011).
8. Bhabha, G. *et al.* Divergent evolution of protein conformational dynamics in dihydrofolate reductase. *Nat. Struct. Mol. Biol.* **20**, 1243–1249 (2013).
9. Fraser, J.S. *et al.* Hidden alternative structures of proline isomerase essential for catalysis. *Nature* **462**, 669–673 (2009).
10. Gobeil, S.M. *et al.* Maintenance of native-like protein dynamics may not be required for engineering functional proteins. *Chem. Biol.* **21**, 1330–1340 (2014).
11. Jackson, C.J. *et al.* Conformational sampling, catalysis, and evolution of the bacterial phosphotriesterase. *Proc. Natl. Acad. Sci. USA* **106**, 21631–21636 (2009).
12. Glowacki, D.R., Harvey, J.N. & Mulholland, A.J. Taking Ockham's razor to enzyme dynamics and catalysis. *Nat. Chem.* **4**, 169–176 (2012).
13. Kamerlin, S.C. & Warshel, A. At the dawn of the 21st century: Is dynamics the missing link for understanding enzyme catalysis? *Proteins* **78**, 1339–1375 (2010).
14. O'Brien, P.J. & Hollfelder, F. Hitting a moving target?—Understanding how conformational diversity impacts enzymatic catalysis. *Curr. Opin. Chem. Biol.* **14**, 634–635 (2010).
15. Fraser, J.S. & Jackson, C.J. Mining electron density for functionally relevant protein polysterism in crystal structures. *Cell. Mol. Life Sci.* **68**, 1829–1841 (2011).
16. Ramanathan, A., Savol, A., Burger, V., Chennubhotla, C.S. & Agarwal, P.K. Protein conformational populations and functionally relevant substates. *Acc. Chem. Res.* **47**, 149–156 (2014).
17. Klinman, J.P. & Kohen, A. Evolutionary aspects of enzyme dynamics. *J. Biol. Chem.* **289**, 30205–30212 (2014).
18. Colletier, J.P. *et al.* Sampling the conformational energy landscape of a hyperthermophilic protein by engineering key substitutions. *Mol. Biol. Evol.* **29**, 1683–1694 (2012).
19. Tokuriki, N. & Tawfik, D.S. Protein dynamism and evolvability. *Science* **324**, 203–207 (2009).
20. James, L.C. & Tawfik, D.S. Conformational diversity and protein evolution—a 60-year-old hypothesis revisited. *Trends Biochem. Sci.* **28**, 361–368 (2003).
21. Tokuriki, N. *et al.* Diminishing returns and tradeoffs constrain the laboratory optimization of an enzyme. *Nat. Commun.* **3**, 1257 (2012).
22. Dellus-Gur, E. *et al.* Negative epistasis and evolvability in TEM-1 β-lactamase—the thin line between an enzyme's conformational freedom and disorder. *J. Mol. Biol.* **427**, 2396–2409 (2015).
23. Caldwell, S.R., Newcomb, J.R., Schlecht, K.A. & Raushel, F.M. Limits of diffusion in the hydrolysis of substrates by the phosphotriesterase from Pseudomonas diminuta. *Biochemistry* **30**, 7438–7444 (1991).
24. Kaltenbach, M., Jackson, C.J., Campbell, E.C., Hollfelder, F. & Tokuriki, N. Reverse evolution leads to genotypic incompatibility despite functional and active site convergence. *eLife* **4**, e06492 (2015).
25. Bora, R.P., Mills, M.J., Frushicheva, M.P. & Warshel, A. On the challenge of exploring the evolutionary trajectory from phosphotriesterase to arylesterase using computer simulations. *J. Phys. Chem. B* **119**, 3434–3445 (2015).
26. Doncheva, N.T., Assenov, Y., Domingues, F.S. & Albrecht, M. Topological analysis and interactive visualization of biological networks and protein structures. *Nat. Protoc.* **7**, 670–685 (2012).
27. Fetics, S.K. *et al.* Allosteric effects of the oncogenic RasQ61L mutant on Raf-RBD. *Structure* **23**, 505–516 (2015).
28. Sethi, A., Eargle, J., Black, A.A. & Luthey-Schulten, Z. Dynamical networks in tRNA:protein complexes. *Proc. Natl. Acad. Sci. USA* **106**, 6620–6625 (2009).
29. Jackson, C.J. *et al.* In crystallo capture of a Michaelis complex and product-binding modes of a bacterial phosphotriesterase. *J. Mol. Biol.* **375**, 1189–1196 (2008).
30. van den Bedem, H., Bhabha, G., Yang, K., Wright, P.E. & Fraser, J.S. Automated identification of functional dynamic contact networks from X-ray crystallography. *Nat. Methods* **10**, 896–902 (2013).
31. van den Bedem, H., Dhanik, A., Latombe, J.C. & Deacon, A.M. Modeling discrete heterogeneity in X-ray diffraction data by fitting multi-conformers. *Acta Crystallogr. D Biol. Crystallogr.* **65**, 1107–1117 (2009).
32. Burnley, B.T., Afonine, P.V., Adams, P.D. & Gros, P. Modelling dynamics in protein crystal structures by ensemble refinement. *eLife* **1**, e00311 (2012).
33. Ortlund, E.A., Bridgham, J.T., Redinbo, M.R. & Thornton, J.W. Crystal structure of an ancient protein: evolution by conformational epistasis. *Science* **317**, 1544–1548 (2007).
34. Chao, F.A. *et al.* Structure and dynamics of a primordial catalytic fold generated by in vitro evolution. *Nat. Chem. Biol.* **9**, 81–83 (2013).
35. Giger, L. *et al.* Evolution of a designed retro-aldolase leads to complete active site remodeling. *Nat. Chem. Biol.* **9**, 494–498 (2013).
36. Khersonsky, O. *et al.* Optimization of the in-silico-designed kemp eliminase KE70 by computational design and directed evolution. *J. Mol. Biol.* **407**, 391–412 (2011).
37. Preiswerk, N. *et al.* Impact of scaffold rigidity on the design and evolution of an artificial Diels-Alderase. *Proc. Natl. Acad. Sci. USA* **111**, 8013–8018 (2014).
38. Sykora, J. *et al.* Dynamics and hydration explain failed functional transformation in dehalogenase design. *Nat. Chem. Biol.* **10**, 428–430 (2014).
39. Morley, K.L. & Kazlauskas, R.J. Improving enzyme properties: when are closer mutations better? *Trends Biotechnol.* **23**, 231–237 (2005).

Acknowledgments

We thank D.S. Tawfik for stimulating discussions. C.J.J. thanks the Australian Research Council for a Future Fellowship (FT140101059) and Discovery Project (DP130102144). This research was undertaken on the MX1 and MX2 beamlines at the Australian Synchrotron,

Victoria, Australia. F.H. thanks the Biotechnology and Biological Sciences Research Council and European Research Council (starting investigator grants). M.K. thanks the EU Innovative Training Network (ProSA) for a studentship. N.T. is funded as a Canadian Institutes of Health Research new investigator and a Michael Smith Foundation of Health Research (MSFHR) career investigator. N.T. thanks Natural Sciences and Engineering Research Council of Canada Discovery Grant RGPIN 418262-12. A.M.B. is funded as a National Health and Medical Research Senior Research Fellow (1022688). This work was supported by the Victorian Life Sciences Computation Initiative, an initiative of the Victorian Government, Australia.

Author contributions

E.C., M.K., G.J.C., P.D.C., B.T.P., E.K.L. and L.A.-J. performed experiments and analyzed results; A.M.B. and M.W. analyzed results; F.H. conceived the project, designed experiments and analyzed results; N.T. conceived the project, designed experiments, analyzed results and wrote the manuscript; and C.J.J. conceived the project, designed experiments, performed experiments, analyzed results and wrote the manuscript.

Competing financial interests

The authors declare no competing financial interests.

Additional information

Any supplementary information, chemical compound information and source data are available in the online version of the paper. Reprints and permissions information is available online at http://www.nature.com/reprints/index.html. Correspondence and requests for materials should be addressed to N.T. or C.J.J.

ONLINE METHODS

Construction of combinatorial mutants. Mutants E1a (encoding Glu233Asp), E1b (Leu271Phe/Leu272Met/Phe306Ile/Ile313Phe), E2a (Asp233Glu/Leu271Phe/Leu272Met/Phe306Ile/Ile313Phe), E2b (His254Arg/Leu271Phe/Leu272Met/Phe306Ile/Ile313Phe) and E3 (His254Arg/Asp233Glu/Leu271Phe/Leu272Met/Phe306Ile/Ile313Phe) were constructed by site-directed mutagenesis as described in the QuikChange Site-Directed Mutagenesis manual (Agilent). All mutations were confirmed by DNA sequencing. The sequences of E2a and E2b were additionally confirmed by X-ray crystallography and inspection of difference map peaks.

Enzyme kinetics. For kinetic measurements, all enzymes were purified by strep-tag affinity chromatography. Plasmids were transformed into *Escherichia coli* BL21 (DE3) and grown at 37 °C in 2YT medium containing 100 μg/mL ampicillin and 200 μM $ZnCl_2$. Expression was induced with 0.4 mM IPTG when cell density reached an OD_{600} of 0.6 and cells were further grown overnight at 20 °C. Cells were lysed using B-PER Protein Extraction Reagent (Thermo Scientific) and the proteins were purified using strep-tactin affinity columns (IBA Lifesciences) according to the manufacturer's protocol.

Initial rates for 2NH and paraoxon hydrolysis were determined at 12 different substrate concentrations (2 to 2,000 μM in 100 mM Tris-HCl, pH 7.5, 100 μM $ZnCl_2$ and 0.02% Triton X-100) in a Synergy H1 Hybrid Microplate Reader (Biotek). Measurements were performed in triplicate and the average values fitted to the Michaelis–Menten equation using KaleidaGraph (Synergy Software) ($v_0 = k_{cat}[E]_0[S]_0/(K_M + [S]_0)$ with v_0: initial rate, $[E]_0$: enzyme concentration, and $[S]_0$: substrate concentration).

Protein expression and purification. PTE variant expression and purification was carried out differently to produce protein for crystallography. First, the twelve genes (R0, R1, R2, R6, R8, R18, R22, E2a, E2b and E3) were cloned into a tag-less vector (pETMCSIII)[40]. A single colony of *E. coli* BL21 (DE3) cells transformed with each construct was used to inoculate LB media (5 mL). This small scale culture was used to inoculate 1 L of Terrific Broth (TB) media supplemented with 100 μM $ZnCl_2$. After incubation at 25 °C for 42 h, cells were pelleted by centrifugation (5,000*g*) and resuspended in buffer A (50 mM HEPES, 100 μM $ZnCl_2$, pH 8.0). The resuspended cells were lysed by sonication (Omni Sonic Ruptor 400), the lysate was sedimented and the supernatant filtered before loading onto a DEAE fractogel equilibrated with buffer A. The protein did not bind to the resin and was collected in the flow-through fraction. The flow-through was then concentrated using a Millipore centrifugal protein concentration device (30 kDa cutoff) and loaded onto a Superdex 200 Hiload 16/600 column (GE Healthcare) equilibrated with buffer C (20 mM HEPES, 50 mM NaCl, 100 μM $ZnCl_2$, pH 8).

Purified PTE variants were concentrated to 10 $mg.mL^{-1}$ in buffer C. Screens were optimized by hanging-drop vapor diffusion at 4 °C. Drops consisting of 2 μL of reservoir and 1 μL of PTE were equilibrated over a 500 μL reservoir using EasyXtal-15-Well Tools (Qiagen). Reservoir solutions were screened between 100 mM sodium cacodylate (pH 6.3–6.7), distilled deionized water and 20–50% (w/v) 2-methyl-2,4-pentanediol (MPD). Crystals formed in the initial screening were manually pulverized for use as microseeds. Six serial dilutions of the pulverized crystals were made, from 1/10 to 1/1,000,000 in factors of 10. New crystal screens were set up using only sodium cacodylate buffer of pH 6.5, and varying MPD concentrations from 12% to 28%. Each well contained 1 μL of protein, 1.5 μL of mother liquor and 0.5 μL of microseed solution. To obtain crystal structures in the same space group and crystallization condition, serial microseeding was used.

X-ray diffraction data collection and refinement. For data collection, crystals were soaked in cryobuffer (100 mM sodium cacodylate, pH 6.5, 40% MPD) for 2 min before flash-cooling to 100K in a stream of nitrogen gas. PTE diffraction data were collected at the Australian Synchrotron (beamline MX1) at a wavelength of 0.9537 Å, or locally on a Marresearch marμX system comprising a Xenocs Genix^{3D} Cu high flux generator and a mar345 image plate detector. The X-ray diffraction data were indexed and integrated using XDS[41] and merged using AIMLESS as implemented within the CCP4 program suite[42]. Data resolution cut-offs were chosen using half data set correlation coefficients, as described by Karplus and Deiderichs[43]. The structures of PTE and variants were solved by molecular replacement (PHASER)[44] using the R18 structure (4GY0)[21]. Refinement was performed using REFMAC and phenix.refine, and manual rebuilding was performed using COOT[45–47]. Automated fitting of multiple conformations was carried out with the QFit web-server[30], with manual inspection and removal of conformations that were not present in good (at least 1.0 σ) electron density.

Computational analysis of protein dynamics. Molecular dynamics simulations were carried out on the crystal structures of R0 and R22. All chain termini were capped with neutral acetyl and methylamide groups. Completed structures were solvated in a cubic simulation box with a minimum distance of 14 Å from any protein atom to the box wall, followed by the addition of roughly 150 mM NaCl to the aqueous phase, neutralizing the total system charge. Simulation systems of R0 and R22 were subjected to energy minimization, followed by a three-stage equilibration protocol with positional restraints holding all protein atoms at 1,000 kJ mol^{-1} nm^{-2}, while initializing velocities at 290K and setting a temperature reference value of 300K for 100 ps. Restraints were released to backbone atoms at 1,000 kJ mol^{-1} nm^{-2} for 100 ps and then to Cα atoms at 100 kJ mol^{-1} nm^{-2} for 100 ps. Completed systems were equilibrated and free simulation performed at 300K in duplicate for 30 ns, with each replicate starting from a different distribution of initial velocities. All simulations were performed using GROMACS ver 4.0.7 (ref. 48) in conjunction with the GROMOS 54A7 united-atom force field[49]. Ionizable residues were set to their standard protonation states at pH 7. Water was represented explicitly using the simple-point-charge (SPC) model[50]. All simulation systems were equilibrated in an NVT ensemble and production runs performed in an NPT ensemble under periodic conditions. Temperature was maintained close to its reference value of 300K by V-rescale temperature coupling. Pressure was maintained close to a reference value of 1 atm by isotropic coupling with a Berendsen pressure bath[51]. Non-bonded interactions were evaluated using a twin-range cut-off scheme: interactions falling within the 8 Å short-range cut-off were calculated every 2 fs whereas interactions within the 14 Å long cut-off were updated every 10 fs, together with the pair list. A generalized reaction-field correction was applied to the electrostatic interactions beyond the long-range cut-off[52], using a relative dielectric permittivity constant of RF = 62 as appropriate for SPC water[53]. All bond lengths to hydrogen atoms were constrained using the P-LINCS algorithm[54] and water geometry was constrained using the SETTLE algorithm[55]. A 2 fs time step was used for integrating the equations of motion. Analyses of simulations were performed using the tools provided in the GROMACS package ver4.0.7 (ref. 48) and custom scripts in conjunction with ProDy[56]. Principal component analysis was performed with the Bio3D package[57]. Allosteric networks between the 'source' residue of A203 (loop 5) and the 'sink' residue of A270 (loop 7) were identified using the Weighted Implementation of Suboptimal Paths (WISP) software[58]. The optimal and 100 suboptimal paths were calculated on the MD simulation trajectories of R0 and R22. In each network, residues are linked by persistent tertiary contacts between side chains during a simulation. Determination of linkage was performed by generation of a correlation matrix of each residue Cα atoms within a 4.5 Å cut-off. All paths were visualized in VMD[59] and analyzed with custom scripts.

To further examine the conformational flexibility of the variants, normal mode analysis of elastic network models was performed. Dimeric structures of R0 and R22, were submitted to the ElNémo server (http://www.igs.cnrs-mrs.fr/elnemo/index.html)[60] using default parameters. The lowest eigenvalue normal modes that involved movement of rigid bodies within each monomer (modes 7 & 8) were analyzed in detail. The computed B-factors from the normal mode analysis were compared against experimentally determined B-factors, yielding correlation coefficients between 0.7 and 0.8. Experimentally determined B-factors were compared against each other by refining with a single major main-chain conformation, averaging values of two chains within each dimer, and normalizing the B-factor, which was achieved by scaling the average B-factor of each chain (with the exception of the loops with variable B-factors) to achieve a comparable baseline.

Time-averaged ensembles were generated for R0 (4PCP), R6 (4XAG), R22 (4PCN) and Rev-R6 (4PBE) with phenix.ensemble_refinement implemented in PHENIX version 1.9-1692. Initially, the protein and zinc ion coordinates

were refined using phenix.refine with default parameters (the ligands MPD and CAC were removed). The R_{free} of the refined models, and the $mF_O - DF_C$ difference density maps, were used to assess the time-averaged refinement protocol. To prepare the structures for ensemble refinement, alternate conformations were removed and occupancies adjusted to 100% (PDB tools). Hydrogen atoms were added (phenix.readyset). Because the carboxylated lysine residues are nonstandard, a restraints file was generated (phenix.elbow) with the geometry taken from the input PDB file. Each monomer of the crystallographic dimer was assigned to a different translation-libration-screw TLS group, with zinc cations assigned to the TLS group of the closest protein monomer. Harmonic restraints were applied to the zinc cations. A grid search was performed to optimize the ensemble refinement simulation parameters p_{TLS} (0.6, 0.7, 0.8 and 0.9) and T_{BATH} (2K, 5K and 10K). Four additional simulations with the ER parameters giving the lowest R_{free} were conducted to assess reproducibility, with initial velocities assigned with different random seeds. RMSF values for the ensembles were calculated with the g_rmsf tool in the GROMACS molecular dynamics suit. CCP4 format electron density maps were calculated with phenix.density and contoured to comparable e/Å^3 levels for comparison. All maps and coordinates were visualized using PyMOL version 1.6 (http://pymol.org). Calculations, modeling and simulations were performed on a range of computing resources: 1 ORCHARD 800 core x86 cluster (Monash University; X-ray ensemble refinement); 2AVOCA/MERRI (VLSCI BlueGene/Q/x86 cluster; atomistic MD).

New data were deposited in the Protein Data Bank.

40. Love, C.A., Lilley, P.E. & Dixon, N.E. Stable high-copy-number bacteriophage lambda promoter vectors for overproduction of proteins in Escherichia coli. *Gene* **176**, 49–53 (1996).
41. Kabsch, W. Xds. *Acta Crystallogr. D Biol. Crystallogr.* **66**, 125–132 (2010).
42. Collaborative, C.P. Collaborative Computational Project, Number 4. The CCP4 suite: programs for protein crystallography. *Acta Crystallogr. D Biol. Crystallogr.* **50**, 760–763 (1994).
43. Karplus, P.A. & Diederichs, K. Linking crystallographic model and data quality. *Science* **336**, 1030–1033 (2012).
44. McCoy, A.J. *et al.* Phaser crystallographic software. *J. Appl. Crystallogr.* **40**, 658–674 (2007).
45. Vagin, A.A. *et al.* REFMAC5 dictionary: organization of prior chemical knowledge and guidelines for its use. *Acta Crystallogr. D Biol. Crystallogr.* **60**, 2184–2195 (2004).
46. Murshudov, G.N., Vagin, A.A. & Dodson, E.J. Refinement of macromolecular structures by the maximum-likelihood method. *Acta Crystallogr. D Biol. Crystallogr.* **53**, 240–255 (1997).
47. Emsley, P. & Cowtan, K. Coot: model-building tools for molecular graphics. *Acta Crystallogr. D Biol. Crystallogr.* **60**, 2126–2132 (2004).
48. Hess, B., Kutzner, C., van der Spoel, D. & Lindahl, E. GROMACS 4: Algorithms for Highly Efficient, Load-Balanced, and Scalable Molecular Simulation. *J. Chem. Theory Comput.* **4**, 435–447 (2008).
49. Schmid, N. *et al.* Definition and testing of the GROMOS force-field versions 54A7 and 54B7. *Eur. Biophys. J.* **40**, 843–856 (2011).
50. Berendsen, H., Postma, J., van Gunsteren, W.F. & Hermans, J. in *Intermolecular Forces* Vol. 14 (ed. Pullman, B.) 331–342 (Springer Netherlands, 1981).
51. Berendsen, H.J.C., Postma, J.P.M., van Gunsteren, W.F., DiNola, A. & Haak, J.R. Molecular dynamics with coupling to an external bath. *J. Chem. Phys.* **81**, 3684 (1984).
52. Tironi, I.G., Sperb, R., Smith, P.E. & van Gunsteren, W.F. A generalized reaction field method for molecular dynamics simulations. *J. Chem. Phys.* **102**, 5451 (1995).
53. Heinz, T.N., van Gunsteren, W.F. & Hünenberger, P.H. Comparison of four methods to compute the dielectric permittivity of liquids from molecular dynamics simulations. *J. Chem. Phys.* **115**, 1125 (2001).
54. Hess, B., Bekker, H., Berendsen, H.J.C. & Fraaije, J.G.E.M. LINCS: a linear constraint solver for molecular simulations. *J. Chem. Phys.* **18**, 1463–1472 (1997).
55. Miyamoto, S. & Kollman, P.A. SETTLE: an analytical version of the SHAKE and RATTLE algorithm for rigid water models. *J. Comput. Chem.* **13**, 952–962 (1992).
56. Bakan, A., Meireles, L.M. & Bahar, I. ProDy: protein dynamics inferred from theory and experiments. *Bioinformatics* **27**, 1575–1577 (2011).
57. Grant, B.J., Rodrigues, A.P., ElSawy, K.M., McCammon, J.A. & Caves, L.S. Bio3d: an R package for the comparative analysis of protein structures. *Bioinformatics* **22**, 2695–2696 (2006).
58. Van Wart, A.T., Durrant, J., Votapka, L. & Amaro, R.E. Weighted Implementation of Suboptimal Paths (WISP): An Optimized Algorithm and Tool for Dynamical Network Analysis. *J. Chem. Theory Comput.* **10**, 511–517 (2014).
59. Humphrey, W., Dalke, A. & Schulten, K. VMD: visual molecular dynamics. *J. Mol. Graphics* **14**, 33–38 (1996).
60. Suhre, K. & Sanejouand, Y.H. ElNemo: a normal mode web server for protein movement analysis and the generation of templates for molecular replacement. *Nucleic Acids Res.* **32**, W610–W614 (2004).

doi:10.1038/nchembio.2175

Supplementary Information

The role of protein dynamics in the evolution of new enzyme function

Eleanor Campbell[1†], Miriam Kaltenbach[2,3†], Galen Correy[1], Paul D. Carr[1], Benjamin T Porebski[4], Emma K Livingstone[1], Livnat Afriat-Jurnou[1], Ashley M Buckle,[4] Martin Weik[5], Florian Hollfelder[3], Nobuhiko Tokuriki[2]*, Colin J Jackson[1]*

[1]Research School of Chemistry, Australian National University, Canberra, ACT, 2601, Australia.

[2]Michael Smith Laboratories, University of British Columbia, Canada.

[3]Department of Biochemistry, University of Cambridge, United Kingdom.

[4]Biomedicine Discovery Institute and Department of Biochemistry and Molecular Biology, Monash University, Clayton, VIC 3800, Australia

[5]Institut de Biologie Structurale, Univ. Grenoble Alpes, CEA, CNRS, F-38044 Grenoble, France.

*Email: colin.jackson@anu.edu.au or tokuriki@msl.ubc.ca

Supplementary Results

Supplementary Figures

Supplementary Figure 1. The mutants studied in this work. The relative catalytic specificities (k_{cat}/K_M) between R0 and R22 change evenly across the intermediates R1-R18, with R6 being bifunctional. The variants obtained through reverse evolution (Rev6, Rev12) regain significant phosphotriesterase activity, with Rev6 being similarly bifunctional to R6.

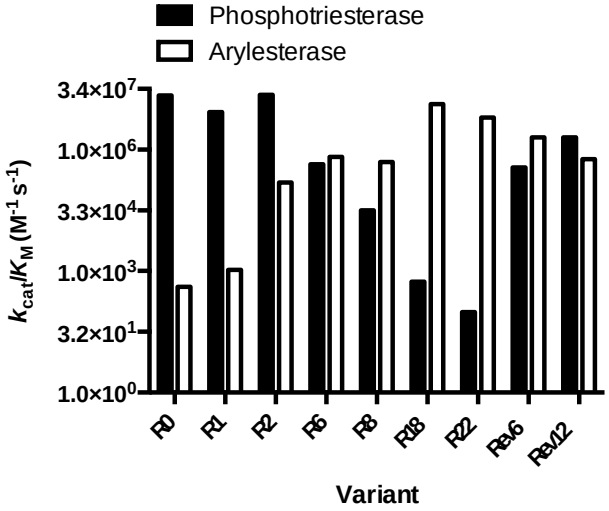

Supplementary Figure 2. Distinct disorder and dynamics in R0 and R22. (a) An averaged plot (A and B chains) of the main-chain B-factors of R0 and R22 reveals that loops 4 (170-175) and 5 (200-210) have become disordered, whereas loop 7 (260-275) has attained greater order. This is portrayed visually (b) as a sausage representation, with increased B-factor shown as fatter, and redder, sausage. (c) Computed B-factors from normal mode analysis with an elastic network model show increased movement of loop 5 and reduced movement of loop 7. This is shown in (d) in a ribbon representation of the lowest frequenting normal mode (mode 7) in which rigid bodies within the protein began to move independently, start (blue) to end (red). The reduced motion of loop 7 and the increased motion of loop 5 are visible. (e) Root mean squared fluctuations of amino acids from molecular dynamics simulations of R0 and R22 reveal loss of mobility in loop 7 and gain in mobility of loop 5. (f) Principal component analysis of the dominant motions in R0 and R22 show reduced movement of loop 7 and increased movement of loop 5.

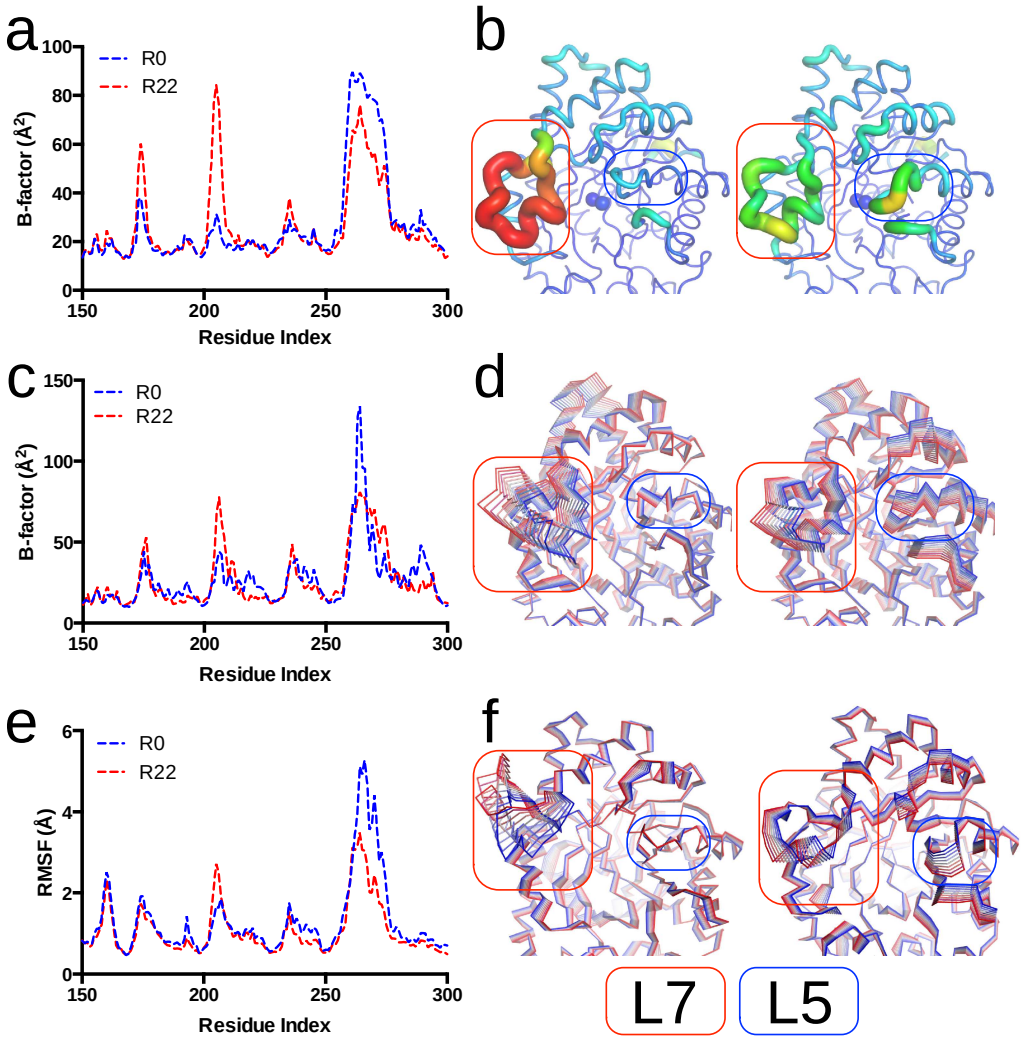

Supplementary Figure 3. Optimal and suboptimal paths connecting loop 5 and loop 7 in R0 and R22. The optimal and suboptimal paths are displayed in blue and red respectively. Bold labelled residues are those that have changed between R0 and R22. As structural and molecular dynamics analysis revealed striking differences in the mobility of loops 5 (200-210) and 7 (260-275) between R0 and R22, we sought to explore respective changes in allosteric communication networks. Using the Weighted Implementation of Suboptimal Paths (WISP) software (Van Wart *et al.* 2014), we calculated the optimal (shortest path) and 100 suboptimal (alternate and longer) pathways. Our analysis reveals that R0 exhibits a predominant pathway from A203 > A203 > T234 > L283 > T279 > S276 > A259 >A270, with two branching pathways that center on D232 and H254. In contrast, R22 exhibits a single major pathway from A203 >T202 >H230 > D232 >R280 >S276 > R275 > G273 > F271 > A270.

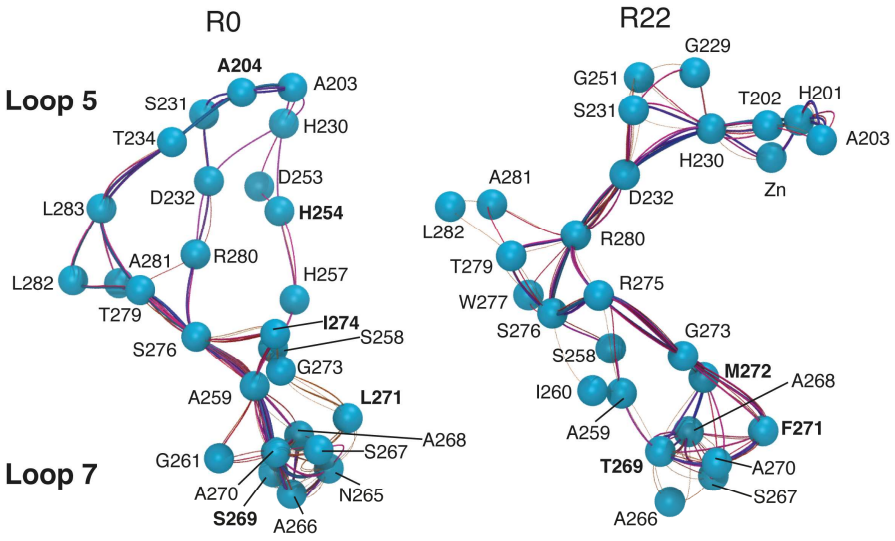

Supplementary Figure 4. A schematic representation of the changes in disorder of the various loops along the trajectory for different regions, in which darker color in represents greater flexibility. Arg254 (red) peaks in R1 and is stable by R6. Loop 7 (cyan) peaks at R2 and continues to decrease to R18. Loop 5 (green) undergoes its most significant increase between R9 and R18.

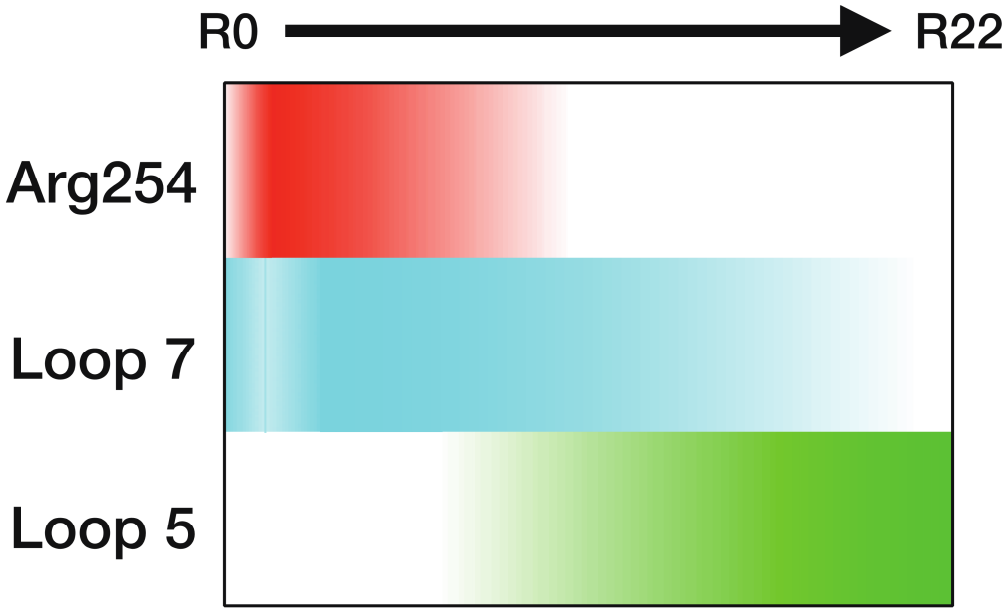

Supplementary Figure 5. Optimisation of ensemble refinement empirical parameters. A grid-search was conducted for each structure to minimise R_{free} by varying the values of p_{TLS} and T_{BATH}. The five repeats with the optimised values of p_{TLS} and T_{BATH} are enclosed by red lines. Although the choice of p_{TLS} appeared to influence the ensemble R_{free}, the value of T_{BATH} did not.

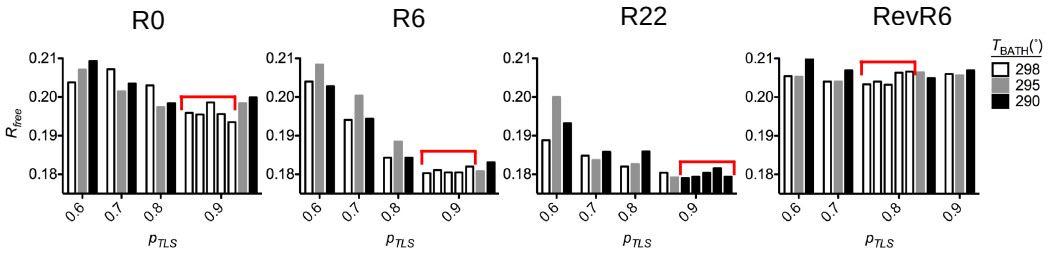

Supplementary Figure 6. Comparison of the mF_O-DF_C difference density between conventional refinement (top) and ensemble refinement (bottom). Difference electron maps are contoured at 0.35, 0.35, 0.36 and 0.42 e/Å^3 for R0, R6, R22 and Rev6 respectively (the densities are equivalent to 3 σ for the single model). The single structure is shown as a cartoon while the ensembles are shown in line representations with backbone atoms only. The active site zinc cations are shown as blue spheres. For ease of interpretation, every second structure from the ensembles is hidden.

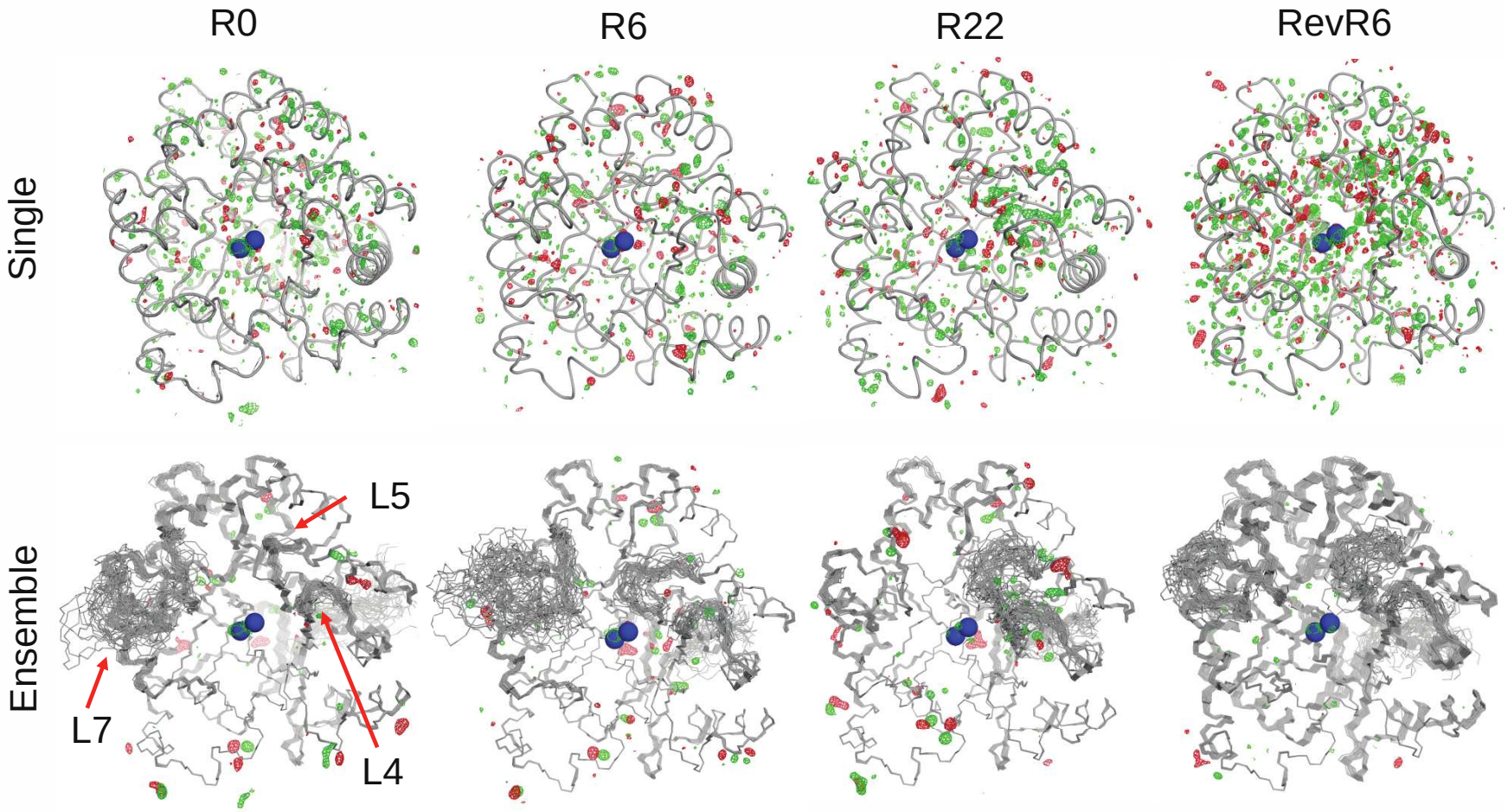

Supplementary Figure 7. The hydrogen bonding interaction between Arg254 and the carbonyl oxygen of the residue at position 271 is weakened through improper alignment when Glu233 is present (left), compared with Asp233.

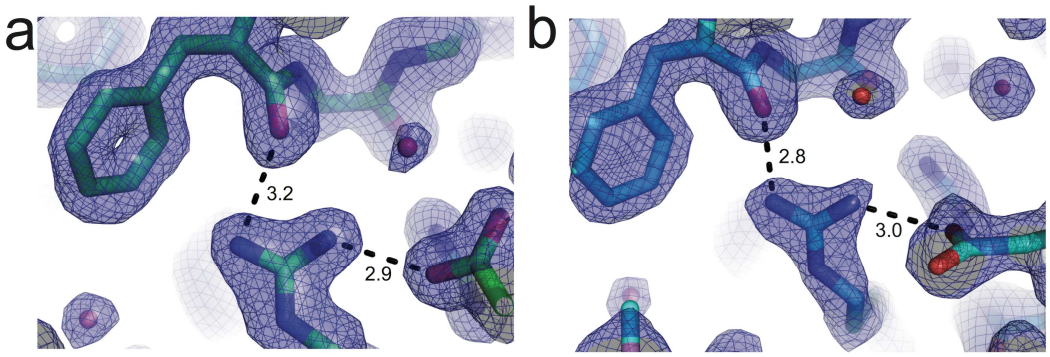

Supplementary Tables

Supplementary Table 1. Kinetic parameters and genotype for all variants produced throughed directed evolution. Data from Tokuriki *et al.* (2012) and Kaltenbach *et al.* (2015).

	Paraoxon			2-Naphthol hexanoate			Mutations (*vs.* R0)
	k_{cat} [s^{-1}]	K_M [μM]	k_{cat}/K_M [$M^{-1}s^{-1}$]	k_{cat} [s^{-1}]	K_M [μM]	k_{cat}/K_M [$M^{-1}s^{-1}$]	
R0	1300 ± 27	57 ± 4.9	2.3×10^7	0.035 ± 0.0017	83 ± 19	4.2×10^2	
R1	62 ± 2.6	7.0 ± 1.4	8.9×10^6	0.27 ± 0.012	250 ± 32	1.1×10^3	H254R
R2	440 ± 9.9	18 ± 1.4	2.4×10^7	24 ± 2.7	150 ± 25	1.6×10^5	H254R/D233E
R6	55 ± 2.1	120 ± 17	4.6×10^5	130 ± 3.4	190 ± 20	6.8×10^5	H254R/D233E/F306L/I274S/T172I/S269T
R8	10 ± 0.55	300 ± 77	3.3×10^4	73 ± 2.0	140 ± 13	5.2×10^5	H254R/D233E/F306L/I274S/T172I/S269T/M138I/T199I
R18	0.73 ± 0.061	1300 ± 197	5.6×10^2	880 ± 34	63 ± 9	1.4×10^7	H254R/D233E/F306I/I274S/T172I/S269T/M138I/T199I/I272M/A80V/S111R/A204G/ I130V/L271F/A49V/K77E/I140M/I313F
R22	0.12 ± 0.0034	1200 ± 60	1.0×10^2	870 ± 45	130 ± 22	6.5×10^6	H254R/D233E/F306I/I274S/T172I/S269T/M138I/T199I/I272M/A80V/S111R/A204G/ I130V/L271F/A49V/K77E/I140M/I313F/S137T/Q180H/T45A/E144V/M314T/I341T/S102T/V176M
Rev6	28 ± 0.32	74 ± 2.2	3.8×10^5	280 ± 3.6	130 ± 8	2.1×10^6	H254R/D233E/F306I/I274S/S269T/M138I/T199I/I272M/A80V/S111R/A204G/ I130M/K77E/I140M/A49V/I313F/S137T/T45A/E144V/I341T/S102T/V176M/S308C/P135S/ A203E/M293K
Rev12	270 ± 5.3	130 ± 5.3	2.1×10^6	110 ± 2.3	180 ± 17	6.1×10^5	H254R/D233E/F306M/I274S/S269T/M138I/T199I/I272M/A80V/S111R/A204G/ I130M/K77E/I140M/I313F/S137T/T45A/E144V/I341T/S102T/V176M/S308C/P135S/ A203E/M293K/G194D/S258N/Y156H

Supplementary Table 2. Data collection statistics for structures described in this work.

	R1	R2	R6	R8	R18	Rev6
Data collection						
Space group	$P2_12_12$	$P2_12_12$	$P2_12_12$	$P2_12_12$	$P2_12_12$	$P2_12_12$
Cell dimensions						
a, *b*, *c* (Å)	85.7, 85.7, 88.4	85.7, 85.9, 88.4	85.9, 86.3, 88.6	85.8, 85.9, 88.7	86.1, 86.2, 88.9	85.6, 86.0, 89.2
α, β, γ (°)	90, 90, 90	90, 90, 90	90, 90, 90	90, 90, 90	90, 90, 90	90, 90, 90
Resolution (Å)	35.71-1.66 (1.72-1.66)	44.19-1.85 (1.92-1.85)	39.41-1.6 (1.66-1.6)	38.41-1.84 (1.91-1.84)	39.48-1.55 (1.61-1.55)	39.59-1.51 (1.56-1.51)
R_{sym} or R_{merge}	0.07831 (0.8946)	0.04736 (0.2506)	0.1212 (1.108)	0.1069 (1.007)	0.08794 (0.9467)	0.08583 (1.023)
$CC_{1/2}$	0.999 (0.806)	0.999 (0.906)	0.998 (0.736)	0.999 (0.81)	0.999 (0.792)	0.999 (0.731)
CC*	1 (0.945)	1 (0.975)	1 (0.921)	1 (0.946)	1 (0.94)	1 (0.919)
Completeness (%)	99.91 (99.91)	90.54 (57.20)	99.98 (99.99)	99.95 (100.00)	99.98 (99.99)	99.95 (99.75)
Redundancy	7.3 (7.4)	6.4 (3.7)	7.4 (7.4)	7.4 (7.4)	7.3 (7.3)	7.3 (7.3)
Refinement						
Resolution (Å)	35.71-1.66 (1.72-1.66)	44.19-1.85 (1.92-1.85)	39.41-1.6 (1.66-1.6)	38.41-1.84 (1.91-1.84)	39.48-1.55 (1.61-1.55)	39.59-1.51 (1.56-1.51)
No. reflections	77440 (7631)	51029 (3184)	87372(8629)	57480 (5673)	96390 (9531)	103658 (10220)
R_{work} / R_{free}	0.1794/0.2196	0.1610/0.2037	0.1640/0.2021	0.1759/0.2192	0.1737/0.2060	0.2096/0.2490
No. atoms						
Protein	5398	5387	5282	5185	5372	5159
Ligand/ion	30	38	41	17	12	17
Water	333	384	468	371	581	532
B-factors						
Protein	25.9	23.1	19.9	26.8	20.5	22.2
Ligand/ion	41.6	40.2	42.7	36.1	45.7	22.4
Water	29.3	28.5	27.6	31.8	30.6	29.2
R.m.s. deviations						
Bond lengths (Å)	0.016	0.007	0.018	0.007	0.016	0.007
Bond angles (°)	1.65	1.08	1.78	1.11	1.52	1.11

*Values in parentheses are for highest-resolution shell.

Supplementary Table 2 (cont.). Structures of R0, R22 and Rev12 have been published previously (Kaltenbach *et al.* (2015)).

	E2a	E2b	E3
Data collection			
Space group	$P2_12_12$	$P2_12_12$	$P2_12_12$
Cell dimensions			
a, *b*, *c* (Å)	85.7, 85.7, 88.4	85.7, 85.9, 88.4	85.9, 86.3, 88.6
α, β, γ (°)	90, 90, 90	90, 90, 90	90, 90, 90
Resolution (Å)	35.71-1.66 (1.72-1.66)	44.19-1.85 (1.92-1.85)	39.41-1.6 (1.66-1.6)
R_{merge}	0.07283 (0.4594)	0.1183 (0.8233)	0.0828 (0.9643)
$CC_{1/2}$	0.996 (0.83)	0.996 (0.693)	0.999 (0.806)
CC*	0.999 (0.952)	0.999 (0.905)	1 (0.945)
$I / \sigma I$	22.91 (2.71)	10.48 (1.87)	16.45 (2.31)
Completeness (%)	90.54 (92.03)	90.45 (91.94)	99.91 (99.94)
Redundancy	6.4 (3.9)	4.4 (4.2)	7.3 (7.3)
Refinement			
Resolution (Å)	35.71-1.66 (1.72-1.66)	44.19-1.85 (1.92-1.85)	39.41-1.6 (1.66-1.6)
No. reflections	60062 (6017)	47005 (4690)	91982 (9078)
R_{work} / R_{free}	0.2141 / 0.2694	0.1755 / 0.2431	0.1738 / 0.2017
No. atoms			
Protein	5132	5164	5126
Ligand/ion	46	38	46
Water	690	599	672
B-factors			
Protein	22.6	24	22.6
Ligand/ion	39.1	43.5	43.3
Water	30.8	32.3	33.8
R.m.s. deviations			
Bond lengths (Å)	0.007	0.007	0.007
Bond angles (°)	1.13	1.09	1.14

*Values in parentheses are for highest-resolution shell.

Supplementary Table 3. Statistics for ensemble refinement of the R0, R6, R22 and Rev6 PTE datasets.

	Data-set			
	R0	R6	R22	RevR6
phenix.ensemble_refinement				
p_{TLS} (%)	90	90	90	90
T_{BATH} (K)	298	298	290	298
τ_X (ps)	0.8	0.8	0.8	0.9
No. of models*	72 ± 8 (77)	73 ± 4 (67)	70 ± 10 (54)	81 ± 7 (74)
R_{work}*	14.9 ± 0.1 (14.7)	13.9 ± 0.1 (13.8)	14.1 ± 0.1 (14.0)	16.1 ± 0.1 (16.0)
R_{free}*	19.6 ± 0.2 (19.4)	18.1 ± 0.1 (18.0)	18.0 ± 0.1 (17.9)	20.5 ± 0.2 (20.3)
RMS (bonds) (Å)*	0.015 ± 0.002 (0.016)	0.016 ± 0.001 (0.016)	0.020 ± 0.001 (0.012)	0.015 ± 0.001 (0.015)
RMS (angles) (°)*	2.40 ± 0.02 (2.39)	2.43 ± 0.01 (2.42)	2.62 ± 0.02 (2.00)	2.37 ± 0.01 (2.37)

* Data is mean ± standard deviation for five repeat refinements. The values in brackets correspond to the ensemble with the lowest R_{free}.

Postcards featuring photograph of a phosphotriesterase crystal, produced for National Science Week, 2017.

CHAPTER 3:
REPLAYING THE TAPE OF LIFE – INVESTIGATING THE REPEATABILITY OF MOLECULAR EVOLUTION

Declaration

The following chapter consists of a manuscript in early stages of preparation for submission.

The structural characterisation and analysis of X-ray data were performed by the author under the supervision of Associate Professor Colin Jackson. The construction and screening of libraries, design and generation of rational mutants, and kinetic characterisation were performed by Dr Charlotte Miton in the laboratory of Dr Nobuhiko Tokuriki. Data were analysed by the author, Dr Miton, and the primary investigators. This manuscript was written primarily by the author, with input from Dr Miton and the primary investigators.

Parallel enzyme evolution reveals distinct molecular mechanisms of adaptation despite nearly identical ancestral states.

Charlotte M. Miton[1], Eleanor C. Campbell[2], Colin J. Jackson[2], Nobuhiko Tokuriki[1]

[1] *Michael Smith Laboratories, University of British Columbia, Vancouver, BC V6T 1Z4, Canada.*

[2] *Research School of Chemistry, Australian National University, Canberra, Australia.*

ABSTRACT

Laboratory directed evolution is a powerful technique that allows the rapid improvement of biocatalysts and can also provide valuable insights into the mechanisms by which highly efficient catalysts evolve in nature. Numerous factors complicate our working knowledge (and thus exploitation) of molecular evolution, and a long-standing question in evolutionary biology asks whether adaptation relies on stochastic events due to historical contingency, or if it follows a deterministic path imposed by specific molecular or environmental constraints. The observation of convergent evolution has led to suggestions that relatives placed under the same selection pressure will converge upon a similar genotypic and phenotypic solution. This implies that two identical phenotypes under the same selective pressure should follow identical paths to the same fitness peak, but how closely related should orthologous proteins be to trigger a repeated evolutionary outcome? Is a single amino acid polymorphism enough to impair repeatability and predictability along evolutionary trajectories? To explore these questions, we 'replayed' the evolution of a bacterial phosphotriesterase that had been previously evolved toward the hydrolysis of an arylester substrate[1]. Starting from an immediate, nearly neutral neighbour, which only differs at the genotype level by a single amino acid mutation (Ser254 instead of Arg254), and is phenotypically similar, they repeated the laboratory evolution under identical experimental conditions. Comparing this trajectory with the previously described PTE to AE trajectory has revealed that the initial constraint (a point mutation) has resulted in the evolutionary trajectory following a new pathway to reach a distinct fitness peak, featuring a different substrate binding mode and vastly altered loop dynamics. This analysis highlights the unpredictability of evolution; replaying an evolutionary process from a genotypic 'neighbour' starting point results in a novel method of adaptation, supporting the hypothesis that adaptive evolution relies on historical contingency.

INTRODUCTION

Stephen Jay Gould famously stated that rewinding the 'tape of life' and letting it play out again would result in a vastly different population of organisms to those we observe today[2]. His assertion was based on the rationale that adaptive evolution is unpredictable, governed by stochastic mutational events and further randomised by environmental factors like mass extinctions and drastic shifts in climate. This idea has been the topic of much debate, with opponents of Gould insisting that adaptive evolution will always converge upon particular solutions to selective pressures[3]. As with many key questions in science, the truth is likely to lie somewhere in the middle[4,5].

The exact nature of the repeatability of evolutionary pathways has substantial implications for biochemists who strive to understand and design the next generation of enzyme catalysts. Will laboratory directed evolution campaigns that start from the same or similar phenotypes always result in the same endpoint? Is the pathway between two known phenotypes generally repeatable, and if it is, can we exploit the mechanisms of evolution to find shortcuts to more efficient catalysts? The existence of convergent evolution suggests that there are a finite number of ideal evolutionary solutions, and that the process of natural selection hones in on these solutions. Convergent evolution is frequently observed in organisms, e.g. the parallel evolution of the focusing eye[6], the 'undulating' pattern of locomotion in birds and sharks[7], and even the evolution of problem-solving skills and 'intelligence' in distantly related species, like apes and crows[8]. Morphological traits in organisms, however, are typically under the control of many genes, meaning that convergence on a particular phenotype can occur via numerous pathways, although 'hotspot' genes for variation of particular traits have been identified[9,10].

The study of convergent evolution in single proteins can circumvent the confounding effects of gene epistasis that arise in the study of organisms. Convergent evolution in molecules is not uncommon; the reoccurrence of similar patterns and geometries of active site residues in enzymes that catalyse similar reactions suggests that there are also a limited number of 'best solutions' for a given reactivity[11]. The convergent evolution of reversible Fe^{3+} binding between ferric-ion-binding protein (FBP) from *Haemophilus influenzae* and prokaryotic tranferrins results in geometrically similar binding sites, and suggests that there are a limited number of ways for a protein to acquire this property[12]. Kinases with different folds have evolved to catalyse the phosphorylation of identical substrates[13,14], and the Ser-His-Asp triad has evolved in a number of distinct folds[15]. Comparison of serum paraoxonase 1 (PON1) with other

organophosphate hydrolases has identified the importance of a hydrophobic binding pocket, a feature that has been converged upon in a number of enzymes capable of hydrolysing organophosphate compounds[16].

The convergent evolution of proteins towards similar phenotypes could be interpreted as evidence of evolutionary determinism; that given enough time, two unrelated (or distantly related) proteins under the same selection pressure would come to resemble each other genetically and phenotypically. There are, however, numerous factors that complicate the evolutionary pathway between two phenotypes; there are typically few mutations that will confer the required function without catastrophically disrupting thermostability[17]; mutational bias makes some nucleotide/amino acid substitutions more likely than others, meaning that not all pathways between phenotypes are equally likely to be followed[18]; and epistasis can result in evolutionary solutions that are dependent on historical contingency, confounded by neutral drift introducing rare permissive substitutions[19,20]. These factors, particularly the existence of historical contingency, impair the predictability of adaptive evolution of orthologous proteins. Different 'starting points' are likely to impose different sets of constraints, and the question of *how different* the starting points need to be to result in unique evolutionary trajectories cannot be readily answered through the study of extant proteins.

The use of ancestral protein reconstruction and directed evolution has facilitated the exploration of 'hypothetical' evolutionary trajectories, allowing the 'tape of life' to be replayed, albeit on a small scale. The directed evolution of a phosphotriesterase from *Pseudomonas diminuta* (PTE) towards the hydrolysis of an arylester substrate resulted in the isolation of a number of evolutionary intermediates, and produced a highly efficient arylesterase (AE) in 18 rounds of selection[1]. In the work presented here, the PTE to AE tape is rewound and replayed, this time starting from a phenotypically similar starting point, varying by a single amino acid. The kinetic and structural characterisation of evolutionary intermediates along this new trajectory reveals that the replayed evolution has followed a new pathway to a distinct fitness peak, resulting in altered loop dynamics and a novel substrate binding mode. This is indicative of the strong dependence of molecular evolution on historical contingency, where a single amino acid substitution fixed at the start of the trajectory can have profound effects on the nature of the endpoint. Further, the analysis of each trajectory's tolerance to the other's substitutions highlights the strong epistasis that governs molecular evolution.

RESULTS

Similarities in the genotypic adaptation lead to a distinct phenotypic improvement between the two evolutionary trajectories. PTE-S5, previously described by Roodveldt *et al.*, served as the starting point for the original PTE to AE trajectory (henceforth referred to as the R-trajectory because of the prominent role of Arg254)[21]. PTE-S5 will be referred to as PTE^{WT} for clarity. In the R-trajectory, the first mutation to be fixed was a naturally occurring polymorphism[22], His254Arg. Previous studies of the R-trajectory have identified the role of this substitution; the flexible arginine residue can adopt a 'bent' conformation (Cβ-Cγ-Cδ-Nε dihedral angle ~ 40 - 70°), which minimises steric hindrance of 2NH binding, and provides stabilising cation-pi interactions with the naphthyl moiety of 2NH[1]. In fact, subsequent mutations in the R-trajectory were found to stabilise this productive 'bent' conformation through intramolecular hydrogen bonding and electrostatic networks[23]. Mutagenic scanning of position 254 has revealed that it is relatively tolerant to mutation, particularly in terms of the promiscuous arylesterase activity **(Supplementary Figure 1).**

In order to investigate the reproducibility of the PTE to AE evolutionary pathway, a new directed evolution experiment was devised, starting from an 'immediate neighbour'; the initial His254Arg mutation was discarded in favour of point mutation His254Ser, resulting in variant S1. S1 is phenotypically similar to PTE^{WT}, showing a 1.4-fold increase in activity with 2NH **(Figure 3.1)**. In this sense, it occupies a similar position on the 'fitness landscape' as PTE^{WT}, more so than other mutants characterised in initial scanning mutagenesis experiments **(Supplementary Figure 1).** S1 was subjected to random mutagenesis, and variants screened for activity with 2NH, resulting in the generation of what will be referred to hereafter as the S-trajectory. Mutagenic libraries were constructed through error-prone PCR and gene shuffling. Seven rounds of directed evolution resulted in the isolation of variant S8, which demonstrated a 400-fold increase in arylesterase (AE) activity relative to PTE^{WT} **(Supplementary Table 2)**. In the R-trajectory, round 8 variant R8 showed a 10,000-fold increase in AE activity, indicating that Ser254 is less productive for the evolution of AE activity in this system; the evolution of AE activity is immediately constrained by this initial, non-ideal substitution **(Figure 3.1)**.

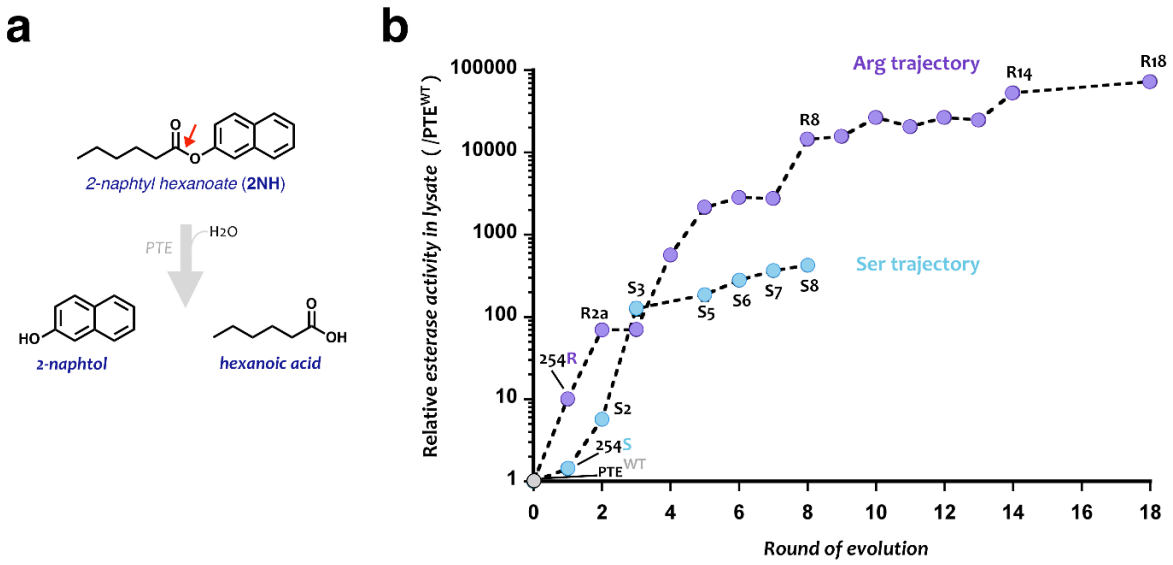

Figure 3.1 | A) Hydrolysis of arylester substrate 2NH by PTE. B) Relative AE activity in both the R-trajectory (purple) and S-trajectory (blue).

The pattern of diminishing returns is apparent in the S-trajectory, as it was in the R-trajectory. The R-trajectory showed substantial increases in AE activity for the first eight rounds of evolution before an obvious plateau; the nine final substitutions resulted in a cumulative 4.4-fold improvement[1]. In the replayed trajectory, this plateau becomes apparent after only two rounds of evolution; there is an improvement of **100-fold** between S2 and S3, representing the largest single improvement in the trajectory, but only **4-fold** increase from S3 to S8. This suggests that the evolutionary potential of S8 for enhanced AE activity may be exhausted, having reached an earlier local maximum on the fitness landscape.

Excluding the initial 254 point mutation, three of the twelve mutations in the S-trajectory occur at sites also mutated in the R-trajectory, although only one of these mutations is identical **(Table 3.1)**. Phe306Ile is accumulated in the first round of screening in the S-trajectory (S2), where Phe306Leu occurs in the fourth round in the R-trajectory (R4), and is later replaced by Ile306 in round seven (R7b). Asp233Ala is fixed in S3. Asp233Glu (R2) played a large role in the stabilisation of Arg254 in the initial trajectory. Leu271His is also acquired in S3, where Leu271Phe is fixed in later rounds of the R-trajectory (R13). The remaining nine mutations in the S-trajectory occur at positions not mutated in the R-trajectory, resulting in a genotypically distinct variant.

	Round	Variant	Mutations												2NH activity
Ser254 trajectory	**8**	**S8**	S	I	T	A	H	L	G	A	G	V	S	H	423
	7	**S7**	S	I	T	A	H	L	G	A	G	V			365
	6	**S6**	S	I	T	A	H	L	G	A	G				279
	5	**S5**	S	I	T	A	H	L	G						187
	3	**S3**	S	I	T	A	H								126
	2	**S2**	S	I	T										6
	1	**S1**	S												1.4
		PTE^{WT}	H												1
Arg254 trajectory	***1***	**R1**	R												10
	2	**R2b**	R			E									70
	4	**R4**	R	L		E									564
	7	**R7b**	R	I		E									4065
	13	**R13a**	R	I		E	F								44983
	18	**R18**	R	I		E	F								72912
			H254	**F306**	**M293**	**D233**	**L271**	**F216**	**V320**	**T234**	**E263**	**I260**	**R91**	**L240**	

Table 3.1 | The identity of mutations accumulated in the S-trajectory (top) and the relative enhancement of AE activity. The mutations acquired in the R-trajectory that shares position and identity to one in the S-trajectory is indicated in blue, while those sharing just position are indicated in purple.

To understand the nature of the constraints on this replayed trajectory, X-ray crystal structures of seven variants on the S-trajectory were obtained; S1, S2, S3, S5, S6, S7, and S8 **(Supplementary Table 1)**. Work previously reported in Campbell *et al.* links the evolution of AE activity in the R-trajectory to the alteration of conformational dynamics in key loop regions, specifically loops 4, 5 and 7[23], so these regions were selected for initial investigation in the S-trajectory variants **(Figure 3.2)**.

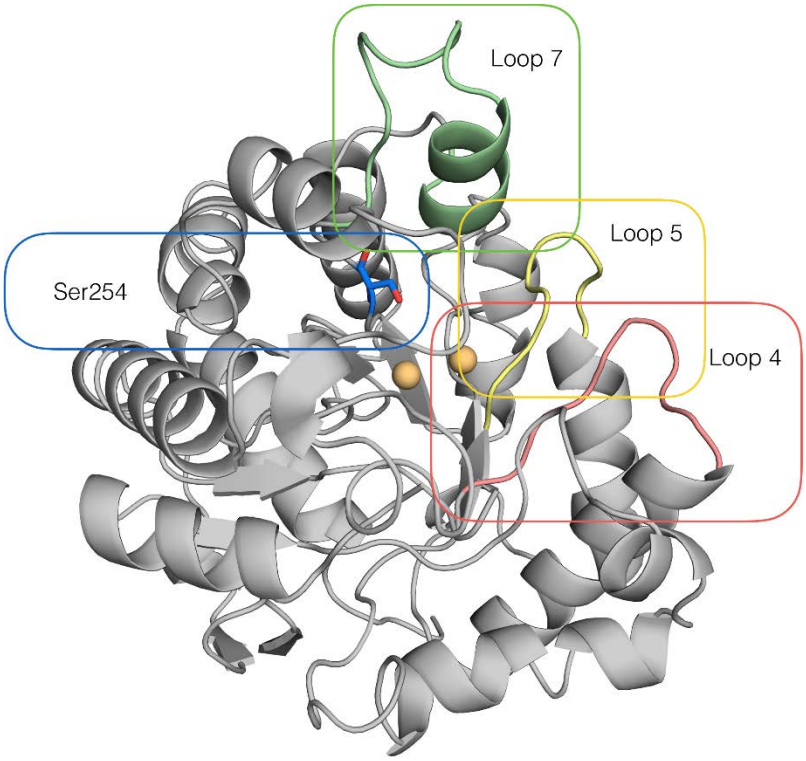

Figure 3.2 | The key regions of structural variation in the evolution of arylester activity; residue 254, and loops 4, 5, and 7.

The substitutions fixed in the R-trajectory demonstrated a radiating pattern; mutations were initially close to the active site but later round substitutions were in outer shells of the protein **(Figure 3.3)**. While the S-trajectory comprises fewer substitutions, this pattern is still observed; mutations acquired in the last round are distant from the active site. Interestingly, all the mutations/positions common to the two trajectories occurred in the first 3 rounds of selection, corresponding to the greatest increases in AE activity. This suggests that these positions are inherently important in the adaptation to this new activity, although the identities of the residues at those sites vary. The last five rounds of evolution on the S-trajectory introduce substitutions at positions unaffected in the R-trajectory.

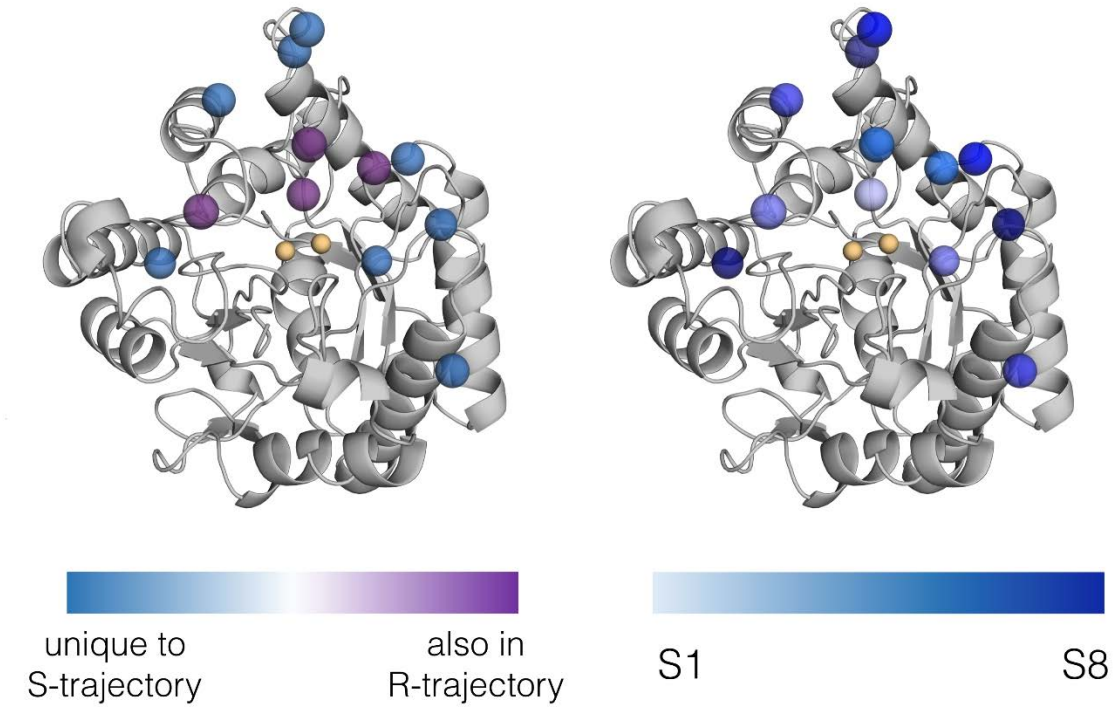

Figure 3.3 | The positions of all mutations acquired during the S-trajectory. Left: four mutations occurred at positions also mutated in the R-trajectory (purple), and the remaining eight were unique to the S-trajectory (blue). Right: the order of accumulation of mutations in the S-trajectory, illustrating that later round substitutions occurred at positions remote from the active site.

Replayed evolution leads to structurally distinct endpoints and substrate binding modes. While the endpoints of the R- and S-trajectories are distinct in terms of their arylesterase activities, they generally have similar C-α positions. With the exception of several loop regions, tertiary structure is well conserved between R18 and S8, with an RMSD of 0.54[24]. Inspection of the active sites of these two evolved variants, however, reveals several distinctions.

One feature of the R-trajectory is the stabilisation of the productive conformation of Arg254; an intricate network of hydrogen bonds not only stabilised the 'bent' conformation, but resulted in a redundancy such that the key Arg254-stabilising mutation Asp233Glu could be reverted without a substantial decrease in AE activity. In this sense, Arg254 was redundantly stabilised, particularly by later round mutations that enhanced the connectedness of the hydrogen bonding network **(Figure 3.4a)**. This is not observed in the S-trajectory. While Arg254 had a very distinct role in the binding and stabilisation of the AE substrate, the role of Ser254, if indeed it serves one, is more obscure. Serine is smaller in size and has fewer degrees of conformational freedom, so a similar pattern of conformational enrichment was not expected. Rather, it was thought that Ser254 might serve as a hub in the centre of a similar hydrogen bonding network

to that observed in the initial trajectory. Network analysis using RING 2.0 revealed that Ser254 remained isolated throughout the S-trajectory; later round mutations did not directly interact with the residue **(Figure 3.4b)**[25]. This represents a substantial difference between the endpoints of these two trajectories; the R-trajectory builds networks and redundancy into the active site of the enzyme, while the S-trajectory does not.

The difference in active site architecture between the two endpoints raised questions about the binding mode of the substrate in the S-trajectory. To investigate the effects of Ser254 and the S-trajectory on substrate binding, co-crystals of S5 with 2NH transition state analogue hexyl(naphthalen-2-yloxy)phosphinic acid (HLN) were obtained **(Supplementary Table 1)**. Screens were also set up in an attempt to co-crystallise S1 with HLN, but the resulting data showed no evidence of bound TS analogue. Co-crystallisation of S8 and HLN was also unsuccessful due to slow hydrolysis of HLN; a structure of S8 with hydrolysis product hexylphosphonic acid was obtained, but the naphthyl moiety could not be visualised. The presence of HLN in the active sites of S5 was, however, immediately apparent. Interestingly, the orientation of HLN in the S5 active site was unlike that of HLN in R18; while the alkyl chain adopted a similar conformation, the naphthyl moiety was modelled in an upright position, rotated approximately 90° relative to the orientation of HLN in R18 **(Figure 3.4c-f)**.

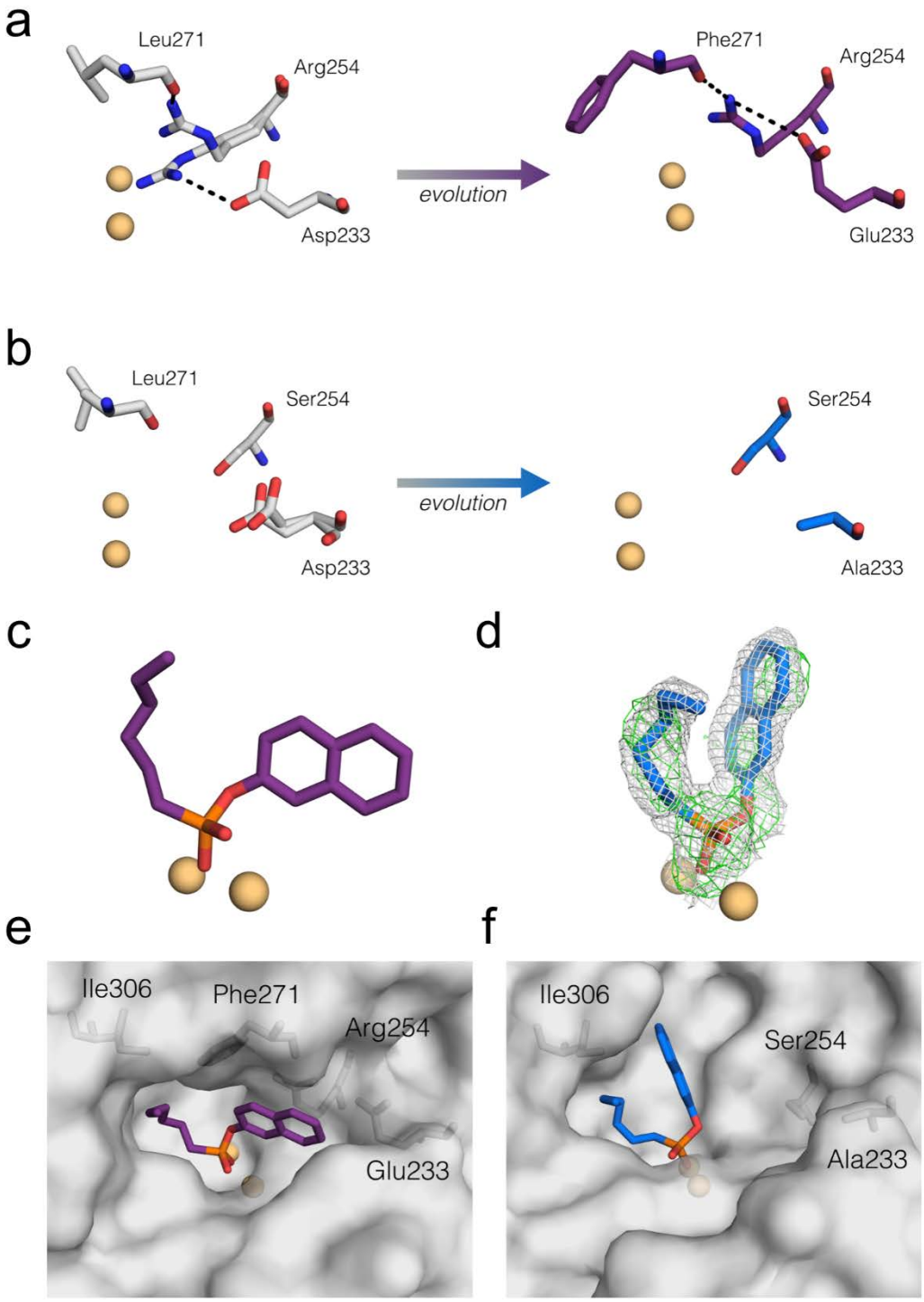

Figure 3.4 | a) The productive conformation of Arg254 is enriched over the course of the R-trajectory[1,23]. Two mutations on this trajectory interact directly with the bent conformation of arginine. b) Ser254 remains isolated throughout the S-trajectory. No mutations form direct interactions with Ser254, and the trajectory does not result in the formation of any new interactions with Ser254. Intramolecular interactions (< 4 Å) are illustrated with dotted lines. c) The orientation of HLN in R18[1]. d) Density map (grey mesh, 0.5 σ) for HLN in S5+HLN, and difference map of omitted HLN in S5+HLN (green mesh, 2.0 σ). e) The binding orientation of HLN in the R18 active site. f) The binding orientation of HLN in S5.

The substrate binding region features the only mutation acquired that was identical in both pathways; Phe306Ile **(Figure 3.4e-f)**. Given how early this mutation was acquired in the S-trajectory (S2), it would seem that the resulting expansion of the alkyl chain binding pocket is vital to the enhancement of 2NH binding affinity. Indeed, the new binding mode observed in the S-trajectory differs only in the position of the naphthyl moiety; the alkyl chain binding position is conserved between the two trajectories.

There are a number of key differences in the binding site of S5 relative to R18 that are potentially responsible the altered binding mode; the absence of Arg254 eliminates the favourable cation-pi interactions that stabilised the 'straight' conformation of the bound substrate in the R-trajectory, and the lack of some key reshaping residues present in the R-trajectory (Leu271Phe, and mutations on loops 4 and 5 that reposition loop 5 to better contact the substrate) results in an active site less well-suited to the arylester substrate. Also significant is the loss of loop 7's closed conformation; in the R-trajectory, Phe271 (R13) sterically prevents the 'upright' conformation of HLN observed in S5 **(Figure 3.4e)**. The absence of this closed loop conformation (discussed below) opens the active site up, allowing for the unusual 'upright' binding mode **(Figure 3.4f)**.

The roles of key loops vary between the two evolutionary trajectories. Previous analysis of the R-trajectory revealed several changes in loop positions and dynamics throughout the evolution of arylesterase activity[23]. B-factor analysis of S-trajectory variants **(Figure 3.5a)** revealed a number of distinctions from those patterns observed in the R-trajectory. During the R-trajectory, the position of loop 5 was observed to change; the tip of loop 5 drew closer to the active site, resulting in a reshaped binding cavity appropriate for the AE substrate. Additionally, the disorder/flexibility of loop 5 increased throughout the trajectory, suggesting it possessed the capacity to adopt multiple conformations. The alteration in position of loop 5 was hypothesised to be involved in the increased specificity for AE substrate, as major changes in loop position correlated with the reduction of PTE activity, rather than the enhancement of AE activity.

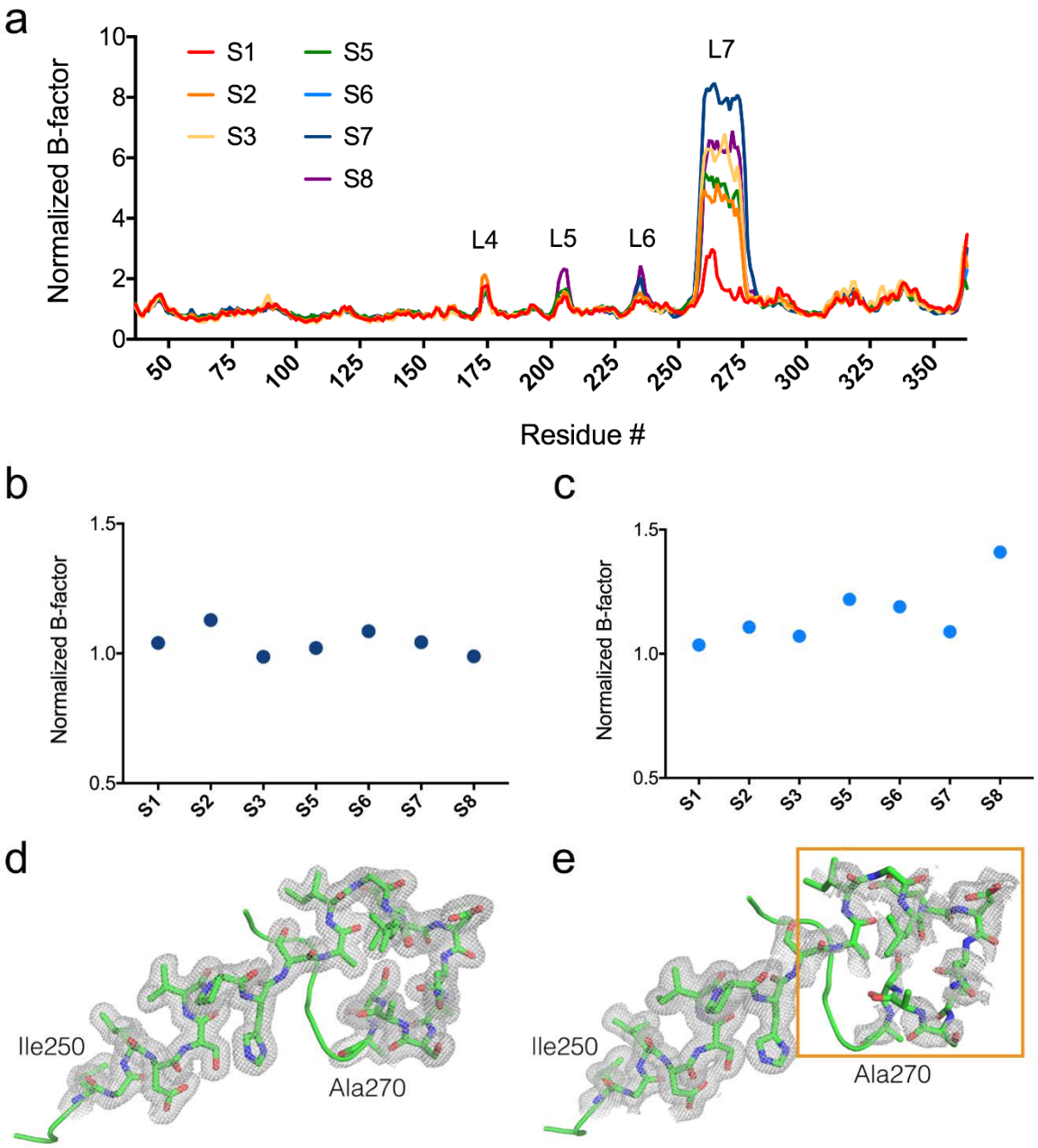

Figure 3.5 | a) Averaged normalised C-α B-factors of S-trajectory variants. b) Averaged normalised B-factors of loop 4 and c) loop 5 throughout the S-trajectory. d) Electron density of loop 7 in S2 and e) loop 7 in S3. Disorder between Ser258 and Ala270 (orange box) in S3 was too great to facilitate accurate loop building (the S2 position of loop 7 is shown for clarity). Maps shown at 0.5σ.

Loop 5 undergoes some positional changes during the S-trajectory, although S8 possesses a different final conformation to R18. Loop 5 can, in fact, be modelled into two distinct

conformations in S8, with the lower occupancy conformation more closely resembling the final position of loop 5 in R18 **(Figure 3.6)**.

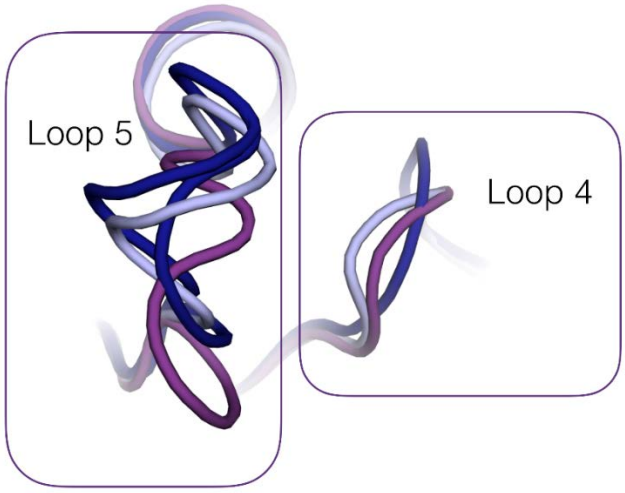

Figure 3.6 | Loops 4 and 5 as modelled in S1 (pale blue), S8 (dark blue) and R18 (purple). Loop 6 omitted for clarity.

Loop 4 also undergoes some change in position; the position of loop 4 in S1 resembles loop 4 in R18, but adopts a distinct conformation in S8. Analysis of the C-α B-factors of these two key loops provides some insight into the changes in loop disorder over the S-trajectory. Unlike the R-trajectory, loop 5 does not gain any notable degree of conformational flexibility between S1 and S8 **(Figure 3.5c)**. Loop 4, which also gains flexibility in the R-trajectory, does not undergo significant change in B-factor throughout the S-trajectory **(Figure 3.5b)**.

As reported previously, loop 7 undergoes a substantial level of stabilisation over the course of the R-trajectory; contacts between Arg254 and the backbone carbonyl of Phe271 link the active site to this key loop region[23]. The loss of mobility of loop 7 throughout the R-trajectory was attributed to the 'freezing out' of unproductive conformational freedom. While loop 7 adopts open and closed conformations associated with the diffusion and hydrolysis of the PTE substrate[26], the open conformation is no longer required for AE diffusion and thus the motions associated with this are diminished to ensure stability of the productive conformation of Arg254[23]. In contrast, loop 7 undergoes major destabilisation over the course of the S-trajectory **(Figure 3.5a)**. Normalised C-α B-factors of loop 7 indicate a large increase in disorder/flexibility from S1 to S2, and from S3 onwards, the disorder of loop 7 is such that it could not be modelled with any confidence **(Figure 3.5d-e)**.

The increase in disorder of loop 7 occurs upon the introduction of two substitutions; Asp233Ala and Leu271His, both of which are positions mutated in the R-trajectory (Asp233Glu and Leu271Phe), and were involved in the intramolecular networks that *stabilised* loop 7 in that original experiment. Asp233Ala eliminates the potential for an intramolecular network linking loop 7 to the active site, (previously facilitated through Arg254), and the mutation of hydrophobic Leu271 to a charged residue may be responsible for the reduced occupancy of the closed loop 7 conformation; position 271 is located at the base of loop 7 and in the R-trajectory, forms contacts with the hydrophobic naphthyl moiety of the arylester substrate. The introduction of histidine at this position changes the polarity of the binding cavity. It is hypothesised that the Leu271His substitution is therefore not involved in substrate binding, and is partly responsible for the increased disorder of loop 7.

Deletion of loop 7 has distinct effects in each trajectory. The disorder/positional variability of loop 7 in S3 onwards suggests that it no longer plays a direct role in the binding of the AE substrate. To investigate this, several loop-deletion variants were constructed; S1ΔL7, S2ΔL7 and S5ΔL7 (from the S-trajectory), R1ΔL7, R2aΔL7, R8ΔL7, R14ΔL7 and R18ΔL7 (from the R-trajectory), and PTE^{WT}ΔL7. The loop 7 deletion in R-trajectory variants was increasingly deleterious to AE activity along the evolutionary pathway **(Figure 3.7a)**. Given the established role of a stabilised loop 7 in the later round R-trajectory variants, this trend was expected. The loop deletion has little effect on AE activity in PTE^{WT}ΔL7, but given that this variant has not been evolved for enhanced AE activity, its tolerance to this deletion is unsurprising **(Figure 3.7a)**. In S1ΔL7 and S2ΔL7, the deletion of loop 7 is deleterious for AE activity, but is neutral in S5ΔL7 **(Figure 3.7a)**. This supports the hypothesis that loop 7 has become irrelevant to the catalytic activity of later round S-trajectory variants, as its removal has no deleterious effects

X-ray crystal structures of three of these loop-deletion variants (S5ΔL7, R18ΔL7, and PTE^{WT}ΔL7) were obtained in order to investigate the structural effects of the deletion of loop 7 **(Supplementary Table 1)**. The truncated loop region was successfully modelled in S5ΔL7 **(Figure 3.7b)** and one subunit of PTE^{WT}ΔL7. R18ΔL7 did not crystallise in the same unit cell dimensions as the other PTE variants; the length of the unit cell was doubled, with four monomers modelled into the asymmetric unit. The truncated loop could only be modelled in two of the four subunits. This highlights the importance of loop 7 as a crystal packing contact; its deletion altered the unit cell despite the use of identical crystallisation conditions to the original R18 structure.

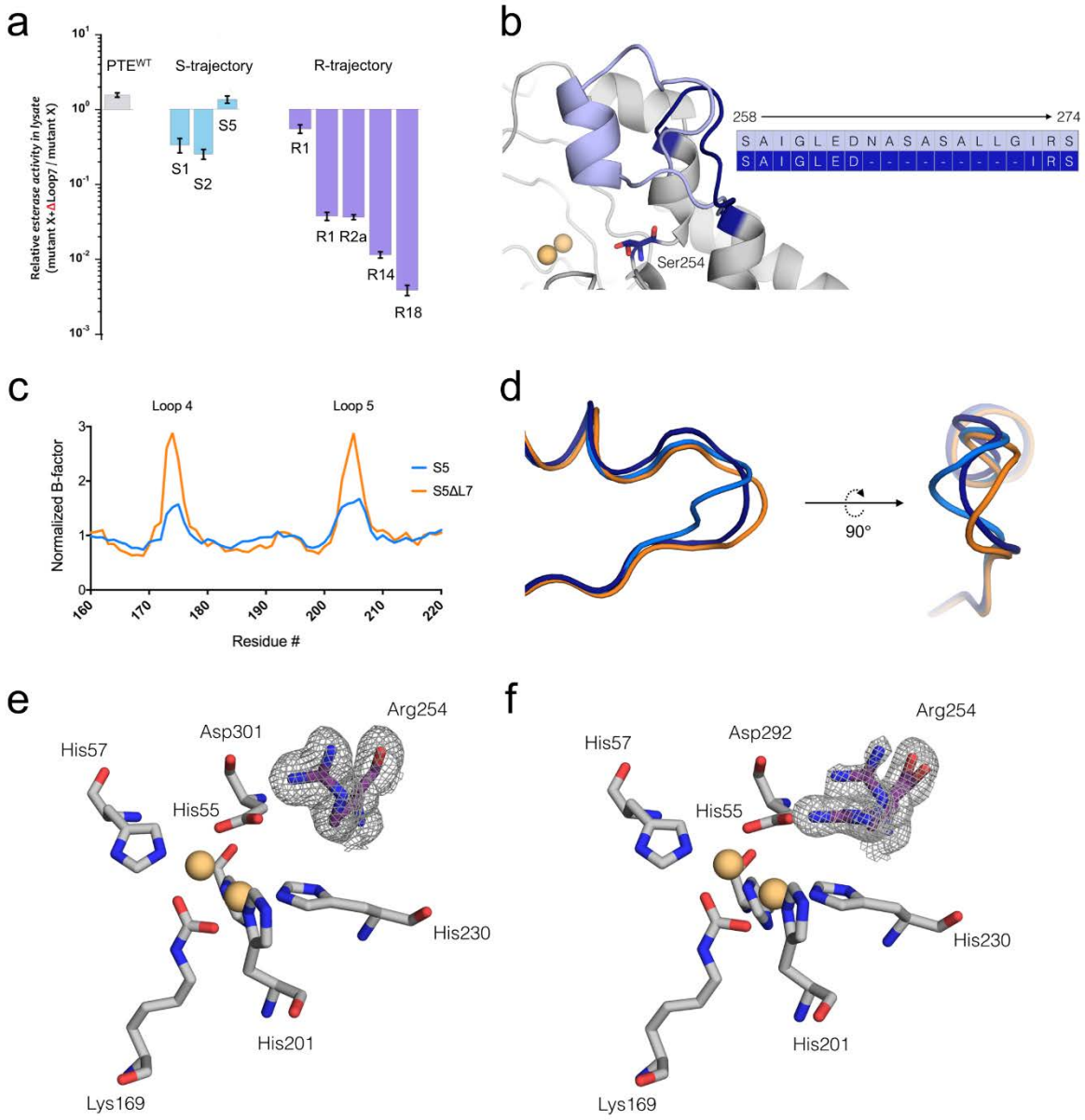

Figure 3.7 | a) Relative AE activity of loop deletion variants, indicating little change to PTE^{WT}ΔL7 and S5ΔL7, but significant loss of activity upon deletion of loop 7 in the R-trajectory. b) Loop 7 in S1 (pale blue), and truncated loop 7 in S5ΔL7 (dark blue). The deleted loop region comprises residues 265 – 271. c) Normalised B-factors of loops 4 and 5 in S5 (blue) and S5ΔL7 (orange), showing the increase in disorder of loops 4 and 5 upon deletion of loop 7. d) The position of loop 5 in S5 (light blue), S5deltaL7 (orange), and the lower-occupancy position of loop 5 in S8 (dark blue). The midpoint of loop 5 (Ser205) is displaced approximately 2.6 Å upon deletion of loop 7 in S5. e) The single, bent conformation of Arg254 in R18 and f) the partially occupied straight conformation of Arg254 in R18ΔL7. Active site residues are illustrated as grey sticks, and Zn^{2+} ions are modelled as pale orange spheres. Map shown at 0.5σ. No difference density was visible for Arg254 in e) or f).

The deletion of loop 7 in S5ΔL7 exerts some effects on the conformational flexibility of other regions of the protein. B-factor analysis of S5 and S5ΔL7 shows an increase in the disorder of loops 4 and 5 upon deletion of loop 7 **(Figure 3.7c)**. In addition to this increase in disorder, the

position of loop 5 shifts substantially in S5ΔL7 relative to S5. Comparing this loop in S5, S5ΔL7, and S8 reveals that the deletion of loop 7 appears to facilitate loop 5 adopting a conformation more similar to the lower-occupancy position of the loop in S8, the end point of the trajectory **(Figure 3.7d)**. This suggests that the high disorder of loop 7 throughout the S-trajectory may be important for repositioning loop 5. Deletion of loop 7 from PTE^{WT} appears to have no effect on the positions of loops 4 and 5 (**Figure 3.8)**.

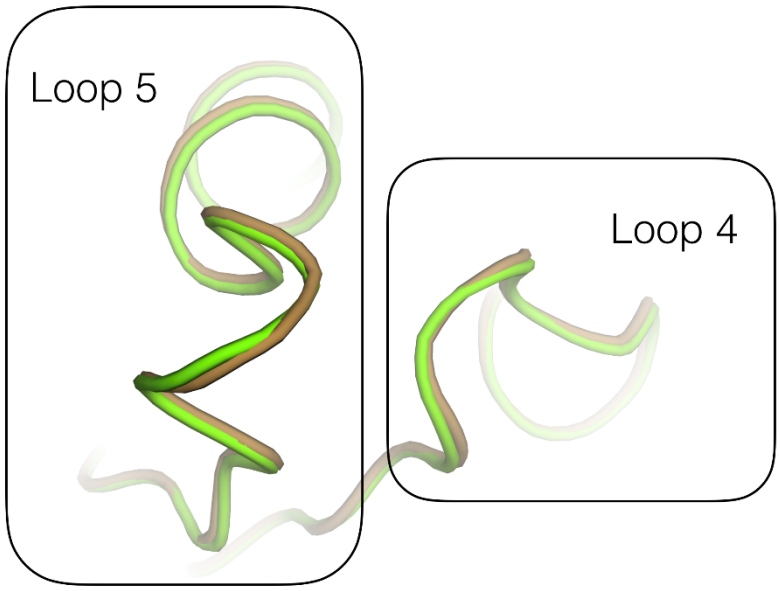

Figure 3.8 | Loops 4 and 5 in PTE^{WT} (brown) and PTE^{WT}ΔL7 (green). The truncation of loop 7 has not affected the positions of loops 4 and 5.

Previous structures of R18 feature a single, bent conformation of Arg254 in both subunits, but the deletion of loop 7 has resulted in substantial occupancy of the straight conformation, which is non-ideal for AE activity, as it sterically prohibits the binding of the AE substrate **(Figure 3.7e-f)**. Given the degree of connectedness between loop 7 and the bent conformation of Arg254 at the conclusion of the R-trajectory, the disruption to the bent conformation is logical. Importantly, S5's tolerance to the loop deletion indicates that the hydrogen bonding network that developed in the R-trajectory to link the active site with loop 7 is not present in this trajectory; a stark phenotypic difference.

Swapping key substitutions between trajectories reveals different degrees of mutational tolerance in each pathway. Site directed mutagenesis revealed that swapping mutations fixed in the S-trajectory into the R-trajectory background is not tolerated: the Arg254Ser substitution

on the R18 background causes a 300-fold decrease in arylesterase hydrolysis. However, the swap (Ser254Arg) is virtually neutral on the S5 background (<10-fold) **(Figure 3.9a)**.

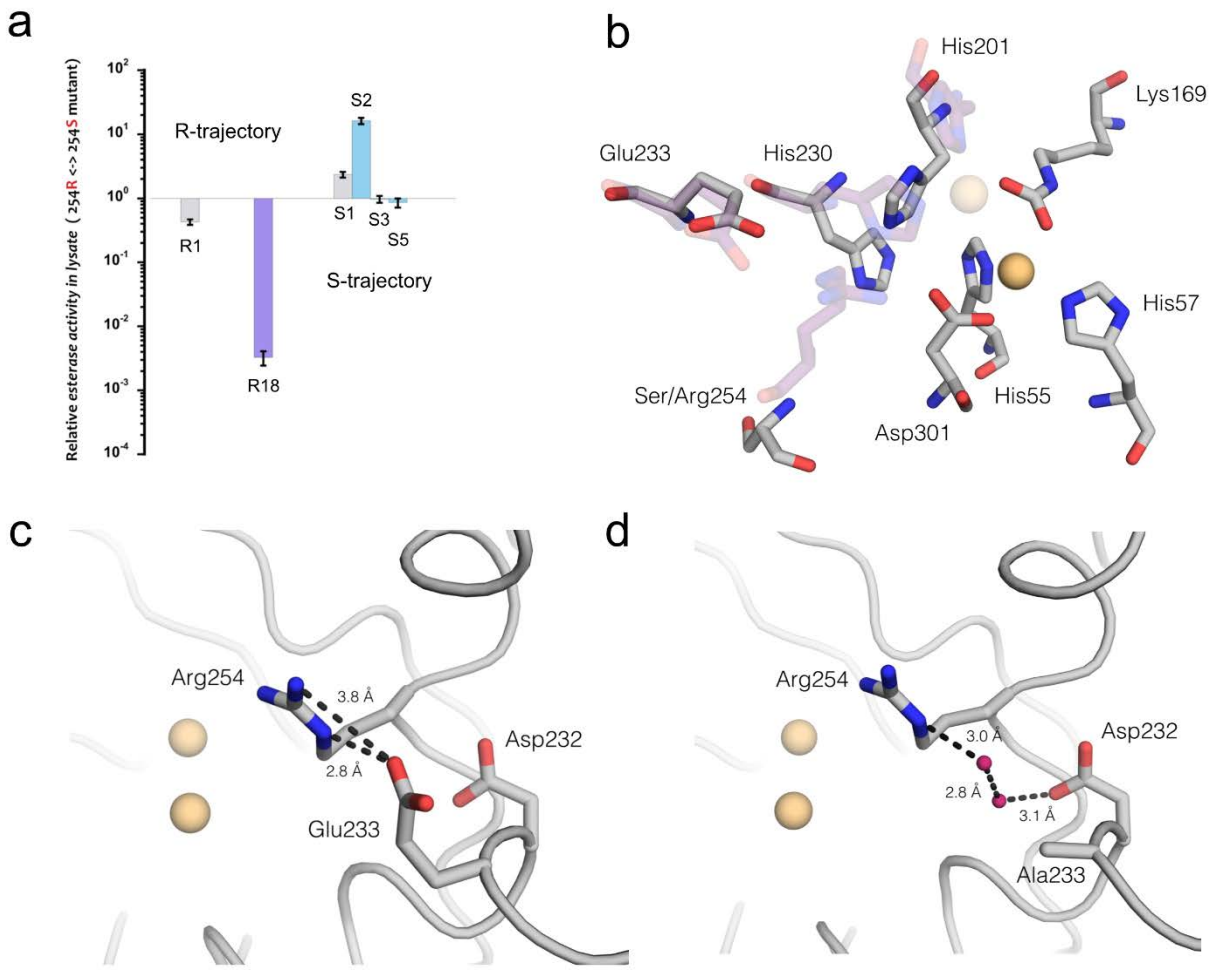

Figure 3.9 | a) The effects of swapping Arg/Ser254 on relative arylesterase activity. b) The active site residues of R18+254S (grey sticks). Positions of His201, His230, Glu233, and Arg254 in R18 are shown as transparent purple sticks. His201 and His230 undergo substantial displacement upon introduction of Ser254 into the R18 background. Zn^{2+} ions are represented as pale orange spheres. Zn^{2+} - β (transparent) is present in low occupancy in subunit A of R18+254S. Positions of Lys169, His55, His57, and Asp301 are unaffected by the Arg254Ser substitution. c) Stabilisation of the bent conformation of Arg254 in R18 through interaction with Glu233. Loop 7 omitted for clarity. d) A solvent network in S5+254R has replaced the stabilising effects of Glu233, utilising Asp232; a position unaffected in either trajectory.

Structures of epistatic variants R18+254S and S5+254R were solved to identify structural reasons for this genetic incompatibility **(Supplementary Table 1)**. Reflecting the tolerance for the Ser254Arg substitution on the S5 background, the typical structure of the active site is conserved in S5+254R. Interestingly, in both subunits of S5+254R, the productive 'bent'

conformation of Arg254 is favoured, despite the continued lack of well-defined electron density for loop 7, and the absence of stabilising interactions from residue 233 **(Figure 3.9)**.

Inspection of S5+254R active site revealed a network of water molecules that may be acting to stabilise the bent conformation of Arg254 **(Figure 3.9d)**. These water molecules are not present in R18, as they occupy the region filled by Glu233. In the S-trajectory, however, the presence of Ala233 leaves a substantial cavity that is occupied by solvent. The presence of solvent in this cavity creates a network between the bent conformation of Arg254 and Asp232. The mutation Ser254Arg is beneficial to arylesterase activity in S2, but neutral in S3. This corresponds to the creation of the cavity that houses the solvent network: Asp233Ala is introduced in S3. Asp232 is located on loop 6, and does not undergo mutation in either the R- or S-trajectory. The mutation Thr234Ala, however, is fixed in S6, and a second mutation on loop 6 is fixed in S8 (Leu240His). Excluding Asp233Glu, no further positions on loop 6 were mutated in the R-trajectory.

The deleterious effects of the Arg254Ser substitution in R18+254S are substantial and far-reaching. Most notably, the introduction of Ser254 on this background results in the introduction of significant disorder to the active site, specifically affecting the active site residues responsible for the coordination of the catalytic Zn^{2+} ions **(Figure 3.14)**. Typically, Zn^{2+} - α is coordinated by His55, His57, Asp301, and carbamylated Lys169. Zn^{2+} - β is coordinated by Lys169, His201, His230, and a bridging water molecule, adopting a tetrahedral geometry. The incorporation of Ser254 has disrupted the architecture of the active site, resulting in His201 adopting a highly unusual ‘flipped’ conformation in subunit A (the more solvent exposed subunit). His230 is also displaced by approximately 3.4 Å. As a result, Zn^{2+} - β is present at low occupancy (~ 40%) in this subunit, despite the excess Zn^{2+}included in purification and crystallisation buffers. The significant reduction in metal binding affinity caused by the displacement of His201 and His230 may be a primary cause of the lowered activity of the R18+254S variant.

DISCUSSION

The complexities of molecular evolution are numerous and are difficult to unpick from one another. The prevalence of non-additive, epistatic effects in evolutionary trajectories has not yet been conclusively quantified, despite the significant degree to which these effects shape evolutionary landscapes. The challenges associated with predicting epistatic effects complicate rational engineering approaches, and the ruggedness of the evolutionary landscape could possibly explain the limited success of some directed evolution campaigns. The 'variation and selection' model of directed evolution suffers from the same problem faced in many optimisation protocols: becoming trapped at a local maximum. While epistasis is often viewed as a factor that 'constrains' the pathways that lead to fitness peaks, it is also responsible for allowing new optimisation possibilities. Permissive mutations that enhance thermostability can facilitate the acquisition of otherwise catastrophically destabilising substitutions in instances of non-specific epistasis. The effects of specific epistasis on evolving systems are, however, more challenging to identify.

In this work, we endeavoured to investigate a 'new pathway', opened by the incorporation of a new, albeit non-ideal, initial substitution. While the starting-point variant S1 was an immediate neighbour of the R-trajectory starting point, the results of the directed evolution experiment were distinct; the final variant (S8) displayed genotypic and phenotypic distinction from the final variant of the R-trajectory (R18). In terms of the final sequences, only one substitution was identical in both trajectories (Phe306Ile), and, excluding the initial Ser254 substitution, only two further sites of substitution were common to both trajectories.

Not only do R18 and S8 differ with respect to their sequences, they have also reached distinct phenotypes. Networks of stabilising intramolecular interactions resulted in loop 7 becoming increasingly rigid throughout the R-trajectory; particularly, the network linking loop 7 to the productive, bent conformation of Arg254 was optimised and stabilised. No such network forms in the S-trajectory; loop 7 becomes increasingly disordered, and the tolerance to deletion of the loop from later round S-variants indicates that this increased disorder correlates with a lack of loop function. The drastically different fate of loop 7 throughout these two trajectories, both aimed at optimising the same function, highlights the phenotypic distinctions between the two final variants, who were initially separated by only one substitution. Additionally, the different active site architecture of the S-trajectory has stabilised a new binding mode of the arylester substrate, indicating that the evolution of arylesterase activity along this pathway is making use

of different mechanisms to those observed in the R-trajectory. Future work should be undertaken towards determining whether this new binding pose is catalytically productive, particularly given that K_M of S8 with the arylester substrate is approximately 10-fold higher than in R18 **(Supplementary Table 2)**. Co-crystallisation of S8 with HLN resulted in the imaging of the hydrolysis product in the enzyme active site, indicating that in its crystalline form, S8 still possesses some catalytic activity. Mix-and-Inject serial crystallography could be used to confirm and quantify this activity, as well as provide information about the nature of the new HLN binding pose[27]. The reintroduction of Arg254 into the S-trajectory confers less benefit as the trajectory continues. This suggests that the S-trajectory is not simply a less effective 'walk' down the same adaptive path as the R-trajectory, but is moving towards a truly distinct fitness peak. This, in addition to the differences in catalytic efficiency between S8 and R18, is indicative of two separate fitness peaks on the PTE → AE evolutionary landscape, isolated from each other by a single initial substitution.

Rational mutagenesis reveals that this isolation is, however, one-way. The incorporation of Ser254 into the R18 background is highly deleterious, indicating that transition from the R-trajectory phenotype to the S- would be highly improbable. This is logical; the intramolecular networks in R18 are far-reaching, highly interconnected, and centre upon the initial (and persistent) Arg254 substitution. Replacing this key residue with serine destabilises the R18 network and renders the redundancy built into the system null, as those redundancies are built around Arg254. This is an example of 'entrenchment', where reversion to the WT identity at a particular position becomes increasingly deleterious along an evolutionary trajectory[20]. Conversely, incorporating Arg254 into the S5 background is relatively neutral. Analysis of intramolecular interactions in S8 reveal few interactions with Ser254, and suggest that a network like that observed in the R-trajectory, is not contingent to the evolution of AE activity in the S-trajectory. As a result, the Ser254Arg substitution is tolerated well in the S-background. Additionally, while Ser254His in the S5 background is deleterious, it is 3 orders of magnitude less so than the Arg254His substitution in the R18 background. Is entrenchment, therefore, a hallmark of an effective evolutionary trajectory towards a highly efficient endpoint?

While the incorporation of Arg254 on the S5 background is tolerated, it does not result in the sudden reacquisition of R-trajectory-like catalytic efficiency, further demonstrating the importance of second- and third-shell mutations in the original trajectory. What this Ser254Arg substitution could represent, however, is a potential one-way 'bridge' from the S-trajectory

fitness peak to some position on the R-trajectory pathway. Could the Ser254Arg substitution allow the evolving system to return to a trajectory more similar to the original R-trajectory experiment? This warrants further investigation.

CONCLUSIONS

The work presented in this paper goes some way to addressing the roles of epistasis, historical contingency, and mutational entrenchment in the evolution of new function. The evolution of a highly efficient arylesterase, R18, from a phosphotriesterase starting point, R0, was contingent on the acquisition of the His254Arg substitution at the start of the trajectory. Evolving the system from a similar phenotypic starting point has resulted in the isolation of an endpoint representing a distinct fitness peak: S8 is structurally and functionally different to R18. The role of loop 7 in the optimisation of arylesterase activity is vastly different in the two trajectories; in R18, loop 7 is rigid and is involved in long-range intramolecular networks that stabilise conformations productive for the hydrolysis of the arylester substrate, whereas loop 7 in the S-trajectory becomes highly disordered, and can be deleted with no ill effect on arylester activity. A new binding mode has been identified in the S-trajectory, partly in response to the loss of the rigid, closed conformation of loop 7. These observations suggest that molecular evolution is highly contingent on historical events.

REFERENCES

1. Tokuriki, N. *et al.* Diminishing returns and tradeoffs constrain the laboratory optimization of an enzyme. *Nat. Commun.* **3,** 1257 (2012).
2. Gould, S. J. *Wonderful life: The Burgess Shale and nature of history*. (W.W. Norton & Co., 1989).
3. Conway Morris, S. *Life's Solution: Inevitable Humans in a Lonely Universe*. (Cambridge University Press, 2003).
4. Orgogozo, V. Replaying the tape of life in the twenty-first century. *Interface Focus* **5,** 20150057 (2015).
5. Lobkovsky, A. E. & Koonin, E. V. Replaying the tape of life: quantification of the predictability of evolution. *Front. Genet.* **3,** 1–8 (2012).
6. Fernald, R. D. Casting a genetic light on the evolution of eyes. *Science* **313,** 1914–1918 (2006).
7. Gleiss, A. C. *et al.* Convergent evolution in locomotory patterns of flying and swimming animals. *Nat. Commun.* **2,** 352 (2011).
8. Emery, N. J. The Mentality of Crows: Convergent evolution of intelligence in corvids and apes. *Science (80-.).* **306,** 1903–1907 (2004).
9. Hoekstra, H. E., Hirschmass, R. J., Bundey, R. A., Insel, P. A. & Crossland, J. P. A single amino acid mutation contributes to the adaptive beach mouse colour pattern. *Science* **2006,** 101–104
10. Gompel, N. & Prud'homme, B. The causes of repeated genetic evolution. *Dev. Biol.* **332,** 36–47 (2009).
11. Gherardini, P. F., Wass, M. N., Helmer-Citterich, M. & Sternberg, M. J. E. Convergent evolution of enzyme active sites is not a rare phenomenon. *J. Mol. Biol.* **372,** 817–845 (2007).
12. Bruns, C. M. *et al.* Structure of Haemophilus influenzae Fe(+3)-binding protein reveals convergent evolution within a superfamily. *Nat. Struct. Biol.* **4,** 919–924 (1997).
13. Cheek, S., Zhang, H. & Grishin, N. V. Sequence and structure classification of kinases. *J. Mol. Biol.* **320,** 855–881 (2002).
14. Bork, P. & Sander, C. Convergent evolution of similar enzymatic function on different protein folds: the hexokinase, ribokinase and galactokinase families of sugar kinases. *Protein Sci.* **2,** 31–40 (1993).
15. Wright, C. S., Alden, R. A. & Kraut, J. Structure of Subtilisin BPN′ at 2.5 Å Resolution. *Nature* **221,** 235–242 (1969).
16. Blaha-Nelson, D., Krüger, D. M., Szeler, K., Ben-David, M. & Kamerlin, S. C. L. Active site hydrophobicity and the convergent evolution of paraoxonase activity in structurally divergent enzymes: The case of Serum paraoxonase 1. *J. Am. Chem. Soc.* **139,** 1155–1167 (2017).
17. Tokuriki, N., Stricher, F., Schymkowitz, J., Serrano, L. & Tawfik, D. S. The stability

effects of protein mutations appear to be universally distributed. *J. Mol. Biol.* **369,** 1318–1332 (2007).

18. Storz, J. F. Causes of molecular convergence and parallelism in protein evolution. *Nat. Rev. Genet.* **17,** 239–250 (2016).

19. Harms, M. J. & Thornton, J. W. Historical contingency and its biophysical basis in glucocorticoid repector evolution. *Nature* **512,** 203–207 (2014).

20. Shah, P., McCandlish, D. M. & Plotkin, J. B. Historical contingency and entrenchment in protein evolution under purifying selection. *Proc. Natl. Acad. Sci.* E3226–E3235 (2015). doi:10.1073/pnas.1412933112

21. Roodveldt, C. & Tawfik, D. S. Directed evolution of phosphotriesterase from Pseudomonas diminuta for heterologous expression in Escherichia coli results in stabilization of the metal-free state. *Protein Eng. Des. Sel.* **18,** 51–58 (2005).

22. Jackson, C. J. *et al.* In Crystallo Capture of a Michaelis Complex and Product-binding Modes of a Bacterial Phosphotriesterase. *J. Mol. Biol.* **375,** 1189–1196 (2008).

23. Campbell, E. *et al.* The role of protein dynamics in the evolution of new enzyme function. *Nat. Chem. Biol.* **12,** 1–13 (2016).

24. Ye, Y. & Godzik, A. FATCAT: A web server for flexible structure comparison and structure similarity searching. *Nucleic Acids Res.* **32,** 582–585 (2004).

25. Piovesan, D., Minervini, G. & Tosatto, S. C. E. The RING 2.0 web server for high quality residue interaction networks. *Nucleic Acids Res.* **44,** W367–W374 (2016).

26. Jackson, C. J. *et al.* Conformational sampling, catalysis, and evolution of the bacterial phosphotriesterase. *Proc. Natl. Acad. Sci.* **106,** 21631–21636 (2009).

27. Olmos, J. *et al.* Authentic Enzyme Intermediates Captured “on-the-fly” by Mix-and-Inject Serial Crystallography. *bioRxiv* 1–40 (2017). doi:doi: https://doi.org/10.1101/202432

28. Tawfik, D. S., Green, B. S., Zemel, R. R., Eshhar, Z. & Arad-Yellin, R. Simple method for selecting catalytic monoclonal antibodies that exhibit turnover and specificity. *Biochemistry* **29,** 9916–9921 (1990).

29. Kaltenbach, M., Jackson, C. J., Campbell, E. C., Hollfelder, F. & Tokuriki, N. Reverse evolution leads to genotypic incompatibility despite functional and active site convergence. *Elife* **4,** 1–20 (2015).

30. Engler, C., Kandzia, R. & Marillonnet, S. A one pot, one step, precision cloning method with high throughput capability. *PLoS One* **3,** (2008).

31. Zhao, H., Giver, L., Shao, Z., Affhoter, J. A. & Arnold, F. H. Molecular evolution by staggered extension process (StEP) in vitro recombination. *Nat. Biotechnol.* **16,** 258–261 (1998).

32. Kabsch, W. XDS. *Acta Crystallogr. Sect. D Biol. Crystallogr.* **D66,** 125–132 (2010).

33. Evans, P. R. & Murshudov, G. N. How good are my data and what is the resolution? *Acta Crystallogr. Sect. D Biol. Crystallogr.* **69,** 1204–1214 (2013).

34. Karplus, P. A. & Diederichs, K. Linking crystallographic model and data quality.

Science (80-.). **336,** 1030–1034 (2012).

35. Vagin, A. & Teplyakov, A. MOLREP: An automated program for molecular replacement. *J. Appl. Crystallogr.* **30,** 1022–1025 (1997).

36. Emsley, P., Lohkamp, B., Scott, W. G. & Cowtan, K. Features and development of Coot. *Acta Crystallogr. Sect. D Biol. Crystallogr.* **66,** 486–501 (2010).

37. Keedy, D. A., Fraser, J. S. & Bedem, H. Van Den. Conformations in X-ray crystallography using qFit. *PLoS Comput. Biol.* 1–22 (2015). doi:10.1371/journal.pcbi.1004507

38. Shannon, P. *et al.* Cytoscape: a software environment for integrated models of biomolecular interaction networks. *Genome Res.* 2498–2504 (2003). doi:10.1101/gr.1239303.metabolite

MATERIALS

2NH was a kind gift from the Tawfik Lab[1], but was also purchased from Sigma. Fast Red TR hemi(zinc chloride) salt (Fast Red) was purchased from Sigma. The transition state analogue of 2NH, hexylphosphonate 2-naphthyl ester (HLN), was synthesised based on previously published procedures[1,28].

METHODS

Cloning. The gene encoding PTE-WT is identical to the one used in previous studies[1,23,29]. Note that PTE-WT had previously been evolved for improved expression levels in *E. coli*[21] and thus contains seven amino acid mutations relative to the naturally occurring PTE (I106L, F132L, K185R, D208G, R319S, A176V, V341I). All PTE serine variants were cloned with flanking NcoI/XhoI sites into a kanamycin resistant pET-27-Strep vector for evolution and purification. These constructs differ from the arginine series of variants (Ampicillin, NcoI/HindIII) to avoid cross-contamination with the original trajectory. PCR products and vectors were digested with FastDigest restriction enzymes (Fermentas) for 1-2 h at 37 °C and subsequently purified from a 1% agarose gel using MicroElute DNA Clean-Up Kit (OMEGA). Ligations were performed at a vector:insert mass ratio of 3:1 using T4 DNA ligase (Fermentas) at 16 °C overnight. Prior to transformation, reactions were purified using the MicroElute DNA Clean-Up Kit (OMEGA). Transformation into electrocompetent *E. cloni* 10G (Lucigen) reliably yielded >20,000 colonies with 100 ng of DNA per ligation. Acyl phosphatase (ACP) cloned into the same pET-27-Strep vector served as a negative control for 2NH activity measurements. All constructs were confirmed by DNA sequencing.

Single point mutations. Mutants were constructed using either the QuikChange Site-Directed Mutagenesis Kit (Agilent), or Type II restriction cloning (adapted from Golden Gate cloning[30]). Briefly, the Type II restriction cloning approach involved re-cloning PTE variants into a pET-27-ΔLguI_Strep vector (which does not contain an LguI site), followed by whole plasmid amplification using primers containing Type II restriction sites (typically LguI), as well as the desired mutation. The amplified linear DNA was purified using MicroElute DNA Clean-Up Kit (OMEGA), and treated with DpnI and LguI (FastDigest, Fermentas) for 2-3 h at 37 °C. DNA was then purified with the MicroElute DNA Clean-Up Kit (OMEGA), and <50ng of this was incubated overnight at 16 °C to allow for self-ligation. The ligated product was transformed into *E. coli* cells, as described above. All mutations were confirmed by DNA sequencing.

Library creation.

Error-prone PCR (epPCR) – PTE libraries were generated via random mutagenesis by error-prone PCR (epPCR) using the 'wobble' base analogues dPTP and 8-oxo-dGTP (TriLink), with slight alterations from previously reported protocols[1]. The first of two PCR reactions was performed over 20 cycles (2 min at 95 °C; 20 × [20 s at 98 °C, 15 s at 58 °C, 45 s at 72 °C]; 2 min at 72 °C). The 50 µL reaction contained 1 ng plasmid template, 0.3 µM primers, 0.75 µM dPTP or 60 µM 8-oxo-dGTP, 0.25 mM each of the four standard dNTPs, 2.5 mM $MgCl_2$, and 1× of the supplied buffer (TriLink). The PCR products were then purified with the MicroElute DNA Clean-Up Kit (OMEGA), treated with DpnI for 2 h at 37 °C to digest the template plasmid, purified by gel electrophoresis, and the yield was quantified with a Nanodrop (Thermo Scientific). DNA products from each error-prone PCR reaction were then combined in equimolar quantities, and 10 ng of this mixture was used as a template for the second PCR reaction. The second PCR used the same protocol as above, except that nested primers (which flank the gene), and regular dNTPs, were used. The mutated inserts obtained were then digested and cloned into pET-27-Strep, as described above. This method consistently resulted in the creation of libraries that carried an average of 1.5 amino-acid mutations per gene, calculated from 10 randomly selected clones after transformation into *E. cloni*.

Shuffling mutagenesis – At rounds 3 and 5, staggered extension protocol (StEP) PCR[31] was used to recombine positive variants isolated from epPCR libraries. A 100 µL reaction with 500 ng DNA template, which consisted of equimolar amounts of DNA from each variant of interest, was shuffled in the PCR reaction. The first PCR conditions are identical to the second epPCR, except that 0.1-1 nM primers were used and the PCR cycle profile was as follows: 100 cycles (5 min at 95 °C; 100 × [30 s at 95 °C, 5 s at 58 °C]). PCR products were digested with DpnI, purified with the MicroElute DNA Clean-Up Kit (OMEGA), and then 1.5 µL of this was used as a template for a second PCR: 20 cycles (2 min at 95 °C; 20 × [20 s at 98 °C, 15 s at 58 °C, 45 s at 72 °C]; 2 min at 72 °C) using the EconoTaq Plus protocol (Lucigen). The PCR products were then digested, purified by gel electrophoresis, and cloned into pET-27-Strep as described above.

Creation of saturation libraries. Libraries of variants of PTE-WT, PTE-R18, and PTE-S8 containing all 20 amino acids at positions 254, 233, 271, and 306 were independently created with primers containing randomised DNA sequences at these positions, following the Type II restriction cloning method described above.

Esterase assays on agar plates. Plasmids were extracted from *E. coli* cells using a QIAprep Spin Miniprep Kit (Qiagen), and then re-transformed into *E. coli* BL21 (DE3) containing pGro7 plasmid for overexpression of the GroEL/ES chaperone system. The gene that encodes acyl phosphatase (ACP) was cloned into the pET-27-Strep, which served as a negative control. Transformation reactions were plated on an average of 10 large agar plates (140 mm diameter) containing 50 μg/mL kanamycin and 34 μg/mL chloramphenicol such that each plate contained ~1000 colonies, leading to a final screening capacity of ~10,000 clones. Colonies were blotted onto nitrocellulose membranes (BioTrace NT 0.2 μm, PALL Corp), and transferred facing up onto a second LB agar plate additionally containing 1 mM IPTG, 200 μM $ZnCl_2$ (to ensure availability of Zn^{2+} ions necessary for enzymatic activity) and 0.2% (w/v) arabinose for chaperone overexpression. The original agar plate was placed at 37 °C for colonies to re-grow, while the membrane-containing plate was left overnight at room temperature. The next day, membranes were placed into an empty petri dish and cells were lysed by three freeze/thaw cycles at -20 °C and 37 °C. For the activity assay, 25 mL of 0.5% agarose was dissolved in 50 mM Tris-HCl buffer pH 7.5, 100mM NaCl, 200 μM $ZnCl_2$, 200 μM 2NH, and 1 mM Fast Red, which was then poured onto the nitrocellulose membranes. A red colour developed within 10 - 60 minutes. Positive clones were then picked from the original agar plate.

Esterase assay in cell lysate.

Directed evolution screening – Active clones identified by colony screening were re-grown overnight at 30 °C in 4-6 96-well deep well plates containing 200 μL LB supplemented with 50 μg/mL kanamycin, and 34 μg/mL chloramphenicol for pGro7 selection. This led to a focused library of ~360-560 pre-selected variants. Subsequently, 25 μL aliquots of overnight cultures were transferred to deep well plates containing 425 μL LB per well with kanamycin, chloramphenicol, 200 μM $ZnCl_2$ and 0.2% (w/v) of arabinose (final concentrations) for chaperone co-expression. Cells were grown for ~2 h at 37 °C until the OD_{600} reached ~0.6. Expression of PTE variants was induced with 1mM IPTG, and cultures were incubated for an additional 2 h at 30 °C. Cells were spun down at 4 °C at maximum speed (3320 g) for 10 minutes and the supernatant was drained. Pellets were frozen for a minimum of 1 h at -80 °C, and were subsequently lysed by addition of 200 μL of 50 mM Tris-HCl buffer, 100mM NaCl, pH 7.5 supplemented with 0.1% (w/v) Triton-X100, 200 μM $ZnCl_2$, 100 μg/mL lysozyme and ~ 1 μL of benzonase (Novagen, 25 U/μL) per 100 mL of lysis buffer. After 30 min of lysis, cell debris were spun down at 4 °C at 3320 g for 30 min. Depending on the activity level of the

library, the clarified lysate was diluted prior to the activity assay to obtain a good signal in the initial linear phase of the reaction. Reactions were performed in transparent 96-well plates (Corning Costar) containing 200 µL per well (20 µL lysate + 180 µL of substrate (200 µM of 2NH + 1mM of Fast Red)) previously dissolved in the same lysis buffer. 2NH hydrolysis was monitored at 500 nm *via* complex formation with Fast Red. The gene that encodes acyl phosphatase (ACP) was cloned into pET-27-Strep, and served as a negative control for 2NH activity measurements. Improvements ≥1.3-fold relative to the previous round were considered significant. The best clones were picked, re-grown and re-assayed in triplicate. The initial rates were normalised to cell density (determined by OD_{600}) and the average values were determined. Around 10 improved variants were sequenced after each round.

PTE mutant assays – Single-point mutants of PTE were assayed as described above, except that the overnight cultures were inoculated directly from glycerol stocks of cells in triplicates in 2-3 independent experiments. Saturation mutagenesis libraries were first plated on agar plates where ~85 colonies were randomly picked for overnight cultures, prior to lysate screening as described above.

Protein purification.

Strep-tag purification – To determine their kinetic parameters, selected PTE variants at each round of the directed evolution were purified using Strep-Tactin Superflow High capacity columns (IBA, CV=2.5 mL) according to the manufacturer's instructions (IBA BioTAGnology, Germany). Briefly, pET-Strep-PTE plasmids were transformed into *E. coli* BL21 (DE3) (without pGro7 chaperone expression for higher purity) and a single colony was used to grow a 2 mL LB culture overnight at 37 °C. Cells were inoculated into Overnight Express Instant TB medium (Novagen) containing 1% (v/v) glycerol, 50 µg/mL kanamycin, 200 µM $ZnCl_2$ and Strep-tagged proteins were expressed at 250 rpm shaking for 8 h at 30 °C, followed by 12 h at 16 °C. Cells were harvested by centrifugation and pellets were frozen overnight at -80 °C. Pellets were resuspended with 20 mL Lysis buffer containing a 1:1 mixture of B-PER Protein Extraction Reagent (Thermo Scientific): 50 mM Tris-HCl buffer, 100 mM NaCl, pH 7.5 supplemented with 200 µM $ZnCl_2$, 100 µg/mL lysozyme and ~0.5 µL of benzonase. After a 1 h incubation on ice, cell debris was removed by centrifugation and the clarified lysate was passed through a 45 µm filter before loading onto a Strep-Tactin column. Strep-PTE variants were eluted with elution buffer (50 mM Tris-HCl, 100 mM NaCl, pH 7.5, 200 µM $ZnCl_2$, 2.5 mM desthiobiotin) according to the manufacturer's instructions (IBA).

Fractions containing pure PTE (determined by SDS-PAGE and 2NH activity measurement) were subsequently pooled, loaded onto an Econo-Pac 10DG desalting column (Bio-Rad), and eluted with the same elution buffer without desthiobiotin. When needed, PTE variants were concentrated to 0.5 - 2 mg/mL using a 10 kDa MWCO spin concentrator (Microsep Advance centrifugal device, PALL Corp), their concentrations were measured in triplicate using the Pierce BCA Protein assay kit (Thermo Scientific) and they were stored at 4 °C.

Purification of untagged variants for protein crystallisation – PTE variants were cloned into pET32-trx plasmid (ampicillin resistant) without Strep-tag using FastDigest NcoI and HindIII as described in the cloning section, transformed into *E. coli* BL21 (DE3), and grown for 72 h at 30 °C in TB medium containing 100 μg/mL ampicillin and 500 μM $ZnCl_2$. Cells were harvested by centrifugation at 3320×g and 4 °C for 10 min, resuspended in 20 mM Tris-HCl, pH 8 containing 100 μM $ZnCl_2$ and lysed by sonication (OMNI Sonic Ruptor 400, Thermo Scientific, 50% pulse, 50% amplitude). Cell debris were removed by centrifugation at 30,000×g and 4 °C for 60 min and the lysate was filtered through a 45 μm filter (Millipore). The lysate was loaded onto a Fractogel DEAE anion exchange column (Merck). PTE elutes in the flowthrough as well as in the early wash fractions. Fractions deemed to be >95% pure were pooled. Protein was concentrated to 12 mg/mL and stored at 4 °C.

Enzyme kinetics. Initial velocities (v_0) were determined in duplicate, at 16 different substrate concentrations (0–2 mM) in 50 mM Tris-HCl, 100 mM NaCl, pH 7.5, 200 μM $ZnCl_2$ and 0.1% Triton X-100, at 25 °C. Hydrolysis rates were monitored using a microplate reader (Synergy H1, Biotek) by following product formation at 500 nm for 2NH (in the presence of FAST- Red, at a ratio of 1:5). Steady-state kinetic parameters were derived by fitting the experimental data to the Michaelis-Menten equation: $v_0/[E] = k_{cat} \bullet [S]/(K_M + [S])$, where v_0 is the initial rate, [E] is the enzyme concentration, and [S] is the substrate concentration. In some cases, we observed substrate inhibition, or could not reach full saturation, in which case we used a linear fit: $v_0/[E] = (k_{cat}/K_M) \bullet [S]$ or a substrate inhibition fit: $v_0/[E] = k_{cat} \bullet [S]/(K_M + [S] \bullet (1 + [S]/K_i))$, where K_i represents the inhibition constant. The data were corrected for the buffer-catalysed background reaction measured under the same conditions without enzyme.

Crystallisation of PTE variants. Purified tag-less PTE variants were concentrated to 12 mg/mL in 20 mM HEPES, 50 mM NaCl, 100 μM $ZnCl_2$, pH 8. Crystals were grown at 4 °C in EasyXtal-15-Well Tools plates (Qiagen), using hanging-drop vapour diffusion. Drops consisting of 2 μL of reservoir solution and 1 μL of PTE were equilibrated over 500 μL of

reservoir solution. Reservoir solutions contained 100 mM sodium cacodylate (pH 6.3 - 6.7), distilled deionised water and 10 - 50% (w/v) 2-methyl-2,4-pentanediol (MPD). Crystals formed in initial screens were manually pulverised, and used for microseeding. Six serial dilutions of the pulverised crystals were made, from 1/10 to 1/1,000,000 in factors of 10. New crystal screens were set up varying MPD concentrations from 10% to 20%. Each well contained 1 µL of protein, 1.5 µL of reservoir solution and 0.5 µL of the microseed solution. To obtain crystal structures in the same space group and crystallisation condition, serial microseeding was used. Co-crystallisation of PTE variants with the transition state analogue HLN was achieved by adding a 4 times molar excess of HLN to crystallisation wells. Diffraction-quality crystals typically formed within one week.

X-ray diffraction data collection and refinement. For data collection, crystals were soaked in cryobuffer (100 mM sodium cacodylate, pH 6.5, 40% MPD) for 2 minutes before flash-cooling to 100 K in a stream of nitrogen gas. PTE diffraction data were collected at the Australian Synchrotron (beamlines MX1 and MX2) at a wavelength of 0.9537 Å. The X-ray diffraction data were indexed and integrated using XDS[32] and merged using AIMLESS as implemented within the CCP4 program suite[33]. Data resolution cut-offs were chosen using half dataset correlation coefficients, as described by Karplus and Deiderichs[34]. The structures of PTE variants were solved by molecular replacement (MOLREP)[35] using the PTE-R0 structure (4PCP). Refinement was performed using REFMAC and phenix.refine, and manual rebuilding was performed in Coot[36]. Automated fitting of multiple conformations was carried out with the QFit web-server[37], with manual inspection and removal of conformations that were not present in good (at least 1.0 σ) electron density. Network analysis was performed using RING 2.0[25], and results were visualised with Cytoscape[38]. Cα RMSD calculations were performed using FATCAT[24]. B-factors were compared to each other by refining with a single major main-chain conformation, averaging values of all chains within each structure, and normalising the B-factor. Normalisation was achieved by scaling the average B-factor of each chain (with the exception of the loops with variable B-factors) to achieve a comparable baseline.

Supplementary Table 1: Data collection statistics

	S1	S2	S3	S5	S6
Data collection					
Space group	$P2_12_12$	$P2_12_12$	$P2_12_12$	$P2_12_12$	$P2_12_12$
Cell dimensions					
a, *b*, *c* (Å)	85.7, 85.8, 88.2	85.2, 85.5, 88.2	85.5, 85.9, 88.4	85.2, 85.7, 88.5	85.6, 85.9, 88.4,
α, β, γ (°)	90, 90, 90	90, 90, 90	90, 90, 90	90, 90, 90	90, 90, 90
Resolution (Å)	30.72 – 1.74 (1.80 – 1.74)	39.2 – 1.75 (1.81 – 1.75)	38.62 – 1.46 (1.51 – 1.46)	28.95 – 1.98 (8.98 – 1.96)	29.0 – 1.50 (1.55 – 1.50)
R_{sym} or R_{merge}	0.4675 (0.6436)	0.1081 (0.987)	0.1052 (1.845)	0.0993 (1.043)	0.07566 (0.7204)
$CC_{1/2}$	0.77 (0.875)	0.999 (0.889)	0.999 (0.575)	0.997 (0.603)	0.999 (0.952)
CC*	0.933 (0.966)	1 (0.97)	1 (0.854)	0.999 (0.867)	1 (0.988)
$I / \sigma I$	17.2 (5.6)	22.28 (3.16)	13.76 (1.18)	9.6 (1.3)	18.62 (3.50)
Completeness (%)	99.91 (99.74)	99.96 (99.98)	99.42 (97.44)	99.7 (99.9)	99.81 (99.52)
Redundancy	9.5 (9.2)	14.7 (14.8)	7.5 (7.5)	3.5 (3.5)	13.6 (13.3)
Refinement					
Resolution (Å)	30.74 – 1.74 (1.80 – 1.74)	39.2 – 1.75 (1.81 – 1.75)	38.62 – 1.46 (1.51 – 1.46)	28.95 – 1.98 (8.98 – 1.96)	29.0 – 1.50 (1.55 – 1.50)
No. reflections	642277 (60701)	963908 (95788)	855643 (84865)	46830 (4623)	1421131 (136639)
R_{work} / R_{free}	0.1660/0.1979	0.1450/0.1826	0.2139/0.2377	0.2116/0.2329	0.1514/0.1747
No. atoms					
Protein	5183	5296	4829	4800	5198
Ligand/ion	38	70	38	38	62
Water	375	487	230	144	393
B-factors					
Protein	26.47	24.80	30.17	33.63	26.32
Ligand/ion	34.14	36.20	33.02	42.06	37.06
Water	31.25	33.38	29.69	31.40	34.60
R.m.s. deviations					
Bond lengths (Å)	0.008	0.018	0.010	0.005	0.017
Bond angles (°)	1.19	1.50	1.14	0.92	1.53
PDB ID	5W6B	5WCQ	5WCW	5WIZ	5WCP

	S7	S8	S5+HLN	S5+254R	R18+254S
Data collection					
Space group	$P2_12_12$	$P2_12_12$	$P2_12_12$	$P2_12_12$	$P2_12_12$
Cell dimensions					
a, *b*, *c* (Å)	85.7, 86.1, 176.9	85.1, 85.8, 88.7	84.7, 85.0, 87.9	85.4, 85.8, 88.3	85.7, 86.0, 88.7
α, β, γ (°)	90, 90, 90	90, 90, 90	90, 90, 90	90, 90, 90	90, 90, 90
Resolution (Å)	42.83 – 1.6 (1.657 – 1.6)	39.38 – 1.46 (1.512 – 1.46)	30.56 – 1.77 (1.87 – 1.77)	29.43 – 1.65 (1.709 – 1.65)	22.18 – 1.4 (1.45 – 1.4)
R_{sym} or R_{merge}	0.06579 (0.6699)	0.06952 (1.051)	0.845 (3.337)	0.1786 (2.36)	0.02632 (0.5627)
$CC_{1/2}$	0.999 (0.964)	0.999 (0.895)	0.872 (0.152)	0.999 (0.593)	0.999 (0.652)
CC*	1 (0.991)	1 (0.972)	0.965 (0.513)	1 (0.863)	1 (0.888)
I / σI	21.83 (4.49)	19.50 (2.89)	22.97 (2.11)	14.05 (1.18)	20.04 (1.35)
Completeness (%)	99.86 (99.98)	99.75 (99.35)	97.82 (96.87)	99.87 (99.64)	99.9 (99.90)
Redundancy	13.7 (13.3)	13.5 (13.6)	16.5 (14.8)	14.6 (14.2)	14.3 (13.8)
Refinement					
Resolution (Å)	42.83 – 1.6 (1.657 – 1.6)	39.38 – 1.46 (1.512 – 1.46)	30.56 – 1.77 (1.87 – 1.77)	29.43 – 1.65 (1.709 – 1.65)	22.18 – 1.35 (1.43 – 1.35)
No. reflections	2358496 (227175)	1524437 (150805)	60646 (5905)	1149452 (110655)	2042161 (283339)
R_{work} / R_{free}	0.2699/0.2985	0.1530/0.1749	0.1957/0.2295	0.2151/0.2483	0.1670/0.1981
No. atoms					
Protein	9740	5485	5060	4933	6117
Ligand/ion	100	70	92	62	49
Water	466	410	275	206	304
B-factors					
Protein	32.35	29.01	26.77	27.80	23.88
Ligand/ion	33.55	44.98	46.31	47.69	54.74
Water	29.86	37.39	29.58	27.63	28.22
R.m.s. deviations					
Bond lengths (Å)	0.007	0.016	0.007	0.010	0.011
Bond angles (°)	0.89	1.49	0.97	1.09	1.45
PDB ID	5WMS	6AML	6B2F	5WJ0	6BH7

	S5ΔL7	R18ΔL7	PTE^{WT}ΔL7
Data collection			
Space group	$P2_12_12$	$P2_12_12$	$P2_12_12$
Cell dimensions			
a, *b*, *c* (Å)	85.1, 85.5, 88.5	85.8, 86.2, 177.7	86.1, 86.2, 88.8
α, β, γ (°)	90, 90, 90	90, 90, 90	90, 90, 90
Resolution (Å)	30.75 – 1.40 (1.45 – 1.40)	29.61 – 1.40 (1.45 – 1.40)	39.45 – 1.75 (1.81 – 1.75)
R_{sym} or R_{merge}	0.0321 (0.3897)	0.01875 (0.3268)	0.0285 (0.6971)
$CC_{1/2}$	0.999 (0.594)	1 (0.874)	0.999 (0.611)
CC*	1 (0.863)	1 (0.966)	1 (0.871)
I / σI	7.1 (0.9)	17.91 (2.21)	13.09 (0.95)
Completeness (%)	100.0 (99.9)	99.85 (99.86)	99.89 (99.92)
Redundancy	2.0 (1.9)	13.6 (13.8)	2.0 (2.0)
Refinement			
Resolution (Å)	30.75 – 1.40 (1.45 – 1.40)	29.61 – 1.40 (1.45 – 1.40)	39.45 – 1.75 (1.81 – 1.75)
No. reflections	249659 (23283)	515979 (51092)	67134 (6646)
R_{work} / R_{free}	0.1341/0.1614	0.1595/0.1797	0.1849/0.2012
No. atoms			
Protein	6096	10513	4988
Ligand/ion	78	128	30
Water	538	1029	178
B-factors			
Protein	16.08	24.09	40.24
Ligand/ion	44.56	47.06	46.66
Water	28.98	36.23	37.95
R.m.s. deviations			
Bond lengths (Å)	0.008	0.011	0.007
Bond angles (°)	1.26	1.19	0.82
PDB ID	6BHL	6BHK	5WCR

Supplementary Table 2: Kinetic data for Ser-trajectory variants

Variant	k_{cat} (s^{-1})	K_M (μM)	k_{cat}/K_M ($M^{-1}.s^{-1}$)
2-napthyl hexanoate			
PTE^{WT}	0.08 ± 0.00	179 ± 21.0	$4.19 \times 10^2 \pm 5.4 \times 10^1$
S1	0.06 ± 0.00	104 ± 16.3	$6.00 \times 10^2 \pm 1.03 \times 10^2$
S2	2.35 ± 0.85	557 ± 240	$4.21 \times 10^3 \pm 2.37 \times 10^3$
S3	3.71 ± 0.45	230 ± 45.3	$1.61 \times 10^4 \pm 3.72 \times 10^3$
S5	6.47 ± 1.07	297 ± 63.5	$2.17 \times 10^4 \pm 5.86 \times 10^3$
S6	17.55 ± 5.53	819 ± 300	$2.14 \times 10^4 \pm 1.03 \times 10^4$
S7	18.60 ± 4.01	444 ± 118	$4.19 \times 10^4 \pm 1.44 \times 10^4$
S8	19.88 ± 19.75	705 ± 745	$2.82 \times 10^4 \pm 4.09 \times 10^4$
S5+254R	12.71 ± 1.37	164 ± 34.9	$7.73 \times 10^4 \pm 1.84 \times 10^4$
R18+254S	1.69 ± 0.19	109 ± 17.8	$1.55 \times 10^4 \pm 3.05 \times 10^3$
Paraoxon ethyl			
PTE^{WT}	1270 ± 27.0	57 ± 5.00	$2.23 \times 10^7 \pm 2.01 \times 10^6$
S1	290 ± 290	35 ± 2.50	$8.33 \times 10^6 \pm 6.11 \times 10^5$
S2	69 ± 0.80	508 ± 18.76	$1.36 \times 10^5 \pm 5.26 \times 10^3$
S5	14 ± 0.34	5259 ± 194	$2.59 \times 10^3 \pm 1.15 \times 10^2$

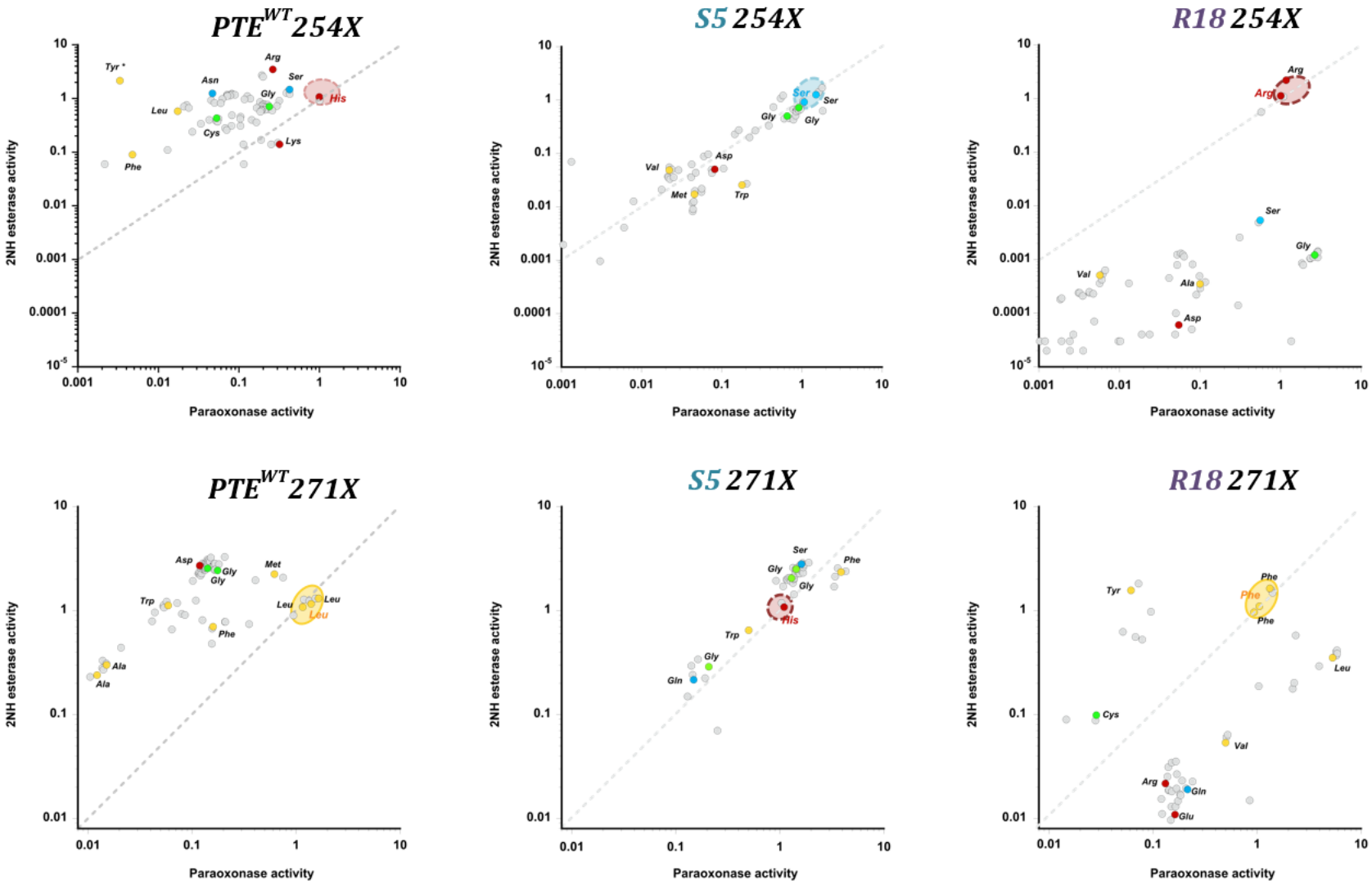
PTE^WT 254X
S5 254X
R18 254X
PTE^WT 271X
S5 271X
R18 271X
2NH esterase activity
Paraoxonase activity

Previous page: Supplementary Figure 1 | Mutational tolerance at position 254 and 271 in PTE-WT, S5 and R18 backgrounds. Libraries were built with the saturation mutagenesis method at position 254X (top) and 271X (bottom), enabling all possible 20 amino acid (AA) substitutions at these positions for variants PTE^{WT} (left), S5 (centre) and R18 (right). Library variants are shown as grey dots. A 2D scatter is obtained by plotting the evolved 2NH activity on the y-axis and the original paraoxonase activity on the x-axis for each variant. A deviation from the y = x axis (grey dotted line) indicates a change in specificity for a given clone. Clones that have been sequenced are labelled and coloured by AA type, *i.e.* yellow for hydrophobic, red for charged, blue for polar uncharged and green for special cases (Cys, Gly or Pro). Lysate activities are normalised on the original parental background (PTE^{WT}, S5, R18), which is displayed by a coloured halo.

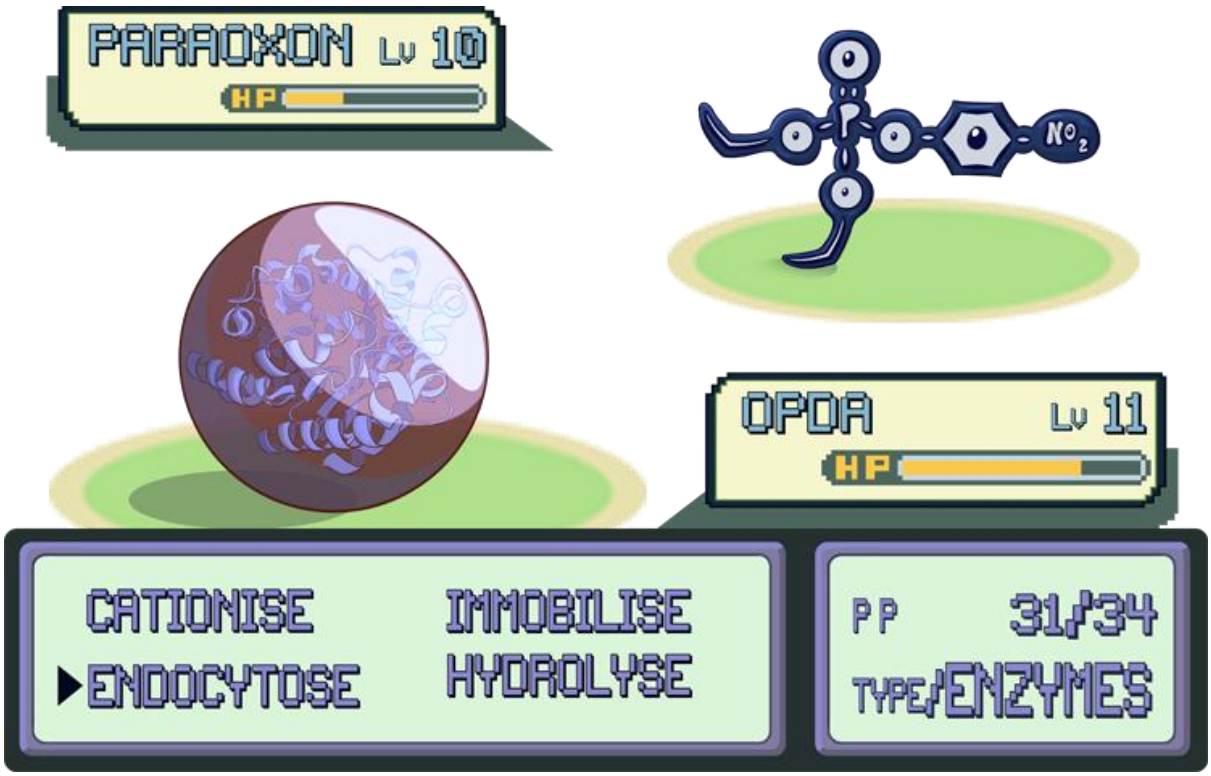

Original artwork inspired by ar*PTE/OpdA engineering, designed by Oscar Mortlock as part of Shirty Science, 2016. Image used with permission.*

CHAPTER 4:
ENGINEERING AND IMMOBILIZATION OF ORGANOPHOSPHATE HYDROLASE *ar*PTE

Declaration

The following article was peer-reviewed and published as a communication in *Advanced Biosystems*.

All experimental work except where otherwise stated was carried out by the author under the supervision of Associate Professor Colin Jackson.

The contribution of other authors are as follows: Dr Jacob Grant synthesized the substrates for continuous flow experiments and performed the HPLC analysis under the supervision of Associate Professor David Lupton. Mr. Mahakaran Sandhu performed batch analysis of the enantioselectivity of variant G60A under the supervision of the author. Ms. Yi Wang synthesised the Fmoc hydrogels and performed the TEM and FTIR characterisation of the enzyme-hydrogel constructs under the supervision of Dr David R. Nisbet and Dr Richard J. Williams. Dr Adam W. Perriman, Associate Professor Colin J. Jackson, and the author conceived the experiments. The manuscript was written by the author and the primary investigators.

Note that the page numbering in the follow article has been adjusted for publication in this thesis. The online version of this article can be found at the DOI listed below.

‘Hydrogel-immobilized supercharged proteins’

DOI: 10.1002/adbi.201700240

ADVANCED BIOSYSTEMS
www.adv-biosys.com

Hydrogel-Immobilized Supercharged Proteins

Eleanor C. Campbell, Jacob Grant, Yi Wang, Mahakaran Sandhu, Richard J. Williams, David R. Nisbet, Adam W. Perriman, David W. Lupton,* and Colin J. Jackson**

The remarkable catalytic potential of enzymes in chemical synthesis, environmental bioremediation, and medical therapeutics is limited by their longevity and stability. Immobilization of enzymes on solid supports is demonstrated to improve the stability of biocatalysts but often relies on multiple chemical steps for covalent attachment and is limited by the physical properties of the various supports. Here, production of enzyme: hydrogel complexes is described via engineering of a cationic supercharged phosphotriesterase. These enzyme: hydrogel complexes are remarkably robust displaying no loss of catalytic activity after 80 d of use and up to 10^5 turnovers when used in a flow reactor at catalyst loadings as low as 0.0008 mol%. In addition, exceptional resilience to organic solvents is observed. The use of enzyme: hydrogel complexes is likely to be of value in a diverse range of applications such as enantioselective continuous-flow chemistry, detoxification of poisons, and the formation of functionalized biomaterials.

The catalytic power and specificity of enzymes is well documented,[1] but their use in industry and medicine can be limited by several factors. For example, many industrial processes require the use of organic solvents, which can be destabilizing to otherwise effective biocatalysts,[2] while enzymes in solution have a limited lifespan due to their tendency to unfold and aggregate[3] and are often not reusable in modern applications, which increases their cost.[4] Many of these deficiencies result from enzymes having evolved to function in vivo, where conditions are generally aqueous and of moderate temperature. Additionally, since they can be readily resynthesized in vivo, enzymes generally have relatively short lifespans in solution. Although there are examples where proteins have been engineered to tolerate nonaqueous solvents and to display greater stability,[5,6] the requirement to perform engineering and optimization on each individual enzyme to achieve this means that it is only cost effective in a small number of cases. An alternative, generalizable, approach could involve extensive displacement of the solvent by a matrix that remains permeable to the substrate, thereby immobilizing and stabilizing proteins for diverse applications.

Immobilization of biocatalysts on solid supports has been achieved and is often a more desirable alternative to the application of free enzymes in solution. Immobilized enzymes can have extended lifespans,[7,8] greater stability to temperature extremes,[9,10] tolerate nonaqueous solvents,[11,12] and display enhanced reaction rates.[13] Immobilized enzymes can also be added to and removed from reaction mixtures with ease. However, enzyme immobilization has limitations. Covalent attachment, generally considered the most robust form of immobilization, requires covalent tethering of the biocatalyst to a solid support. The chemical operations in these processes can be costly, time consuming, and require additional protection steps after enzyme immobilization.[14] Additionally, covalent attachment often results in enzymes adopting unfavorable orientations on the solid media, and unless the site for attachment is rigorously tested and selected, reduced activity can result from occlusion of the active site. Covalent chemical attachment also complicates recycling of the solid support since stripping degraded enzyme from the support requires further chemical processing and priming for reapplication of new enzyme.

There are alternatives[15] to covalent tethering, including the generation of catalytically active inclusion bodies (CatIBs), and gel encapsulation. The former technique involves the immobilization of precipitated, catalytically active enzyme through

E. C. Campbell, M. Sandhu, Dr. C. J. Jackson
Research School of Chemistry
Australian National University
Canberra, ACT 2601, Australia
E-mail: colin.jackson@anu.edu.au
Dr. J. Grant, Prof. D. W. Lupton
School of Chemistry
Monash University
Clayton, VIC 3800, Australia
E-mail: david.lupton@monash.edu
Y. Wang, Dr. D. R. Nisbet
Laboratory of Advanced Biomaterials
Research School of Engineering
The Australian National University
Canberra, ACT 2601, Australia
Dr. R. J. Williams
School of Engineering
RMIT University
Melbourne 3001, Australia
Dr. A. W. Perriman
School of Cellular and Molecular Medicine
University of Bristol
Bristol BS8 1TD, UK
E-mail: chawp@bristol.ac.uk

DOI: 10.1002/adbi.201700240

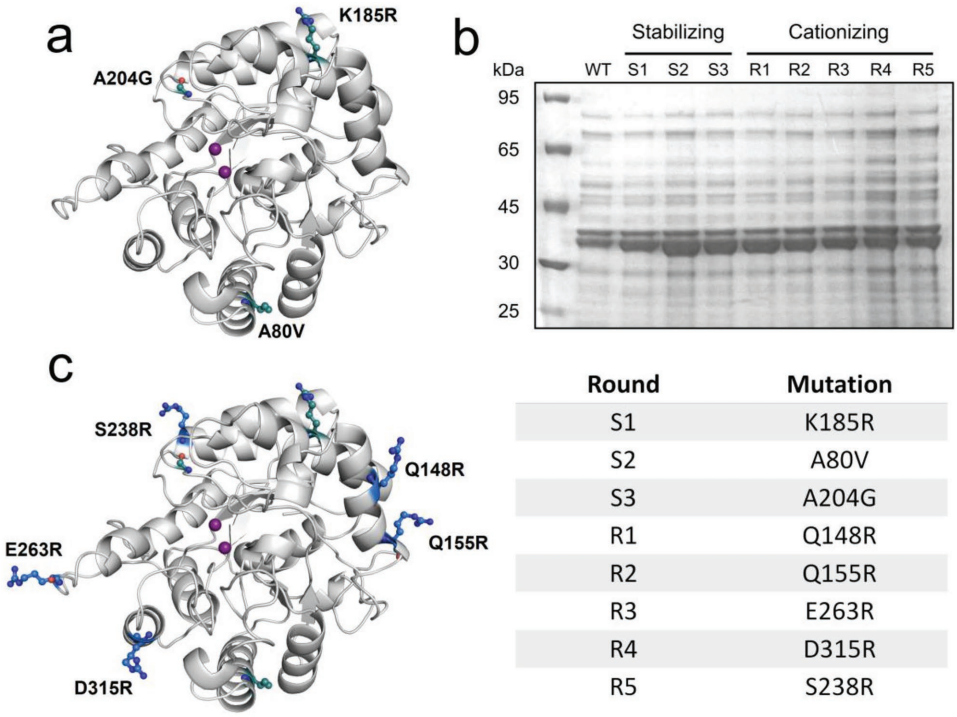

Round	Mutation
S1	K185R
S2	A80V
S3	A204G
R1	Q148R
R2	Q155R
R3	E263R
R4	D315R
R5	S238R

Figure 1. Engineering cationized *ar*PTE. a) Positions of solubilizing mutations (K185R, A80V, and A204G) highlighted on WT-*ar*PTE (2D2J).[32] Purple spheres represent Co^{2+}. b) SDS–PAGE of WT-*ar*PTE and each variant produced during the iterative engineering process. *ar*PTE is visible at ≈35 kDa. c) Positions and identities of solubilizing and final cationizing mutations highlighted on R5-*ar*PTE (5W7H).

crosslinking.[16] Recent work has shown CatIBs to be long lived and stable toward organic solvents,[17] but their effective utilization requires encapsulation in alginate or agar beads,[18,19] and while CatIBs offer interesting functional properties, their use is not widespread. Gel encapsulation involves the entrapment of a soluble enzyme in the matrix of a synthetic or natural gel. This can allow exploitation of the protective effects of the gel microenvironment, increasing enzymes' resilience to pH extremes and high temperatures.[20,21] The loss of enzymatic activity upon gelation or as a result of protein diffusing out of the matrix, however, has limited the application of such systems.[21] Protein "supercharging", in which the surface charge of a protein is drastically altered, is a proven approach to modify enzyme surface properties.[22] While supercharging has received significant attention in cell biology applications,[23–25] its application in protein purification and the generation of functionalized materials has been limited,[26] and it has not been examined in the context of hydrogel immobilization for applications in biocatalysis.

Here, we report on a genetically supercharged bacterial phosphotriesterase from *Agrobacterium radiobacter, ar*PTE, that can be immobilized on both commercially available synthetic hydrogels and biologically compatible amino acid derived hydrogels. *ar*PTE hydrolyses and detoxifies a broad range of organophosphorus compounds, including chemical warfare agents.[27,28] The increased surface charge of supercharged *ar*PTE (R5-*ar*PTE) places it in the top 0.001% of soluble proteins in *Escherichia coli* by isoelectric point and allows one-step purification and ionic immobilization on various anionic hydrogels. The resultant immobilized enzyme displays remarkable stability in the presence of organic solvents, high substrate turnover, enantioselectivity, and longevity. These properties have allowed the demonstration of applications in enantioselective synthesis, detoxification, and the formation of novel biocompatible enzyme-hydrogel constructs.

Wild-type (WT)-*ar*PTE was optimized for surface engineering through the incorporation of three point mutations previously demonstrated to increase its soluble expression: Ala60Val, Ala204Gly, and Lys185Arg[29] (**Figure 1**A). The relative thermostabilities of WT-*ar*PTE and the engineered variant (S3-*ar*PTE) were investigated through differential scanning fluorimetry (DSF)[30] (Figure S1, Supporting Information). The proteins have almost identical melting temperatures (WT = 60.7 ± 0.085 °C, S3 = 59.5 ± 0.052 °C), indicating that no major stabilizing or destabilizing effects were imparted through the incorporation of the three solubilizing mutations, consistent with previous work suggesting that the increased soluble expression was not a result of stabilization of the holoenzyme.[31]

S3-*ar*PTE was used as the basis for subsequent iterative screening of cationizing mutations. A series of target acidic amino acids was identified for mutation to positively charged amino acids (lysine or arginine), using the Rosetta supercharge protocol[22] with the structure of WT-*ar*PTE (2D2J).[32] Absolute Surface Area View (ASAView)[33] was then used to calculate the solvent accessibility of WT-*ar*PTE residues, since the more exposed residues make up a larger proportion of the protein surface. This was used to remove amino acids identified by the supercharge protocol that were too buried or within the dimer interface. Three additional polar amino acids (Ser238, Thr274, and Thr311) were added to the list of candidate mutations based on high solvent accessibility (Figure 1B). FoldX, which can accurately

predict the stabilizing effect of point mutations, was then used to determine whether arginine or lysine was the least destabilizing amino acid mutation to make at each position.[34] The effects of the mutations on expression were then tested by sodium dodecyl sulfate polyacrylamide gel electrophoresis (SDS–PAGE) (Table S1, Supporting Information). Those mutations that caused substantial loss of soluble expression were excluded, while those that did not were combined in a stepwise fashion. The final variant, R5-*ar*PTE, comprised Gln148Arg, Gln155Arg, Ser238Arg, Glu263Arg, and Asp315Arg (Figure 1C and Table S2, Supporting Information). A decrease in soluble expression was observed throughout the construction of R5-*ar*PTE. The loss of soluble expression upon incorporation of these additional positively charged residues is consistent with previous work that has suggested soluble expression of proteins correlates with a lack of positively charged surface,[35] but overexpression remained substantial (Figure 1D), confirming that the supercharging approach can allow high-yield enzyme production.

We then analyzed the effects of these mutations on stability, activity, structure, and net charge. Differential scanning fluorimetry indicated that no direct stabilizing effects were imparted by the incorporation of the cationizing mutations (R5 = 61.1 ± 0.29 °C) (Figure S1, Supporting Information). The kinetic parameters of the purified variants were characterized through assays with the substrate paraoxon-ethyl, monitoring the formation of *p*-nitrophenolate. The initial stabilizing mutations result in a decrease in activity of an order of magnitude, which can be attributed to the well-documented trade-off between enzyme stability and activity.[36] Because *ar*PTE is a highly dynamic and active enzyme, it is likely that the solubilizing mutations cause subtle changes in the conformational sampling to reduce the rate of substrate turnover; the relationship between conformational dynamism and turnover rate has been demonstrated previously.[29,37] While these initial solubilizing mutations decrease the catalytic efficiency of the enzyme approximately ninefold (which is offset by the twofold increase in soluble expression), the cationizing mutations have negligible effects on the activity, relative to S3-*ar*PTE (Table S3, Supporting Information). The overall catalytic efficiency of R5-*ar*PTE remained very high (k_{cat}/K_M = 3.77 × 10^6 M^{-1} s^{-1}). Diffraction-quality crystals of R5-*ar*PTE were obtained in 0.2 M $NaNO_3$, 10% polyethylene glycol (PEG) 3350, pH 6.1. The structure of R5-*ar*PTE was solved using molecular replacement with the structure of WT *ar*PTE (2D2J)[32] (Table S4, Supporting Information). Analysis of the R5-*ar*PTE structure revealed that the C-α positions were essentially identical to that of the WT structure, with an root-mean-square deviation (RSMD) value of 0.76 Å.[38] The only region of note was loop 7 (residues 258–272), which is already very mobile but adopted a slightly different conformation than in the WT structure. One of the cationizing mutations, Glu263Arg, is located on this loop, and may be responsible for differences in C-α position, but is unlikely to be significant, given that the activity of R5-*ar*PTE is essentially identical to S3-*ar*PTE. Using the empirical structures of WT-*ar*PTE and R5-*ar*PTE, we were able to calculate the isoelectric point (pI) of each protein using PROPKA, which has been shown to be the most accurate computational method for calculation of pK_a and pI values, with a level of error comparable to the best experimental methods.[39] The pI of R5-*ar*PTE was estimated to be 10.01, a marked increase from the WT-*ar*PTE pI of ≈6.79 (**Figure 2**).[40,41]

The Proteome-pI database indicates that of the 4314 known proteins in the *E. coli* (K12) proteome, 146 have an isoelectric point greater than 10.[43] Of these 145 proteins, only four have been experimentally determined to exist in the cytoplasm, and none in the periplasm. The remainder are either membrane-associated (60), ribosomal (23) or have not been conclusively assigned a location in the cell (or are hypothetical proteins) (59).[44] This puts R5-*ar*PTE in the top ≈0.001% of soluble proteins identified in the *E. coli* (K12) proteome based on isoelectric point. Indeed, R5-*ar*PTE could be purified from crude *E. coli* lysate in a single step over carboxymethyl (CM) Ceramic HyperD resin (Figure S2, Supporting Information).

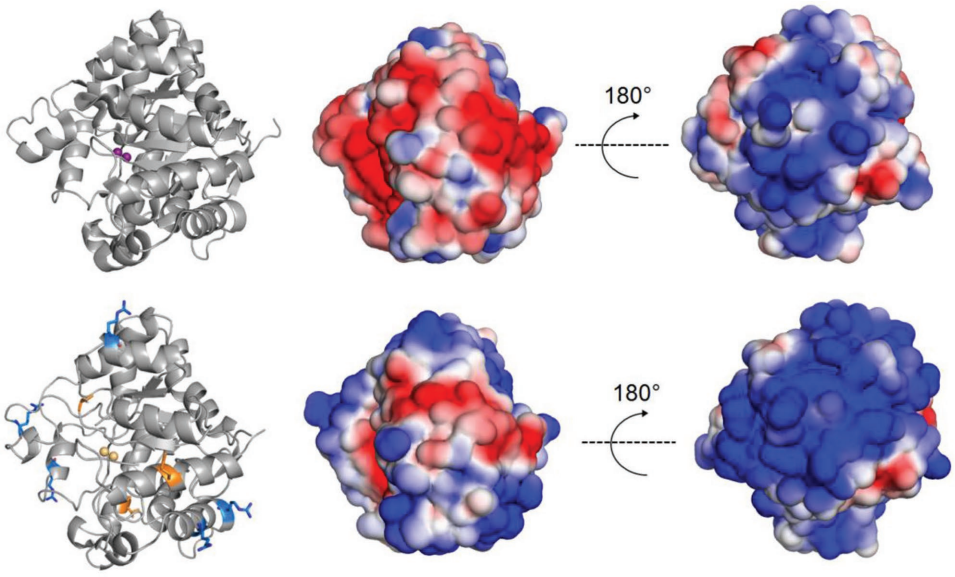

Figure 2. Monomer structures and electrostatic surface potentials of WT-*ar*PTE (2D2J)[32] (top) and R5-*ar*PTE (5W7H) (bottom) colored from −2.5 kT e^{-1} (red) to +2.5 kT e^{-1} (blue). Isoelectric points as predicted by PROPKA[42] increase from 6.79 (WT) to 10.01 (R5) as a result of surface engineering.

To test the catalytic properties of ionically immobilized R5-*ar*PTE, we used CM Ceramic HyperD resin, which is a commercially available ceramic-encapsulated hydrogel. The hydrogel consists of a hydrophilic polymer containing 250–400 CM acidic groups (μEq mL^{-1}), making it a weak cation exchanger. A 600 μL column of CM Ceramic HyperD resin has a protein binding capacity of 36 mg, although only 1 mg of purified R5-*ar*PTE was loaded as the activity of the protein is so high that loss of activity could only be determined at lower loadings. Full binding was confirmed through the absence of any enzymatic activity in the flowthrough after loading. A second identical column was packed with resin only for use as an experimental control.

To determine the longevity of R5-*ar*PTE immobilized in the hydrogel-resin, both in terms of protein "leaching" from the hydrogel and the long-term thermostability/denaturation, the substrate turnover by the immobilized enzyme was measured over the course of 85 d. Because the rate of hydrolysis of paraoxon-ethyl is very high ($k_{cat}/K_M = 4 \times 10^6$ M^{-1} s^{-1}), any loss of activity is difficult to observe, since full substrate turnover is possible with only a small amount of active enzyme. Accordingly, we used *p*-nitrophenyl butyrate, which is promiscuously turned over by *ar*PTE at ≈1/1000th the rate of paraoxon-ethyl (Table S3, Supporting Information). Hydrolysis could be monitored directly via the formation of *p*-nitrophenolate, and the concentration and flow rate were adjusted such that the initial total hydrolysis was ≈70%, meaning that any loss of activity would be in a detectable range. Hydrolysis was measured at the same flow rate, over the same column, at 2 g L^{-1} substrate loading, at 25 intervals over a period of 85 d. This resulted in exposure of the immobilized enzyme to over 2 L of buffer (≈3000 column volumes with a biocatalyst loading of 0.0005 g L^{-1}) with no evidence of reduced enzymatic activity (**Figure 3**A). On average, 67% of the loaded substrate was converted with each injection. The increase in activity observed after initial measurements was attributed to activation-period inactivation. This phenomenon has been observed in immobilization experiments a number of times.[45–47] The initial immobilization process can limit the conformational dynamism of the immobilized enzyme, increasing thermostability but decreasing catalytic activity. After being exposed to destabilizing conditions—in this instance, prolonged time spent at room temperature—conformationally limited proteins are liberated, resulting in an increase of activity, before the steady loss of activity commences.

Having demonstrated that the supercharged protein was effectively irreversibly immobilized and was extremely stable when bound to the hydrogel, with no detectable loss of activity over a period of 85 d, we then sought to estimate the level of substrate throughput that was achievable. From the long-term longevity analysis, we observe a turnover number of ≈7000 $mol_{substrate}/mol_{catalyst}$, with no loss of activity. We then set out to investigate the destruction of the neurotoxic pesticide paraoxon-ethyl. The World Health Organization's recommended maximum concentration of parathion (the precursor molecule converted to paraoxon in vivo) is only 10 μg L^{-1},[48] while European Union directives limit pesticide concentration in drinking water to 0.1 μg L^{-1}.[49] Here, we used concentrations several orders of magnitude higher than this, from 2.5 to 0.5 g L^{-1} in 10% methanol, with a small amount of catalyst immobilized on the resin (1.5 mg/600 μL resin, or 4.2×10^{-8} mol, which is ≈4% of the maximum loading capacity of the column) (**Table 1**). After several runs to determine the optimal conditions, an optimum flow rate and substrate loading of 0.5 g L^{-1} at 1 mL min^{-1} was identified. With these conditions, it was possible to hydrolyze ≈95% of 350 mg paraoxon-ethyl passed over the column over 11 h. Across the various experiments detailed in Table 1, the column achieved turnover of 1.07×10^5 $mol_{product}/mol_{catalyst}$ over the course of ≈17 h.

To investigate the potential application of the ionically immobilized supercharged proteins in chiral resolution based enantioselective catalysis, the chiral organophosphate methyl (*p*-nitrophenyl) phenyl phosphate (MPP) was synthesized as a model substrate (Methods in the Supporting Information). While R5-*ar*PTE showed no evidence of enantioselectivity with MPP (Figure 3B) previous work has shown that the related PTE from *Pseudomonas diminuta* could be engineered to confer enantioselectivity for the *S*- over the *R*-enantiomer.[50] Thus, we introduced one of the mutations previously observed to confer enantioselectivity (Gly60Ala) to R5-*ar*PTE. The reaction of G60A-R5 and MPP was monitored spectrophotometrically, with the addition of NaOH used to determine the end-point of the hydrolysis. The hydrolysis of substrate MPP by G60A-R5 was observed to plateau at 50% end-point hydrolysis, consistent with an enantioselective enzyme-catalyzed hydrolysis of primarily one enantiomer of a racemic mixture (Figure 3B). Using the previously described immobilization protocol, 1 mg of G60A-R5 was applied to a 600 μL column containing the ceramic-encapsulated hydrogel. The enantioselectivity of immobilized G60A-R5 was then investigated using high-performance liquid chromatography (HPLC) analysis with chiral stationary phases. MPP was injected at flow rates of 2–10 mL min^{-1} over the immobilized G60A-R5, and the flowthrough was analyzed by HPLC (**Table 2**). The flowthrough was determined to contain MPP with an enantiomeric excess of >99%. The reaction could be carried out on a preparative scale, producing synthetically relevant quantities of enantiomerically enriched *R*-MPP in 30 min.

The stability of the immobilized R5-*ar*PTE hydrogel in nonaqueous solvents was investigated. A column was packed and loaded with R5-*ar*PTE as described above. The destabilizing effects of methanol on enzymes are well established,[51] so this solvent was selected to test the stability of the immobilized enzyme. Increasing concentrations of methanol were passed over the R5-*ar*PTE column, and the hydrolysis of *p*-nitrophenyl butyrate at each concentration measured (Figure 3C). The activity of R5-*ar*PTE decreased consistently from 20% to 70% methanol, which is not unexpected given the catalytic mechanism is dependent on free water molecules to act as nucleophiles. However, activity could be restored by washing the column with buffer containing no methanol (Figure 3D). The loss of activity was essentially fully reversible in methanol concentrations up to 70%, and partially reversible up to 90% methanol (≈80% recovery). It was only in 100% methanol that significant irreversible loss of activity occurred (<20% recovery) (Figure 3D). The reversible loss of activity in methanol is likely to be due to the stripping of catalytic water molecules by the polar organic solvent, which are then restored by the aqueous washes.[52] Exposure to concentrations of 80% methanol and above, however, may have resulted in the stripping of structurally important water molecules, resulting in irreversible denaturing of the enzyme. The solvent resistance of

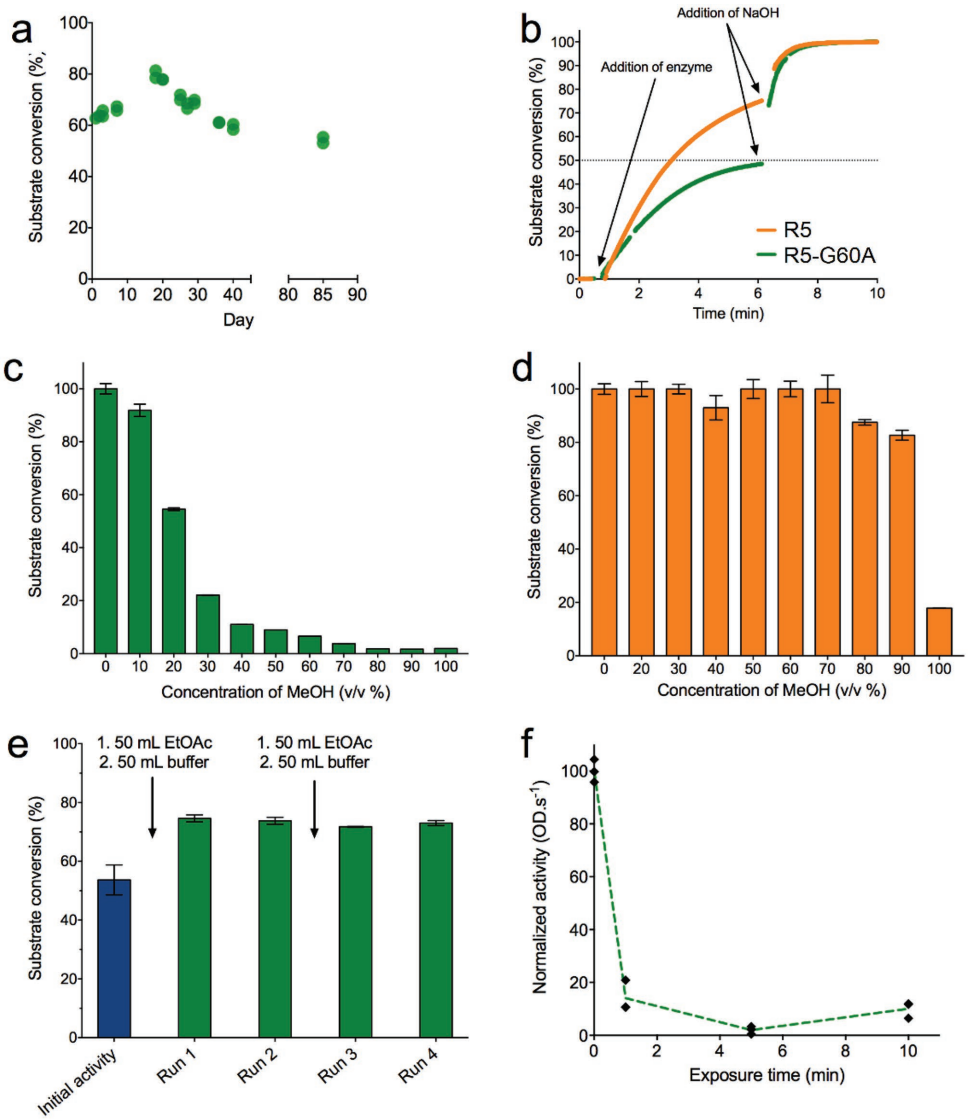

Figure 3. Properties of immobilized R5-*ar*PTE. a) The longevity of immobilized R5-*ar*PTE stored at room temperature, as measured by hydrolysis of *p*-nitrophenyl butyrate injected over the immobilized enzyme. b) Enantioselectivity of *ar*PTE variants R5 and R5-G60A. At 6 min, addition of 5 M NaOH fully hydrolyses the substrate. 50% conversion is marked with a dotted line. c) Enzymatic hydrolysis of *p*-nitrophenyl butyrate in increasing concentrations of MeOH. d) Enzymatic hydrolysis of *p*-nitrophenyl butyrate after exposure to increasing concentrations of MeOH and restoration to aqueous buffer. e) Enzymatic hydrolysis of *p*-nitrophenyl butyrate after exposure to 100% EtOAc, and subsequent restoration to aqueous buffer. f) Activity of R5-*ar*PTE in solution after exposure to and extraction from 100% EtOAc.

immobilized R5-*ar*PTE was also tested with a less polar solvent, ethyl acetate. An enzyme-bound column was subjected to 10 min of exposure to 100% ethyl acetate at a flow rate of 5 mL min $^{-1}$. The column was then flushed with buffer for a further 10 min at the same flow rate, before activity was tested with *p*-nitrophenyl butyrate at substrate loading of 2 g L^{-1}. No reduction in catalytic activity was observed after exposure to a cumulative 100 mL of ethyl acetate (Figure 3E). As a control, free R5-*ar*PTE in solution was exposed to ethyl acetate, and subsequently extracted from the aqueous fraction after solvent partitioning. Almost complete loss of activity was observed after only 1 min of contact time, indicating that the ionic adsorption of the enzyme onto the encapsulated hydrogel imparts significant additional stability to organic solvents (Figure 3F).

While synthetic hydrogels, such as the immobilized CM-based hydrogel described above, have value in industry, self-assembled peptide hydrogels have been shown to have potential applications as scaffolds in transplant and new regenerative therapies, as they can more closely mimic the environment of the cell via the inclusion of bioactive amino acid sequences.[53] Enzymes embedded within these materials have been shown to have improved stability and retained function over extended time periods.[54] This combination of properties is of interest, as it could allow precise (therapeutic) delivery of enzymatic activity, with the biocompatible hydrogel acting to constrain enzymatic activity to the physical location. This has been achieved by control of the surface chemistry via the peptide sequence. The side chains of the peptides are presented at a high density within

Table 1. Destruction of paraoxon-ethyl using R5-*ar*PTE in flow.

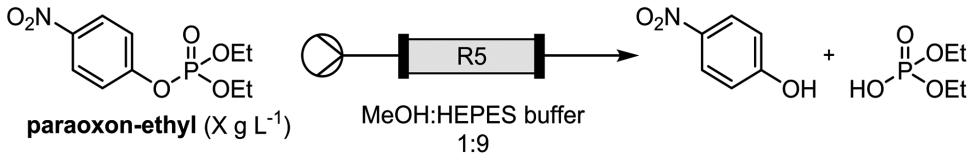

Run	Substrate loading [g L^{-1}]	Flow rate [mL min^{-1}]	Mass paraoxon [mg]	Time [min]	Conversion[a] [%]
1	1.25	5	375	60	67
2	2.5	2.5	375	60	76
3	2.5	1	375	150	86
4	1	1	50	50	91
5	0.5	1	350	700	95
Total	0.5–2.5	1–5	1525	1020	81
Catalyst loading [mol %]			0.0008		
Turnover [$mol_{substrate}$/$mol_{catalyst}$]			1.07×10^5		

[a]Determined by ^{1}H NMR of the crude residue after extraction with Et_2O.

the final assembled structure. This localization of properties creates dense regions which enable biomacromolecule inclusion by noncovalent incorporation. As the entire solvent is entrapped by the gelation process, all of the payload is incorporated within the system, and is dependent on the properties of the biomacromolecules and matrix. This presents via supramolecular interactions with the self-assembled matrix, such as hydrophobic,[55] steric,[56] and electrostatic interactions.[57] Previous studies have demonstrated the effects of electrostatic interactions on the rates of protein diffusion out of hydrogels, specifically showing that proteins with the opposite net charge of the hydrogel matrix in which they are encapsulated have a lower rate of diffusion.[58] With this in mind, we modified our previously described hydrogel,[57] which is comprised of Fmoc-DIKVAV (DX) and has been shown to be biocompatible and to self-assemble at physiological pH, to Fmoc-DIKVAVD (DXD), which includes aspartic acid at the C-terminus to create a complementary anionic matrix for the cationic enzyme. Samples of DX and DXD hydrogels were prepared by solid phase peptide synthesis. Solutions of R5-*ar*PTE were added to the liquid phase gels to yield a final concentration of 1 mg (protein) mL $(hydrogel)^{-1}$. The hydrogels were allowed to set, washed with phosphate buffered saline (PBS) to remove unbound enzyme, and tested for activity with paraoxon-ethyl. The structures of the hydrogels were not greatly perturbed by the addition of the supercharged protein, as estimated from transmission electron microscopy (TEM) and Fourier transform infrared spectroscopy (FTIR) (**Figure 4**A–E). Solutions of 200×10^{-3} M paraoxon-ethyl were applied to the surfaces of the DX: R5 and DXD: R5 gels, allowed to incubate at 25 °C with gentle shaking for 5 min, and then extracted for spectrophotometric analysis. The gels were then washed with PBS to remove excess substrate. This process was repeated five times. The neutral hydrogel DX: R5 complex showed a steady decrease in hydrolytic activity over the five rounds of washing and substrate addition, consistent with leaching of R5-*ar*PTE from the hydrogel, whereas DXD: R5 retained constant activity throughout the experiment (Figure 4F). This is consistent with R5-*ar*PTE and DXD forming

Table 2. Kinetic resolution of (±)-MPP using R5-G60A in flow.

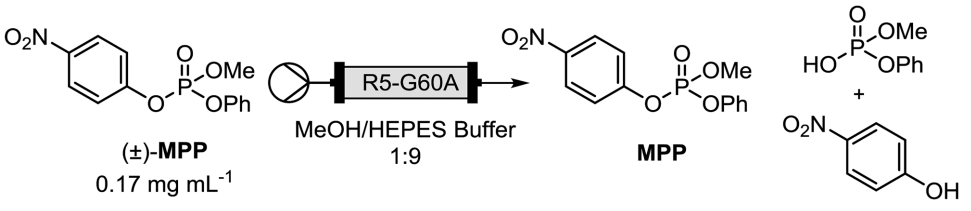

Flow rate [mL min^{-1}]	*t* [min]	Yield[a] [%]	e.r.[b]
2	10	–	>99:1
5	10	–	>99:1
10	10	–	>99:1
10	30	40	>99:1

[a]Isolated yield following column chromatography; [b]e.r. determined by HPLC on the RegisCell chiral stationary phase from Regis technologies.

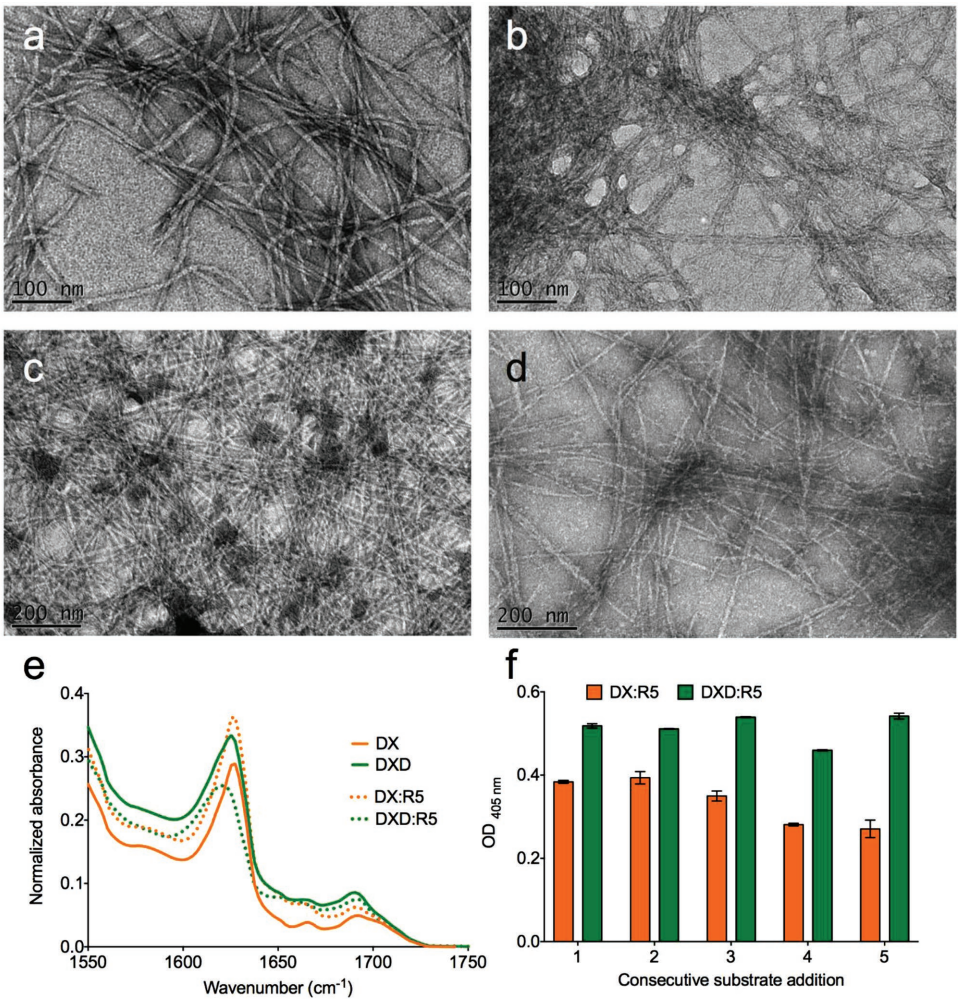

Figure 4. Hydrogel-enzyme constructs and their properties. TEM of a) DX hydrogel, b) DX: R5 construct, c) DXD hydrogel, d) DXD: R5 construct, showing that the nanofibrous morphology is largely unaffected by the addition of the enzyme. e) FTIR characterization of DX and DXD hydrogels imbued with R5-*ar*PTE, showing consistent β-sheet formation, a further indication that the structural assembly is not affected by the enzyme addition. f) Addition of paraoxon-ethyl to the surface of DX and DXD gels imbued with R5-*ar*PTE verifies catalytic activity of the constructs. DX: R5 shows a statistically significant decrease in catalytic activity over the course of the experiment, as determined by unpaired student's *t*-test ($p = 0.0006$) while DXD: R5 does not ($p = 0.112$).

a strong ionic interaction, resulting in immobilization of the enzyme in the hydrogel under neutral conditions.

For the application of biocatalysts in industrial processes, ensuring enzymes can be produced and purified quickly and at low cost is vital. The supercharged *ar*PTE variant, R5-*ar*PTE, presented in this work was isolated in high purity over a single cation exchange column step using robust hydrogel-ceramic beads that can tolerate high pressure and are reusable. The same hydrogel-ceramic resin has been demonstrated here to act as a versatile immobilization matrix for R5-*ar*PTE. Significantly, this represents an efficient industrial biocatalysis platform utilizing a single-step process from crude *E. coli* lysate to pure, immobilized, catalytically active protein. A further benefit of ionic immobilization is the potential for rapid recycling of the resin when enzymatic activity eventually deteriorates. R5-*ar*PTE can be stripped from the column with high salt buffer (2 M NaCl), allowing the resin to be recharged with fresh enzyme. The simplicity and flexibility that ionic immobilization allows cannot be achieved with covalent crosslinking to media.[59] Additionally, in contrast to previous examples of ionic adsorption methods, the immobilization and desorption processes are rapid, are essentially irreversible under normal conditions, do not require prior purification or modification of the enzyme and do not require long incubation periods.[60,61]

The immobilized R5-*ar*PTE system could find application in bioremediation, particularly in agricultural settings wherein pesticides applied to crops can leach into groundwater. One of the advantages of continuous-flow chemistry is its ability to scale-up efficiently.[62] Thus, the encapsulated hydrogel system could be readily scaled up and incorporated into waste–water drainage systems in these settings; the ceramic-encapsulated hydrogels are resistant to high flow rates and pressures, and after depletion of enzymatic activity, the material can be stripped with an innocuous NaCl solution and recharged with fresh enzyme.

Immobilized R5-*ar*PTE maintained significant hydrolytic activity, even in the presence of substantial methanol concentrations, and could recover 100% of its catalytic activity after exposure to ethyl acetate (in comparison, the free enzyme is irreversibly denatured). These observations suggest that the anionic hydrogel microenvironment stabilizes the natively folded state of the cationic protein. Polar solvents have been previously demonstrated to "strip" catalytic and structurally important water molecules from enzymes.[52] In the hydrogel, reduction in the polarity of the solvent will increase the strength of the ionic bonds between the surface of the protein and the hydrogel matrix, effectively stabilizing the structure and preventing structural rearrangement upon unfolding that could result in hydrophobic surfaces interacting, which normally leads to misfolding and aggregation. Indeed, tight interaction between the charged surface and the hydrogel may enhance any local refolding that might occur. Ionic immobilization of supercharged proteins could therefore prove useful in flow chemistry applications where enzymes are required to function in organic solvents, such as in the acylation of alcohols by lipases.[63]

Catalysts, including enzymes, have found widespread application in synthetic chemistry for the preparation of enantiopure compounds. The value of immobilized catalysts is particularly apparent in continuous-flow reactors, which are becoming more advanced and accessible. In flow chemistry applications, chemical transformations utilizing the specificity and selectivity of biocatalysts ideally require solvent-resistant components that can be readily stripped and recycled. The simplicity, durability, and reusability of supercharged enzyme: hydrogel matrices as described here could substantially reduce the costs and enhance the versatility of such components.

Finally, the nanostructured hydrogels formed by Fmoc-self assembling peptides have recently gained interest for the potential in regenerative medicine applications. The flexibility afforded by these systems is exemplified by their deployment in the brain where they interface with the surrounding parenchyma, have no adverse effect on the immune system, and do not impede cell migration or growth. While self-assembling organophosphate hydrolase gels have been previously described,[64] the flexibility afforded by a hybrid enzyme: hydrogel material is distinct; ionic entrapment in designer hydrogels could be readily generalized to any soluble enzyme, and both enzyme and gel properties could be tuned for specific applications. Further, the biocompatibility of enzyme-impregnated Fmoc complexes broadens the scope of potential medical applications of such materials. We anticipate that the inclusion of further functionality to such hydrogels, *via* supercharged proteins as presented here, could extend their uses by conferring catalytic activity, delivering bound ligands, or including components to promote the formation of protein: protein complexes at the site of transplant.

In this study, we have demonstrated robust ionic immobilization of an engineered, cationically supercharged, *ar*PTE onto anionic hydrogels, resulting in a system capable of detoxifying organophosphates and catalyzing enantioselective reactions in flow. The substantial catalytic lifespan of the R5-*ar*PTE-hydrogel system, both in terms of prolonged use and extended storage at room temperature, has been demonstrated. The cationic surface of R5-*ar*PTE allows a simple ion exchange purification protocol, which could be readily scaled up for industrial application of the enzyme, and the rapid immobilization on and desorption from the hydrogel results in an easily recyclable system, where degraded enzyme can be rapidly stripped from the gel and replaced with fresh protein. The flexibility and longevity of this system addresses some of the main drawbacks of current immobilization techniques; the high costs associated with purification of biocatalysts, the harsh conditions required for covalent attachment, and the propensity for ionically immobilized proteins to leach from media with prolonged use. The advances demonstrated above provide insight into potential application of biocatalysis in industry, synthesis, and bioremediation.

Experimental Section

Site Directed Mutagenesis and Expression Tests: The *ar*PTE gene was cloned into the pETMSCI expression vector between the Nde1 and EcoR1 restriction sites.[65] Mutants were constructed by the Gibson Assembly method.[66] Fragments containing the desired point mutation were generated using a pair of mutagenic QuikChange primers and a pair of gene-specific primers. pETMSCI vector was digested with Nde1 and EcoR1. Fragments and digested vector were purified via gel excision, then combined with a Gibson Assembly aliquot. The product of the Gibson reaction was transformed into electrocompetent *E. coli* Top 10 cells, and the cells plated on lysogeny broth (LB) agar with amp (100 μg mL^{-1} ampicillin) and incubated overnight. Colonies were selected, and colony polymerase chain reaction (PCR) performed with T7 forward and reverse primers. PCR product was sequenced to verify incorporation of the desired mutations.

Soluble expression of each *ar*PTE variant was tested under consistent growth conditions. *ar*PTE variant plasmids were transformed into electrocompetent *E. coli* BL21(DE3) cells, and the cells plated on LB agar with amp (100 μg mL^{-1} ampicillin) and incubated overnight. Colonies were selected and used to inoculate small-scale (10 mL) LB cultures, all supplemented with amp (100 μg mL^{-1} ampicillin) and 100×10^{-6} M $CoCl_2$. Small-scale cultures were incubated overnight at 30 °C with shaking at 200 rpm. To quantify the soluble protein expression in each set of conditions, 1 mL of cells was pelleted, resuspended in lysis buffer (Buffer B: 50×10^{-3} M (4-(2-hydroxyethyl)-1-piperazineethanesulfonic acid) (HEPES), 100×10^{-6} M $ZnCl_2$, 1.5 M NaCl, pH 8.0) with 10% v/v BugBuster (Novagen) and shaken for 1 h. The lysate was centrifuged at $4000 \times g$ for 10 min and both the supernatant and insoluble pellet were analyzed by SDS–PAGE.

Analysis of soluble expression was performed using ImageJ.[67] An internal standard against which *ar*PTE expression could be compared was selected. This ensured that variability caused by heterogeneous loading of samples would not affect perceived soluble expression, and allowed for expression to be compared across multiple SDS–PAGE experiments.

Preparative Scale Enzyme Expression and Purification: Electrocompetent *E. coli* BL21(DE3) cells were transformed with *ar*PTE mutant plasmids by electroporation. Transformants were plated on LB agar with amp (100 μg mL^{-1} ampicillin) and incubated overnight. Colonies were grown in LB medium supplemented with 100 μg mL^{-1} ampicillin for 8 h. These cultures were transferred to 1 L terrific broth (TB) medium supplemented with 100 μg mL^{-1} ampicillin and 100×10^{-6} M $CoCl_2$, and incubated at 30 °C with shaking overnight. *ar*PTE variants R4 and R5 were grown in large scale TB cultures supplemented with 10 g L^{-1} NaCl. Cells were pelleted by centrifugation at $4000 \times g$ for 15 min at 4 °C.

All enzymes in this study were purified through ion exchange chromatography.

WT, S1, S2, S3, R1, R2, R3: Pelleted cells were resuspended in Buffer A (50×10^{-3} M HEPES, 100×10^{-6} M $ZnCl_2$, pH 8.0) and lyzed through sonication. Lysate was centrifuged at 26 $200 \times g$ for 60 min at 4 °C to remove cell debris. The resulting supernatant was loaded onto a Fractogel diethylaminoethyl (DEAE) anion exchange column (Merck), equilibrated with Buffer A. *ar*PTE was collected in the flowthrough after

elution with Buffer A. Fractions were analyzed with SDS–PAGE. Purity of combined fractions was determined to be between 90% and 95%.

R4, R5: Pelleted cells were resuspended in Buffer B (50×10^{-3} M HEPES, 1.5 M NaCl, 100×10^{-6} M $ZnCl_2$, pH 8.0) and lyzed through sonication. Lysate was centrifuged at 26 200 × *g* for 30 min at 4 °C to remove cell debris, and the clarified lysate was subjected to a heat purification step. The lysate was suspended in a water-bath heated to 60 °C for 15 min, and then centrifuged at 26 200 × *g* for 30 min at 4 °C to pellet precipitated material. The resulting supernatant was diluted tenfold with Buffer C (50×10^{-3} M HEPES, 100×10^{-6} M $ZnCl_2$, pH 6.5) and loaded onto a column containing CM Ceramic HyperD resin (Pall LifeSciences). Unbound protein was washed away with Buffer C, and *ar*PTE eluted with an increasing concentration of Buffer D (50×10^{-3} M HEPES, 100×10^{-6} M $ZnCl_2$, 1.5 M NaCl, pH 7.0). Fractions were analyzed with SDS–PAGE. Pure fractions were pooled and purity was determined to be greater than 95%.

Enzyme Kinetics: Kinetic assays of *ar*PTE variants were carried out according to a previously published protocol.[68] In brief, kinetic constants for the hydrolysis of paraoxon-ethyl and *p*-nitrophenyl butyrate were determined by monitoring the production of *p*-nitrophenolate at 405 nm (ε_{405} = 17 700 M^{-1} cm^{-1}) at room temperature. Reactions were performed in 20×10^{-3} M Tris (pH 8.5), 100×10^{-3} M NaCl, 100×10^{-6} M $ZnCl_2$, and 1 mg mL^{-1} bovine serum albumin. All k_{cat} and K_M values were determined by fitting initial velocity data to the Michaelis–Menten equation. All assays were performed in duplicate, and MeOH concentration was kept below 2.5% total reaction volume.

Structural Determination: Purified R5-*ar*PTE was concentrated to ≈5 mg mL^{-1} in 20×10^{-3} M HEPES, 50×10^{-3} M NaCl, 100 µL $ZnCl_2$. Screens were optimized by hanging-drop vapor diffusion at 18 °C. Drops consisting of 4 µL of reservoir and 2 µL of protein were equilibrated over a 500 µL reservoir in Crystalgen pregreased 24-well plates. Conditions were screened between 100×10^{-3} M sodium nitrate (pH 6.1–6.7), distilled deionized water and 4 – 20% (w/v) PEG 3350 g mol^{-1}. Crystals were observed after 24 h of growth, with the largest crystals growing in 9% PEG 3350, pH 6.1.

For data collection, crystals were coated in cryobuffer (100×10^{-3} M sodium nitrate, pH 6.1, 40% PEG 3350) and cooled to 100 K in a stream of nitrogen gas. Diffraction data were collected at the Australian Synchrotron (MX2 beamline) at a wavelength of 0.9537 Å. X-ray diffraction data were indexed and integrated using X-ray detector software (XDS)[69] and merged using AIMLESS,[70] within the CCP4 program suite. The structure was solved by molecular replacement (MolRep)[71] using WT *ar*PTE structure (2D2J).[32] Refinement was performed using PHENIX,[72] and manual rebuilding was performed using *Coot*.[73]

Immobilization of R5-arPTE: A small volume column (0.667 mL) was packed with CM Ceramic HyperD resin (Pall LifeSciences) and equilibrated with 20 column volumes of Buffer D (50×10^{-3} M HEPES, 100×10^{-6} M $ZnCl_2$, 1.5 M NaCl, pH 7.0), followed by 20 column volumes of Buffer C (50×10^{-3} M HEPES, 100×10^{-6} M $ZnCl_2$, pH 6.5). For activity tests, 1 mg of purified R5-*ar*PTE was loaded in Buffer C. The successful immobilization of R5-*ar*PTE was verified by collecting the flowthrough from the loading step and observing UV absorbance at 280 nm. No evidence of protein was observed in the flowthrough. The "R5-*ar*PTE column" was stored at room temperature in 50×10^{-3} M HEPES, 100×10^{-6} M $ZnCl_2$, pH 8.

Tests of Immobilized R5-arPTE Activity: To test the activity, longevity, and solvent stability of immobilized R5-*ar*PTE, a flow-assay protocol was developed. In each case, 100 µL of 100×10^{-3} M *p*-nitrophenyl butyrate in MeOH was injected over the R5-*ar*PTE column at a flow rate of 5 mL min^{-1}, and the concentration of *p*-nitrophenolate in 20 mL of flowthrough was determined spectrophotometrically. 100 µL of 5 M NaOH was added to 1 mL of this flowthrough to determine absorbance for 100% hydrolysis. This provided an internal standard for measurements carried out over the course of 85 d. An "empty" column, containing CM Ceramic HyperD resin (Pall LifeSciences) and no enzyme, was used to establish background hydrolysis of the substrate under identical reaction conditions. Stability of the immobilized R5-*ar*PTE in methanol was determined by carrying out the standard flow-assay protocol in increasing concentrations of methanol in flow buffer (50×10^{-3} M HEPES, 100×10^{-6} M $ZnCl_2$, pH 8). Due to the limited miscibility of water in ethyl acetate, stability was tested only after exposure to 100% ethyl acetate rather than to increasing concentrations. 50 mL of ethyl acetate was pumped over the R5-*ar*PTE column at 5 mL min^{-1}, followed by 50 mL of flow buffer. Hydrolysis of substrate was then measured using the injection protocol described above. This experiment was performed over two separate washes with ethyl acetate, and hydrolysis measurements were taken after washes with 50 and 100 mL of flow buffer. MeOH flow-assay measurements were made in triplicate. All other flow-assay measurements were made in duplicate.

Synthesis of Paraoxon-Ethyl: To a solution of *p*-nitrophenol (4.2 g, 30 mmol) and potassium carbonate (4.2 g, 30 mmol) in acetone was added diethyl chlorophosphate (4.8 mL, 33 mmol) dropwise, and the reaction allowed to stir overnight. After this time, the solution was filtered and concentrated to yield the paraoxon as a pale yellow oil (6.4 g, 77%). **^{1}H NMR** (400 MHz, $CDCl_3$) δ 8.24 (d, J = 9.2 Hz, 2H), 7.37 (dd, J = 9.2, 0.8 Hz, 2H), 4.30–4.19 (m, 4H), 1.37 (t, J = 7.2, 3H), 1.33 (t, J = 7.2, 3H); **^{13}C NMR** (101 MHz, $CDCl_3$) δ 155.7 (d, J = 6.3 Hz), 144.8, 125.8, 120.7 (d, J = 5.4 Hz), 65.3 (d, J = 6.3 Hz), 16.2 (d, J = 6.6 Hz); **^{31}P NMR** (162 MHz, $CDCl_3$) δ −7.11; **IR** *ν*max (cm^{-1}) 2986, 1592, 1522, 1491, 1346, 1225, 1020 (br), 921.

Synthesis of MPP: To a solution of methyl phosphodichloridate (1.4 g, 9.5 mmol) and phenol (0.73 g, 9.5 mmol) in dichloromethane (40 mL) at 0 °C was added triethylamine (0.959 g, 9.5 mmol) dropwise, and the reaction allowed to warm to room temperature overnight. After this time, the reaction was cooled to 0 °C, and *p*-nitrophenol (1.16 g, 9.5 mmol) and triethylamine (0.959 g, 9.5 mmol) were added. The reaction was again allowed to warm to room temperature overnight. The solvent was then removed under reduced pressure, and the crude residue diluted with Et_2O. After washing with dilute $NaHCO_3$, the organic later was dried with $MgSO_4$, filtered, concentrated under reduced pressure, and the residue purified by column chromatography (1:9 → 1:1, v/v EtOAc: hexanes) to afford MPP as a brown oil (1.04 g, 34% yield). **Rf** 0.49 (1:1, v/v EtOAc: hexanes); **HPLC** RegisCell L40, λ = 254 nm, hexane: iPrOH 95:5, flow rate 1 mL min^{-1}, Rt 20.93 and 35.43 min; **^{1}H NMR** (400 MHz, CDCl3) δ 8.25 (dd, J = 9.6, 0.8 Hz, 2H), 7.41–7.34 (m, 4H), 7.26–7.19 (m, 3H), 4.01 (d, J = 11.6 Hz, 3H); **^{13}C NMR** (101 MHz, CDCl3) δ 155.2(2) (d, J = 0.6 Hz), 150.2(3) (d, J = 0.8 Hz), 145.2, 130.2 (d, J = 0.5 Hz), 126.0 (d, J = 1.1 Hz), 125.9, 120.8 (d, J = 5.4 Hz), 120.0 (d, J = 4.8 Hz), 56.1 (d, J = 6.5 Hz); **^{31}P NMR** (162 MHz, CDCl3) δ −11.65; **IR** *ν*max (cm^{-1}) 3115, 3081, 1590, 1519, 1487, 1346, 1187, 932 (br).

Enantioselectivity Assays: To determine if *ar*PTE variants R5 and G60A-R5 resolved racemic MPP, enzyme reactions were monitored using a Cary 60 UV–vis spectrophotometer. 800 µL of 80×10^{-6} M MPP in assay buffer (20×10^{-3} M Tris (pH 8.5), 100×10^{-3} M NaCl, 100×10^{-6} M $ZnCl_2$, and 1 mg mL^{-1} bovine serum albumin) was added to a 1 mL plastic cuvette, and baseline absorbance at 405 nm was established before the addition of 200 µL of enzyme solution to a final concentration of 40×10^{-9} M. Thorough mixing ensured a homogenous reaction mixture. Absorbance was monitored for ≈6 min, or until an obvious plateau was observed, suggesting the reaction had reached completion. 100 µL of 5 M NaOH was then added to the cuvette, mixed thoroughly, and subsequent absorbance monitored. Dilution of the reaction mixture upon addition of NaOH was factored into calculations.

Kinetic Resolution of MPP Under Continuous-Flow: Continuous-flow experiments were performed using a Vapourtec E-series easy-Medchem integrated flow chemistry system. The flow system was set up with reservoirs containing flow buffer and MPP (5×10^{-3} M in MeOH). The outlet of the column discharged into a beaker of Et_2O. Buffer was passed over the column at 0.9 mL min^{-1} and MPP at 0.1 mL min^{-1}, such that the column solvent was 1:9 buffer: MeOH. This ratio was maintained when flow rates were varied. Reaction time was measured from first observance of *p*-nitrophenolate at the column outlet. After the reaction time, the collected buffer/Et_2O was extracted with Et_2O until the yellow *p*-nitrophenolate was not visible in the aqueous layer. The combined organics were dried with Na_2SO_4, filtered, and concentrated under reduced pressure. The crude residue was analyzed by ^{1}H NMR and HPLC on a chiral stationary phase (RegisCell chiral stationary phase (4.6 mm × 25 cm) column from Regis).

Destruction of Paraoxon-Ethyl in Flow: The flow system was set up with reservoirs containing flow buffer and paraoxon-ethyl (0.5–2.5 g L^{-1} in MeOH). The outlet of the column discharged into a beaker of Et_2O. Buffer was passed over the column at 0.9 mL min^{-1} and paraoxon-ethyl at 0.1 mL min^{-1}, such that the column solvent was 1:9 buffer: MeOH. This ratio was maintained when flow rates were varied. Reaction time was measured from first observance of *p*-nitrophenolate at the column outlet. After the reaction time (see Table 1), the collected buffer/Et_2O was extracted with Et_2O until the yellow *p*-nitrophenolate was not visible in the aqueous layer. The combined organics were dried with Na_2SO_4, filtered, and concentrated under reduced pressure. The crude residue was analyzed by ^1H NMR.

Differential Scanning Fluorimetry: Determination of T_m for WT-*ar*PTE, S3-*ar*PTE, and R5-*ar*PTE was carried out by DSF with SYPRO Orange (Sigma) as the reporter dye. Assay solutions consisted of 10×10^{-6} M protein and a final concentration of 1 × SYPRO Orange, and were made up to a total volume of 30 µL with 20×10^{-3} M HEPES, 50×10^{-3} M NaCl, 100 µL $ZnCl_2$, pH 8. Temperature ramping was performed using a 7900HT Fast RealTime PCR (ThermoFisher, Applied Biosystems), and fluorescence data were collected (Excitation = 490 nm, Emission = 575 nm), before analysis with the SDS 2.4 software package (Applied Biosystems). DSF thermal shift assays were performed in triplicate.

Fmoc-Self-Assembling Peptide (SAP) Hydrogel Gelation: Fmoc-SAPs were engineered by solid phase peptide synthesis using a custom made rotating glass reaction vessel as previously reported.[74] Fmoc protected amino acids, hydroxybenzotriazole (HOBt), *O*-benzotriazole-*N*,*N*,*N*′,*N*′-tetramethyl-uronium-hexa-fuoro-phosphate and Wang based resins were purchased from Pepmic (China). All other chemicals were purchased from Sigma-Aldrich. Fmoc-SAPs hydrogels were prepared at 15 mg mL^{-1}. Briefly, 10 mg of peptide was dissolved into 200 µL of deionized water with 100 µL 0.5 M sodium hydroxide. Then 0.1 M of hydrochloric acid was slowly added with continuously vortexing and the pH of peptide solution was monitored until it reached physiological relevant pH. Typically, 300 µL of 0.1 M HCl was used to achieve this. Once the gel formed with the optimal pH attained, PBS was added to bring the gel up into 15 mg mL^{-1} concentration. The pH of the gels was measured by an Oaktron pH 700 micro pH electrode (Thermo Scientific).

FTIR Spectroscopy of Fmoc-SAP Hydrogels: FTIR spectra were collected by using an Alpha Platinum Platinum Attenuated total reflectance FTIR (Bruker Optics). Approximately 30 µL of peptide hydrogel (15 mg mL^{-1}) was placed on the single reflection diamond and allowed to sit for 10 min evaporating the solvent, which enables minimal contribution from the solvent to the spectra. Absorbance scans of the amide I region (1550–1750 cm^{-1}) were obtained for each peptide, and the background buffer scan subtracted.

TEM of Fmoc-self-assembling peptide (SAP) Hydrogels: TEM was performed on a Hitachi H7100FA electron microscope using a 100 kV beam with a LaB_6 cathode. Formvar coated copper grids were glow-discharged for 30 s at 15 mA. Hydrogel samples were negatively stained with 0.75% uranyl formate (UF): after glow discharge the grids were gently immersed in the sample for 30 s, briefly immersed in two consecutive drops of deionized water, before two drops of the UF negative stain solution was added for 20 s. The grids were gently blotted dry between immersions.

Determination of R5-arPTE Activity in Biocompatible Hydrogels: R5-*ar*PTE was incorporated into DX and DXD gel samples (0.66 mL gel), to a final concentration of 1 mg (enzyme) mL $(gel)^{-1}$. PBS was incorporated into identical DX and DXD samples to act as experimental controls. After gelation, the surfaces of DX + R5 and DXD + R5 were washed with 5 mL of PBS to remove unbound enzyme. Solutions of paraoxon-ethyl (200×10^{-3} M) were added to the surfaces of the enzyme-gel constructs, and the constructs were shaken gently at room temperature for 5 min. After the incubation period, solutions were removed from the surfaces of the gels and their absorbance at 405 nm was measured. The gels were washed with PBS to remove excess substrate (5 min incubation with PBS), and the addition of substrate was repeated. This process was repeated a total of five times.

Statistical Analysis: Wherever error is presented in figures, it is in the format mean ± SE. SE (standard error) is calculated using

$$SE = \frac{S}{\sqrt{n}} \quad (1)$$

where S is standard deviation from the mean and n is the sample size. Unless otherwise stated in the text, $n = 2$.

For enzyme kinetics, k_{cat} and K_M values were derived by fitting collected data to the Michaelis–Menten equation

$$V_0 = \frac{V_{max}[S]}{(K_M + [S])} \quad (2)$$

where V_0 is initial velocity, V_{max} is maximum velocity, and [S] is substrate concentration.

Determination of statistical significance was carried out using an unpaired student's *t*-test.

Supporting Information

Supporting Information is available from the Wiley Online Library or from the author.

Acknowledgements

A.W.P. would like to acknowledge the Engineering and Physical Research Council (EPSRC) for support (Early Career Fellowship EP/K026720/1). C.J.J. and D.W.L. would like to acknowledge the Australian Research Council (ARC) for support (Discovery Projects (DP) and FT programs). E.C. would like to thank the Australian Government for support through the Australian Postgraduate Award (APA), and the Australian National University (ANU) for funding through the Alan Sargeson and Research School of Chemistry Scholarships. E.C. performed experiments and analyzed results and wrote the paper. J.G., Y.W., and M.S. performed experiments and analyzed results. R.J.W. and D.R.N. designed experiments and analyzed results. A.W.P. conceived the project and analyzed results. D.W.L. designed experiments and analyzed results. C.J.J. conceived the project, designed experiments, analyzed results, and wrote the paper with input from all authors.

Conflict of Interest

The authors declare no conflict of interest.

Keywords

biocatalysis, biocompatible hydrogels, enzyme immobilization, enzyme-hydrogel hybrids, flow chemistry

Received: December 7, 2017
Revised: April 3, 2018
Published online:

[1] K. M. Koeller, C. H. Wong, *Nature* **2001**, *409*, 232.
[2] H. E. Schoemaker, D. Mink, M. Wubbolts, *Science* **2003**, *299*, 1694.
[3] V. V. Mozhaev, *Trends Biotechnol.* **1993**, *11*, 88.
[4] D. Klein-Marcuschamer, P. Oleskowicz-Popiel, B. A. Simmons, H. W. Blanch, *Biotechnol. Bioeng.* **2012**, *109*, 1083.
[5] K. Chen, F. H. Arnold, *Nat. Biotechnol.* **1991**, *9*, 1073.
[6] S. K. Ma, J. Gruber, C. Davis, L. Newman, D. Gray, A. Wang, J. Grate, G. W. Huisman, R. A. Sheldon, *Green Chem.* **2010**, *12*, 81.
[7] C. Ispas, I. Sokolov, S. Andreescu, *Anal. Bioanal. Chem.* **2009**, *393*, 543.
[8] P. Wang, S. Dai, S. D. Waezsada, A. Y. Tsao, B. H. Davidson, *Biotechnol. Bioeng.* **2001**, *74*, 249.

[9] D. S. Jiang, S. Y. Long, J. Huang, H. Y. Xiao, J. Y. Zhou, *Biochem. Eng. J.* **2005**, *25*, 15.
[10] H. R. Luckarift, J. C. Spain, R. R. Naik, M. O. Stone, *Nat. Biotechnol.* **2004**, *22*, 211.
[11] H. Takahashi, B. Li, T. Sasaki, C. Miyazaki, T. Kajino, S. Inagaki, *Chem. Mater.* **2000**, *12*, 3301.
[12] Y. Zhang, A. J. Patil, A. W. Perriman, S. Mann, *Chem. Commun.* **2013**, *49*, 9561.
[13] R. Fernandez-Lafuente, P. Armisen, P. Sabuquillo, G. Fernandez-Lorente, J. M. Guisan, *Chem. Phys. Lipids* **1998**, *93*, 185.
[14] C. Garcia-Galan, Á. Berenguer-Murcia, R. Fernandez-Lafuente, R. C. Rodrigues, *Adv. Synth. Catal.* **2011**, *353*, 2885.
[15] R. A. Sheldon, S. van Pelt, *Chem. Soc. Rev.* **2013**, *42*, 6223.
[16] U. Krauss, V. D. Jäger, M. Diener, M. Pohl, K. E. Jaeger, *J. Biotechnol.* **2017**, *258*, 136.
[17] M. Diener, B. Kopka, M. Pohl, K. E. Jaeger, U. Krauss, *ChemCatChem* **2016**, *8*, 142.
[18] J. Nahálka, A. Vikartovská, E. Hrabárová, *J. Biotechnol.* **2008**, *134*, 146.
[19] J. Nahálka, P. Gemeiner, M. Bůko, P. Wang, *Artif. Cells, Blood Substitutes, Biotechnol.* **2006**, *34*, 515.
[20] J. Lee, H. Ko, E. Lin, P. Wallace, H. D. Maynard, *Polym. Chem.* **2015**, *6*, 3443.
[21] A. M. Mariani, M. E. Natoli, P. Kofinas, *Biotechnol. Bioeng.* **2013**, *110*, 2994.
[22] M. S. Lawrence, K. J. Phillips, D. R. Liu, *J. Am. Chem. Soc.* **2007**, *129*, 10110.
[23] J. J. Cronican, D. B. Thompson, K. T. Beier, B. R. McNaughton, C. L. Cepko, D. R. Liu, *ACS Chem. Biol.* **2010**, *5*, 747.
[24] B. R. McNaughton, J. J. Cronican, D. B. Thompson, D. R. Liu, *Proc. Natl. Acad. Sci. USA* **2009**, *106*, 6111.
[25] J. A. Zuris, D. B. Thompson, Y. Shu, J. P. Guilinger, J. L. Bessen, J. H. Hu, M. L. Maeder, J. K. Joung, Z.-Y. Chen, D. R. Liu, *Nat. Biotechnol.* **2014**, *33*, 73.
[26] T. Gräslund, G. Lundin, M. Uhlén, P. A. Nygren, S. Hober, *Protein Eng.* **2000**, *13*, 703.
[27] F. Ely, K. S. Hadler, L. R. Gahan, L. W. Guddat, D. L. Ollis, G. Schenk, *Biochem. J.* **2010**, *432*, 565.
[28] D. P. Dumas, S. R. Caldwell, J. R. Wild, F. M. Raushel, *J. Biol. Chem.* **1989**, *264*, 19659.
[29] C. J. Jackson, J.-L. Foo, N. Tokuriki, L. Afriat, P. D. Carr, H.-K. Kim, G. Schenk, D. S. Tawfik, D. L. Ollis, *Proc. Natl. Acad. Sci. USA* **2009**, *106*, 21631.
[30] K. Huynh, C. L. Partch, *Curr. Protoc. Protein Sci.* **2015**, *79*, 28.9.1.
[31] E. Sugrue, N. J. Fraser, D. H. Hopkins, P. D. Carr, J. L. Khurana, J. G. Oakeshott, C. Scott, C. J. Jackson, *Appl. Environ. Microbiol.* **2015**, *81*, 2612.
[32] C. Jackson, H. K. Kim, P. D. Carr, J. W. Liu, D. L. Ollis, *Biochim. Biophys. Acta, Proteins Proteomics* **2005**, *1752*, 56.
[33] S. Ahmad, M. Gromiha, H. Fawareh, A. Sarai, *BMC Bioinformatics* **2004**, *5*, 51.
[34] J. Schymkowitz, J. Borg, F. Stricher, R. Nys, F. Rousseau, L. Serrano, *Nucleic Acids Res.* **2005**, *33*, 382.
[35] P. Chan, R. A. Curtis, J. Warwicker, *Sci. Rep.* **2013**, *3*, 41.
[36] N. Tokuriki, F. Stricher, L. Serrano, D. S. Tawfik, *PLoS Comput. Biol.* **2008**, *4*, 35.
[37] E. Campbell, M. Kaltenbach, G. J. Correy, P. D. Carr, B. T. Porebski, E. K. Livingstone, L. Afriat-Jurnou, A. M. Buckle, M. Weik, F. Hollfelder, N. Tokuriki, C. J. Jackson, *Nat. Chem. Biol.* **2016**, *12*, 944.
[38] Y. Ye, A. Godzik, N. T. P. Road, L. Jolla, *Nucleic Acids Res.* **2004**, *32*, 582.
[39] M. N. Davies, C. P. Toseland, D. S. Moss, D. R. Flower, **2006**, *12*, 1.
[40] L. P. Kozlowski, *Biol. Direct* **2016**, *11*, 55.
[41] E. Gasteiger, C. Hoogland, A. Gattiker, S. Duvaud, M. R. Wilkins, R. D. Appel, A. Bairoch, in *The Proteomics Protocols Handbook*, Ed. 1, Humana Press, New York **2005**, p. 571.
[42] M. N. Davies, C. P. Toseland, D. S. Moss, D. R. Flower, *BMC Biochem.* **2006**, *7*, 18.
[43] L. P. Kozlowski, *Nucleic Acids Res.* **2017**, *45*, D1112.
[44] The Uniprot Consortium, *Nucleic Acids Res.* **2016**, *45*, D158.
[45] J. Huang, H. Fang, C. Liu, E. Gu, D. Jiang, *Anal. Lett.* **2008**, *41*, 1430.
[46] A. J. H. Al-Adhami, J. Bryjak, B. Greb-Markiewicz, W. Peczyńska-Czoch, *Process Biochem.* **2002**, *37*, 1387.
[47] M. Polakovič, P. Vrábel, *Process Biochem.* **1996**, *31*, 787.
[48] World Health Organisation, *Guidelines for Drinking-Water Quality*, World Health Organization, Geneva, Switzerland **2011**.
[49] The Council of the European Union, *Off. J. Eur. Communities* **1998**, *L330*, 32.
[50] M. Chen-Goodspeed, M. A. Sogorb, F. Wu, S. B. Hong, F. M. Raushel, *Biochemistry* **2001**, *40*, 1325.
[51] V. N. Uversky, N. V Narizhneva, S. O. Kirschstein, S. Winter, G. Lober, *Folding Des.* **1997**, *2*, 163.
[52] L. S. Gorman, J. S. Dordick, *Biotechnol. Bioeng.* **1992**, *39*, 392.
[53] D. R. Nisbet, R. J. Williams, *Biointerphases* **2012**, *7*, 1.
[54] R. J. Williams, A. M. Smith, R. Collins, N. Hodson, A. K. Das, R. V. Ulijn, *Nat. Nanotechnol.* **2009**, *4*, 19.
[55] R. J. Williams, T. E. Hall, V. Glattauer, J. White, P. J. Pasic, A. B. Sorensen, L. Waddington, K. M. McLean, P. D. Currie, P. G. Hartley, *Biomaterials* **2011**, *32*, 5304.
[56] R. Li, N. L. Mcrae, D. R. McCulloch, M. Boyd-Moss, C. J. Barrow, D. R. Nisbet, N. Stupka, R. J. Williams, *Biomacromolecules* **2018**, *19*, 825.
[57] A. L. Rodriguez, T. Y. Wang, K. F. Bruggeman, R. Li, R. J. Williams, C. L. Parish, D. R. Nisbet, *Nano Res.* **2016**, *9*, 674.
[58] K. Nagy-Smith, Y. Yamada, J. P. Schneider, *J. Mater. Chem. B* **2016**, *4*, 1999.
[59] C. Z. Guidini, J. Fischer, L. N. S. Santana, V. L. Cardoso, E. J. Ribeiro, *Biochem. Eng. J.* **2010**, *52*, 137.
[60] D. Ling, G. Wu, C. Wang, F. Wang, G. Song, *Enzyme Microb. Technol.* **2000**, *27*, 516.
[61] B. F. Shaw, G. F. Schneider, B. Bilgiçer, G. K. Kaufman, J. M. Neveu, W. S. Lane, J. P. Whitelegge, G. M. Whitesides, *Protein Sci.* **2008**, *17*, 1446.
[62] S. G. Newman, K. F. Jensen, *Green Chem.* **2013**, *15*, 1456.
[63] S. W. Chang, J. F. Shaw, *New Biotechnol.* **2009**, *26*, 109.
[64] H. D. Lu, I. R. Wheeldon, S. Banta, *Protein Eng., Des. Sel.* **2010**, *23*, 559.
[65] C. Neylon, S. E. Brown, A. V. Kralicek, C. S. Miles, C. A. Love, N. E. Dixon, *Biochemistry* **2000**, *39*, 11989.
[66] D. G. Gibson, L. Young, R. Y. Chuang, J. C. Venter, C. A. Hutchison, H. O. Smith, *Nat. Methods* **2009**, *6*, 343.
[67] J. Schindelin, I. Arganda-Carreras, E. Frise, V. Kaynig, M. Longair, T. Pietzsch, S. Preibisch, C. Rueden, S. Saalfeld, B. Schmid, J.-Y. Tinevez, D. J. White, V. Hartenstein, K. Eliceiri, P. Tomancak, A. Cardona, K. Liceiri, P. Tomancak, *Nat. Methods* **2012**, *9*, 676.
[68] C. Roodveldt, D. S. Tawfik, *Protein Eng. Des. Sel.* **2005**, *18*, 51.
[69] W. Kabsch, *Acta Crystallogr., Sect. D: Biol. Crystallogr.* **2010**, *D66*, 125.
[70] P. R. Evans, G. N. Murshudov, *Acta Crystallogr., Sect. D: Biol. Crystallogr.* **2013**, *69*, 1204.
[71] A. Vagin, A. Teplyakov, *J. Appl. Crystallogr.* **1997**, *30*, 1022.
[72] P. D. Adams, P. V. Afonine, G. Bunkóczi, V. B. Chen, I. W. Davis, N. Echols, J. J. Headd, L. W. Hung, G. J. Kapral, R. W. Grosse-Kunstleve, A. J. McCoy, N. W. Moriarty, R. Oeffner, R. J. Read, D. C. Richardson, J. S. Richardson, T. C. Terwilliger, P. H. Zwart, *Acta Crystallogr., Sect. D: Biol. Crystallogr.* **2010**, *66*, 213.
[73] P. Emsley, B. Lohkamp, W. G. Scott, K. Cowtan, *Acta Crystallogr., Sect. D: Biol. Crystallogr.* **2010**, *66*, 486.
[74] A. L. Rodriguez, T. Y. Wang, K. F. Bruggeman, C. C. Horgan, R. Li, R. J. Williams, C. L. Parish, D. R. Nisbet, *J. Mater. Chem. B* **2014**, *2*, 7771.

Supplementary Data

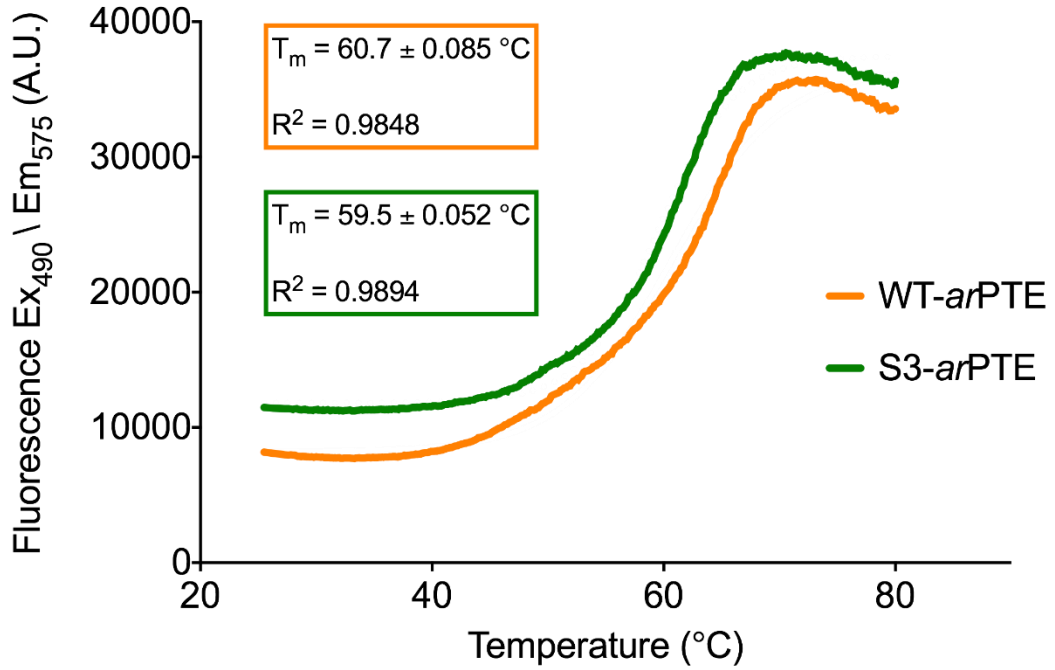

Supplementary Figure 1 | Thermal shift assays of WT-*ar*PTE and S3-*ar*PTE, indicating a predicted T_m of 60.7 ± 0.085 °C for WT, and 59.5 ± 0.052 °C for S3. Line fit statistics and predicted T_m values are in-set.

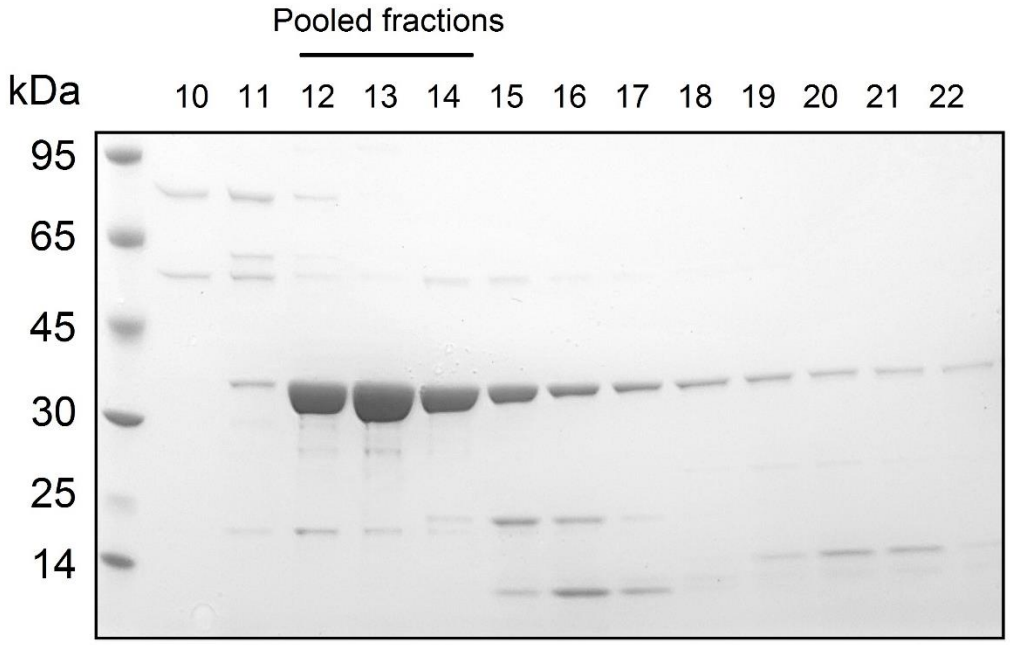

Supplementary Figure 2 | Purification of R5-*ar*PTE (approximately 35 kDa) over cation exchange resin. SDS-PAGE of eluted fractions 10 to 22 shows <95% purity in fractions 12 to 14.

Position	Mutated to	Effect on expression (relative to background onto which incorporated)	
Glu81	Arg	0.76‡	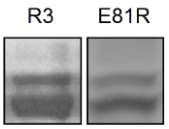
Asp121	Lys	0.81	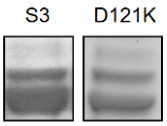
Gln148	Arg	1.03†	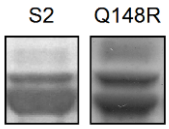
Gln155	Arg	0.94	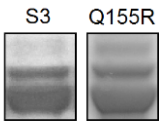
Asp160	Lys	0.46	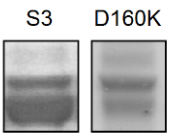
Gln206	Arg	0.02#	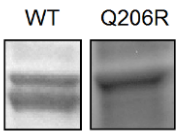
Glu210	Arg	0.47†	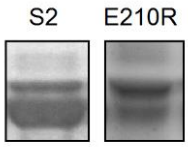
Ser238	Arg	0.79	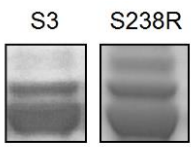

Glu263	Arg	1.04	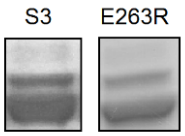
Thr274	Arg	0.83	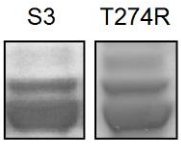
Asp289	Arg	0.58	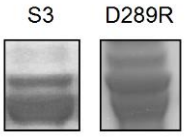
Thr311	Arg	0.59	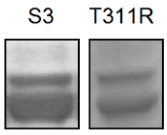
Asp315	Arg	0.73‡	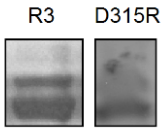
Glu338	Arg	0.69‡	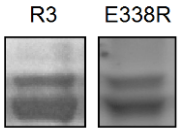
Glu344	Arg	0.75‡	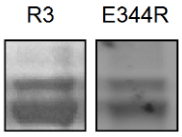

Supplementary Table 1 | The identities of the 15 cationizing mutations. The effects of the mutations on soluble protein expression were assessed using SDS-PAGE and image densitometry (ImageJ[56,57]), and are presented here as ratios relative to the genetic background into which they were incorporated. Numbers > 1 represent an increase in soluble expression. Mutations were made on S3-*ar*PTE unless indicated otherwise. † made on S2-*ar*PTE, ‡ made on R3-*ar*PTE, # made on WT-*ar*PTE.

	K185R	A80V	A204G	Q148R	Q155R	E263R	D315R	S238R
WT								
S1	X							
S2	X	X						
S3	X	X	X					
R1	X	X	X	X				
R2	X	X	X	X	X			
R3	X	X	X	X	X	X		
R4	X	X	X	X	X	X	X	
R5	X	X	X	X	X	X	X	X

Supplementary Table 2 | The identities of the stabilising and cationizing mutations accumulated in each round of testing.

Variant	k_{cat} (s^{-1})	K_M (μM)	k_{cat}/K_M (M^{-1} s^{-1})
Ethyl Paraoxon			
WT	509 ± 12	16 ± 0.018	3.18×10^7
S1	50.7 ± 0.89	23 ± 0.89	2.18×10^6
S2	41.0 ± 0.23	17 ± 1.5	2.35×10^6
S3	130 ± 3.5	36 ± 3.2	3.63×10^6
R1	117 ± 4.2	43 ± 2.6	2.74×10^6
R2	105 ± 3.3	35 ± 0.38	3.00×10^6
R3	126 ± 3.1	44 ± 3.6	2.84×10^6
R4	49.1 ± 0.87	20 ± 3.0	2.47×10^6
R5	69.8 ± 2.5	19 ± 0.88	3.77×10^6
***p*-nitrophenyl butyrate**			
WT	6.02 ± 0.72	950 ± 189	6.33×10^3
R5	3.16 ± 0.10	1072 ± 34	2.95×10^3

Supplementary Table 3 | Kinetic parameters of *ar*PTE variants with paraoxon-ethyl and *p*-nitrophenyl butyrate. Means and s.e. of parameters were calculated from two independent measurements.

	R5-*ar*PTE
Data collection	
Space group	$P2_12_12_1$
Cell dimensions	
a, *b*, *c* (Å)	48.391, 110.076, 112.277
α, β, γ (°)	90.0, 90.0, 90.0
Resolution (Å)	34.88 - 2.75 (2.848 - 2.75)
R_{sym} or R_{merge}	0.1527 (0.5932)
$CC_{1/2}$	0.998 (0.94)
CC*	0.999 (0.984)
$I / \sigma I$	15.03 (4.54)
Completeness (%)	91.52 (100.00)
Redundancy	12.8 (13.0)
Refinement	
Resolution (Å)	34.88 - 2.75 (2.848 - 2.75)
No. reflections	188301 (20742)
R_{work} / R_{free}	0.2254/0.2769
No. atoms	
Protein	5056
Ligand/ion	4
Water	69
B-factors	
Protein	42.20
Ligand/ion	28.50
Water	27.10
R.M.S. deviations	
Bond lengths (Å)	0.003
Bond angles (°)	0.83
PDB ID	5W7H

Supplementary Table 4 | Data collection and refinement statistics for R5-*ar*PTE

I was captured for life by chemistry and crystals. – Dorothy Crowfoot Hodgkin

CHAPTER 5:
CONCLUSIONS

The work presented in this thesis seeks to improve our understanding of biocatalysts and broaden their application in chemical synthesis, therapeutics, and industry. Fundamental research into the mechanisms that underpin molecular evolution can provide valuable insights into the nature of highly efficient catalysts, and provide strategies for the rational improvement of designed enzymes.

In Chapter 2 of this thesis, the study of evolutionary intermediates isolated from a directed evolution experiment (the R-trajectory) revealed several factors that influence the improvement of promiscuous activity during adaptive evolution selecting for that trait. We determined that adaptive evolution enriched productive conformations, with later round substitutions tuning the dynamics of loop regions to minimize motions that were important in the native activity, but did not play a productive role in the new activity. Structural characterisation of intermediates isolated from a 'reversal' of this evolutionary trajectory (starting from the endpoint of the R-trajectory, and selecting for native activity) revealed convergence upon the native active site structure, albeit via a different evolutionary pathway. This demonstrates that phenotypic reversion is constrained by an 'epistatic ratchet' that prohibits the stepwise reversion of individual mutations, and provides an example of convergence in molecular evolution.

Work presented in Chapter 3 of this thesis aimed to further investigate evolutionary convergence by characterizing variants isolated from a directed evolution campaign starting from a phenotypic 'neighbour' of the starting point of the R-trajectory. The results presented demonstrate that the new evolutionary trajectory (the S-trajectory) followed a different adaptive pathway to a distinct fitness peak; the final variant of this trajectory has lost the requirement of a closed loop conformation that was specifically enriched in the old trajectory, and has stabilized a new substrate binding mode. While the final variant of this trajectory is not as catalytically efficient as the final variant of the R-trajectory, it represents a different solution to the evolutionary problem with which it was faced. This speaks to the importance of historical contingency in adaptive evolution, and the pervasive nature of epistasis in the enhancement of traits; a single polymorphism forced evolution to take a new route. Further, the reduced tolerance of 'swapping' mutations from one trajectory's genetic background to the other is an example of mutational entrenchment, in which a mutation becomes increasingly deleterious to reverse to its ancestral state along an evolutionary pathway. This effect is more profound in the substitution of Arg254Ser in the R-trajectory background, where Arg254 had served as the hub in an intricate intramolecular bonding network.

In Chapter 4 of this thesis, enzyme immobilization was investigated as a method of broadening the scope of biocatalyst application. Immobilization on a solid support can improve the lifespan of enzymes, and can enhance their resistance to organic solvents. Making use of commercially available and specifically designed charged hydrogels, a supercharged *ar*PTE variant was successfully ionically immobilized. This ionic immobilization technique bypassed the need for harsh reaction conditions typically required for covalent immobilization, allowed for rapid adsorption and desorption of enzyme, thus ensuring the recyclability of the solid support, and resulted in catalytically active hydrogel-enzyme constructs. We successfully demonstrated the enhanced longevity of the immobilized enzyme, its significant resistance to organic solvents (including methanol, which is highly polar), and its application in the kinetic resolution of a chiral organophosphate in flow. Further, the super-cationic *ar*PTE variant could be purified in a single step, greatly enhancing its appeal in large scale industrial processes, where efficient production of catalysts is vital for cost-effective methodologies.

Taken as a whole, the work presented in this thesis represents both fundamental research into the design of efficient biocatalysts through the exploitation of nature's preferred method, evolution, and the production of next-generation biocatalysts that take advantage of novel materials to maximise the applicability of enzymes in synthesis, medicine, and industry. Continued work in these fields aims to build a future in which we can identify a desired reaction, rapidly produce a designer biocatalyst, and incorporate it into a functional biomaterial for maximum efficiency.

REFERENCES FOR CHAPTER 1

1. Chen, K. & Arnold, F. H. Tuning the activity of an enzyme for unusual environments : Sequential random mutagenesis of subtilisin E for catalysis in dimethylformamide. *Proc. Natl. Acad. Sci.* **90,** 5618–5622 (1993).

2. Chen, K. & Arnold, F. H. Enzyme engineering for nonaqueous solvents: random mutagenesis to enhance activity of Subtilisin E in polar organic media. *Nat. Biotechnol.* **9,** 1073–1077 (1991).

3. Stemmer, W. P. Rapid evolution of a protein in vitro by DNA shuffling. *Nature* **370,** 389–391 (1994).

4. Stemmer, W. P. C. DNA shuffling by random fragmentation and reassembly: In vitro recombination for molecular evolution. *Proc. Natl. Acad. Sci. U. S. A.* **91,** 10747–10751 (1994).

5. Cadwell, R. C. & Joyce, G. F. Randomization of genes by PCR mutagenesis. *Genome Res.* **2,** 28–33 (1992).

6. Leung, D. W., Chen, E. & Goeddel, D. V. A method for random mutagensis of a defined DNA segment using a modified polymerase chain reaction. *Technique* **1,** 11–15 (1989).

7. Zaccolo, M., Williams, D. M., Brown, D. M. & Gherardi, E. An approach to random mutagenesis of DNA using mixtures of triphosphate derivatives of nucleoside analogues. *J. Mol. Biol.* **255,** 589–603 (1996).

8. Wells, J. A., Vasser, M. & Powers, D. B. Cassette mutagenesis: an effcient method for generation of multiple mutations at defined sites. *Gene* **34,** 315–323 (1985).

9. Huang, W., Petrosino, J., Hirsch, M., Shenkin, P. S. & Palzkill, T. Amino acid sequence determinants of β-Lactamase structure and activity. *J. Mol. Biol.* **258,** 688–703 (1996).

10. Zhao, H., Giver, L., Shao, Z., Affhoter, J. A. & Arnold, F. H. Molecular evolution by staggered extension process (StEP) in vitro recombination. *Nat. Biotechnol.* **16,** 258–261 (1998).

11. Packer, M. S. & Liu, D. R. Methods for the directed evolution of proteins. *Nat. Rev. Genet.* **16,** 379–394 (2015).

12. Esvelt, K. M., Carlson, J. C. & Liu, D. R. A system for the continuous directed evolution of biomolecules. *Nature* **472,** 499–503 (2011).

13. Chen, K. & Rajewsky, N. The evolution of gene regulation by transcription factors and microRNAs. *Nature Reviews Genetics* **8,** 93–103 (2007).

14. Phillips, P. C. Epistasis - the essential role of gene interactions in the structure and evolution of genetic systems. *Nat. Rev. Genet.* **9,** 855–67 (2008).

15. Pfeiffer, T., Schuster, S. & Bonhoeffer, S. Cooperation and competition in the evolution of ATP-producing pathways. *Science* **292,** 504–507 (2001).

16. Ghalambor, C. K., Walker, J. A. & Reznick, D. N. Multi-trait selection, adaptation,

and constraints on the evolution of burst swimming performance. *Integr. Comp. Biol.* **43,** 431–438 (2003).

17. Koshi, J. M. & Goldstein, R. A. Probabilistic reconstruction of ancestral protein sequences. *J. Mol. Evol.* **42,** 313–320 (1996).

18. Paritala, H., Palde, P. B. & Carroll, K. S. Functional site discovery in a sulfur metabolism enzyme by using directed evolution. *ChemBioChem* 1873–1878 (2016). doi:10.1002/cbic.201600264

19. Röthlisberger, D. *et al.* Kemp elimination catalysts by computational enzyme design. *Nature* **453,** 190–196 (2008).

20. Khersonsky, O. *et al.* Evolutionary optimization of computationally designed enzymes: Kemp eliminases of the KE07 series. *J. Mol. Biol.* **396,** 1025–42 (2010).

21. Althoff, E. A. *et al.* Robust design and optimization of retroaldol enzymes. *Protein Sci.* **21,** 717–726 (2012).

22. Preiswerk, N. *et al.* Impact of scaffold rigidity on the design and evolution of an artificial Diels-Alderase. *Proc. Natl. Acad. Sci.* **111,** 8013–8018 (2014).

23. Karanicolas, J. *et al.* A De Novo Protein Binding Pair By Computational Design and Directed Evolution. *Mol. Cell* **42,** 250–260 (2011).

24. Tokuriki, N. *et al.* Diminishing returns and tradeoffs constrain the laboratory optimization of an enzyme. *Nat. Commun.* **3,** 1257 (2012).

25. O'Brien, P. J. & Herschlag, D. Catalytic promiscuity and the evolution of new enzymatic activities. *Chem. Biol.* **6,** R91–R105 (1999).

26. Kondrashov, F. A., Rogozin, I. B., Wolf, Y. I. & Koonin, E. V. Selection in the evolution of gene duplications. *Genome Biol.* **3,** 1–9 (2002).

27. Poelwijk, F. J., Vos, M. G. J. De & Tans, S. J. Tradeoffs and optimality in the evolution of gene regulation. *Cell* **146,** 462–470 (2011).

28. Maclean, R. C., Perron, G. G. & Gardner, A. Diminishing returns from beneficial mutations and pervasive epistasis shape the fitness landscape for rifampicin resistance in Pseudomonas aeruginosa. *Genetics* **186,** 1345–1354 (2010).

29. Hartl, D. L., Dykhuizen, D. E. & Dean, A. M. Limits of adaption: the evolution of seletive neutrality. *Genetics* **111,** 655–674 (1985).

30. Stebbins, J. The law of diminishing returns. *Science* **99,** 267–271 (1944).

31. Chou, H., Chiu, H., Delaney, N. F., Segrè, D. & Marx, C. J. Diminishing returns epistasis among beneficial mutations decelerates adaptation. *Science* **332,** 1190–1193 (2011).

32. Weinreich, D. M. The rank ordering of genotypic fitness values predicts genetic constraint on natural selection on landscapes lacking sign epistasis. *Genetics* **171,** 1397–1405 (2005).

33. Kvitek, D. J. & Sherlock, G. Reciprocal sign epistasis between frequently experimentally evolved adaptive mutations causes a rugged fitness landscape. *PLoS Genet.* **7,** (2011).

34. Poelwijk, F. J., Kiviet, D. J., Weinreich, D. M. & Tans, S. J. Empirical fitness landscapes reveal accessible evolutionary paths. *Nature* **445,** 383–386 (2007).

35. Ortlund, E. A., Bridgham, J. T., Redinbo, M. R. & Thornton, J. W. Crystal structure of an ancient protein: evolution by conformational epistasis. *Science* **317,** 1544–1548 (2007).

36. Bridgham, J. T., Ortlund, E. A. & Thornton, J. W. An epistatic ratchet constrains the direction of glucocorticoid receptor evolution. *Nature* **461,** 515–519 (2009).

37. Harms, M. J. & Thornton, J. W. Analyzing protein structure and function using ancestral gene reconstruction. *Curr. Opin. Struct. Biol.* **20,** 360–366 (2010).

38. Romero, P. A. & Arnold, F. H. Exploring protein fitness landscapes by directed evolution. *Nat. Rev. Mol. Cell Biol.* **10,** 866–876 (2009).

39. Yang, G., Hong, N., Baier, F., Jackson, C. J. & Tokuriki, N. Conformational tinkering drives evolution of a promiscuous activity through indirect mutational effects. *Biochemistry* **55,** 4583–4593 (2016).

40. Weinreich, D. M., Delaney, N. F., Depristo, M. A. & Hartl, D. L. Darwinian evolution can follow only very few mutational paths to fitter proteins. *Science* **312,** 111–115 (2006).

41. Jiang, H., Xu, L. & Gu, Z. Growth of novel epistatic interactions by gene duplication. *Genome Biol. Evol.* **3,** 295–301 (2011).

42. Henzler-Wildman, K. A. *et al.* A hierarchy of timescales in protein dynamics is linked to enzyme catalysis. *Nature* **450,** 913–916 (2007).

43. Warshel, A. & Bora, R. P. Perspective: Defining and quantifying the role of dynamics in enzyme catalysis. *J. Chem. Phys.* **144,** (2016).

44. Okazaki, K. & Takada, S. Dynamic energy landscape view of coupled binding and protein conformational change: Induced-fit versus population-shift mechanisms. *Proc. Natl. Acad. Sci.* **105,** 11182–11187 (2008).

45. Boehr, D. D., Nussinov, R. & Wright, P. E. The role of dynamic conformational ensembles in biomolecular recognition. *Nat. Chem. Biol.* **5,** 789–796 (2009).

46. Levsh, O. *et al.* Dynamic conformational states dictate selectivity toward the native substrate in a substrate-permissive acyltransferase. *Biochemistry* **55,** 6314–6326 (2016).

47. Liu, X. *et al.* Distinct roles for conformational dynamics in protein-ligand interactions. *Structure* **24,** 2053–2066 (2016).

48. Grant, B. J., Gorfe, A. A. & Mccammon, J. A. Large conformational changes in proteins: signaling and other functions. *Curr. Opin. Struct. Biol.* **20,** 142–147 (2010).

49. Henzler-Wildman, K. & Kern, D. Dynamic personalities of proteins. *Nature* **450,** 964–972 (2007).

50. Beadle, B. M. & Shoichet, B. K. Structural bases of stability-function tradeoffs in enzymes. *J. Mol. Biol.* **321,** 285–296 (2002).

51. Meiering, M., Serrano, L. & Fersht, A. R. Effect of active site residues in barnase on

activity and stability. *J. Mol. Biol.* **225,** 585–589 (1992).

52. Thomas, V. L., Mcreynolds, A. C. & Shoichet, B. K. Structural bases for stability-function tradeoffs in antibiotic resistance. *J. Mol. Biol.* **396,** 47–59 (2010).

53. Tokuriki, N., Stricher, F., Schymkowitz, J., Serrano, L. & Tawfik, D. S. The stability effects of protein mutations appear to be universally distributed. *J. Mol. Biol.* **369,** 1318–1332 (2007).

54. Wang, X., Minasov, G. & Shoichet, B. K. Evolution of an antibiotic resistance enzyme constrained by stability and activity trade-offs. *J. Mol. Biol.* **320,** 85–95 (2002).

55. Shoichet, B. K., Baase, W. a., Kuroki, R. & Matthews, B. W. A relationship between protein stability and protein function. *Proc. Natl. Acad. Sci.* **92,** 452–456 (1995).

56. Warshel, A. Electrostatic origin of the catalytic power of enzymes and the role of preorganized active sites. *J. Biol. Chem.* **273,** 27035–27038 (1998).

57. Bloom, J. D. *et al.* Thermodynamic prediction of protein neutrality. *Proc. Natl. Acad. Sci.* **102,** 606–611 (2005).

58. Bloom, J. D., Labthavikul, S. T., Otey, C. R. & Arnold, F. H. Protein stability promotes evolvability. *Proc. Natl. Acad. Sci.* **2006,** 5869–5874 (2006).

59. Bershtein, S., Segal, M., Bekerman, R., Tokuriki, N. & Tawfik, D. S. Robustness – epistasis link shapes the fitness landscape of a randomly drifting protein. *Nature* **444,** 929–932 (2006).

60. Nobeli, I., Favia, A. D. & Thornton, J. M. Protein promiscuity and its implications for biotechnology. *Nat. Biotechnol.* **27,** 157–167 (2009).

61. Koshland, D. E. Correlation of structure and function in enzyme action. *Science (80-.).* **142,** 1533–1542 (1963).

62. Fischer, E. No Title. *Ber. Dtsch. Chem. Ges.* **23,** 2611 (1890).

63. James, L. C. & Tawfik, D. S. Conformational diversity and protein evolution - A 60-year-old hypothesis revisited. *Trends Biochem. Sci.* **28,** 361–368 (2003).

64. Ekroos, M. & Sjogren, T. Structural basis for ligand promiscuity in cytochrome P450 3A4. *Proc. Natl. Acad. Sci.* **103,** 13682–13687 (2006).

65. Newton, M. S. *et al.* Structural and functional innovations in the real-time evolution of new $(\beta\alpha)_8$ barrel enzymes. *Proc. Natl. Acad. Sci.* **114,** 4727–4732 (2017).

66. James, L. C. & Tawfik, D. S. The specificity of cross-reactivity: Promiscuous antibody binding involves specific hydrogen bonds rather than nonspecific hydrophobic stickiness. *Protein Sci.* **12,** 2183–2193 (2003).

67. Montanari, F., Shields, D. C. & Khaldi, N. Differences in the number of intrinsically disordered regions between yeast duplicated proteins, and their relationship with functional divergence. *PLoS One* **6,** e24989 (2011).

68. Siddiq, M. A., Hochberg, G. K. & Thornton, J. W. Evolution of protein specificity: insights from ancestral protein reconstruction. *Curr. Opin. Struct. Biol.* **47,** 113–122 (2017).

69. Kaltenbach, M. *et al.* Evolution of chalcone isomerase from a non-catalytic ancestor.

bioRxiv (2017). doi:10.1101/174128

70. Clifton, B. E., Kaczmarski, J. A., Carr, P. D., Gerth, M. L. & Tokuriki, N. Evolution of an enzyme from a solute- binding protein. *bioRxiv* (2017). doi:10.1101/157495

71. Dellus-Gur, E. *et al.* Negative epistasis and evolvability in TEM-1 B-lactamase - The thin line between an enzyme's conformational freedom and disorder. *J. Mol. Biol.* **427,** 2396–2409 (2015).

72. Nguyen, V. *et al.* Evolutionary drivers of thermoadaptation in enzyme catalysis. *Science* **355,** 289–294 (2017).

73. Biel, J. T., Thompson, M. C., Cunningham, C. N., Corn, J. E. & Fraser, J. S. Flexibility and design: Conformational heterogeneity along the evolutionary trajectory of a redesigned ubiquitin. *Structure* **25,** 739–749.e3 (2016).

74. Campbell, E. *et al.* The role of protein dynamics in the evolution of new enzyme function. *Nat. Chem. Biol.* **12,** 944–950 (2016).

75. Campbell, E. C. *et al.* Laboratory evolution of protein conformational dynamics. *Curr. Opin. Struct. Biol.* **50,** 49–57 (2018).

76. Tóth-Petróczy, Á. & Tawfik, D. S. The robustness and innovability of protein folds. *Curr. Opin. Struct. Biol.* **26,** 131–138 (2014).

77. Dellus-Gur, E., Toth-Petroczy, A., Elias, M. & Tawfik, D. S. What makes a protein fold amenable to functional innovation? Fold polarity and stability trade-offs. *J. Mol. Biol.* **425,** 2609–2621 (2013).

78. Seibert, C. M. & Raushel, F. M. Structural and catalytic diversity within the amidohydrolase superfamily. *Biochemistry* **44,** 6383–6391 (2005).

79. Di Nardo, A. A., Larson, S. M. & Davidson, A. R. The relationship between conservation, thermodynamic stability, and function in the SH3 domain hydrophobic core. *J. Mol. Biol.* **333,** 641–655 (2003).

80. Cygler, M. *et al.* Relationship between sequence conservation and three-dimensional structure in a large family of esterases, lipases, and related proteins. *Protein Sci.* **2,** 366–382 (1993).

81. Echave, J., Spielman, S. J. & Wilke, C. O. Causes of evolutionary rate variation among protein sites. *Nat. Rev. Genet.* **17,** 109–121 (2016).

82. Babbitt, P. C. & Gerlt, J. Understanding enzyme superfamilies. *J. Biol. Chem.* **272,** 30591–30594 (1997).

83. Boehr, D. D., Dyson, H. J. & Wright, P. E. An NMR perspective on enzyme dynamics. *Chem. Rev.* **106,** 3055–3079 (2006).

84. Karplus, M. & Mccammon, J. A. Molecular dynamics simulations of biomolecules. *Nat. Struct. Mol. Biol.* **9,** 646–652 (2002).

85. Ringe, D. & Petsko, G. A. Mapping protein dynamics by X-ray diffraction. *Prog. Biophys. Mol. Biol.* **45,** 197–235 (1985).

86. Fraser, J. S. & Jackson, C. J. Mining electron density for functionally relevant protein polysterism in crystal structures. *Cell. Mol. Life Sci.* **68,** 1829–1841 (2011).

87. Kuzmanic, A., Pannu, N. S. & Zagrovic, B. X-ray refinement significantly underestimates the level of microscopic heterogeneity in biomolecular crystals. *Nat. Commun.* **5,** 1–10 (2014).

88. Keedy, D. A., Fraser, J. S. & Bedem, H. Van Den. Conformations in X-ray crystallography using qFit. *PLoS Comput. Biol.* 1–22 (2015). doi:10.1371/journal.pcbi.1004507

89. Van Den Bedem, H., Dhanik, A., Latombe, J. C. & Deacon, A. M. Modeling discrete heterogeneity in X-ray diffraction data by fitting multi-conformers. *Acta Crystallogr. Sect. D Biol. Crystallogr.* **65,** 1107–1117 (2009).

90. Lang, P. T. *et al.* Automated electron-density sampling reveals widespread conformational polymorphism in proteins. *Protein Sci.* **19,** 1420–1431 (2010).

91. Furnham, N., Blundell, T., Depristo, M. A. & Terwilliger, T. C. Is one solution good enough? *Nat. Struct. Mol. Biol.* **13,** 184–185 (2006).

92. Levin, E. J., Kondrashov, D. A., Wesenberg, G. E. & Phillips, G. N. Ensemble refinement of protein crystal structures: validation and application. *Structure* **15,** 1040–1052 (2007).

93. Tom Burnley, B., Afonine, P. V., Adams, P. D. & Gros, P. Modelling dynamics in protein crystal structures by ensemble refinement. *Elife* **2012,** 1–29 (2012).

94. Woldeyes, R. A., Sivak, D. A. & Fraser, J. S. E pluribus unum, no more: from one crystal, many conformations. *Curr. Opin. Struct. Biol.* **28,** 56–62 (2014).

95. Juers, D. H. & Matthews, B. W. Reversible lattice repacking illustrates the temperature dependence of macromolecular interactions. *J. Mol. Biol.* **311,** 851–862 (2001).

96. Fraser, J. S., Bedem, H. Van Den, Samelson, A. J., Lang, P. T. & Holton, J. M. Accessing protein conformational ensembles using room-temperature X-ray crystallography. *Proc. Natl. Acad. Sci.* **108,** 16247–16252 (2011).

97. Fraser, J. S. *et al.* Hidden alternative structures of proline isomerase essential for catalysis. *Nature* **462,** 669–673 (2009).

98. Eisenmesser, E. Z. *et al.* Intrinsic dynamics of an enzyme underlies catalysis. *Nature* **438,** 117–121 (2005).

99. Zhang, Y. *et al.* Conformational stabilization of ubiquitin yields potent and selective inhibitors of USP7. *Nat. Chem. Biol.* **9,** 51–58 (2013).

100. Huber, H. & Stetter, K. O. Hyperthermophiles and their possible potential in biotechnology. *J. Biotechnol.* **64,** 39–52 (1998).

101. Feller, G. & Gerday, C. Psychrophilic enzymes: hot topics in cold adaption. *Nat. Rev. Microbiol.* **1,** 200–208 (2003).

102. Mevarech, M., Frolow, F. & Gloss, L. M. Halophilic enzymes: proteins with a grain of salt. *Biophys. Chem.* **86,** 155–164 (2000).

103. Kimura, T. *et al.* Purification, characterization, and molecular cloning of acidophilic xylanase from Penicillium sp.40. *Biosci. Biotechnol. Biochem.* **64,** 1230–1237 (2000).

104. Ito, S. *et al.* Alkaline detergent enzymes from alkaliphiles: enzymatic properties,

genetics, and structures. *Extremophiles* **2,** 185–190 (1998).

105. Nelson, J. M. & Griffin, E. G. Adsorption of invertase. *J. Am. Chem. Soc.* **38,** 1109–1115 (1916).

106. Ohmiya, K., Tanimura, S., Kobayashi, T. & Shimizu, S. Preparation and properties of proteases immobilized on anion exchange resin with glutaraldehyde. *Biotechnol. Bioeng.* **20,** 1–15 (1978).

107. Wu, B., Zhang, G., Shuang, S. & Choi, M. M. F. Biosensors for determination of glucose with glucose oxidase immobilized on an eggshell membrane. *Talanta* **64,** 546–553 (2004).

108. Schoffelen, S. & Van Hest, J. C. M. Chemical approaches for the construction of multi-enzyme reaction systems. *Curr. Opin. Struct. Biol.* **23,** 613–621 (2013).

109. Takahashi, H. *et al.* Catalytic activity in organic solvents and stability of immobilized enzymes depend on the pore size and surface characteristics of mesoporous silica. *Chem. Mater.* **12,** 3301–3305 (2000).

110. Ispas, C., Sokolov, I. & Andreescu, S. Enzyme-functionalized mesoporous silica for bioanalytical applications. *Anal. Bioanal. Chem.* **393,** 543–554 (2009).

111. Fernandez-Lafuente, R., Armisen, P., Sabuquillo, P., Fernandez-Lorente, G. & Guisan, J. M. Immobilization of lipases by selective adsorption on hydrophobic supports. *Chem. Phys. Lipids* **93,** 185–197 (1998).

112. Hernandez, K. & Fernandez-Lafuente, R. Control of protein immobilization: Coupling immobilization and site-directed mutagenesis to improve biocatalyst or biosensor performance. *Enzyme Microb. Technol.* **48,** 107–122 (2011).

113. Luckarift, H. R., Spain, J. C., Naik, R. R. & Stone, M. O. Enzyme immobilization in a biomimetic silica support. *Nat. Biotechnol.* **22,** 211–213 (2004).

114. Akbarian, F., Lin, A., Dunn, B. S., Valentine, J. S. & Zink, J. I. Spectroscopic determination of cholinesterase activity and inhibition in sol-gel media. *J. Sol-Gel Sci. Technol.* **8,** 1067–1070 (1997).

115. Tang, C. *et al.* Cross-linked polymer nanofibers for hyperthermophilic enzyme immobilization: Approaches to improve enzyme performance. *ACS Appl. Mater. Interfaces* **6,** 11899–11906 (2014).

116. Rapson, T. D. *et al.* Micromolar biosensing of nitric oxide using myoglobin immobilized in a synthetic silk film. *Biosens. Bioelectron.* **62,** 214–220 (2014).

117. Kowalewska, B. & Jakubow, K. The impact of immobilization process on the electrochemical performance, bioactivity and conformation of glucose oxidase enzyme. *Sensors Actuators, B Chem.* **238,** 852–861 (2017).

118. Gao, Y., Truong, Y. B., Cacioli, P., Butler, P. & Kyratzis, I. L. Bioremediation of pesticide contaminated water using an organophosphate degrading enzyme immobilized on nonwoven polyester textiles. *Enzyme Microb. Technol.* **54,** 38–44 (2014).

119. Mateo, C., Abian, O., Fernandez-Lafuente, R. & Guisan, J. M. Increase in conformational stability of enzymes immobilized on epoxy-activated supports by

favoring additional multipoint covalent attachment. *Enzyme Microb. Technol.* **26,** 509–515 (2000).

120. Wang, A. *et al.* Rational immobilization of lipase by combining the structure analysis and unnatural amino acid insertion. *J. Mol. Catal. B. Enzym.* **132,** 54–60 (2016).

121. Petkar, M., Lali, A., Caimi, P. & Daminati, M. Immobilization of lipases for non-aqueous synthesis. *J. Mol. Catal. B Enzym.* **39,** 83–90 (2006).

122. Feng, D. *et al.* Stable metal-organic frameworks containing single-molecule traps for enzyme encapsulation. *Nat. Commun.* **6,** 1–8 (2015).

123. Holland-Nell, K. & Beck-Sickinger, A. G. Specifically immobilised Aldo/Keto reductase AKR1A1 shows a dramatic increase in activity relative to the randomly immobilised enzyme. *ChemBioChem* **8,** 1071–1076 (2007).

124. Khan, F., He, M. & Taussig, M. J. Double-hexahistidine tag with high-affinity binding for protein immobilization, purification, and detection on Ni-nitrilotriacetic acid surfaces. *Anal. Chem.* **78,** 3072–3079 (2006).

125. Bolivar, J. M. & Nidetzky, B. Oriented and selective enzyme immobilization on functionalized silica carrier using the cationic binding module Zbasic2: Design of a heterogeneous D-amino acid oxidase catalyst on porous glass. *Biotechnol. Bioeng.* **109,** 1490–1498 (2012).

126. Richins, R. D., Mulchandani, A. & Chen, W. Expression, immobilization, and enzymatic characterization of cellulose-binding domain-organophosphorus hydrolase fusion enzymes. *Biotechnol Bioeng* **69,** 591–596 (2000).

127. Wiesbauer, J., Bolivar, J. M., Mueller, M., Schiller, M. & Nidetzky, B. Oriented immobilization of enzymes made fit for applied biocatalysis: Non-covalent attachment to anionic supports using Zbasic2 module. *ChemCatChem* **3,** 1299–1303 (2011).

128. Torres, R. *et al.* Reversible immobilization of glucoamylase by ionic adsorption on sepabeads coated with polyethyleneimine. *Biotechnol. Prog.* **20,** 1297–1300 (2004).

129. Montes, T. *et al.* Genetic modification of the penicillin G acylase surface to improve its reversible immobilization on ionic exchangers. *Appl. Environ. Microbiol.* **73,** 312–319 (2007).

130. Tsai, P. C. *et al.* Structural determinants for the stereoselective hydrolysis of chiral substrates by phosphotriesterase. *Biochemistry* **49,** 7988–7997 (2010).

131. Uversky, V. N. Proteins without unique 3D structures: Biotechnological applications of intrinsically unstable/disordered proteins. *Biotechnol. J.* **10,** 356–366 (2015).

132. Schein, C. Solubility as a function of protein structure and solvent components. *Nat. Biotechnol.* **8,** 308–317 (1990).

133. Lawrence, M. S., Phillips, K. J. & Liu, D. R. Supercharging proteins can impart unusual resilience. *J. Am. Chem. Soc.* **129,** 10110–10112 (2007).

134. Shaw, B. F. *et al.* Lysine acetylation can generate highly charged enzymes with increased resistance toward irreversible inactivation. *Protein Sci.* **17,** 1446–1455 (2008).

135. Perriman, A. W., Cölfen, H., Hughes, R. W., Barrie, C. L. & Mann, S. Solvent-free

protein liquids and liquid crystals. *Angew. Chemie - Int. Ed.* **48,** 6242–6246 (2009).

136. Brogan, A. P. S., Siligardi, G., Hussain, R., Perriman, A. W. & Mann, S. Hyper-thermal stability and unprecedented re-folding of solvent-free liquid myoglobin. *Chem. Sci.* **3,** 1839 (2012).

137. Gräslund, T., Lundin, G., Uhlén, M., Nygren, P. A. & Hober, S. Charge engineering of a protein domain to allow efficient ion-exchange recovery. *Protein Eng.* **13,** 703–709 (2000).

138. Reichhardt, C. *Solvents and Solvent Effects in Organic Chemistry*. (Wiley-VCH, 2003).

139. Sun, H., Yang, H., Huang, W. & Zhang, S. Immobilization of laccase in a sponge-like hydrogel for enhanced durability in enzymatic degradation of dye pollutants. *J. Colloid Interface Sci.* **450,** 353–360 (2015).

140. Wang, Q., Yang, Z., Wang, L., Ma, M. & Xu, B. Molecular hydrogel-immobilized enzymes exhibit superactivity and high stability in organic solvents. *Chem. Commun.* 1032–1034 (2007). doi:10.1039/b615223f

141. Li, R. *et al.* Tuning the mechanical and morphological properties of self-assembled peptide hydrogels via control over the gelation mechanism through regulation of ionic strength and the rate of pH change. *RSC Adv.* **5,** 301–307 (2015).

142. Cuatrecasas, P. Protein purification by affinity chromatography: Derivatizations of agarose and polyacrylamide beads. *J. Biol. Chem.* **245,** 3059–3065 (1970).

143. Overview of affinity purification. *Thermofisher Scientific* (2017). Available at: https://www.thermofisher.com/au/en/home/life-science/protein-biology/protein-biology-learning-center/protein-biology-resource-library/pierce-protein-methods/overview-affinity-purification.html#/legacy=www.piercenet.com. (Accessed: 14th August 2017)

144. Nisbet, D. R. & Williams, R. J. Self-assembled peptides: Characterisation and in vivo response. *Biointerphases* **7,** 1–14 (2012).

APPENDIX 1:
LABORATORY EVOLUTION OF PROTEIN CONFORMATIONAL DYNAMICS

Declaration

The following review, ‘Laboratory evolution of protein conformational dynamics’, was published in the *Sequences and Topology* edition of *Current Opinion in Structural Biology*. The author wrote the sections titled **Laboratory directed evolution and ancestral protein reconstruction** and **Studying the evolution of protein dynamics through laboratory evolution and ancestral reconstruction,** contributed to the introduction, and edited the remainder of the manuscript. The contributions of other authors are as follows: Mr. Galen Correy wrote the sections titled **Biophysical and computational analysis of protein structural dynamics** and **The study of designed enzymes**; Associate Professor Colin Jackson wrote the section **Engineering protein dynamics**; all authors contributed to the editing of the manuscript.

Note that the page numbering in the follow article has been adjusted for publication in this thesis. The online version of this article can be found at the DOI listed below.

‘Laboratory evolution of protein conformational dynamics’

DOI: 10.1016/j.sbi.2017.09.005

Available online at www.sciencedirect.com

ScienceDirect

Current Opinion in Structural Biology

Laboratory evolution of protein conformational dynamics

Eleanor C Campbell[1,5], Galen J Correy[1,5], Peter D Mabbitt[1,4,5], Ashley M Buckle[2], Nobuhiko Tokuriki[3] and Colin J Jackson[1]

This review focuses on recent work that has begun to establish specific functional roles for protein conformational dynamics, specifically how the conformational landscapes that proteins can sample can evolve under laboratory based evolutionary selection. We discuss recent technical advances in computational and biophysical chemistry, which have provided us with new ways to dissect evolutionary processes. Finally, we offer some perspectives on the emerging view of conformational dynamics and evolution, and the challenges that we face in rationally engineering conformational dynamics.

Addresses
[1] Research School of Chemistry, Australian National University, Canberra, ACT 2601, Australia
[2] Department of Biochemistry and Molecular Biology, Biomedicine Discovery Institute, Monash University, Clayton, Victoria 3800, Australia
[3] Michael Smith Laboratories, University of British Columbia, Vancouver, British Columbia V6T 1Z2, Canada

Corresponding author: Jackson, Colin J (colin.jackson@anu.edu.au)
[4] Current address: MRC Protein Phosphorylation and Ubiquitylation Unit, Sir James Black Centre, School of Life Sciences, University of Dundee, Dundee DD1 5EH, Scotland, UK.

Current Opinion in Structural Biology 2018, **50**:49–57

This review comes from a themed issue on **Sequences and topology**

Edited by **Joseph Marsh**

https://doi.org/10.1016/j.sbi.2017.09.005

Introduction

The conformational dynamism of proteins is well established. Polypeptide chains are inherently flexible and undergo conformational change in solution at a variety of time scales. On the shortest of these timescales (fs–ps), bonds vibrate and side chains rotate. On longer time scales (ns–ms), macroscale motions can take place; loops 'open' and 'close', and domains can twist relative to each other or move on hinge-like regions. One important question in modern protein science asks how these conformations affect the function of the enzyme. The continued improvement in available biophysical techniques, including X-ray crystallography and NMR, in combination with advances in computational protein simulations, has allowed deeper analysis of protein motions. For example, the role of protein dynamics in substrate binding and product release is well studied [1–4], and cascades of conformational change are now known to underpin numerous biological functions [5]. There remains some controversy around the role of conformational dynamics in the catalytic step of enzymes; some works have proposed a role for conformational dynamics in the chemical step [6], while others suggest that experimental models have not yet conclusively demonstrated this link [7].

Given that protein structural dynamics clearly play important roles in several aspects of protein function, it is reasonable to assume that they must have evolved, or become optimized through selective pressure. Thus, one of the biggest questions relating to protein structural dynamics regards the role of molecular evolution, and how/if pathways for conformational change can be altered. During the evolution of new enzyme function, an enzyme active site must reorganize and adapt to a new substrate and/or new chemical reaction. It is generally, and reasonably, assumed that the adaptation of an enzyme to catalyze a new chemical reaction predominantly involves modification of the active site via mutation to better stabilize the transition state. However, the composition of active sites among homologous enzymes is often very similar, despite markedly different catalytic specificities [8], and laboratory (directed) evolution routinely demonstrates that remote mutations somehow have drastic effects on enzyme turnover rates or substrate preference [9–11]. These observations — in addition to our established understanding of allosteric communication between remote sites [12] — imply an important role for second/third/outer shell residues in modulating enzyme function, perhaps via control of protein structural dynamics/conformational sampling. The difficulty in studying the evolution of any trait, but especially structural dynamics, when relying on comparison between different extant proteins, is that we are comparing already highly evolved (and complex) states. To understand how something can change or evolve, it is much more informative to study the evolutionary process directly.

[5] Equal author contribution.

Figure 1

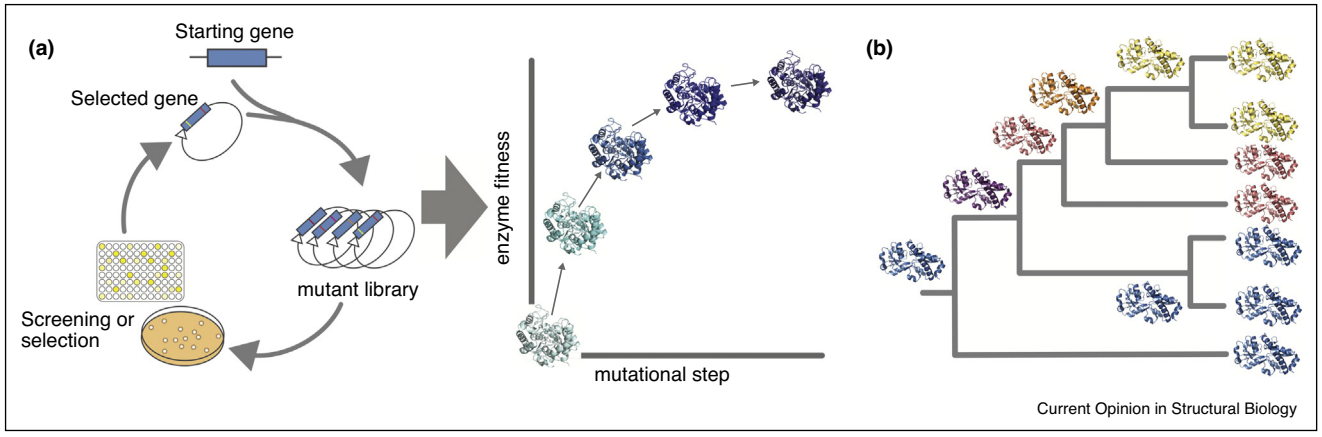

(a) The workflow of laboratory directed evolution involves the generation of a library of mutants of the gene of interest, and a screening or selection process to iteratively enhance a desired phenotype. **(b)** Ancestral protein reconstruction requires that the phylogenetic relationships between extant proteins are established, allowing ancestral sequences to be inferred and constructed.

Laboratory directed evolution and ancestral protein reconstruction

Laboratory directed evolution [Figure 1a] has been extensively used in an engineering context to produce many different proteins with a variety of improved functions, such as increased or novel catalytic activity [13], increased thermostability [14], and enhanced spectral properties [15]. However, directed evolution also provides great advantages over the study of natural homologs when it comes to the study of evolutionary processes. First, we focus on the evolution of (often) a single gene/protein of interest, rather than proteins that evolved in concert with the whole organism, which can involve complicated inter-gene epistatic relationships. Second, the high throughput screening of randomly generated mutants of a particular gene can result in the rapid enhancement of a desired phenotype over far fewer generations than is typical in natural systems, because directed evolution experiments allow for tight control of selection pressure, while natural evolutionary processes typically must balance several requirements to maximise the reproductive success of the organism. This results in significantly less neutral sequence variation, which can confound functional analysis. Finally, perhaps the most important advantage of laboratory evolution is that it allows for the study of as many intermediates along an evolutionary trajectory as desired, which can provide novel insights that cannot be gleaned through comparison of extant enzymes where only one current state can be assessed.

Ancestral protein reconstruction [Figure 1b] also seeks to remedy the shortcomings of studying extant proteins in isolation. Through the alignment of related sequences and the calculation of phylogenetic relationships between those sequences, points of diversification, or nodes, representing the predicted ancestors of extant proteins can be identified and probable sequences for these ancestral states inferred. This allows for the expression and characterization of these ancestral proteins that represent evolutionary intermediates, which can facilitate the study of evolutionary divergence [16].

Directed evolution and ancestral protein reconstruction have been instrumental in revealing fundamentally important molecular processes that underlie many protein functions. For example, our understanding of catalytic promiscuity has been substantially broadened through studying the evolution of substrate preference [17•,18]; we have gained insights into the complex relationships between thermostability and activity observed during the acquisition and optimization of new function [19,20]; and the constraints of epistasis on evolutionary trajectories can be more readily analysed thanks to the accessibility of evolutionary intermediates [21]. Most recently, attention has shifted to the study of how structural dynamics of proteins can change throughout an evolutionary trajectory, which has been facilitated by developments in computational structural biology and biophysical techniques.

Biophysical and computational analysis of protein structural dynamics

Studying the evolution of protein structural dynamics would not be possible without the use of computational and biophysical methodologies that allow structural dynamics to be dissected in different protein variants. To provide some context to the subsequent discussion of recent discoveries related to structural dynamics through evolutionary studies, we must first provide a brief overview of some the key experimental approaches to the study of structural dynamics.

Often, a single technique is not sufficient to characterize structural dynamics on the wide range of timescales of interest in biological systems, and understanding the evolution of protein structural dynamics requires integrative structural biology [22]. X-ray crystallography is the most commonly used tool and is valuable because proteins often remain active in the crystalline state, which has similar solvent content (~30–80%) to the crowded environment of cells [23]. Advances in modelling anharmonic disorder using time-averaged ensemble refinement [24] and multi-conformer models [25] have proven to be particularly useful as they can allow less common ('hidden') conformational sub-states that exist among the billions of molecules in a crystal lattice to be modelled and studied. Likewise, the hunt for minor conformational sub-states has reignited interest in room temperature X-ray diffraction, which can eliminate the structural bias introduced by crystal cryo-cooling, which may 'freeze-out' higher energy sub-states [26,27]. Advances in NMR have also allowed detailed study of protein dynamics. Although often lacking the resolution of X-ray crystallography, NMR can characterize transient, low occupancy conformational sub-states, and the exchange kinetics between sub-states, with timescales ranging from pico-second-to-seconds [28]. While frequently limited to the study of small proteins, isotope labelling can extend the scope of NMR methods to study structural dynamics of larger proteins [29] and the synergistic use of NMR with X-ray crystallography can provide an integrated picture of protein dynamics [30]. Finally, computational simulations are now probing dynamic processes on increasing timescales [31] with improved accuracy and sampling [32]. As with NMR, combining computational simulations of molecular dynamics with empirically derived X-ray structures can provide a more detailed analysis of the conformational sampling of amino acid sidechains and loop regions that often have functional relevance [33]. Altogether, the numerous biophysical and computational techniques we now have at our disposal have given us the ability to better dissect the molecular and dynamic changes that occur through laboratory directed evolution and ancestral protein reconstruction, providing unique insight into the evolution of these complex traits.

Studying the evolution of protein dynamics through laboratory directed evolution and ancestral protein reconstruction

The application of laboratory directed evolution to bacterial phosphotriesterase (PTE), which had previously been shown to undergo functionally important conformational fluctuations that could be modulated by mutations [34], has resulted in several insights into the mechanisms of protein evolution, particularly with regards to dynamics [Figure 2]. Tokuriki *et al.* exploited the promiscuous activity of PTE for arylester hydrolysis, and carried out a 22 generation directed evolution experiment towards arylesterase (AE) activity, followed by a 12 generation

Figure 2

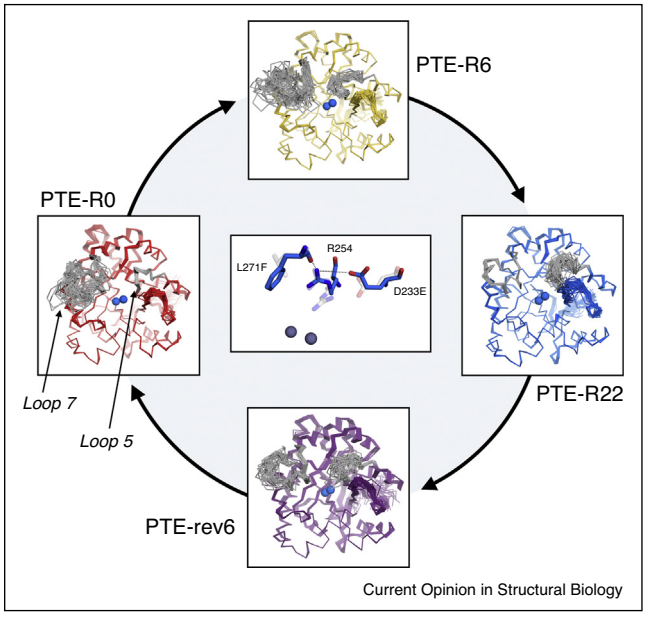

The directed evolution of PTE. Ensemble refinement of PTE variants R0, R6, R22 and rev6 illustrate the changing conformational dynamism of key loops (loop 5 and loop 7). R0 (PTE activity) possesses a large degree of flexibility in loop 7, while R22 (AE activity) possesses very little flexibility in loop 7 but enhanced dynamism in loop 5. Bifunctional 'midpoint' variants R6 and rev6 retain conformational flexibility in both regions, facilitating catalysis of both activities. The central panel illustrates the stabilization of the productive conformation of Arg254 (the first substitution fixed in the forward trajectory), by later round substitutions.

'reversal', starting from the optimized arylesterase and selecting for native PTE activity [35,36••,37]. Over the course of the forward evolution, AE activity increased approximately 40 000-fold, and PTE activity dropped 40 000-fold. The reverse trajectory resulted in a 20 000-fold increase in PTE activity. There were two particularly notable characteristics of this evolutionary process: a minority of the mutations were located in the active site, despite the vast changes in activity, and the change in activity was noticeably gradual and smooth. Mutational analysis revealed that mutations were highly epistatic, with many of the remote mutations interacting with and modulating the effects of the active site mutations. The ability to capture every intermediate allowed us to extend beyond a simple description of mutation-activity-structure and probe what happened to the conformational landscape at each step. X-ray crystallographic data and molecular dynamics simulations of several intermediates revealed a pattern of shifting dynamics throughout the trajectory; large-scale motions of a 'lid' loop were minimized through intramolecular hydrogen bonding networks, and the productive conformation of a key active site residue was enriched by a radiating pattern of substitutions [36••]. The midpoint of this trajectory, R6 (and

Rev6 in the reverse direction), was of particular interest as it demonstrated high efficiency with both substrates. Crystallographic ensemble refinement of these midpoints revealed that their bifunctionality was due to their abilities to sample conformational sub-states similar to both the original and 'evolved' variants. These intermediates, only accessible through directed evolution experiments, highlight the role of conformational flexibility in the exploitation and evolution of promiscuous activities.

This pattern is observed in a different context in work by Biel *et al.* [38••] in which room-temperature X-ray crystallography was utilized to investigate the conformational heterogeneity of ubiquitin variants developed by Zhang *et al.* [39] a 'core' variant was designed for increased binding to deubiquitinase USP7, and then subjected to 'affinity maturation', in which random surface mutations were incorporated and variants screened for enhanced binding. Structures of the 'core' and 'affinity matured' variants were solved through room temperature X-ray crystallography, allowing for the elucidation of conformational heterogeneity in several regions, including the hinge-like β1β2 loop. The 'core' variant possessed substantial heterogeneity in this region, while the 'affinity matured' variant did not, due to the introduction of stabilizing interactions. The enrichment of a less-populated conformation through the rational selection of the 'core' mutations was proposed to disrupt the natural dynamics of protein, allowing the variant to sample a broader ensemble of sub-states (some of which are valuable in binding the target USP7), while the 'affinity maturation' froze out non-functional states, resulting in a stabilized, specialized variant. This mirrors the flexible, bifunctional PTE variants, which were then stabilized and specialized for their target activities.

Ancestral protein reconstruction experiments can also provide insights into the role of dynamics in protein evolution, by filling in some of the previously mysterious gaps in the evolutionary trajectories to modern-day proteins. For example, the ancestral reconstruction of GFP-like proteins by Kim *et al.* led to the identification of long-range conformational effects responsible for the evolution of green-to-red photoconversion. Interestingly, these effects were not accompanied by any substantial rearrangement of the active site residues or changes to the protein backbone, highlighting the importance of conformational sampling of amino acid sidechains and the contribution of outer-shell regions [40]. The evolution of mesophilic enzymes as organisms adapted to a cooler Earth has also been investigated through ancestral protein reconstruction. Nguyen *et al.* reconstructed ancient adenylate kinases (Adk), and determined their thermostabilities and activities, which showed no evidence of activity/stability trade-offs occurring [19]. One ancestral Adk variant possessed substantial activity at low temperatures as well as significant thermostability. This is in-keeping with the hypothesis that the magnitude of thermal motions is not directly important to catalytic activity, and is in fact often 'frozen out' (a rigid, thermostable ancestor was still capable of enhancing reaction rates at low temperatures), but rather conformational flexibility may serve as a useful starting point for the evolution of novel functions.

Perhaps the clearest example of the value for ancestral protein reconstruction in the study of protein dynamics is in deciphering the role of protein dynamics in the emergence of promiscuous activities and the evolution of specialist enzymes. In a study of amino acid binding proteins (AABP), Clifton *et al.* constructed proteins that represented common ancestors of modern AABP subfamilies [17•]. One of these ancestors, AncQR, displayed strong L-arginine binding, and promiscuous L-glutamine binding. X-ray structures of AncQR in complex with either L-arginine or L-glutamine revealed conformational differences in the active sites of the two complexes, with residual electron density in the AncQR-Arg complex matching the conformation of the AncQR-Glu complex active site. This suggested that the adventitious sampling of alternative states by AncQR underlies its promiscuous binding of glutamine, with evolution then stabilizing the minor Gln-specific to produce contemporary Gln-specific proteins. Recent work by Risso *et al.* studied ancestrally reconstructed β-lactamases, revealing that incorporation of a rationally selected mutation into highly dynamic ancestral β-lactamases allowed promiscuous Kemp eliminase activity, while the same substitution in more rigid, modern β-lactamases had no effect [41•]. These studies again highlight the importance of conformation freedom in the acquisition of new functions; with numerous accessible conformations increasing the likelihood of sampling a productive conformation.

These studies reinforce the case for a model in which functional promiscuity and conformational dynamism are interlinked as proposed by Tawfik and Tokuriki [42], where rare, adventitious, conformational sub-states can become productive in changing environmental conditions and be selected for and enriched through evolution. This model, and the generally positive view of protein dynamics that exists in the literature, has limitations, however. High conformational freedom is associated with low structural stability, a factor already identified as being valuable in evolution. Indeed, work by Dellus-Gur *et al.* highlights that while conformational flexibility can be important in the evolution of new function, the introduction of too much dynamism or disorder can impede evolution through negative epistasis [43•]. Similar observations were made in the study of PTE and ubiquitin, where it was clear that one of the strongest selective pressures was to *minimize* conformational dynamics, that is, rather than making the enzyme more dynamic, the optimization of the new activity involved stabilization of

Figure 3

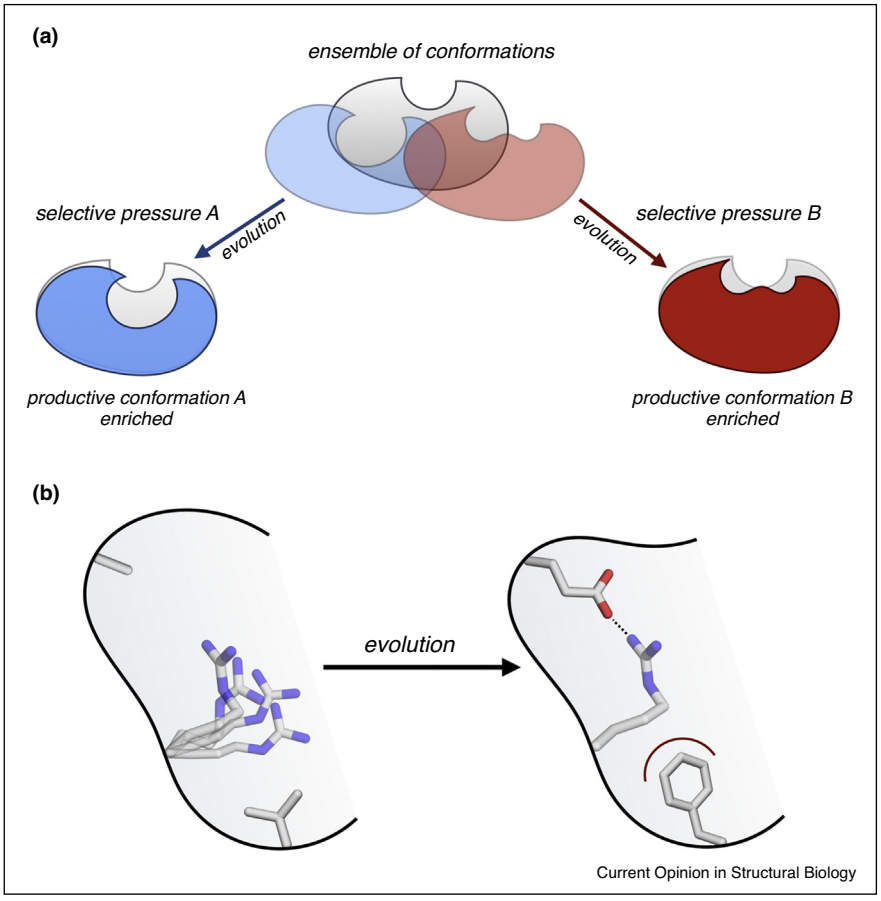

Evolution minimizes unnecessary motions. **(a)** An ensemble of conformations results in catalytic promiscuity. Selection for one of these activities results in the enrichment of the relevant conformation, and the 'freezing out' of non-productive motions. **(b)** Multiple conformations of a key residue are minimized through acquisition of substitutions that stabilize the productive conformation.

productive states. Thus, we should be cautious in terms of how we view the role of dynamics in molecular evolution and protein function — while they can make proteins more evolvable by allowing sampling of unique states, and some motions may be important for activity, proteins in general evolve to maximise the sampling of productive states (by minimizing the sampling of non-productive ones) [Figure 3].

The study of designed enzymes

The design of efficient enzymes continues to challenge our understanding of protein structure and function. Progress in protein design [44] has remarkably allowed the *de novo* creation of enzymes, although their substrate turnover (k_{cat}) values are typically several orders of magnitude lower than natural enzymes [45]. The low initial activity of some designed enzymes has meant that directed evolution is frequently, and successfully, used to optimize their activity. These studies are particularly important because they can reveal how designs are improved, and how subtle changes can turn a poor enzyme into an efficient one.

The low initial activity of designed enzymes can in some cases be traced to excessive active-site dynamics, which allows catalytic residues to depart from their designed conformations and sample non-productive states [Figure 4]. For example, in a designed Diels–Alderase [46], computational simulations suggested that the catalytic tyrosine was sampling a non-productive conformation due to a hydrogen bond with the backbone of a nearby alanine. This prompted the substitution of the alanine with a bulkier asparagine, which shifted the tyrosine to the designed conformation, and improved substrate activation [46]. In the designed KE07 Kemp eliminase [47], the catalytic glutamate was adversely affected by a salt bridge to a nearby lysine. Directed evolution corrected this mistake by introducing a new salt-bridge which shifted the lysine away from the catalytic glutamate, thereby increasing the basicity of the glutamate [48]. A similar correction was identified in the

Figure 4

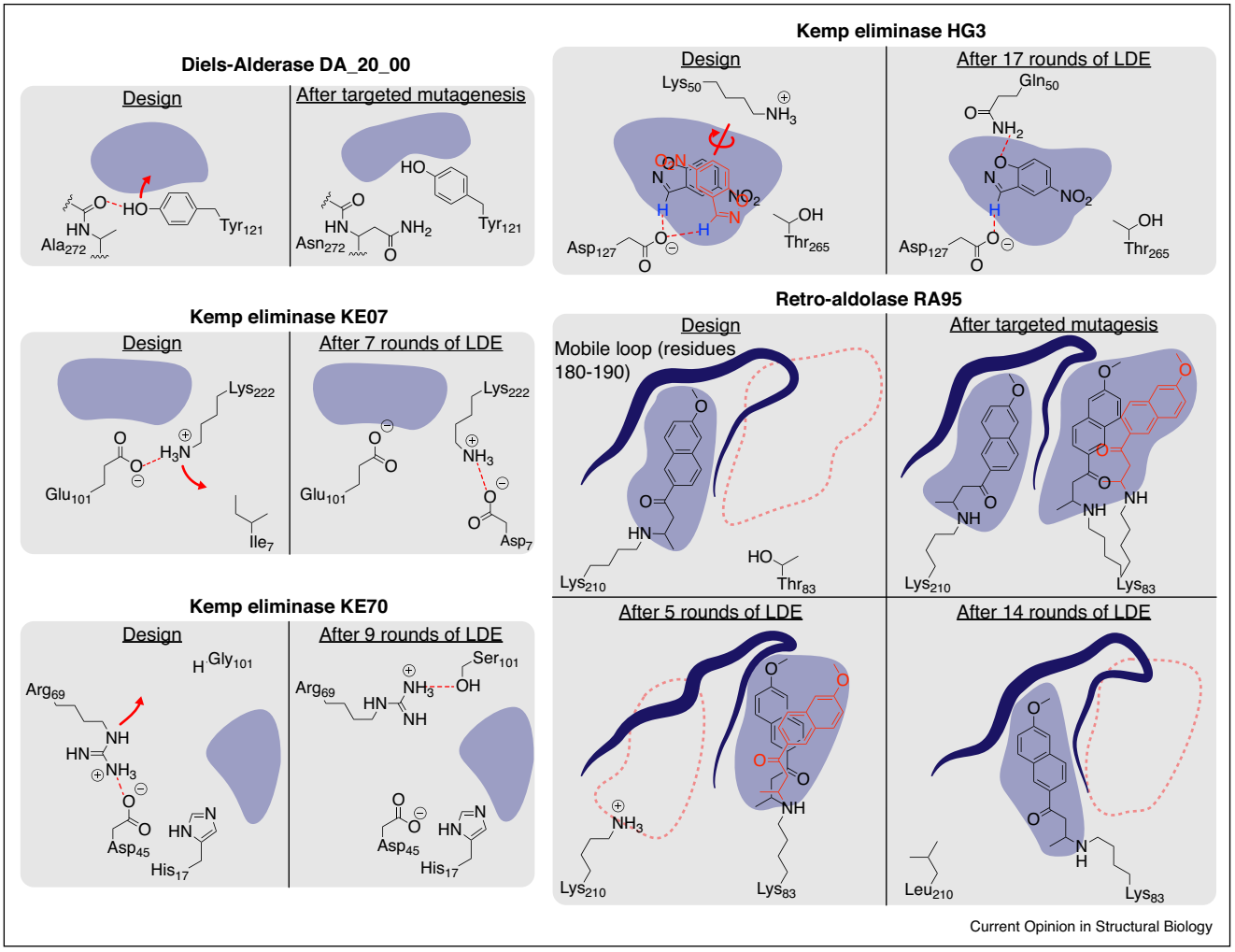

Overview of the role of flexibility in the optimization of designed enzymes. **Left three panels**: examples of designed enzymes where amino acid side-chain flexibility enabled catalytic residues to sample non-productive states. Targeted mutagenesis/laboratory directed evolution (LDE) selected productive states. **Right top panel**: an alternative substrate binding mode was selected and optimized in the laboratory directed evolution of the HG3 kemp eliminase. **Right bottom panel**: loop mobility was essential for the emergence and subsequent fine-tuning of a new binding site in the RA95 retro-aldolase.

optimization of the KE70 Kemp eliminase [49] in which directed evolution removed a deleterious interaction between the histidine-aspartic acid catalytic dyad and a nearby arginine.

As observed in ancestral reconstruction, active site flexibility has allowed alternative substrate binding modes, which has promoted evolution [Figure 4]. In the designed HG3 Kemp eliminase, the substrate was flipped by 90° relative to the design [50]. Although this new conformation precluded productive interaction with the designed hydrogen bond donor, directed evolution introduced a new hydrogen bond donor via a lysine to glutamine substitution [51]. This new catalytic residue could only function in the alternative substrate binding mode, and was critical to the ~230-fold increase in k_{cat}. Flexibility was also essential in the optimization of the RA95 retro-aldolase [52], where loop mobility was exploited to create a new substrate binding pocket with a new catalytic lysine [53,54]. In subsequent rounds of directed evolution, the original substrate binding pocket was re-created, however the new catalytic lysine was retained [55•].

These examples of directed evolution of designed proteins mirror previous examples from directed evolution of natural proteins, illustrating that enzyme evolvability and dynamism are linked [56], but also that excessive dynamics result in low efficiency that must be rescued through the gradual elimination of non-productive sampling.

Engineering protein dynamics

As our understanding of protein dynamics, and how protein dynamics can evolve to enhance protein function, develops, it is natural for attention to turn to the rational design and implementation of protein structural dynamics in an engineering setting. There are two related aspects of structural dynamics that could potentially be engineered: the conformational sampling of different states, and the rates at which different regions move. There have already been many studies in which rational changes to protein structure been shown to alter protein dynamics [36••,57,58]. However, we are still some way from being able to routinely improve protein function by manipulating conformational sampling, although there have been some notable achievements towards this ambitious goal [59•,60,61,62], and most protein design approaches do incorporate optimization of second-shell residues to constrain sampling of the active site [63–65]. Arguably, the biggest obstacle is the need to first understand the conformational landscape of the protein to be engineered, which is itself a major task. Interestingly, in the case of enzyme loop dynamics, it has been demonstrated that changes to the millisecond-timescale dynamics of various loop-motions in some β-lactamase variants did not have a substantial effect on activity, highlighting the dependence of enzymatic turnover rates on the rate limiting step, which is often chemical [58,66]. Similar results have been obtained from computational studies of adenylate kinase [67], suggesting that the rates of certain motions are unlikely to affect turnover rates until they approach the rate of the rate-limiting step, which in many cases is the chemical (bond making/breaking) step.

Conclusions

The examples described in this short review exemplify the profound insight that we can gain into complex processes, such as the evolution of protein dynamics, through observing intermediates in evolutionary processes. In this sense, laboratory evolution and ancestral protein reconstruction have been instrumental in building our understanding of how protein dynamics impact function, and how the conformational sampling of different sub-states can be subtly manipulated, in particular by remote outer-shell mutations, which have for a long time remained relatively mysterious. Two clear trends emerge from these studies: first, it is clear that structural dynamism allows sampling of states that could confer new activities; second, beyond this initial capture of promiscuous activity, evolution seems to progressively eliminate non-productive sampling, in a sense reducing non-essential dynamics.

References and recommended reading

Papers of particular interest, published within the period of review, have been highlighted as:

- • of special interest
- •• of outstanding interest

1. Okazaki K-I, Takada S: **Dynamic energy landscape view of coupled binding and protein conformational change: induced-fit versus population-shift mechanisms**. *Proc Natl Acad Sci U S A* 2008, **105**:11182-11187.
2. Boehr DD, Nussinov R, Wright PE: **The role of dynamic conformational ensembles in biomolecular recognition**. *Nat Chem Biol* 2009, **5**:789-796.
3. Levsh O *et al.*: **Dynamic conformational states dictate selectivity toward the native substrate in a substrate-permissive acyltransferase**. *Biochemistry* 2016, **55**:6314-6326.
4. Liu X *et al.*: **Distinct roles for conformational dynamics in protein–ligand interactions**. *Structure* 2016, **24**:2053-2066.
5. Grant BJ, Gorfe AA, Mccammon JA: **Large conformational changes in proteins: signaling and other functions**. *Curr Opin Struct Biol* 2010, **20**:142-147.
6. Henzler-Wildman KA *et al.*: **A hierarchy of timescales in protein dynamics is linked to enzyme catalysis**. *Nature* 2007, **450**:913-916.
7. Warshel A, Bora RP: **Perspective: defining and quantifying the role of dynamics in enzyme catalysis**. *J Chem Phys* 2016, **144**.
8. Hou G, Cui Q: **Stabilization of different types of transition states in a single enzyme active site: QM/MM analysis of enzymes in the alkaline phosphatase superfamily**. *J Am Chem Soc* 2013, **135**:10457-10469.
9. Leferink NGH *et al.*: **Impact of residues remote from the catalytic centre on enzyme catalysis of copper nitrite reductase**. *Nat Commun* 2014, **5**:1-8.
10. Singh P, Francis K, Kohen A: **Network of remote and local protein dynamics in dihydrofolate reductase catalysis**. *ACS Catal* 2015, **5**:3067-3073.
11. Morley KL, Kazlauskas RJ: **Improving enzyme properties: when are closer mutations better?** *Trends Biotechnol* 2005, **23**:231-237.
12. Guarnera E, Berezovsky IN: **Allosteric sites: remote control in regulation of protein activity**. *Curr Opin Struct Biol* 2016, **37**:1-8.
13. Kan SBJ, Lewis RD, Chen K, Arnold FH: **Directed evolution of cytochrome c for carbon–silicon bond formation: bringing silicon to life**. *Science (80-)* 2016, **354**:1048-1051.
14. Alvizo O *et al.*: **Directed evolution of an ultrastable carbonic anhydrase for highly efficient carbon capture from flue gas**. *Proc Natl Acad Sci U S A* 2014, **111**:16436-16441.
15. Stoltzfus CR *et al.*: **Two-photon directed evolution of green fluorescent proteins**. *Sci Rep* 2015, **5**:11968.
16. Merkl R, Sterner R: **Ancestral protein reconstruction: techniques and applications**. *Biol Chem* 2016, **397**:1-21.
17. • Clifton BE, Jackson CJ: **Ancestral protein reconstruction yields insights into adaptive evolution of binding specificity in solute-binding proteins**. *Cell Chem Biol* 2016, **23**:236-245.
This study utilized ancestral protein reconstruction to investigate the specificities of ancestral amino acid binding proteins. X-ray crystallography revealed a promiscuous ancestor could sample distinct conformations for the binding of two different substrates.
18. Khersonsky O, Tawfik DS: **Structure-reactivity studies of serum paraoxonase PON1 suggest that its native activity is lactonase**. *Biochemistry* 2005, **44**:6371-6382.
19. Nguyen V *et al.*: **Evolutionary drivers of thermoadaptation in enzyme catalysis**. *Science (80-)* 2017, **355**:289-294.
20. Babkova P, Sebestova E, Brezovsky J, Chaloupkova R, Damborsky J: **Ancestral haloalkane dehalogenases show robustness and unique substrate specificity**. *ChemBioChem* 2017, **18**:1448-1456.
21. Miton CM, Tokuriki N: **How mutational epistasis impairs predictability in protein evolution and design**. *Protein Sci* 2016, **25**:1260-1272.

22. van den Bedem H, Fraser JS: **Integrative, dynamic structural biology at atomic resolution—it's about time**. *Nat Methods* 2015, **12**:307-318.

23. Gierasch LM, Gershenson A: **Post-reductionist protein science, or putting Humpty Dumpty back together again**. *Nat Chem Biol* 2009, **5**:774-777.

24. Burnley BT, Afonine PV, Adams PD, Gros P: **Modelling dynamics in protein crystal structures by ensemble refinement**. *Elife* 2012, **1**:e00311.

25. Keedy DA, Fraser JS, van den Bedem H: **Exposing hidden alternative backbone conformations in X-ray crystallography using qFit**. *PLoS Comput Biol* 2015, **11**:1-22.

26. Keedy DA *et al.*: **Mapping the conformational landscape of a dynamic enzyme by multitemperature and XFEL crystallography**. *Elife* 2015, **4**:1-26.

27. Fraser JS *et al.*: **Hidden alternative structures of proline isomerase essential for catalysis**. *Nature* 2009, **462**:669-673.

28. Baldwin AJ, Kay LE: **NMR spectroscopy brings invisible protein states into focus**. *Nat Chem Biol* 2009, **5**:808-814.

29. Isogai S *et al.*: **Backbone NMR reveals allosteric signal transduction networks in the β1-adrenergic receptor**. *Nature* 2016, **314**:1-17.

30. Fenwick RB, van den Bedem H, Fraser JS, Wright PE: **Integrated description of protein dynamics from room-temperature X-ray crystallography and NMR**. *Proc Natl Acad Sci U S A* 2014 http://dx.doi.org/10.1073/pnas.1323440111.

31. Lindorff-Larsen K, Maragakis P, Piana S, Shaw DE: **Picosecond to millisecond structural dynamics in human ubiquitin**. *J Phys Chem B* 2016, **120**:8313-8320.

32. Bernardi RC, Melo MCR, Schulten K: **Enhanced sampling techniques in molecular dynamics simulations of biological systems**. *Biochim Biophys Acta Gen Subj* 2015, **1850**:872-877.

33. Romero-Rivera A, Garcia-Borràs M, Osuna S: **Computational tools for the evaluation of laboratory-engineered biocatalysts**. *Chem Commun* 2017, **53**:284-297.

34. Jackson CJ *et al.*: **Conformational sampling, catalysis, and evolution of the bacterial phosphotriesterase**. *Proc Natl Acad Sci U S A* 2009, **106**:21631-21636.

35. Tokuriki N *et al.*: **Diminishing returns and tradeoffs constrain the laboratory optimization of an enzyme**. *Nat Commun* 2012, **3**:1257.

36. •• Campbell E *et al.*: **The role of protein dynamics in the evolution of new enzyme function**. *Nat Chem Biol* 2016, **12**:944-950.
X-ray crystallographic ensemble refinement and MD simulations revealed the changes in conformational dynamics throughout the directed evolution of bacterial phosphotriesterase. Non-productive conformational dynamics were 'frozen out' throughout the trajectory.

37. Kaltenbach M, Jackson CJ, Campbell EC, Hollfelder F, Tokuriki N: **Reverse evolution leads to genotypic incompatibility despite functional and active site convergence**. *Elife* 2015, **4**:1-20.

38. •• Biel JT, Thompson MC, Cunningham CN, Corn JE, Fraser JS: **Flexibility and design: conformational heterogeneity along the evolutionary trajectory of a redesigned ubiquitin**. *Structure* 2016, **25** 739–749.e3.
In this study, room-temperature X-ray crystallography was used to identify conformational heterogeneity in a designed ubiquitin variant. Affinity maturation eliminated non-productive sub-states and enriched conformations for binding the target substrate.

39. Phillips AH *et al.*: **Conformational dynamics control ubiquitin-deubiquitinase interactions and influence in vivo signaling**. *Proc Natl Acad Sci U S A* 2013, **110**:11379-11384.

40. Kim H *et al.*: **A hinge migration mechanism unlocks the evolution of green-to-red photoconversion in GFP-like proteins**. *Structure* 2015, **23**:34-43.

41. • Risso VA *et al.*: **De novo active sites for resurrected Precambrian enzymes**. *Nat Commun* 2017, **8**:16113.
Ancestral protein reconstruction of β-lactamase variants revealed substitutions incorporated into a flexible ancestor allowed the acquisition of Kemp eliminase activity, while the same substitution in modern β-lactamases did not.

42. Tokuriki N, Tawfik DS: **Protein dynamism and evolvability**. *Science (80-)* 2009, **324**:203-207.

43. • Dellus-Gur E *et al.*: **Negative epistasis and evolvability in TEM-1 B-lactamase – the thin line between an enzyme's conformational freedom and disorder**. *J Mol Biol* 2015, **427**:2396-2409.
The crystallographic investigation of sign epistasis between two substitutions in TEM-1 β-lactamase conferring antibiotic resistance revealed the introduction of local disorder. Non-productive conformations dominated, highlighting the limitations of excessively flexible proteins.

44. Huang P-S, Boyken SE, Baker D: **The coming of age of de novo protein design**. *Nature* 2016, **537**:320-327.

45. Mak WS, Siegel JB: **Computational enzyme design: transitioning from catalytic proteins to enzymes**. *Curr Opin Struct Biol* 2014, **27**:87-94.

46. Siegel JB *et al.*: **Computational design of an enzyme catalyst for a stereoselective bi-molecular Diels–Alder reaction**. *Science (80-)* 2010, **329**:309-314.

47. Khersonsky O *et al.*: **Kemp elimination catalysts by computational enzyme design**. *Nature* 2008, **453**:190-195.

48. Khersonsky O *et al.*: **Evolutionary optimization of computationally designed enzymes: Kemp eliminases of the KE07 series**. *J Mol Biol* 2010, **396**:1025-1042.

49. Khersonsky O *et al.*: **Optimization of the in-silico-designed Kemp eliminase KE70 by computational design and directed evolution**. *J Mol Biol* 2011, **407**:391-412.

50. Privett HK *et al.*: **Iterative approach to computational enzyme design**. *Proc Natl Acad Sci U S A* 2012, **109**:3790-3795.

51. Blomberg R *et al.*: **Precision is essential for efficient catalysis in an evolved Kemp eliminase**. *Nature* 2013, **503**:418-421.

52. Jiang L *et al.*: **De novo computational design of retro-aldol enzymes**. *Science (80-)* 2008, **319**:1387-1391.

53. Giger L *et al.*: **Evolution of a designed retro-aldolase leads to complete active site remodeling**. *Nat Chem Biol* 2013, **9**:494-498.

54. Althoff EA *et al.*: **Robust design and optimization of retroaldol enzymes**. *Protein Sci* 2012, **21**:717-726.

55. • Obexer R *et al.*: **Emergence of a catalytic tetrad during evolution of a highly active artificial aldolase**. *Nat Chem* 2017, **9**:50-56.
This study used an ultrahigh-throughput screen to further optimize the activity of the computationally designed RA95 retro-aldolase. A co-crystal structure of the evolved variant with a mechanism-based inhibitor revealed the role of loop mobility in the restoration of the original designed substrate binding site.

56. Tokuriki N, Tawfik DS: **Protein dynamism and evolvability**. *Science (80-)* 2009, **324**:203-208.

57. Osuna S, Jiménez-Osés G, Noey EL, Houk KN: **Molecular dynamics explorations of active site structure in designed and evolved enzymes**. *Acc Chem Res* 2015, **48**:1080-1089.

58. Gobeil SMC *et al.*: **Maintenance of native-like protein dynamics may not be required for engineering functional proteins**. *Chem Biol* 2014, **21**:1330-1340.

59. • Hoersch D, Kortemme T: **A model for the molecular mechanism of an engineered light-driven protein machine**. *Structure* 2016, **24**:576-584.
The rational engineering of a light-driven re-engineered chaperonin was achieved through in silico experiments and analysis of the conformational cycle, which allowed for rational manipulation of domain dynamics.

60. Davey JA, Chica RA: **Multistate approaches in computational protein design**. *Protein Sci* 2012, **21**:1241-1252.

61. Davey JA, Damry AM, Euler CK, Goto NK, Chica RA: **Prediction of stable globular proteins using negative design with non-native backbone ensembles**. *Structure* 2015, **23**:2011-2021.

62. Pandelieva AT *et al.*: **Brighter red fluorescent proteins by rational design of triple-decker motif**. *ACS Chem Biol* 2016, **11**:508-517.

63. Teze D, Daligault F, Ferrières V, Sanejouand YH, Tellier C: **Semi-rational approach for converting a GH36 α-glycosidase into an α-transglycosidase**. *Glycobiology* 2015, **25**:420-427.

64. Tinberg CE *et al.*: **Computational design of ligand binding proteins with high affinity and selectivity**. *Nature* 2014, **501**:212-216.

65. Tomatis PE, Rasia RM, Segovia L, Vila AJ: **Mimicking natural evolution in metallo-beta-lactamases through second-shell ligand mutations**. *Proc Natl Acad Sci U S A* 2005, **102**:13761-13766.

66. Tokuriki N, Jackson CJ: **Enzyme dynamics and engineering: one step at a time**. *Chem Biol* 2014, **21**:1259-1260.

67. Pisliakov AV, Cao J, Kamerlin SCL, Warshel A: **Enzyme millisecond conformational dynamics do not catalyze the chemical step**. *Proc Natl Acad Sci U S A* 2009, **106**:17359-17364.